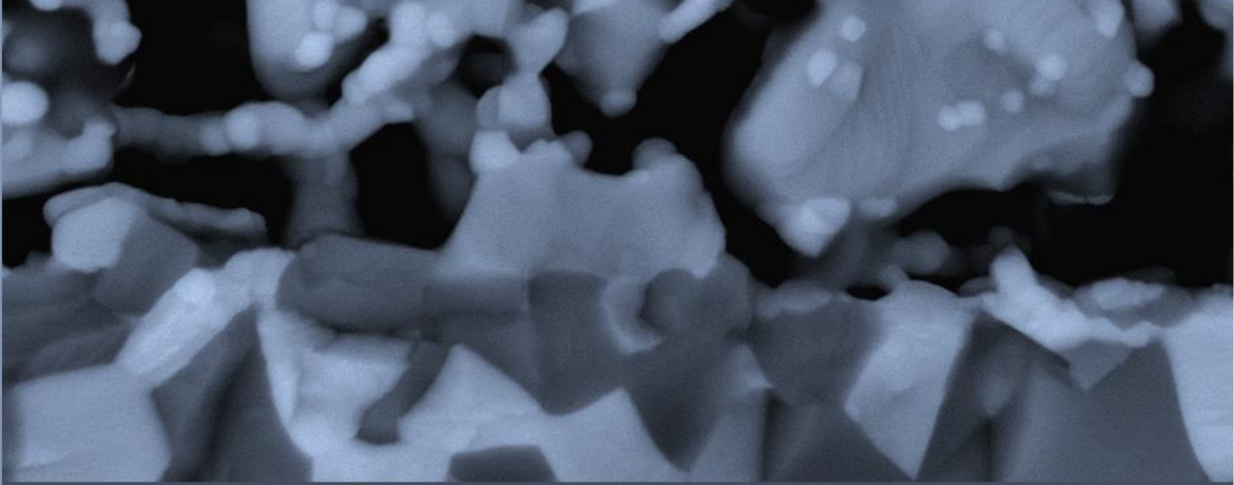

Development of ceramic MIEC membranes for oxygen separation: Application in catalytic industrial processes

Thesis submitted by
Julio García Fayos
To apply for the Degree of Doctor

Supervisor:
Prof. José Manuel Serra Alfaro

Valencia, July 2017

UNIVERSITAT
POLITÈCNICA
DE VALÈNCIA

INSTITUTO DE
TECNOLOGÍA
QUÍMICA

CSIC

Acknowledgements

The time goes by, *the Sun is the same (in a relative way) but we are older*. New milestones are achieved, and new horizons appear ahead. While I am getting lost in these kind of thoughts, the Word cursor is blinking impatiently, waiting for me to finish the writing.

First of all, I would like to thank Sonia, for talking me about a vacancy for a PhD thesis in the ITQ, conversation that allowed me to start working in an amazing research group in the ITQ: Sonia, María Fabuel, María Balaguer, Vicente, Laura, Raquel, Cecilia, Fidel, Núria, Mateusz, David, Cyril, Sara, Juan, and Álvaro; thanks to you all, my colleagues during all this time. Thanks for your direct contribution in the realization of this thesis: mentoring and guiding me at the beginning, helping me in the preparation of samples and supplying me with some nice ones, discussing the results and all the science behind these, making suggestions and helping me when I needed… And in addition to this, thanks for all the non-scientific moments, full of conversations and jokes that helped to release the daily stress. I could list a lot of things, but it could take a whole chapter. Each of you know the moments we have shared, you can be sure I remember and appreciate them.

I also want to express my gratitude to the ITQ people (workshop department, characterization and administration staff) for all the help in the construction and maintenance of test benches and gas supply, the characterization of samples and all the issues concerning contracts, travels and thesis paperwork.

I would also like to thank NASA-OTM and GREEN-CC projects, both funded from the European Community's Seventh Framework Program. Participating in these projects has been a very good opportunity for meeting awesome scientists and persons, and for conducting very nice works and studies, some of them presented in this thesis. Amongst all the research groups, I would like to specially thank people from Forschungszentrum Jülich, Risø National Laboratory for Sustainable Energy, University of Twente and Imperial College.

Family and friends have had an important role during these years. My parents, always at my side, ready for offering help and support, gràcies! And I also thank my friends, despite I have told you only a little of this scientific stuff, thanks for all these good moments around a table full of beers, running on the mountains, playing with our kids in the playground, sharing holidays and celebrations… Moltes gràcies també a tú Emili, per l’energia i els ànims que em vas transmetre, sempre et duré al cor amic.

And finally, I would like to thank José M. Serra, for giving me the opportunity of joining such an amazing research group and trusting me to carry out this work, for all the ideas, indications and help provided during this time that allowed me to learn a lot and having very good results, and for (despite the heavy workload) making things easier when I needed to take care of personal matters.

A Marta, a Júlia i a Pere

Per tots els somriures,

per totes les cançons,

per tots els dies

gaudint amb vosaltres del món

```
LOAD "" L
```

OUTLINE

0. Preamble. 15
  Summary 15
  Resumen 17
  Resum 19
  Context and scope of the Thesis 21
1. Introduction 25
  1.1. Gas separation membranes. 25
  1.2. Mixed ionic-electronic conduction. 26
    1.2.1. Fluorites. 27
    1.2.2. Perovskites. 27
    1.2.3. Composite materials. 28
  1.3. Oxygen transport mechanisms. 29
    1.3.1. Bulk diffusion. 30
    1.3.2. Surface exchange reactions. 32
  1.4. Performance optimization. 33
    1.4.1. Material properties. 34
    1.4.2. Operation conditions. 34
    1.4.3. Thickness reduction. 35
    1.4.4. Surface modification. 36
    1.4.5. Protective layers. 36
  1.5. Applications of Oxygen Transport Membranes. 37
    1.5.1. Available technologies for the production of oxygen. 37
    1.5.2. Application of OTMs in Power Generation and CCS: Oxyfuel and Gasification technologies. 39
    1.5.3. Chemical Industry Applications. 42
  1.7. References. 46
2. Experimental. 57
  2.1. Material synthesis. 57
    2.1.1. Co-precipitation. 57
    2.1.2. Pechini or sol-gel route 58

2.2. Material processing. Sample preparation. 58

2.2.1. Membranes and electrolytes. 58

2.2.2. Production of LSCF porous supports by freeze-casting. 59

2.2.3. Rectangular bars. 60

2.2.4. Catalytic layer/Electrode deposition. 60

2.3. Structural characterization. 61

2.3.1. Scanning Electron Microscopy. 61

2.3.2. X-Ray Diffraction. 62

2.3.4. Raman spectroscopy. 63

2.4. Thermal analysis. 64

2.4.1. Thermo-gravimetry (TG). 64

2.5. Electrochemical characterization. 64

2.5.1. DC total electrical conductivity. 64

2.5.2. Electrochemical Impedance Spectroscopy (EIS). 65

2.6. Membrane performance characterization. 68

2.6.1. Experimental set-up. Planar membranes. 68

2.6.2. Experimental set-up. Capillary membranes. 70

2.6.3. Oxygen flux calculation. 72

2.6.4. Conversion, selectivity and yield calculation. 73

2.7. References. 74

3. Permeation studies on BSCF membranes. 77

3.1. Introduction. 77

3.2. Planar membranes. 78

3.2.1. Membrane microstructure. 78

3.2.2. Oxygen permeation: thickness variation. 80

3.2.3. Oxygen permeation: catalytic activation. 85

3.2.4. Oxidative De-Hydrogenation of Ethane (ODHE) on BSCF membrane reactors. 90

3.3. Tubular membranes. 96

3.3.1. Capillary membrane description. 97

3.3.2. Oxygen permeation. 99

3.3.3. Oxidative Coupling of Methane. 102

3.4. Conclusions. 116

3.5. References. 118

4. Permeation studies on LSCF membranes 125

4.1. Introduction. 125

4.2. Tape-cast supported LSCF membranes. 126

4.2.1. Characterization of the membrane assembly microstructure. 126

4.2.2. Effect of sweep gas flux on the oxygen permeation. 126

4.2.3. Effect of oxygen partial pressure in feed on the oxygen permeation. 129

4.2.4. Effect of catalytic layer on the oxygen permeation. 134

4.2.5. Effect of CO_2 content in sweep stream on the oxygen permeation. 136

4.3. Freeze-cast supported LSCF membranes. 138

4.3.1. Production of porous supports by means of freeze casting. 138

4.3.2. Effect of the freeze-cast porous support. 140

4.3.3. Effect of membrane catalytic activation. 146

4.4. Conclusions. 153

4.5. References. 155

5. Oxygen permeation on an Asymmetric CGO-Co membrane. 163

5.1. Introduction. 163

5.2. Membrane assembly microstructure. 164

5.3. Oxygen permeation tests. 166

5.3.1. Temperature and sweep gas dependence. 166

5.3.2. Effect of oxygen partial pressure in feed stream. 168

5.3.3. Effect of CO_2 content in sweep stream. 169

5.3.4. Effect of CH_4 content in sweep stream 171

5.3.5. Carbon dioxide stability test. 172

5.4. Conclusions. 177

5.5. References. 178

6. Composite oxygen-transport membranes for operation in CO_2/SO_2-rich gas environments. 183

6.1. Introduction. 183

6.2. Oxygen permeation and stability of dual-phase bulk membranes. 184

6.2.1. Microstructural characterization. 184

6.2.2. EC measurements. 186

6.2.3. Oxygen permeation characterization. 187

6.3. Catalytic study on the activation of the system 60NFO-40CTO. 194

6.3.1. Electrochemical characterization of reference case. 195

6.3.2. Electrochemical characterization of activated cases. 197

6.3.3. Oxygen permeation tests. 202

6.4. Oxygen permeation in thin supported dual-phase membranes. 206

6.4.1. Chemical compatibility. 206

6.4.2. Microstructural study 207

6.4.3. Oxygen permeation tests. 209

6.5. Conclusions. 214

6.6. References. 216

7. Conclusions and remarks. 225

8. Scientific contribution. 231

8.1. Publications. 231

8.2. Patents. 232

8.3. Congress participations. 232

Oral presentations 232

Selected posters presentations 233

9. Acronyms and symbols. 235

10. Figures and Tables list. 237

10.1. Figures. 237

10.2. Tables. 245

0. PREAMBLE

0. Preamble.

Summary

The present Thesis is focused on the development of ceramic membranes for the production of O_2 as possible substitute for conventional Air Separation Units in several industrial applications (e.g. steel industry, power generation, chemical industry…). For that aim, different materials (perovskites, fluorites and composites) and different membrane architectures (planar monolithic and asymmetric, and tubular) have been considered. Catalytic activation has also been taken into account for the optimization of membranes permeation, as well as for improving the selectivity/yield of chemical reactions.

With regard to the considered materials, two materials were selected amongst perovskites: BSCF ($Ba_{0.5}Sr_{0.5}Co_{0.8}Fe_{0.2}O_{3-\delta}$) and LSCF ($La_{0.6}Sr_{0.4}Co_{0.2}Fe_{0.8}O_{3-\delta}$); CGO ($Ce_{0.8}Gd_{0.2}O_{2-\delta}$) amongst fluorites; and as a composite material, a mixture consisting of different ratios of Fe_2NiO_4 spinel and $Ce_{0.8}Tb_{0.2}O_{2-\delta}$ fluorite (NFO-CTO) has been selected.

In the chapter dedicated to BSCF, the influence of thickness and the use of porous supports in the permeation was studied by considering membranes with thicknesses in the range of 0.75-0.16 mm and thin supported membranes presenting thicknesses of 20-60 μm. As expected, an improvement in the oxygen fluxes was observed for the thinner membranes. With respect to the porous supports, it was found that they contribute with an additional resistance within the permeation process, reducing the potential improvement when reducing thickness. The conducted tests also allowed to study more in deep the different processes affecting oxygen membranes, as well as defining a permeation model for monolithic and asymmetric membranes. An optimization strategy for the permeation improvement was defined, thus establishing the most suitable conditions regarding gas flow rates, pO_2 and temperature. Aiming to improve the surface reactions involved in the oxygen permeation the use of catalytic layers was considered, by means of the addition of porous BSCF backbones. The best results were obtained when coating both sides of membranes with catalytic layers. Furthermore, for the case of asymmetric membranes a study consisting of the catalytic promotion with Ag and Pd nanoparticles on BSCF porous backbones was conducted, thus improving oxygen reduction reactions at permeate side and subsequently the oxygen permeation. The best results were obtained with Pd activation, especially at low temperatures. The concept of BSCF activated membranes was also considered for the production of ethylene by means of the oxidative de-hydrogenation of ethane, obtaining high C_2H_4 yields. BSCF membranes presenting tubular geometry were characterized for applications such as production of O_2 and production of ethylene by means of oxidative coupling of methane.

Due to the limited stability of BSCF under certain conditions, LSCF was considered for conducting studies under CO_2-containing atmospheres (oxyfuel applications). For that aim, all-LSCF asymmetric membranes were developed by means of

sequential tape casting and freeze casting. By using these techniques, very thin LSCF membranes in the range of 30 μm were produced, being supported over porous LSCF substrates. The application of these techniques results in different substrates porosity, i.e. a random porosity for the case of tape casted support and a hierarchical porosity for the freeze casted support. For both systems, a complete permeation study with a focus on permeation performance under CO_2 environments was conducted. Furthermore a study focused on the different substrates was carried out for determining the structure presenting the lower gas diffusion resistance. Despite very good results were obtained for both membrane types, even under CO_2 conditions, freeze casted membranes reached higher oxygen fluxes, being optimized with the catalytic activation of membranes.

The materials presenting fluorite structure stand out for their stability properties under reaction conditions (reducing atmospheres) or when exposed to CO_2 environments (power generation applications). Nevertheless, delivered oxygen fluxes are typically low. Hence, a thin 40 μm-thick CGO-Co membrane activated with Pd nanoparticles was considered for conducting a study on O_2 permeation performance, and its behaviour when exposed to CO_2 and CH_4-containing atmospheres. A good stability was demonstrated, as well as a significant improvement in oxygen permeation when exposed to CH_4 concentrations up to 80% in Argon. Thus, CGO-Co membranes present promising properties for their application in oxyfuel processes and for the conduction of chemical reactions.

Finally, a study on composite materials based on Fe_2NiO_4- $Ce_{0.8}Tb_{0.2}O_{2-\delta}$ was carried out, with a special focus on their consideration for oxyfuel applications. A first evaluation on the CTO content and its relation with oxygen permeation was conducted, determining that a higher ionic phase ratio in the membrane results in a higher permeation. A composite consisting of 50% Fe_2NiO_4 – 50% $Ce_{0.8}Tb_{0.2}O_{2-\delta}$ was considered for performing a permeation study under harsh application conditions, with a presence of 250 ppm SO_2 in the gas stream. Despite the significant loss in permeation, the composite material resulted to be stable after a long exposure to SO_2. A broad study about the effect of CO_2 and SO_2 on the oxygen surface reactions was conducted by means of Electrochemical Impedance Spectroscopy (EIS) measurements on 60NFO-40CTO electrodes. It was observed a significant effect of SO_2 on the surface exchange reactions by promoting the deactivation of the O_2 active sites, due to a SO_2 adsorption on them. This effect was minimized by catalytically activating 60NFO-40CTO porous backbones with different catalysts, being characterized by EIS under CO_2&SO_2 conditions. This improvement in the performance was later confirmed when performing oxygen permeation tested under the same conditions. Oxygen permeation on composite membranes was also improved in a notable way by reducing their thickness down to 10 μm. These thin membranes were produced by depositing a thin 60NFO-40CTO layer on a LSCF freeze casted support.

Resumen

La presente Tesis Doctoral trata sobre el desarrollo de membranas cerámicas para la producción de O_2, así como de su uso en distintas aplicaciones industriales (producción de energía, industria química…). Para ello se han considerado distintos tipos de materiales (perovskitas, fluoritas y composites) y distintas arquitecturas de membrana (planas monolíticas, planas soportadas y tubulares). También se ha recurrido a la activación catalítica para optimizar la permeación de las membranas, así como la selectividad/rendimiento en reacciones químicas.

En cuanto a materiales, dentro del grupo de las perovskitas se ha considerado dos tipos de materiales: el BSCF ($Ba_{0.5}Sr_{0.5}Co_{0.8}Fe_{0.2}O_{3-\delta}$) y el LSCF ($La_{0.6}Sr_{0.4}Co_{0.2}Fe_{0.8}O_{3-\delta}$); dentro de las fluoritas el CGO ($Ce_{0.8}Gd_{0.2}O_{2-\delta}$), y como material composite un mezcla de 60% vol. de espinela Fe_2NiO_4 y 40% vol. fluorita ($Ce_{0.8}Tb_{0.2}O_{2-\delta}$), denominado como 60NFO-40CTO.

En el capítulo dedicado al BSCF se realizó un estudio sobre la influencia del espesor y el uso de soportes porosos en la permeación de O_2. Se observó una mejora de los flujos de O_2 para las membranas más finas, y también el papel de los soportes porosos, los cuales contribuyen con una resistencia adicional en el proceso de permeación, disminuyendo así la potencial mejora al reducir el espesor. El estudio llevado a cabo permitió también conocer más en profundidad los procesos que afectan a los distintos tipos de membranas, y establecer un modelo de permeación para membranas monolíticas y soportadas. Con ello se estableció una estrategia de optimización de la permeación al considerar la operación bajo las condiciones de caudal, pO_2 y T más adecuadas. Con el fin de mejorar las reacciones superficiales involucradas en la permeación, se recurrió a la activación catalítica mediante la adición de capas porosas de BSCF, obteniendo así mejores resultados para las membranas con capas en ambos lados. Para el caso de membranas soportadas se realizó un estudio de activación catalítica con adición de nanopartículas de Ag y Pd para la mejora de las reacciones de reducción de O_2. Los mejores resultados se obtuvieron con la activación con Pd, especialmente a bajas temperaturas. El concepto de membranas de BSCF activadas superficialmente se consideró también para la producción de etileno a partir de la deshidrogenación oxidativa de etano (ODHE), obteniendo rendimientos de C_2H_4 muy elevados. Membranas de BSCF con geometría tubular fueron caracterizadas para aplicaciones de producción de O_2 y etileno mediante acoplamiento oxidativo de metano (OCM).

Debido a las limitaciones de estabilidad que presenta el BSCF, se consideró al LSCF para su uso en aplicaciones con atmósferas conteniendo CO_2 (oxicombustión). Para ello se desarrollaron membranas asimétricas soportadas en soportes porosos de LSCF mediante dos técnicas: tape casting y freeze-casting. Dichas técnicas de fabricación resultan en porosidades muy distintas, una porosidad desordenada para el caso de tape casting y una con porosidad vertical orientada para el caso de freeze-casting. Completos estudios de permeación se realizaron para ambos casos, además de estudiar el tipo de soporte poroso

ofreciendo menos resistencia a la difusión de los gases. Pese que para ambos tipos de membranas se obtuvieron muy buenos flujos de oxígeno, incluso bajo condiciones de CO_2, para el caso de membranas con soporte fabricado mediante freeze-casting se consiguieron mayores valores de permeación, optimizándolos incluso con la activación catalítica.

Los materiales con estructura fluorita destacan por sus propiedades de estabilidad bajo condiciones de reacción (atmósferas reductoras) o cuando son expuestos a CO_2 (aplicaciones de producción de energía). Sin embargo, los valores de permeación suelen ser muy bajos. Así pues, se consideró una membrana de CGO-Co de 40 μm de espesor activada con nanopartículas de Pd para llevar a cabo un estudio de sus propiedades para la producción de O_2, su comportamiento en contacto con CO_2 y con atmósferas conteniendo CH_4. La buena estabilidad demostrada y la mejora sustancial de los flujos de O_2 bajo ambientes reductores de hasta el 80% CH_4 en argón, hacen que este tipo de materiales posean propiedades prometedoras para aplicaciones de oxicombustión y reacciones químicas.

Finalmente, se realizó un estudio sobre materiales composites formados por 60% Fe_2NiO_4 – 40% $Ce_{0.8}Tb_{0.2}O_{2-\delta}$ y su implementación en aplicaciones de oxicombustión. Para ello se realizó una primera evaluación del contenido en CTO y su relación con la permeación de O_2, determinando que una mayor proporción de la fase iónica en la membrana resulta en unos mayores valores de permeación. Un composite consistente en 50% Fe_2NiO_4 – 50% $Ce_{0.8}Tb_{0.2}O_{2-\delta}$ se consideró para la realización de tests de permeación bajo condiciones agresivas de oxicombustión, con presencia de 250 ppm de SO_2. Pese al notable descenso en los flujos de O_2, el material resultó ser completamente estable tras una exposición continuada al SO_2. Un amplio estudio del efecto del CO_2 y del SO_2 sobre las reacciones superficiales se realizó mediantes medidas de espectroscopia de impedancia electroquímica (EIS) en electrodos de 60NFO-40CTO, demostrando que el SO_2 afecta significativamente a las reacciones superficiales mediante procesos de adsorción competitiva en los centros activos. Se consiguió minimizar el efecto del SO_2 sobre las reacciones de intercambio superficial al activar las membranas con capas catalíticas porosas de 60NFO-40CTO con distintos catalizadores, siendo caracterizadas por EIS bajo condiciones de SO_2, y confirmando posteriormente esta mejora en tests de permeación en las mismas condiciones. Así mismo, se optimizó de una manera notable la permeación de las membranas de 60NFO-40CTO mediante una reducción del espesor. Dichas membranas finas se soportaron sobre sustratos porosos de LSCF fabricados mediante freeze-casting.

Resum

La present tesi doctoral tracta sobre el desenvolupament de membranes ceràmiques per a la producció d’oxigen, així com del seu ús en diferents aplicacions industrials (producció d’energia. Industria química...). Amb aquest objectiu s’han considerat distints tipus de materials (perovskites, fluorites i composites) i distintes arquitectures de membrana (planes monolítiques, planes suportades i tubulars). També s’ha considerat l’activació catalítica per a optimitzar la permeació de les membranes, així com la selectivitat/rendiment de reaccions químiques.

En quant als materials, dintre del grup de les perovskites s’han considerat dos tipus de materials: el BSCF ($Ba_{0.5}Sr_{0.5}Co_{0.8}Fe_{0.2}O_{3-\delta}$) i el LSCF ($La_{0.6}Sr_{0.4}Co_{0.2}Fe_{0.8}O_{3-\delta}$); dintre de les fluorites el CGO ($Ce_{0.8}Gd_{0.2}O_{2-\delta}$), i com a material composite una combinació de 60% vol. d’espinela Fe_2NiO_4 i 40% vol. fluorita ($Ce_{0.8}Tb_{0.2}O_{2-\delta}$), anomenat com 60NFO-40CTO.

Al capítol dedicat al BSCF es va realitzar un estudi sobre la influència de l’espessor i l’ús de suports porosos en la permeació d’O_2. Es va observar una millora dels fluxos d’O_2 per al cas de les membranes més fines, i també el paper dels suports porosos, els quals contribueixen afegint una resistència al procés de permeació, disminuint així la potencial millora deguda a la reducció de l’espessor. L’estudi també va permetre conèixer més en profunditat els processos que afecten als diferents tipus de membranes, i establir un model de permeació per a membranes monolítiques i suportades. Amb allò es va establir una estratègia d’optimització de la permeació al considerar l’operació baix les condicions de caudals, pO_2 i temperatura més adients. Amb el fi de millorar les reaccions superficials involucrades en la permeació, es va recórrer a l’activació catalítica mitjançant l’adició de capes poroses de BSCF, obtenint així millors resultats per a les membranes activades a ambdós costats. Per al cas de les membranes suportades es va realitzar un estudi d’activació catalítica amb l’adició de partícules de Ag i Pd, amb l’objectiu de millorar les reaccions de reducció de l’O_2. Els millors resultats es van obtindré amb l’activació amb Pd, especialment a baixes temperatures. El concepte de membranes de BSCF activades superficialment es va considerar també per a la producció d’etilè a mitjançant la deshidrogenació oxidativa d’età (ODHE), obtenint rendiments de C_2H_4 molt elevats. Membranes de BSCF amb geometria tubular van ser caracteritzades per a aplicacions de producció d´O_2 i C_2H_4 mitjançant l’acoplament oxidatiu de metà (OCM).

Degut a les limitacions d’estabilitat que presenta el BSCF, es va considerar al LSCF per al seu ús en aplicacions amb atmosferes contenint CO_2 (oxicombustió). Així doncs, es van desenvolupar membranes asimètriques suportades sobre suports porosos de LSCF fabricats fent servir dos tècniques: tape càsting i freeze càsting. Aquestes tècniques de fabricació resulten en porositats de substrat molt diferents: una porositat desordenada per al cas de tape càsting i una porositat vertical orientada per al cas de freeze càsting. Es van realitzar estudis complets de permeació per a ambdós casos, a més d’estudiar el tipus de suport porós que

ofereix una menor resistència a la difusió dels gasos. Malgrat que es van obtindré molts bons fluxos d’O_2 per als dos tipus de membranes, inclús sota condicions amb CO_2, per al cas de les membranes amb suport fabricat per freeze càsting es van aconseguir majors valors de permeació, sent inclús optimitzats amb l’activació catalítica.

Els materials amb estructura fluorita destaquen per les seues propietats d’estabilitat sota condicions de reacció (atmosferes reductores) o quan són exposats a CO_2 (aplicacions per a la producció d’energia). Malgrat això, els valors de permeació solen ser molt baixos. Així doncs, es va considerar una membrana de CGO-Co de 40 μm d’espessor activada amb partícules de Pd per a realitzar un estudi sobre les seues propietats en quant a la producció d’O_2, el seu comportament amb el contacte amb CO_2 i atmosferes reductores contenint CH_4. La bona estabilitat demostrada i una millora substancial dels fluxos d’O_2 sota ambients reductors amb una concentració de metà de fins al 80% en Argó, fan que aquest tipus de material presente propietats prometedores per a aplicacions d’oxicombustió i reaccions químiques.

Finalment, es va realitzar un estudi sobre materials composites formats per 60% Fe_2NiO_4 – 40% $Ce_{0.8}Tb_{0.2}O_{2-\delta}$ i la seua implementació en aplicacions d’oxicombustió. Amb aquest fi es va realitzar una primera avaluació del contingut en CTO i la seua relació amb la permeació d’O_2, observant una millora de la permeació amb un major contingut de CTO. Un composite consistent en 50% Fe_2NiO_4 – 50% $Ce_{0.8}Tb_{0.2}O_{2-\delta}$ es va considerar per a la realització de tests de permeació amb condicions agressives d’oxicombustió, amb presència de 250 ppm de SO_2. Malgrat el notable descens en els fluxos d’O_2, el material resulta ser completament estable després d’una exposició continuada al SO_2. L’estudi es va ampliar al mesurar també l’efecte del CO_2 i del SO_2 sobre les reaccions superficials, allò es va realitzar fent ús de la tècnica d’espectroscòpia d’impedància electroquímica (EIS) en elèctrodes de 60NFO-40CTO. Així es va demostrar que el SO_2 afecta significativament a les reaccions superficials mitjançant processos d’adsorció competitiva O_2-SO_2 als centres actius. Es va aconseguir minimitzar l’efecte del SO_2 sobre les reaccions d’intercanvi superficial al activar les membranes amb capes catalítiques poroses de 60NFO-40CTO amb diferents catalitzadors. Aquestes capes van ser caracteritzades per EIS sota condicions de SO_2, confirmant posteriorment la millora observada al realitzar tests de permeación considerant les mateixes condicions. Així mateix, es va optimitzar d’una manera notable la permeació de les membranes de 60NFO-40CTO mitjançant una reducció de l’espessor. Aquestes membranes fines es van suportar a sobre de substrats porosos de LSCF fabricats per freeze càsting.

Context and scope of the Thesis

Oxygen is considered as a key product for a wide variety of industrial processes. With more than 100 Mton produced annually is the third largest commodity worlwide. This huge production is mainly consumed by three sectors: steel industry (40.7%), power generation (29.4%) and chemical industry (22.4%). Currently, O_2 is mainly obtained by means of cryogenic distillation of air, nevertheless this process presents important drawbacks mainly related to the high production energy costs, since it operates at very low temperatures and high pressures, being only economically viable for large installations. Another way for producing oxygen is by means of Pressure Swing Adsorption (PSA), where N_2 is selectively adsorbed on zeolites or on carbon molecular sieves, thus obtaining an O_2-rich stream. PSA is suitable for the production of O_2 at small scale, but it is a discontinuous process and presents very high production costs if O_2 purities above 95% are needed. This avoids its consideration for industrial processes requiring the supply of high purity O_2.

Oxygen Transport Membranes (OTM) are ceramic materials presenting mixed electronic-ionic conductivity (MIEC) that can produce O_2 of high purity (>99.999%) due to the ability of diffusing O^{2-} through their crystal lattice at high temperature (>500 ºC). Despite the need of high operation temperatures for performing the oxygen separation, OTMs are in a very good position for replacing conventional air distillation for pure O_2 production in small and medium-scale applications. The main reasons are the higher O_2 purity that can be obtained (up to 100%) as well as the fact that O_2 production costs can be reduced up to 35%[1]. OTMs can provide the perfect balance between energy consumption and overall plant efficiency due to the proper thermal integration in several industrial processes, such as fuel fired power plants. Furthermore, the use of OTMs can pave the way to the introduction of power generation processes more efficient and environmentally sustainable, since by using pure O_2 only CO_2 and H_2O are generated on the combustion of fuels. Therefore, CO_2 can be easily captured and stored, thus reducing drastically CO_2 emissions.

The present Thesis is focused on the research and development of materials and membranes for the production of O_2, with a special focus on their implementation as oxygen supply units in industrial processes, such as steel industry, power generation and chemicals production. For that aim, several cases consisting of different compositions have been studied and characterized under application-representative conditions. Furthermore, issues such as membrane thickness, membrane architecture and geometry, and catalytic activation have also been considered in the studies carried out throughout the Thesis. Therefore, the main objective of the Thesis is the development of MIEC membranes and architectures presenting suitable features for being considered in the construction of OTM-based Air Separation Units. The achievement of high permeation fluxes would allow the needing of lower membrane surface areas, hence a cost reduction in materials and savings in related energy issues can be achieved. Other objectives also considered in the conduction of the thesis are the following:

---

[1] S. Smart, C. X. C. Lin, L. Ding, K. Thambimuthu and J. C. Diniz da Costa. Ceramic Membranes for Gas Processing in Coal Gasification. Energy Environ. Sci. 2010, 3, 268-278.

- to study the performance of the considered materials under different conditions, determining the influence on the oxygen permeation of the following parameters: temperature, feed and sweep flow rates, pO_2 gradient across membranes, harsh environments with presence of CO_2, SO_2 and reducing species
- to progress in the comprehension of the processes governing the oxygen permeation, thus defining the best operation conditions and membrane architectures
- to study the implementation of OTMs as Catalytic Membrane Reactors for the production of chemicals
- to develop materials presenting enough stability under CO_2 and SO_2-containing oxyfuel atmospheres
- to develop catalytic layers for the optimization of the oxygen permeation, especially at low temperatures
- to suggest optimization strategies for the improvement of the membranes performance

1. INTRODUCTION

1. Introduction

1.1. Gas separation membranes.

Applied to gas separation technology, a membrane can be defined as a barrier placed between two enclosures permitting the preferential pass (or permeation) of one gas while the other gases are left on the feed stream. This selective permeation occurs due to the existence of a driving force that can be either an electrical or a chemical potential gradient (i.e. gas component partial pressure).

Membranes used for oxygen production are mainly inorganic membranes. These can be divided into the following categories:

- *Porous membranes*. Both metal and ceramic membranes are included in this category. These membranes are formed by mechanically strong substrates consisting of porous structures. Membrane permeation and permselectivity will depend on the morphology and microstructure of the barrier layers. The main transport mechanisms leading to gas separation in these porous structures are viscous flow, Knudsen diffusion, surface diffusion, capillary condensation and molecular sieving.
- *Dense membranes.* These are the most used membranes for conducting oxygen separation due to the high permselectivity that can be achieved (even infinite permselectivity). Ceramic membranes, metal membranes and liquid-immobilized membranes are the three main types of dense membranes that can be found. Ceramic and metal membranes consist of materials which allow preferentially the passage of O_2 in the form or atoms or ions through the crystal structure, whereas the third category comprises a liquid (semipermeable for O_2) filling a porous structure.

Amongst all the aforementioned membranes, dense ceramic membranes are the preferred for applications involving oxygen production or separation. Ceramic membranes presenting high oxygen ionic and electronic conductivity have been proven to be a very appealing alternative to traditional oxygen production technologies [1]. The fact that these materials are able to separate O_2 in a spontaneous manner (oxygen is separated by simple diffusion through material lattice) at temperatures above 700 ºC have attracted much attention during the last decades, since simpler, cleaner and more economic processes can be designed.

Main applications where oxygen separation membranes can be used are:

1. Small and medium-scale O_2 production, permitting the supply of oxygen in processes where O_2 is needed and in-situ O_2 generation is not economically feasible.
2. Carbon Capture and Storage (CCS), by supplying an oxygen-rich gas into combustion chambers it is possible to obtain flue gases composed mainly by CO_2 and water, thus facilitating carbon dioxide sequestration. CO_2 can

also be used (CCUS) as a value-added commodity. Some of the uses can be concrete curing, biomass conversion (via algae farming), in the oil industry for Enhanced Oil Recovery (EOR), and many others industrial processes using CO_2.

3. Chemical processing, taking the advantage that ceramic membranes can provide oxygen in the ionic form O^{2-}, several chemical reactions can be favored towards higher selectivity and yields on products of interest, e.g. Partial Oxidation of Methane (POM) for syngas production, Oxidative Coupling of Methane (OCM) and Oxidative De-Hydrogenation of Ethane (ODHE) for ethylene production…

These and other applications will be explained more in detail in subsequent points.

1.2. Mixed ionic-electronic conduction.

Ceramic materials exhibiting both ionic and electronic conductivity are known for their good properties in oxygen separation since the 1970 decade [2-4]. These ceramic materials consist of dense layer(s) of multi-metallic oxides presenting alkali, alkali-earth, rare-earth or transitions metals together in the same crystalline structure. The solid-state permeation of oxygen through these materials is possible due to the presence of oxygen vacancies in the crystalline lattice since they are non-porous membranes. At high temperatures (>500 ºC), oxygen is transported through the ceramic crystalline material hopping from vacancy to vacancy and, in parallel to ionic diffusion, the counter-diffusion of electronic carriers for charge compensation takes place. In other words, mixed ionic and electronic conductivity (MIEC) is required for these membrane materials to allow oxygen transport.

The driving force allowing oxygen permeation to occur is the chemical potential gradient applied through the membrane. Therefore, high differences between the oxygen concentration at feed and permeate sides will result in high oxygen permeation rates. Since MIEC membranes are dense, O_2 transport across membrane is not done in the molecular form but in the ionic form O^{2}.

When referring to materials presenting mixed ionic-electronic conductivity for oxygen permeation, those with the better performance present a crystalline structure based on fluorite and perovskite systems [5]. Besides these materials, other compounds exhibiting interesting oxygen transport properties are pyrochlore ($A_2B_2O_7$), brownmillerite ($A_2B_2O_5$), Ruddlesden-Popper series ($A_{n+1}B_nO_{3n+1}$), orthorhombic K_2NiF_4-type structure materials and $Sr_4Fe_{6-x}Co_xO_{13}$ [6-9], nevertheless, their lower performance in comparison with fluorites and perovskites withdraw the interest in these materials. Another option are dual-phase composite materials comprising two different crystalline materials, each one providing a specific conductivity (electronic or ionic). These structures are attracting much attention within the last years, due to their good values in terms of oxygen permeation and stability in harsh environments.

1.2.1. Fluorites.

Materials presenting fluorite structure consist of anions forming a simple cubic packing with cations occupying half of the interstices. As can be observed in Figure 1.1, fluorite structure presents a face-centered cubic packing, with an empty interstice located within the inner space of the anionic structure. The most considered fluorites for oxygen permeation applications are ceria (CeO_2) and zirconia (ZrO_2).

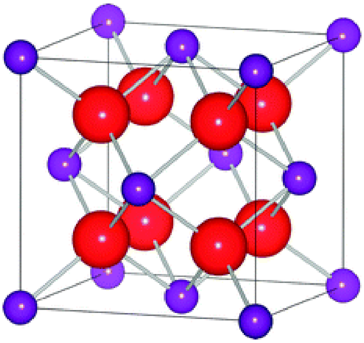

Figure 1.1: Ideal fluorite structure. Cations are represented as blue atoms, occupying face-centred positions and the corners of the unit cell. Image from [10]

Typically, fluorites present high ionic conductivity and hence, they are commonly used as electrolytes in Solid Oxide Fuel Cells (SOFC). Nevertheless most of them are pure ionic conductors, by convenient cationic doping is possible to obtain materials with enough MIEC properties for oxygen permeation [11]. Main interest in fluorites is focused on their high ionic conductivity and the stability under certain conditions.

1.2.2. Perovskites.

The general structure of a perovskite material is ABO_3, where A and B are cations. A is typically an alkali earth metal or a transition metal, whereas B is a transition metal or rare-earth metal. Perovskites present cubic packing, where A cation occupies central position in the cube, and B cations are located in the corners, being coordinated with oxygen anions forming a BO_6 octahedral. In Figure 1.2 is depicted the ideal perovskite structure.

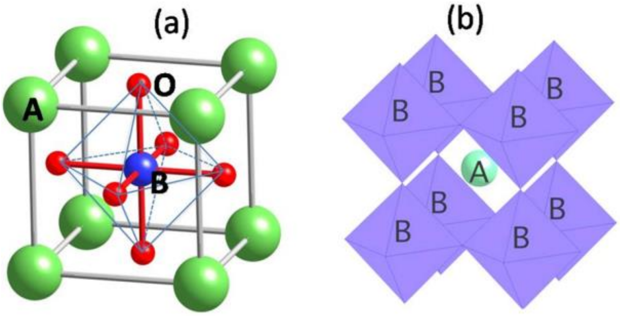

Figure 1.2: (a) Perovskite unit cell and (b) BO_6 octahedral coordination around B cation. Image extracted from [12]

Several perovskites present high mixed ionic and electronic conductivity values, thus, the highest reported oxygen fluxes correspond to materials with this structure [13, 14]. Furthermore, perovskites can be easily doped in both A and B positions by another cations, tuning the materials for a wide range of applications and also for improving their mixed conductivity and stability. The latter can be done by increasing the oxygen vacancies or oxygen non-stoichiometry, stated as δ. Typical perovskites presenting mixed-conduction are those with the general formula $(Ba,Sr,La,Ca)(Fe,Cr,Co,Ga)O_{3-\delta}$. Depending on the formulation, different properties can be obtained, hence the R&D efforts are focused on the development of membrane compositions presenting high mixed-conductivity and chemical and mechanical stability.

1.2.3. Composite materials.

Fluorites exhibit very good stability under harsh environments that can be found in most of the targeted industrial applications, nevertheless the low electronic conductivity that also present leads to very low oxygen permeation. On the contrary, perovskites exhibit outstanding permeation fluxes, but at the same time unpractical stability behaviors that make them unsuitable for most of the industrial applications.

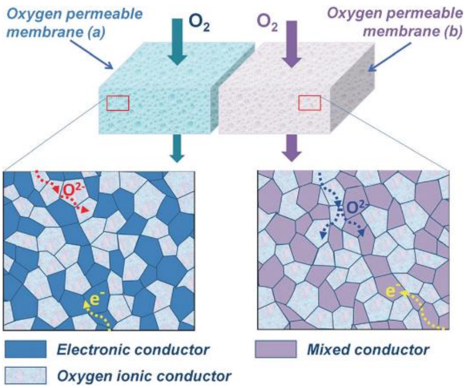

Figure 1.3: Schematic picture of dual-phase membranes. Image extracted from [15].

Therefore, dual-phase composite materials comprising two different materials (one providing electronic conductivity and the other ionic conductivity) are a very promising option for obtaining stable materials with enough mixed-conduction for fulfilling oxygen permeation requirements. Some examples of composites materials for oxygen applications are:

- Ceramic – metal composites [16-18]
- Ceramic – ceramic composites: fluorite/spinel [19-22], perovskite/spinel [23], fluorite/perovskite [24-26]

1.3. Oxygen transport mechanisms.

As it has been stated, oxygen permeation through dense ceramic membranes occurs mainly due to the ionic diffusion of oxygen anions (O^{2-}) across the crystal lattice from the feed side to the permeate side. Nevertheless, oxygen permeation process consists of several steps, described here below and depicted in Figure 1.4:

1. O_2 diffusion from feed stream to membrane surface.
2. O_2 adsorption on membrane surface at feed side.
3. Dissociation surface exchange reaction: $O_2 + 4e^- \rightarrow 2O^{2-}$
4. Incorporation of the oxygen ion into membrane crystal lattice.
5. Ion diffusion through lattice and electron diffusion through electronic bands.
6. O^{2-} adsorption on membrane surface at permeate side.
7. Re-combination surface exchange reaction: $2O^{2-} \rightarrow O_2 + 4e^-$
8. O_2 molecule desorption from membrane surface.
9. O_2 diffusion from membrane surface to permeate stream.

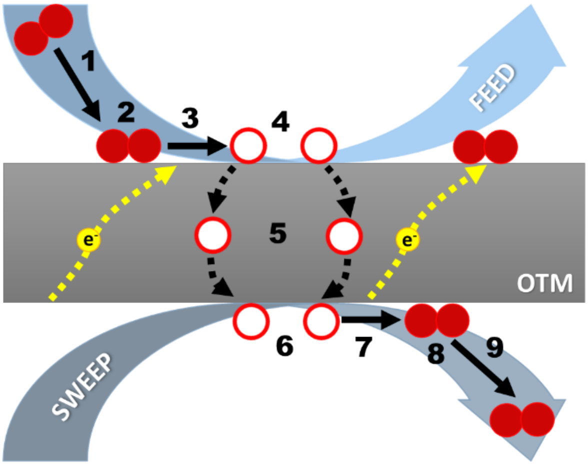

Figure 1.4: Steps involved in the permetion of oxygen through an oxygen transport membrane.

Therefore, two main transport processes are the responsible of the oxygen permeation in MIEC membranes: bulk diffusion and surface exchange reactions.

1.3.1. Bulk diffusion.

According to the theory, an infinite O_2 permselectivity can be achieved with the use of MIEC membranes. This is mainly due to the fact that oxygen transport is done through a dense bulk material only allowing the passage of oxygen anions. The basis of the bulk transport is the flux of O^{2-} through the crystal lattice by hopping from an oxygen vacancy to the next, as depicted in Figure 1.5 for the case of a perovskite. This flux of oxygen ions needs to be charge compensated by a simultaneous flux of electrons or electron holes in the opposite direction.

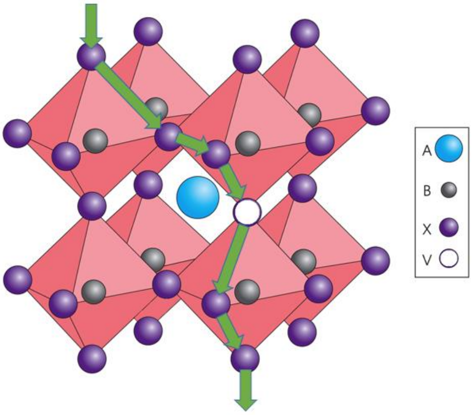

Figure 1.5: Description of the oxygen anions diffusion through the oxygen vacancies present in a perovskite's crystal lattice. Image adapted from [27].

The flux of particles diffusing through the lattice is described by the Wagner equation and depends on the material conductivity (σ_k), the charge number (z_k) and the gradient of the electrochemical potential ($\nabla\eta_k$) when neglecting cross terms between fluxes [5]:

$$J_k = \frac{\sigma_k}{z_k^2 \cdot F^2} \cdot \nabla\eta_k \tag{1.1}$$

The electrochemical gradient is the driving force mainly responsible of the diffusion through the bulk, being defined by the gradient in chemical ($\nabla\mu_k$) and electrical potential ($\nabla\phi_k$) as described by equation 1.2:

$$\nabla\eta_k = \nabla\mu_k + z_k F \nabla\phi_k \tag{1.2}$$

The electrical potential gradient can be neglected by assuming that at steady state no charge accumulation occurs and, therefore, electro neutrality is reached:

$$2J_{O^{2-}} = J_{h^{\cdot}} - J_{e'} \tag{1.3}$$

Combining equations (1.1) to (1.3) and considering that $j_{O_2} = \frac{1}{2} j_{O^{2-}}$, the flux of oxygen can be expressed as:

$$J(O_2) = \frac{1}{4^2F^2}\frac{\sigma_{el}\sigma_{ion}}{\sigma_{el}+\sigma_{ion}}\nabla\mu_{O_2} \qquad (1.4)$$

Where σ_{ion} and σ_{el} are the ionic and electronic conductivity, respectively. Oxygen flux in equation (1.4) refers to a local point in the bulk, integrating this expression across the membrane thickness (L) by using the relation $\nabla\mu_{O_2} = \partial RTlnpO_2/\partial x$ it is obtained a modified Wagner equation describing the oxygen permeation through a MIEC membrane:

$$J(O_2) = \frac{RT}{4^2F^2L}\int_{lnpO_2'}^{lnpO_2''}\frac{\sigma_{el}\sigma_{ion}}{\sigma_{el}+\sigma_{ion}}dlnpO_2 \qquad (1.5)$$

In the equation, pO_2'' and pO_2' correspond to the oxygen partial pressures at feed and permeate sides, respectively; *F* is the Faraday constant, *R* is the gas constant and *T* stands for the temperature.

1.3.2. Surface exchange reactions.

Equation (1.5) is valid only when the bulk diffusion of oxygen limits oxygen permeation. Typically, this occurs at intermediate and high temperatures (> 700 ºC) and for membrane thicknesses above a value known as characteristic membrane thickness (L_c). This thickness, firstly introduced by Bouwmeester et al. [5], establishes the value at which oxygen permeation is equally governed by bulk diffusion and the kinetics taking place at membrane surface, also known as surface exchange reactions. Therefore, at temperatures below 700 ºC and for membranes thinner than L_c oxygen permeation cannot be predicted by Eq. (1.5) and another expression is thus necessary.

Molecular oxygen diffuses from the feed stream to the membrane surface, where sequential reactions occur prior to the incorporation of O^{2-} into the crystal lattice and the subsequent bulk diffusion. These surface reactions involve a number of steps that may include adsorption, dissociation, charge transfer, surface diffusion of intermediate species and finally incorporation in the lattice [28]. Such reactions are depicted in Figure as steps 1 to 4. Once oxygen bulk transport is produced, same reactions in the reverse direction take place on permeate side membrane surface (steps 6 to 9 in Figure 1.4) completing this way the oxygen permeation from feed side to permeate side.

In contrast to bulk diffusion, it is quite difficult to obtain a general expression that models oxygen dynamics on membrane surface. In addition to the fact that surface reactions are not completely well known, aspects like used sweep gas (argon, nitrogen, methane…) may influence rate-limiting steps. Moreover, other surface phenomena like the competitive adsorption between O_2 and certain compounds (e.g. CO_2 and SO_2) on surface active sites also affects oxygen reactions [29-31], adding new parameters and uncertainties.

The Onsager equation [5] can be used for describing the oxygen flux through the solid-gas interface on membrane surface:

$$J(O_2) = J_{ex}^{O} \frac{\Delta\mu_{O_2}^{int}}{RT} \tag{1.6}$$

Where $\Delta\mu_{O_2}^{int}$ is the oxygen chemical potential difference across the interface and J_{ex}^{O} is the exchange rate when no oxygen chemical potential gradient is present. As aforementioned, when membrane thickness is equal to L_c, then the total driving force is shared between bulk transport and surface kinetics, and L_c can be defined as:

$$L_c = \frac{RT}{16F^2} \frac{\sigma_{el}\sigma_{ion}}{\sigma_{el} + \sigma_{ion}} \frac{1}{J_{ex}^{O}} \tag{1.7}$$

If linear kinetics of the relevant rate laws are assumed when both bulk diffusion and surface exchange reactions are governing permeation, and combining equations (1.6) and (1.7) then the oxygen flux can be expressed by means of the following expression [32]:

$$J(O_2) = \frac{1}{1 + 2L_c/L} \frac{1}{16F^2} \frac{\sigma_{el}\sigma_{ion}}{\sigma_{el} + \sigma_{ion}} \frac{\Delta\mu_{O_2}^{total}}{L} \tag{1.8}$$

where $\Delta\mu_{O_2}^{total}$ is the total oxygen chemical potential difference across the membrane.

1.4. Performance optimization.

Observing the equations describing oxygen permeation, i.e. equations (1.5) and (1.8) it is clear that $J(O_2)$ depends on parameters related to operation conditions (temperature and oxygen partial pressure gradient), membrane material (ionic and electronic conductivities) and membrane dimensions (thickness). Therefore, by acting on these variables it is possible to improve and optimize the oxygen permeation performance of a membrane. The main reason for obtaining high $J(O_2)$ is due to the fact that with high permeating membranes the required membrane surface area in OTM modules will be lower, thus resulting in lower process and manufacturing costs. Typically, oxygen fluxes of 5-10 $ml \cdot min^{-1} \cdot cm^{-2}$ are the considered for reaching the techno-economic targets for practical applications [33].

1.4.1. Material properties.

From the observation of equations 1.1-1.8 it is clear that an important parameter affecting directly the oxygen permeation is the material conductivity, with a special emphasis on the mixed ionic-electronic conductivity. Therefore, for improving the oxygen permeation one strategy that can be addressed is the increasing of ionic and electronic conductivities, i.e. σ_{ion} and σ_{el}, respectively.

Materials presenting perovskite structure are good electronic conductors, therefore the permeation for these materials is limited by the ionic conductivity, which is low in comparison to the electronic conductivity. For improving the oxygen permeation of these materials is then necessary to enhance their ionic conductivity, this can be done by increasing the oxygen vacancies in the crystal lattice. The generation of defects or oxygen vacancies can be obtained by reducing the valence of the cations in the B position, or by substituting the elements in A position with cations presenting a lower oxidation state. Therefore, by doping conveniently a perovskite higher conductivity can be obtained, subsequently resulting in higher $J(O_2)$. Nevertheless, the generation of oxygen vacancies could be detrimental to the material stability, worsening this aspect.

For the case of materials presenting low electronic conductivity, such as fluorites, the situation is the contrary. Increasing the electronic conductivity of fluorites can be achieved by adding certain elements that can lead to the generation of electronic paths through grain boundaries [34], thus providing mixed electronic-ionic conductivity. However, this procedure cannot be sufficient for achieving suitable material conductivities for the oxygen permeation. A more effective strategy is the production of dual-phase materials (see 1.2.3).

1.4.2. Operation conditions.

As $J(O_2)$ depends directly on temperature, then higher oxygen fluxes can be obtained by operating at higher temperatures. Nevertheless, for industrial applications the trend is focused on lowering the temperature of operation maintaining good $J(O_2)$ values at the same time. The reason for this is because at high temperatures the materials that are required for membrane modules and housing are more expensive, as well as high energy consumption will increase costs. Depending on the application, the target temperatures that are normally considered are in the range of 800-900 ºC.

Another strategy for improving oxygen permeation can be done by increasing the oxygen partial pressure gradient between the two sides of the membrane (feed and permeate sides):

- Increasing pO_2 at feed side: this is done by using a pressurized feed stream (typically, pressures of 15-20 bar are considered [35], however it will depend on the system and/or application).
- Decreasing pO_2 at permeate side: different sweep gases induce different oxygen partial pressures, e.g. Argon sweep generates a local pO_2 on

sweep side of about $5 \cdot 10^{-5}$ bar [36]. Moreover, the operation with high sweep flows causes the adsorbed O_2 molecules to be easily released from membrane surface, decreasing oxygen concentration on permeate surface. Another way for inducing a low pO_2 is by using a vacuum system instead of a sweep stream. With this technique it is possible to achieve lower partial pressures and thus, higher $J(O_2)$. Main drawbacks are related with the higher costs and technical complexity. Another way for having low pO_2 at permeate side is the use of sweep reducing gases, such as light hydrocarbons that can be used for both improving $J(O_2)$ and conducting chemical reactions of interest.

1.4.3. Thickness reduction.

The most obvious option for increasing oxygen fluxes is the reduction of membrane thickness. According to Wagner's equation (Eq. 1.5) it is possible to increase J_{O2} by a factor 10 if thickness is reduced from 1 mm to 100 μm. Nevertheless, membranes in the micrometer range become considerably brittle so it is necessary the use of porous supports for ensuring a mechanical robustness of the membrane assembly. Main requirements for porous supports are:

- Similar Thermal Expansion Coefficient (TEC) than membrane layer material.
- Chemical compatibility with membrane material at operation and manufacture conditions.
- Mechanical and chemicall stability under the operation conditions
- Establishment of a diffusive way for O_2 molecules to/from membrane surface, in the way that no further resistances that limit oxygen permeation are added.

For avoiding chemical and mechanical incompatibilities, supports consisting of the same materials than membrane are mostly considered. However, high material cost can be a major drawback for a practical application case. Therefore, porous substrates made of cheaper materials are also being considered for OTMs, e.g. MgO [37], alumina [38], YSZ [39] and metallic alloys [40].

Membrane thickness reduction will enhance oxygen permeation as long as thickness value is above L_c. Consequently, it is pointless to reduce the thickness below this level since permeation is limited by surface kinetics and therefore no gain in permeation will be obtained with thinner layers.

For the case of perovskites, L_c is in the range of 10-100 μm, whereas for fluorites this value is much higher, from mm to cm [5]. Then, the determination of membrane characteristic thickness is a very useful tool for establishing the optimal thickness of an oxygen membrane. This determination can be done from the chemical diffusion coefficient D_{chem} ($cm^2 \cdot s^{-1}$) and the surface exchange coefficient k_{chem} ($cm \cdot s^{-1}$). D_{chem} quantifies the diffusion of oxygen species through the material crystal lattice (involving electronic and ionic conductivity), whereas k_{chem} measures the kinetics of surface processes involving oxygen oxidation-reduction reactions.

$$L_c = \frac{D_{chem}}{k_{chem}} \tag{1.9}$$

D_{chem} and k_{chem} can be measured by means of Electrical Conductivity Relaxation (ECR) and Pulse Isotropic Exchange (PIE) techniques, respectively.

1.4.4. Surface modification.

As aforementioned in the previous point, thickness reduction will improve oxygen permeation up to a limit, established by the material characteristic thickness. No appreciable gain in $J(O_2)$ will be obtained with thinner membranes unless the value of k_{chem} is significantly increased.

By means of modification of membrane surface it is possible to improve surface reaction rates, thus increasing $J(O_2)$. Main strategies for proceeding with surface modification on oxygen membranes are:

- Increase of surface specific area: a membrane presenting higher surface area will also present a higher number of active sites for oxygen reactions. Therefore, more sites available for O_2 molecules to be incorporated/released to/from membrane will improve oxygen permeation. Some of the most used techniques for increasing surface area are: chemical etching [41, 42] and deposition of porous layers [14].
- Surface catalytic activation: there are several elements presenting high activity towards oxygen exchange reactions (adsorption, dissociation, recombination, desorption), thus, their incorporation to membrane surface can speed up surface kinetics and enhance oxygen permeation. Commonly, active species are included by means of particle deposition over membrane surface [43], as deposited porous layers or by means of infiltration in porous backbones [44]. Moreover, catalytic activation is also used in membrane reactor technology for improving yields and selectivity of hydrocarbon conversion reactions (e.g. OCM, ODHE…) [45].

1.4.5. Protective layers.

As well as for the production of oxygen, OTMs can be used in other applications such as oxyfuel technology and production of several compounds (e.g. syngas, ethylene and ammonia) in the chemical industry. Under the operation conditions that can be found in these processes (i.e. presence of CO_2, H_2O, SO_2, NO_x, reducing atmospheres…) most of the considered membrane materials become chemically and mechanically unstable [46] [47-49]. Thus, materials presenting good permeation rates cannot be used in these applications.

One option for overcoming these limitations consists of the protection of the membrane exposed area. Several studies have yield promising results by means of the addition of protective layers [50-53], resulting in that materials gain in stability or even become fully stable under operation conditions, with slight permeation losses. The materials used for protecting membranes are mainly fluorites and dual-phase composites. These materials, in spite of being stable under the referred conditions, present lower performance

Protective layers are deposited on membrane exposed areas. Several techniques are considered for conducting layer deposition: spin-coating, pulsed laser deposition, physical vapor deposition, chemical vapor deposition, spray pyrolysis and RF magnetron sputtering.

1.5. Applications of Oxygen Transport Membranes.

Oxygen is a key product for several industrial processes, being the third largest volume chemical produced worldwide with approximately 100 million tons every year [54]. The produced O_2 is mainly consumed by three industrial sectors: steel industry (40.7%), power generation (29.4%) and chemical industry (22.4%). Moreover, oxygen demand is expected to increase within the next years due to the implementation of cleaner and more efficient processes requiring pure oxygen. These target applications are mainly small and medium-scale industrial processes (with O_2 demands ranging from 10 to 100 ton/day) where carbon-based fuels are burned for producing heat, power or products of interest.

1.5.1. Available technologies for the production of oxygen.

Nowadays, almost all oxygen extracted from air for industrial applications is obtained by using cryogenic distillation. However, this process presents important drawbacks mainly related to the high production energy costs, since it operates at very low temperatures and high pressures. Therefore, this technology is only economically viable for large installations, with typical plant sizes in the range 30,000-50,000 Nm^3 O_2/h (9,000-15,000 TPD[2]) and providing oxygen purities >99% [55].

Another way for producing oxygen is by means of Pressure Swing Adsorption (PSA), where N_2 is selectively adsorbed on zeolites or on carbon molecular sieves. Then, an oxygen-rich gas stream is obtained. Despite PSA is suitable for small scale O_2 production (ca. 1,500 Nm^3 O_2/h [55]), the fact of being a discontinuous process and the very high production costs if O_2 purities above 95% are needed, avoid its consideration for industrial processes requiring high purity O_2 supply.

Therefore, for these target applications OTMs are in a good position for replacing conventional air distillation for pure O_2 production [56-58] (normally done by bulk supply), because of their low energy consumption and the high-purity of oxygen

---

[2] TPD stands for tons per day

(100%) that are capable of deliver. The main drawbacks of OTM technology are the high temperatures needed for practical operation, typically between 700 and 1000 ºC, and the presumably modest chemical and mechanical stability of the materials. As a rule of thumb, the higher the temperature the higher the oxygen permeation is but the more expensive the ancillary materials and the equipment are. As previously mentioned, the chemical and mechanical behavior of these OTMs is influenced by the nature of the gas environment in contact with both sides of the membrane. Specifically, environments with low O_2 partial pressure (pO_2) and/or containing CO_2, SO_2 gases and reducing species (i.e. light hydrocarbons, hydrogen, water, etc.) affect the membrane performance and the material integrity, even causing the membrane mechanical failure [59-62]. Within the objective to overcome these operational limitations, a large number of research groups have made great efforts in OTM development and new materials have been formulated with improved O_2 flux at lower temperatures and under harsh atmospheres, approaching the conditions of industrial target applications as oxyfuel, gasification and chemical and petrochemical reactions [1, 45, 52, 63-70]. Currently, this technology is at a demonstrative stage, with two notable developments conducted by Praxair and Air Products. These developments (widely described in point 1.5.2. of the present chapter) consist of OTM modules presenting tubular (Praxair) and planar (Air Products) configurations, producing up to 1 TPD O_2 and 100 TPD O_2, respectively. Also worth to mention –despite their lower dimension– is the case of the pilot modules developed by RWTH-Aachen within OXYCOAL-AC Project for a zero-CO_2 combustion of coal-fired power plants [35], presenting a tubular configuration (15 m^2 membrane area with 570 tubes) and a capability of 0.6 TPD O_2 for generating up to 120 kW. In addition to RWTH-Aachen engineers, in this project have also participated companies such as E.ON Energy, Linde, RWE Power, MAN, Turbo and Hitachi Power Europe, as well as the German administration support through the German Federal Ministry of Economics and Technology and the Ministry of Innovation and Technology of North-Rhine Westphalia.

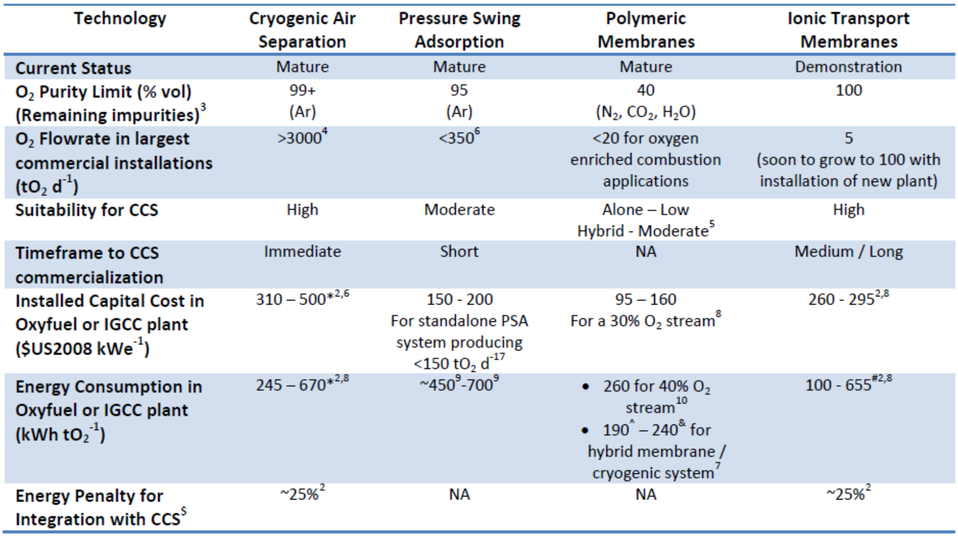

Technology	Cryogenic Air Separation	Pressure Swing Adsorption	Polymeric Membranes	Ionic Transport Membranes
Current Status	Mature	Mature	Mature	Demonstration
O_2 Purity Limit (% vol) (Remaining impurities)[3]	99+ (Ar)	95 (Ar)	40 (N_2, CO_2, H_2O)	100
O_2 Flowrate in largest commercial installations ($tO_2\ d^{-1}$)	>3000[4]	<350[6]	<20 for oxygen enriched combustion applications	5 (soon to grow to 100 with installation of new plant)
Suitability for CCS	High	Moderate	Alone – Low Hybrid - Moderate[5]	High
Timeframe to CCS commercialization	Immediate	Short	NA	Medium / Long
Installed Capital Cost in Oxyfuel or IGCC plant ($US2008 kWe^{-1})	310 – 500*[2,6]	150 - 200 For standalone PSA system producing <150 $tO_2\ d^{-1}$[7]	95 – 160 For a 30% O_2 stream[8]	260 - 295[2,8]
Energy Consumption in Oxyfuel or IGCC plant ($kWh\ tO_2^{-1}$)	245 – 670*[2,8]	~450[9]-700[9]	• 260 for 40% O_2 stream[10] • 190^ – 240& for hybrid membrane / cryogenic system[7]	100 - 655#[2,8]
Energy Penalty for Integration with CCS$	~25%[2]	NA	NA	~25%[2]

Figure 1.6: Details of Air Separation Unit (ASU) technologies oriented to CCS applications (extracted from [71]).

The table above (extracted from the *State of Art (SOTA) Report on Dense Ceramic Membranes for Oxygen Separation from Air* [71]) summarizes and compares some of the most important facts for the application of O_2 production technologies in CCS processes. Therefore, and despite having the same energy penalty than cryogenic air separation, according to the purity, suitability and capital costs, OTM technologies are in a very good position for their use in medium and small-scale applications, as it has been previously stated.

1.5.2. Application of OTMs in Power Generation and CCS: Oxyfuel and Gasification technologies.

World energy demand is expected to increase within the next years [72, 73] and, despite the efforts and advances in the implementation of renewable energy technologies, this demand will be satisfied mainly by burning fossil fuels [72]. Nowadays, coal is still growing in use whereas price is downing due to the increasing in natural gas and oil reservoirs coming from the hydraulic fracturing of shale rocks [74, 75]. In this scenario, with cheaper coal and an ever-increasing gas and oil availability, power generation is going to be generated mainly by means of such sources. Therefore, CO_2 waste emissions will remain to be a problem.

Oxyfuel technology is then presented as a feasible solution for minimizing CO_2 emissions as well as improving process efficiency in power generation and other industries [76-78]. Oxyfuel applied to a power plant consists of burning the fuel with an oxygen-rich stream, in order to obtain a flue gas composed mainly by CO_2 and H_2O. Thus, CO_2 can be easily separated, pressurized and stored, avoiding any emission to the atmosphere.

Depending on the fuel used, other species in addition to CO_2 and H_2O can be generated. This is the case of sulphur-containing fuels that will lead to the formation of SO_x. Therefore, membrane materials must be stable in the presence of these compounds as well as not suffering a significant decay in the performance. Some studies have established a $J(O_2)$ rate over 5-10 $ml \cdot min^{-1} \cdot cm^{-2}$ for considering the use of OTMs as techno-economically feasible [33]. Thus, ensure such fluxes via proper material selection, catalytic activation, thickness reduction, module and process engineering… is imperative for proceeding with the integration of OTMs in real applications.

Besides the oxyfuel technology, there are other alternatives to implement CCS strategies in thermal power plants, such as post-combustion and pre-combustion approaches. Post-combustion involves huge CO_2-separation plants after fuel combustion, typically amine washing or calcium looping process, in which CO_2 is absorbed on the amines or calcium and then thermally desorbed to regenerate amine/calcium carrier and produce CO_2. Otherwise, in the pre-combustion approach, fuel is gasified and the gasification gases are equilibrated in water gas shifting (WGS) reactors to form a mixture comprising principally H_2 and CO_2, the latter being separated previously to a combustion process. The most efficient gasification plant for power generation is the so-called Integrated Gasification Combined Cycle (IGCC) plant. In both pre-combustion and oxy-fuel approaches, an oxygen source is required, therefore an ASU must be installed nearby of such big plants. Some studies considering a partial integration of OTMs in IGCC plants have resulted in promising conclusions, such as a 9 % cost reduction ($/kW) of the IGCC plant, obtaining a net power (MWe) output increase of 15% and increasing plant efficiency in a 1.2%, reducing at the same time in a 25% the cost ($/short TPD) of O_2 production [79].

In this scenario, OTMs should provide the perfect balance between energy consumption and overall plant efficiency due to the proper thermal integration in fuel fired power plants [1]. Apart from several research groups currently investigating on the integration of OTMs in gasification processes, the most advanced and major developments are those performed by Praxair and Air Products [80, 81] reaching very high technology readiness level, i.e., demonstration plants for oxygen production. These two companies have worked in the field of ceramic membranes for O_2 separation for more than 20 years, developing industrial OTM modules and systems for IGCC and related applications. Praxair focused on developing OTMs for oxycombustion and syngas applications through U.S. DoE granted projects (DE-FC26-07NT43088 and DE-FC26-01NT41147), by means of the use of advanced boilers and heaters using OTM technology in combustion processes. Several U.S. Patents have been resulted from these developments [82] and [83], specially an OTM boiler that enables steam generation and power cycle with CCS [84], [85] and [86], and an OTM syngas system for autothermal reforming of NG enabling downstream synthesis and oxycombustion power cycle [87]. Praxair's OTM technology consists of tubular membrane modules that are integrated in an Advanced Power Cycle layout as Partial Oxidation equipment and OTM boiler. After completing phases I and II, which comprised the development of materials, design of an OTM-enabled coal power cycle, single tube testing, and basic engineering of OTM modules; Praxair has achieved in phase III, a successful integration of membranes into systems, what is paving the way to the scale-up to systems including 1 TPD O_2 OTMs.

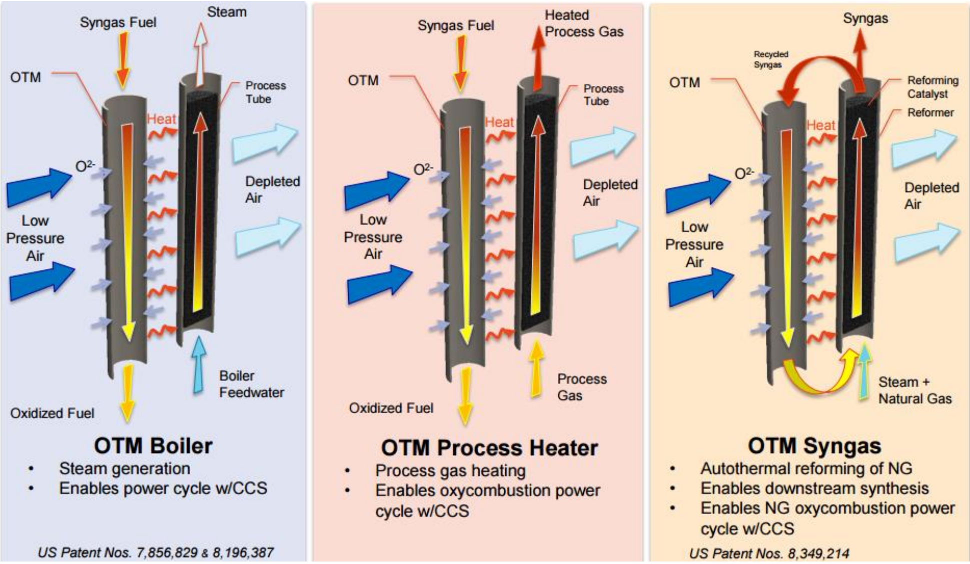
Syngas Fuel
Steam
OTM
Process Tube
Heat
O^{2-}
Depleted Air
Low Pressure Air
Boiler Feedwater
Oxidized Fuel
OTM Boiler
Steam generation
Enables power cycle w/CCS
US Patent Nos. 7,856,829 & 8,196,387
Syngas Fuel
Heated Process Gas
OTM
Process Tube
Heat
O^{2-}
Depleted Air
Low Pressure Air
Process Gas
Oxidized Fuel
OTM Process Heater
Process gas heating
Enables oxycombustion power cycle w/CCS
Syngas
Recycled Syngas
OTM
Reforming Catalyst
Reformer
Heat
O^{2-}
Depleted Air
Low Pressure Air
Steam + Natural Gas
OTM Syngas
Autothermal reforming of NG
Enables downstream synthesis
Enables NG oxycombustion power cycle w/CCS
US Patent Nos. 8,349,214

Figure 1.7: Praxair's high temperature processes with integrated OTMs[3].

Air Products started its R&D activities on OTMs in 1988, since then, more than 90 U.S. Patents related to materials, catalysts, membrane and modules structures, process cycles, applications, and integrations have been produced [88]. Furthermore, Air Products and the U.S. DoE entered into a Cooperative Agreement (DE-FC26-98FT40343) in 1998 to develop oxygen membrane technology to the point of pre-commercialization[4]. As a result of these activities, an intermediate scale testing with a capacity of 100 TPD O_2 (corresponding to an IGCC output of 12 MW) was developed and installed in their test facilities located in Convent, Louisiana [89]. Simultaneously, a 2000 TPD O_2 module was also under development. And once completed, next phase would comprise the construction of energy installations yielding power outputs of 250 MW (IGCC) and 110 MW (oxy-combustion). Air Products OTM modules present a planar wafer design as described in Repasky J.M. et al. [90] and [81]. Air Products developments are the most advanced in terms of facilities size, oxygen production, and proximity to commercialization. Nevertheless it looks like all the activities regarding OTM developments have been abandoned since 2015 due to a deep company restructuring.

---

[3] https://www.netl.doe.gov/File%20Library/Events/2014/2014%20NETL%20CO2%20Capture/S-Kelly-PRAXAIR-Praxair-s-Oxygen-Transport-Membranes.pdf

[4] https://www.netl.doe.gov/File%20Library/Research/Coal/energy%20systems/gasification/FC26-98FT40343.pdf

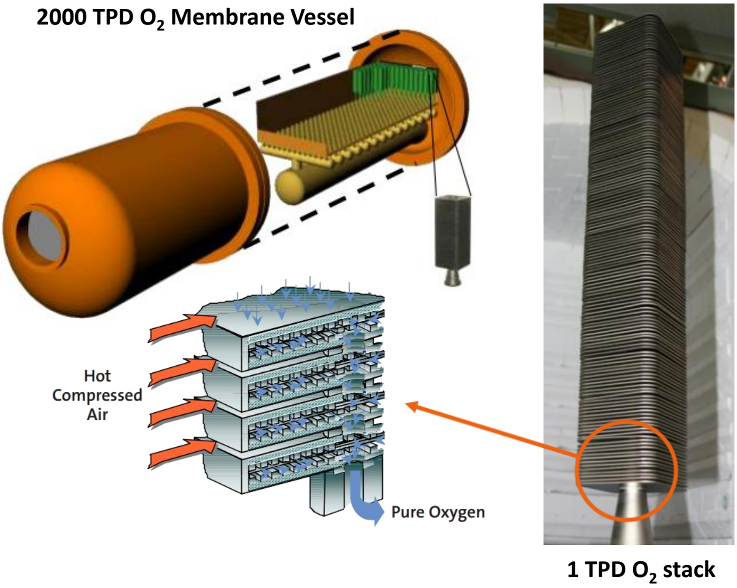

Figure 1.8: Air Products and Chemicals Inc. ITM developments for oxygen production. Extracted from [88].

1.5.3. Chemical Industry Applications.

Within world economy top industries, chemical and petrochemical industries are amongst the most important. Furthermore, these industries are the main consumers of energy and resources, and are also the responsible of most of the pollution (CO_2, NO_x emissions) produced yearly. Additionally, the fact that chemical processes typically involve a series of multi-step reactions and sub-processes make necessary the engineering and design of very complex equipment and processes that subsequently require the treatment of several streams.

Therefore, in the past decades CMRs have been taken into account for the conduction of several reactions in the chemical industry. The main reasons for this are (i) the gain in process simplicity when combining an ASU and a chemical reactor in only one process unit (this is by definition a Catalytic Membrane Reactor), (ii) the possibility of synergetic integration within the whole process and (iii) the achievement of higher hydrocarbons yields/conversion, for explosion limits are not reached and it is possible to conduct the reactions more safely. Consequently, the integration of OTMs in chemical processes can result in a gain of process sustainability and safety, important energy savings, minimization of the waste emissions and an improvement in the performance due to the higher selectivity and yields that can be obtained.

Some examples of chemical reaction that can be performed in a CMR are the following:

1) Partial Oxidation of Methane (POM) for the production of syngas [63, 91]

$$CH_4 + {}^{1}\!/_{2}\, O_2 \rightarrow 2H_2 + CO \qquad \text{(R1)}$$

2) Oxidative Coupling of Methane (OCM) to ethylene and ethane [92, 93].

$$2CH_4 + O_2 \rightarrow C_2H_4 + 2H_2O \qquad \text{(R2)}$$

$$2CH_4 + {}^{1}\!/_{2}\, O_2 \rightarrow C_2H_6 + H_2O \qquad \text{(R3)}$$

3) Oxidation reforming of Methane to syngas, that can be performed via CO_2 reforming and steam reforming.

$$CH_4 + CO_2 \rightarrow 2CO + 2H_2 \qquad \text{(R4)}$$

$$CH_4 + H_2O \rightarrow CO + 3H_2 \qquad \text{(R5)}$$

4) Oxidative dehydrogenation of alkanes for producing ethylene and propylene by means the oxidative dehydrogenation of ethane (ODHE) [64, 94] and propane, respectively.

$$C_2H_6 + {}^{1}\!/_{2}\, O_2 \rightarrow C_2H_4 + H_2O \qquad \text{(R6)}$$

$$C_3H_8 + {}^{1}\!/_{2}\, O_2 \rightarrow C_3H_6 + H_2O \qquad \text{(R7)}$$

5) Hydrogen cyanide (HCN) synthesis via the Andrussow reaction from methane and ammonia in the presence of O_2

$$CH_4 + NH_3 + {}^{3}/_{2}\,O_2 \rightarrow HCN + 3H_2O \qquad \text{(R8)}$$

This process, typically conducted with the use of Pt catalysts, presents a very significant interest in the field of OTMs, nevertheless no successful results have been published yet. In spite of this, there is a patent on catalytic layers for the oxygen activation of SOFC electrolytes that claims the use of such architecture for the conduction of the Andrussow reaction in OTMs [95].

Moreover, a very interesting feature of CMRs is the possibility of conducting the coupling of multiple reactions, i.e. two different reactions can be conducted on each side of the membrane as can be seen in Figure 1.9 where water splitting or nitrous oxide dissociation can be performed in one side whereas Partial Oxidation of Methane (POM) or Oxidative De-Hydrogenation of Ethane (ODHE) are conducted on the other reaction chamber [96].

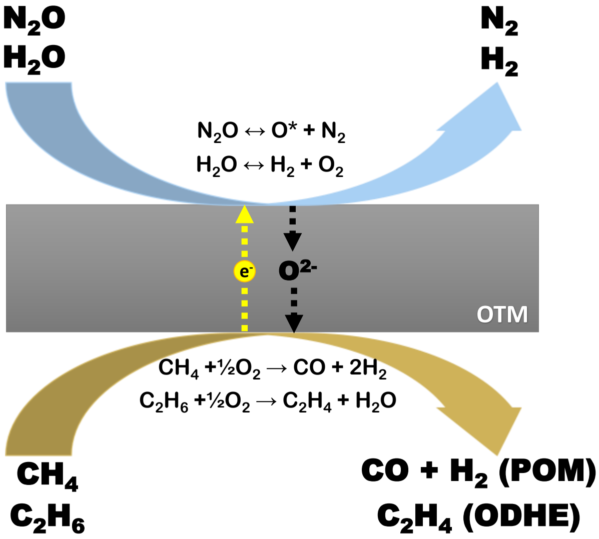
N_2O
H_2O
N_2
H_2
$N_2O \leftrightarrow O^* + N_2$
$H_2O \leftrightarrow H_2 + O_2$
e^-
O^{2-}
OTM
$CH_4 + ½O_2 \rightarrow CO + 2H_2$
$C_2H_6 + ½O_2 \rightarrow C_2H_4 + H_2O$
CH_4
C_2H_6
$CO + H_2$ (POM)
C_2H_4 (ODHE)

Figure 1.9: Coupling of multiple reactions in an OTM. Image adapted from [96]

By considering this concept, several interesting reactions can be conducted in parallel to other, thus improving OTMs performance by obtaining more valuable products or for the removal of harmful pollutants. Some of the reactions that are typically considered for being coupled are the following:

1) Production of H_2 from water splitting: the thermal dissociation of H_2O produces a very low amount of H_2 (0.1% at 1600 ºC) due to the thermodynamic limitations

$$H_2O \leftrightarrow {}^{1}\!/_{2}\, O_2 + H_2 \qquad \text{(R9)}$$

Nevertheless, this reaction can be notably displaced forward if high amounts of O_2 are removed. Several studies have considered water splitting coupled with POM when using perovskite [97], cer-met and composite membranes. Concerning the latter, promising results have been obtained recently [98].

2) Thermal decomposition of CO_2 (TDCD), alike in the previous case OTMs can be used for enhancing thermodynamically limited reaction such as the decomposition of CO_2 to CO and O_2.

$$CO_2 \leftrightarrow {}^{1}\!/_{2}\, O_2 + CO \qquad \text{(R10)}$$

Several studies have considered this reaction coupled with POM in a single OTM unit using Pd/$SrCo_{0.4}Fe_{0.5}Zr_{0.1}O_{3-\delta}$ catalysts. 100% CO selectivity at 15.8% CO_2 conversion have been obtained [99].

3) Nitrous oxide (N_2O) decomposition to N_2 and O_2. This direct conversion is a very interesting option for N_2O removal and even more when it is considered one of the most harmful pollutants generated in several combustion processes.

$$N_2O \leftrightarrow N_2 + O^{*} \qquad \text{(R11)}$$

This reaction, coupled with POM, was studied by Jiang et al. [96] obtaining a complete N_2O decomposition (from an initial gas stream containing 20% N_2O) at 850 ºC, whereas at the other side a 80% CO yield is obtained when performing the partial oxidation of methane.

Oxygen is used in the chemical industry for conducting several oxidation processes of big interest. As can be seen in Table 1.1, O_2 is used for the production of ethylene and propylene oxides, acetic acid and polyethylene, amongst others. Moreover, oxygen is used for the production of syngas, hydrogen peroxide, nitric acid, vinyl chloride and phtalic acid. The yearly amount of O_2 consumed worldwide by the chemical industry ascended to 17.4 Mton in 2004, thus constituting a significant number to be taken into account.

Table 1.1: World use of oxygen for the production of chemicals and steel in 2004 [55].

Product	**Production (Mton/yr)**	**O_2 use (Mton/yr)**
Steel	1241.0	104.0
Ethylene oxide	15.1	7.2
Ethylene dichloride	49.1	4.0
Propylene oxide	5.8	2.0
Acetic acid	8.1	1.6
Titanium oxide	4.3	0.9
Vynil acetate	5.0	0.8
Acetaldehyde	2.4	0.7
Perchloroethylene	0.7	0.1
Acetic anhydride	1.9	0.1
Polyethylene (LDPE)	18.7	0.01
Cyclododecanol	0.01	0.02
Total		**121.4**

1.7. References.

[1] R. Castillo, Thermodynamic analysis of a hard coal oxyfuel power plant with high temperature three-end membrane for air separation, Applied Energy, 88 (2011) 1480-1493.

[2] T. Takahashi, T. Esaka, H. Iwahara, Electrical conduction in the sintered oxides of the system Bi2O3BaO, Journal of Solid State Chemistry, 16 (1976) 317-323.

[3] B. Cales, J.F. Baumard, Oxygen semipermeability and electronic conductivity in calcia-stabilized zirconia, Journal of Materials Science, 17 (1982) 3243-3248.

[4] B. Cales, J.F. Baumard, MIXED CONDUCTION AND DEFECT STRUCTURE OF ZrO//2-CeO//2-Y//2O//3 SOLID SOLUTIONS, Journal of the Electrochemical Society, 131 (1984) 2407-2413.

[5] A.J.B. H.J.M Bouwmeester, Chapter 14: Dense ceramic membranes for oxygen separation, in: P.J.G.a.H.J.M. Bouwmeester (Ed.) CRC Handbook of Solid State Electrochemistry, CRC Press, Boca Raton, 1997.

[6] V.V. Kharton, E.V. Tsipis, A.A. Yaremchenko, N.P. Vyshatko, A.L. Shaula, E.N. Naumovich, J.R. Frade, Oxygen ionic and electronic transport in Gd2-xCaxTi2O7-delta pyrochlores, Journal of Solid State Electrochemistry, 7 (2003) 468-476.

[7] A.L. Shaula, V.A. Kolotygin, E.N. Naumovich, Y.V. Pivak, V.V. Kharton, Oxygen Ionic Transport in Brownmillerite-Type Ca2Fe2O5-delta and Calcium Ferrite-Based Composite Membranes, in: S. Ubizskii, L. Vasylechko, Y. Zhydachevskii (Eds.) Oxide Materials for Electronic Engineering - Fabrication, Properties and Applications2013, pp. 286-292.

[8] J. Xue, Q. Liao, W. Chen, H.J.M. Bouwmeester, H. Wang, A. Feldhoff, A new CO2-resistant Ruddlesden-Popper oxide with superior oxygen transport: A-site

deficient (Pr0.9La0.1)(1.9)(Ni0.74Cu0.21Ga0.05)O4+delta, Journal of Materials Chemistry A, 3 (2015) 19107-19114.

[9] D.M. Bochkov, V.V. Kharton, A.V. Kovalevsky, A.P. Viskup, E.N. Naumovich, Oxygen permeability of La2Cu(Co)O4+δ solid solutions, Solid State Ionics, 120 (1999) 281-288.

[10] L. Malavasi, C.A.J. Fisher, M.S. Islam, Oxide-ion and proton conducting electrolyte materials for clean energy applications: structural and mechanistic features, Chemical Society Reviews, 39 (2010) 4370-4387.

[11] M. Balaguer, C. Solís, J.M. Serra, Structural–Transport Properties Relationships on Ce1–xLnxO2−δ System (Ln = Gd, La, Tb, Pr, Eu, Er, Yb, Nd) and Effect of Cobalt Addition, The Journal of Physical Chemistry C, 116 (2012) 7975-7982.

[12] M.I. Desheng Fu, Ferroelectricity in Silver Perovskite Oxides, Ferroelectrics - Material Aspects, InTech2011.

[13] J. Sunarso, S. Baumann, J.M. Serra, W.A. Meulenberg, S. Liu, Y.S. Lin, J.C.D. da Costa, Mixed ionic-electronic conducting (MIEC) ceramic-based membranes for oxygen separation, Journal of Membrane Science, 320 (2008) 13-41.

[14] S. Baumann, J.M. Serra, M.P. Lobera, S. Escolastico, F. Schulze-Kueppers, W.A. Meulenberg, Ultrahigh oxygen permeation flux through supported Ba0.5Sr0.5Co0.8Fe0.2O3-delta membranes, Journal of Membrane Science, 377 (2011) 198-205.

[15] X. Dong, W. Jin, N. Xu, K. Li, Dense ceramic catalytic membranes and membrane reactors for energy and environmental applications, Chemical Communications, 47 (2011) 10886-10902.

[16] C.S. Chen, B.A. Boukamp, H.J.M. Bouwmeester, G.Z. Cao, H. Kruidhof, A.J.A. Winnubst, A.J. Burggraaf, Microstructural development, electrical properties and oxygen permeation of zirconia-palladium composites, Solid State Ionics, 76 (1995) 23-28.

[17] C.S. Chen, H. Kruidhof, H.J.M. Bouwmeester, H. Verweij, A.J. Burggraaf, Oxygen permeation through oxygen ion oxide-noble metal dual phase composites, Solid State Ionics, 86–88, Part 1 (1996) 569-572.

[18] J. Kim, Y.S. Lin, Synthesis and oxygen permeation properties of ceramic-metal dual-phase membranes, J. Membr. Sci., 167 (2000) 123-133.

[19] H. Luo, H. Jiang, K. Efimov, F. Liang, H. Wang, J. Caro, CO2-Tolerant Oxygen-Permeable Fe2O3-Ce0.9Gd0.1O2-δ Dual Phase Membranes, Industrial & Engineering Chemistry Research, 50 (2011) 13508-13517.

[20] H. Luo, H. Jiang, T. Klande, Z. Cao, F. Liang, H. Wang, J. Caro, Novel Cobalt-Free, Noble Metal-Free Oxygen-Permeable 40Pr(0.6)Sr(0.4)FeO(3-delta)-60Ce(0.9)Pr(0.1)O(2-delta), Dual-Phase Membrane, Chemistry of Materials, 24 (2012) 2148-2154.

[21] F. Liang, H. Luo, K. Partovi, O. Ravkina, Z. Cao, Y. Liu, J. Caro, A novel CO2-stable dual phase membrane with high oxygen permeability, Chemical Communications, 50 (2014) 2451-2454.

[22] U. Pippardt, J. Boeer, C. Bollert, A. Hoffmann, M. Heidenreich, R. Kriegel, M. Schulz, A. Simon, Performance and Stability of Mixed Conducting Composite Membranes Based on Substituted Ceria, Journal of Ceramic Science and Technology, 5 (2014) 309-316.

[23] J. Kniep, Q. Yin, I. Kumakiri, Y.S. Lin, Electrical conductivity and oxygen permeation properties of SrCoFeOx membranes, Solid State Ionics, 180 (2010) 1633-1639.

[24] K.S. Yun, C.-Y. Yoo, S.-G. Yoon, J.H. Yu, J.H. Joo, Chemically and thermo-mechanically stable LSM–YSZ segmented oxygen permeable ceramic membrane, Journal of Membrane Science, 486 (2015) 222-228.

[25] J.H. Joo, K.S. Yun, J.-H. Kim, Y. Lee, C.-Y. Yoo, J.H. Yu, Substantial Oxygen Flux in Dual-Phase Membrane of Ceria and Pure Electronic Conductor by Tailoring the Surface, Acs Applied Materials & Interfaces, 7 (2015) 14699-14707.

[26] W. Fang, F. Liang, Z. Cao, F. Steinbach, A. Feldhoff, A Mixed Ionic and Electronic Conducting Dual-Phase Membrane with High Oxygen Permeability, Angewandte Chemie-International Edition, 54 (2015) 4847-4850.

[27] M.A. Green, A. Ho-Baillie, H.J. Snaith, The emergence of perovskite solar cells, Nat Photon, 8 (2014) 506-514.

[28] M.J. Verkerk, M.W.J. Hammink, A.J. Burggraaf, OXYGEN TRANSFER ON SUBSTITUTED ZrO//2, Bi//2O//3, AND CeO//2 ELECTROLYTES WITH PLATINUM ELECTRODES - 1. ELECTRODE RESISTANCE BY dc POLARIZATION, Journal of the Electrochemical Society, 130 (1983) 70-78.

[29] X. Tan, N. Liu, B. Meng, J. Sunarso, K. Zhang, S. Liu, Oxygen permeation behavior of La0.6Sr0.4Co0.8Fe0.2O3 hollow fibre membranes with highly concentrated CO2 exposure, Journal of Membrane Science, 389 (2012) 216-222.

[30] V.B. Vert, J.M. Serra, Study of CO2 stability and electrochemical oxygen activation of mixed conductors with low thermal expansion coefficient based on the TbBaCo3ZnO7+delta system, Journal of Power Sources, 196 (2011) 4270-4276.

[31] R. Hammami, H. Batis, C. Minot, Combined experimental and theoretical investigation of the CO2 adsorption on LaMnO3+y perovskite oxide, Surface Science, 603 (2009) 3057-3067.

[32] H.J.M. Bouwmeester, H. Kruidhof, A.J. Burggraaf, Importance of the surface exchange kinetics as rate limiting step in oxygen permeation through mixed-conducting oxides, Solid State Ionics, 72, Part 2 (1994) 185-194.

[33] H.J.M. Bouwmeester, Dense ceramic membranes for methane conversion, Catalysis Today, 82 (2003) 141-150.

[34] M. Balaguer, C. Solis, J.M. Serra, Structural-Transport Properties Relationships on Ce(1-x)Ln(x)O(2-delta) System (Ln = Gd, La, Tb, Pr, Eu, Er, Yb,

Nd) and Effect of Cobalt Addition, Journal of Physical Chemistry C, 116 (2012) 7975-7982.

[35] E.M. Pfaff, A. Kaletsch, C. Broeckmann, Design of a Mixed Ionic/Electronic Conducting Oxygen Transport Membrane Pilot Module, Chemical Engineering & Technology, 35 (2012) 455-463.

[36] M. Balaguer, C. Solis, J.M. Serra, Study of the Transport Properties of the Mixed Ionic Electronic Conductor Ce1-xTbxO2-d + Co (x = 0.1, 0.2) and Evaluation As Oxygen-Transport Membrane, Chemistry of Materials, 23 (2011) 2333-2343.

[37] M. Lipińska-Chwałek, L. Kiesel, J. Malzbender, Mechanical properties of porous MgO substrates for membrane applications, Journal of the European Ceramic Society, 34 (2014) 2519-2524.

[38] Z. Zhu, J. Xiao, W. He, T. Wang, Z. Wei, Y. Dong, A phase-inversion casting process for preparation of tubular porous alumina ceramic membranes, Journal of the European Ceramic Society, 35 (2015) 3187-3194.

[39] W. Fang, Y. Zhang, J. Gao, C. Chen, Oxygen permeability of asymmetric membrane of functional La0.8Sr0.2Cr0.5Fe0.5O3−δ(LSCrF)–Zr0.8Y0.2O2−δ(YSZ) supported on porous YSZ, Ceramics International, 40 (2014) 799-803.

[40] Y. Xing, S. Baumann, D. Sebold, M. Ruettinger, A. Venskutonis, W.A. Meulenberg, D. Stoever, Chemical Compatibility Investigation of Thin-Film Oxygen Transport Membranes on Metallic Substrates, Journal of the American Ceramic Society, 94 (2011) 861-866.

[41] Z. Wang, H. Liu, X. Tan, Y. Jin, S. Liu, Improvement of the oxygen permeation through perovskite hollow fibre membranes by surface acid-modification, Journal of Membrane Science, 345 (2009) 65-73.

[42] Y. Wei, Q. Liao, Z. Li, H. Wang, Enhancement of oxygen permeation through U-shaped K2NiF4-type oxide hollow fiber membranes by surface modifications, Separation and Purification Technology, 110 (2013) 74-80.

[43] A. Leo, S. Liu, J.C. Diniz da Costa, The enhancement of oxygen flux on Ba0.5Sr0.5Co0.8Fe0.2O3−δ (BSCF) hollow fibers using silver surface modification, Journal of Membrane Science, 340 (2009) 148-153.

[44] L. Navarrete, C. Solis, J.M. Serra, Boosting the oxygen reduction reaction mechanisms in IT-SOFC cathodes by catalytic functionalization, Journal of Materials Chemistry A, 3 (2015) 16440-16444.

[45] M. Pilar Lobera, S. Escolastico, J. Garcia-Fayos, J.M. Serra, Ethylene Production by ODHE in Catalytically Modified Ba0.5Sr0.5Co0.8Fe0.2O3-delta Membrane Reactors, Chemsuschem, 5 (2012) 1587-1596.

[46] C. Niedrig, S. Taufall, M. Burriel, W. Menesklou, S.F. Wagner, S. Baumann, E. Ivers-Tiffée, Thermal stability of the cubic phase in Ba0.5Sr0.5Co0.8Fe0.2O3 - δ (BSCF)1, Solid State Ionics, 197 (2011) 25-31.

[47] M. Arnold, H. Wang, A. Feldhoff, Influence of CO2 on the oxygen permeation performance and the microstructure of perovskite-type (Ba0.5Sr0.5)(Co0.8Fe0.2)O3−δ membranes, Journal of Membrane Science, 293 (2007) 44-52.

[48] J. Yi, M. Schroeder, T. Weirich, J. Mayer, Behavior of Ba(Co, Fe, Nb)O3-delta Perovskite in CO2-Containing Atmospheres: Degradation Mechanism and Materials Design, Chemistry of Materials, 22 (2010) 6246-6253.

[49] J. Yi, M. Schroeder, High temperature degradation of Ba0.5Sr0.5Co0.8Fe0.2O3-delta membranes in atmospheres containing concentrated carbon dioxide, Journal of Membrane Science, 378 (2011) 163-170.

[50] Z. Zhang, D. Chen, Y. Gao, G. Yang, F. Dong, C. Chen, F. Ciucci, Z. Shao, A CO2-tolerant nanostructured layer for oxygen transport membranes, Rsc Advances, 4 (2014) 25924-25932.

[51] M. Schulz, R. Kriegel, A. Kaempfer, Assessment of CO2 stability and oxygen flux of oxygen permeable membranes, Journal of Membrane Science, 378 (2011) 10-17.

[52] I. Garcia-Torregrosa, M.P. Lobera, C. Solis, P. Atienzar, J.M. Serra, Development of CO2 Protective Layers by Spray Pyrolysis for Ceramic Oxygen Transport Membranes, Advanced Energy Materials, 1 (2011) 618-625.

[53] Z. Zhang, D. Chen, Y. Chen, Y. Hao, M.O. Tade, Z. Shao, Facile fabrication and improved carbon dioxide tolerance of a novel bilayer-structured ceramic oxygen permeating membrane, Journal of Membrane Science, 472 (2014) 10-18.

[54] J. Emsley, Nature's Building Blocks: An A-Z guide to the elements, 2001.

[55] M. den Exter, W. Haije, J. Vente, Viability of ITM Technology for Oxygen Production and Oxidation Processes: Material, System, and Process Aspects, in: A. Bose (Ed.) Inorganic Membranes for Energy and Environmental Applications, Springer New York2009, pp. 27-51.

[56] M.A. Habib, H.M. Badr, S.F. Ahmed, R. Ben-Mansour, K. Mezghani, S. Imashuku, G.J. la O, Y. Shao-Horn, N.D. Mancini, A. Mitsos, P. Kirchen, A.F. Ghoneim, A review of recent developments in carbon capture utilizing oxy-fuel combustion in conventional and ion transport membrane systems, International Journal of Energy Research, 35 (2011) 741-764.

[57] S.S. Hashim, A.R. Mohamed, S. Bhatia, Oxygen separation from air using ceramic-based membrane technology for sustainable fuel production and power generation, Renewable & Sustainable Energy Reviews, 15 (2011) 1284-1293.

[58] P. Markewitz, J. Marx, A. Schreiber, P. Zapp, Ecological evaluation of coal-fired Oxyfuel power plants -cryogenic versus membrane-based air separation, Ghgt-11, 37 (2013) 2864-2876.

[59] S. McIntosh, J.F. Vente, W.G. Haije, D.H.A. Blank, H.J.M. Bouwmeester, Oxygen stoichiometry and chemical expansion of Ba0.5Sr0.5Co0.8Fe0.2O3-delta measured by in situ neutron diffraction, Chemistry of Materials, 18 (2006) 2187-2193.

[60] S. McIntosh, J.F. Vente, W.G. Haije, D.H.A. Blank, H.J.M. Bouwmeester, Structure and oxygen stoichiometry of SrCo0.8Fe0.2O3-delta and Ba0.5Sr0.5Co0.8Fe0.2O3-delta, Solid State Ionics, 177 (2006) 1737-1742.

[61] S. McIntosh, J.F. Vente, W.G. Haije, D.H.A. Blank, H.J.M. Bouwmeester, Phase stability and oxygen non-stoichiometry of SrCo0.8Fe0.2O3-delta measured by in situ neutron diffraction, Solid State Ionics, 177 (2006) 833-842.

[62] D.N. Mueller, R.A. De Souza, T.E. Weirich, D. Roehrens, J. Mayer, M. Martin, A kinetic study of the decomposition of the cubic perovskite-type oxide BaxSr1-xCo0.8Fe0.2O3-delta (BSCF) (x=0.1 and 0.5), Physical Chemistry Chemical Physics, 12 (2010) 10320-10328.

[63] M.P. Lobera, J.M. Serra, S.P. Foghmoes, M. Søgaard, A. Kaiser, On the use of supported ceria membranes for oxyfuel process/syngas production, Journal of Membrane Science, 385–386 (2011) 154-161.

[64] M. Pilar Lobera, S. Escolastico, J.M. Serra, High Ethylene Production through Oxidative Dehydrogenation of Ethane Membrane Reactors Based on Fast Oxygen-Ion Conductors, Chemcatchem, 3 (2011) 1503-1508.

[65] M.P. Lobera, M. Balaguer, J. Garcia-Fayos, J.M. Serra, Rare Earth-doped Ceria Catalysts for ODHE Reaction in a Catalytic Modified MIEC Membrane Reactor, Chemcatchem, 4 (2012) 2102-2111.

[66] W.G. Haije, S.C. Kluiters, R.W. van den Brink, D. Jansen, Systems and materials for mixed ionic electronic conducting membranes in integrated oxyfuel combustion systems, in: J. Gale, C. Hendriks, W. Turkenberg (Eds.) 10th International Conference on Greenhouse Gas Control Technologies2011, pp. 996-1001.

[67] S. Engels, F. Beggel, M. Modigell, H. Stadler, Simulation of a membrane unit for oxyfuel power plants under consideration of realistic BSCF membrane properties, Journal of Membrane Science, 359 (2010) 93-101.

[68] S. Engels, T. Markus, M. Modigell, L. Singheiser, Oxygen permeation and stability investigations on MIEC membrane materials under operating conditions for power plant processes, Journal of Membrane Science, 370 (2011) 58-69.

[69] X. Zhu, H. Liu, Y. Cong, W. Yang, Novel dual-phase membranes for CO2 capture via an oxyfuel route, Chemical Communications, 48 (2012) 251-253.

[70] A. Julbe, D. Farrusseng, C. Guizard, Limitations and potentials of oxygen transport dense and porous ceramic membranes for oxidation reactions, Catalysis Today, 104 (2005) 102-113.

[71] J.C.D. da Costa, S. Smart, J. Motuzas, S. Liu, D. Zhang, State of Art (SOTA) Report on Dense Ceramic Membranes for Oxygen Separation from Air, Australian National Low Emissions Coal Research & Development (ANLEC R&D), Brisbane, 2013.

[72] U.S.E.I. Administration, International Energy Outlook 2013. With Projections to 2040, in: U.S.E.I. Administration (Ed.), 2013.

[73] E.-T.-P.-f.-Z.-E.-.-. Fossil-Fuel-Power-Plants- http://www.zeroemissionsplatform.eu/carbon-capture-and-storage.html, http://www.zeroemissionsplatform.eu/carbon-capture-and-storage.html, 2014.

[74] Q. Wang, X. Chen, A.N. Jha, H. Rogers, Natural gas from shale formation - The evolution, evidences and challenges of shale gas revolution in United States, Renewable & Sustainable Energy Reviews, 30 (2014) 1-28.

[75] A. Yanagisawa, Impacts of shale gas revolution on natural gas and coal demand, The Institute of Energy Economics, Japan, (2013).

[76] N. Perrin, R. Dubettier, F. Lockwood, J.-P. Tranier, C. Bourhy-Weber, P. Terrien, Oxycombustion for coal power plants: Advantages, solutions and projects, Applied Thermal Engineering, 74 (2015) 75-82.

[77] M. Lupion, I. Alvarez, P. Otero, R. Kuivalainen, J. Lantto, A. Hotta, H. Hack, 30 MWth CIUDEN Oxy-CFB Boiler - First experiences, Ghgt-11, 37 (2013) 6179-6188.

[78] J. Monne, C. Prinet, Lacq-Rousse Industrial CCS reference project: Description and operational feedback after two and half years of operation, Ghgt-11, 37 (2013) 6444-6457.

[79] A. Bose, G. Stiegel, P. Armstrong, B. Halper, E.P. Foster, Progress in Ion Transport Membranes for Gas Separation Applications, in: A. Bose (Ed.) Inorganic Membranes for Energy and Environmental Applications, Springer New York2009, pp. 3-25.

[80] C.F. Miller, J. Chen, M.F. Carolan, E.P. Foster, Advances in ion transport membrane technology for Syngas production, Catalysis Today, 228 (2014) 152-157.

[81] W.E.W. John M. Repasky, Christopher F. Miller, Michael F. Carolan, David W. Studer, Clifford M. Lowe, Karl F. Gerdes, Joris Smit. , ITM Syngas: Ceramic Membrane Technology for Lower Cost Conversion of Natural Gas, AIChE Spring National MeetingSan Antonio, TX, 2010.

[82] L.E. Bool, H. Kobayashi, Oxygen separation and combustion apparatus and method. U.S. Patent 6,394,043, 2002.

[83] L.E. Bool, H. Kobayashi, Method and system for combusting a fuel. U.S. Patent 6,562,104, 2003.

[84] L. Rosen, N. Degenstein, M. Shah, J. Wilson, S. Kelly, J. Peck, M. Christie, Development of Oxygen Transport Membranes for Coal-Based Power Generation, 10th International Conference on Greenhouse Gas Control Technologies, 4 (2011) 750-755.

[85] B.R. Kromer, M.M. Litwin, S.M. Kelly, Oxygen transport membrane based advanced power cycle with low pressure synthesis gas slip stream. U.S. Patent 7,856,829, 2014.

[86] M.M. Shah, A. Jamal, R.F. Dmevich, A. van Hassel, G.M. Christie, H. Kobayashi, L.E. Bool, Electrical power generation apparatus: U.S. Patent 8,196,387, 2012.

[87] S.M. Kelly, B.R. Kromer, M.M. Litwin, L.J. Rosen, G.M. Christie, J.R. Wilson, L.W. Kosowski, C. Robinson, Synthesis gas method and apparatus. U.S. Patent 8,349,214, 2013.

[88] D.M. John Repasky, Phillip Armstrong, Michael Carolan, ITM Technology for Carbon Capture on Natural Gas and Hybrid Power Systems, Workshop on Technology Pathways Forward for Carbon Capture & Storage on Natural Gas Power SystemsWhasington DC, 2014.

[89] Air Products invests in new ITM test facility, Filtration Industry Analyst, 2011 (2011) 5.

[90] A.L.L. Repasky J.M., Stein V.E., Armstrong P.A., Foster E.P., ITM Oxygen technology: scale-up toward clean energy applications, International Pittsburgh Coal Conference 2012, 2012.

[91] J. Caro, T. Schiestel, S. Werth, H. Wang, A. Kleinert, P. Kölsch, Perovskite hollow fibre membranes in the partial oxidation of methane to synthesis gas in a membrane reactor, Desalination, 199 (2006) 415-417.

[92] L. Olivier, S. Haag, C. Mirodatos, A.C. van Veen, Oxidative coupling of methane using catalyst modified dense perovskite membrane reactors, Catalysis Today, 142 (2009) 34-41.

[93] H. Jiang, Z. Cao, S. Schirrmeister, T. Schiestel, J. Caro, A Coupling Strategy to Produce Hydrogen and Ethylene in a Membrane Reactor, Angewandte Chemie International Edition, 49 (2010) 5656-5660.

[94] M.P. Lobera, S. Valero, J.M. Serra, S. Escolástico, E. Argente, V. Botti, Optimization of ODHE membrane reactor based on mixed ionic electronic conductor using soft computing techniques, Chemical Engineering Science, 66 (2011) 6308-6317.

[95] A.J.M. SERRA, B.V.B. Vert, R.S. ESCOLÁSTICO, Catalytic layer for oxygen activation on ionic solid electrolytes at high temperature, Google Patents, 2009.

[96] H. Jiang, H. Wang, F. Liang, S. Werth, S. Schirrmeister, T. Schiestel, J. Caro, Improved water dissociation and nitrous oxide decomposition by in situ oxygen removal in perovskite catalytic membrane reactor, Catalysis Today, 156 (2010) 187-190.

[97] Z. Cao, H. Jiang, H. Luo, S. Baumann, W.A. Meulenberg, H. Voss, J. Caro, Simultaneous overcome of the equilibrium limitations in BSCF oxygen-permeable membrane reactors: Water splitting and methane coupling, Catalysis Today, 193 (2012) 2-7.

[98] W. Fang, F. Steinbach, Z.W. Cao, X.F. Zhu, A. Feldhoff, A Highly Efficient Sandwich-Like Symmetrical Dual-Phase Oxygen-Transporting Membrane Reactor for Hydrogen Production by Water Splitting, Angewandte Chemie-International Edition, 55 (2016) 8648-8651.

[99] W. Jin, C. Zhang, X. Chang, Y. Fan, W. Xing, N. Xu, Efficient Catalytic Decomposition of CO2 to CO and O2 over Pd/Mixed-Conducting Oxide Catalyst in

an Oxygen-Permeable Membrane Reactor, Environmental Science & Technology, 42 (2008) 3064-3068.

2. EXPERIMENTAL

2. Experimental.

2.1. Material synthesis.

Different methods have been used to prepare the materials depending on the desirable characteristics for the powders and on the metal precursor nature. BSCF and LSFC were available from commercial suppliers, so no synthesis has been used for such materials. CGO powders have been fabricated by co-precipitation method. Dual-phase composites have been synthesized by Pechini sol-gel route [1]. Catalysts to be infiltrated on porous substrates have been obtained by means of precursors (typically nitrates) dilution in ethanol-water .The details of the fabrication are described below.

2.1.1. Co-precipitation.

The co-precipitation method allows the synthesis of nanometric size powders [2]. This method has been used in this thesis for the production of gadolinium doped ceria (CGO) electrolytes. A schematic view of the co-precipitation routine is provided in Figure 2.10. A clear solution of commercial lanthanide nitrates mixture is prepared in deionized water at 50 ºC. A $(NH_4)_2CO_3$ solution is dropped into the previous solution to achieve total precipitation and the final NO_3^{-1}/CO_3^{-2} molar ratio is 0.75. The resulting precursor powders are dried at 100-150 ºC after filtration and rinsing with water. The cerias have been co-doped with cobalt in order to improve electrolytes sinterability. The Co addition is done over the dried precursor powder by incipient wetness impregnation, *i.e.,* calculated 2% molar of $Co(NO_3)_2{\cdot}6H_2O$ is dissolved in deionized water (volume according with the pore volume) and mixed with the intermediate dried powder. Finally, each powder is calcined during 5 hours in air atmosphere at 800 ºC to decompose the residual nitrates and carbonates and to favour the formation of the fluorite phase.

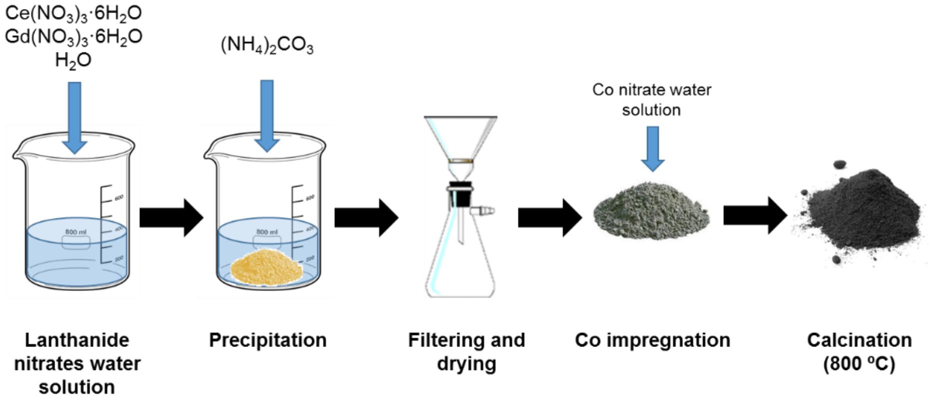

Figure 2.10: Scheme of the fabrication of the Gd-doped ceria.

2.1.2. Pechini or sol-gel route.

Composite powders were prepared by one pot Pechini method. This routine allows the enhancement of the oxygen flux with respect to solid state mixing method due to the improvement in morphology and homogeneity [3]. This is mainly due to the obtaining of carbonate-free, chemically homogeneous final oxide compounds with a high relative density and small size.

Transition metals and lanthanide nitrates were mixed in distilled water in order to obtain a homogeneous solution ($Ce(NO_3)_3{\cdot}6H_2O$ and $Fe(NO_3)_3{\cdot}9H_2O$ provided by Sigma Aldrich; $Tb(NO_3)_3{\cdot}6H_2O$ and $Ni(NO_3)_3{\cdot}6H_2O$ from ABCR). After obtaining complete dissolution, citric acid (Sigma Aldrich) was added as a chelating agent to prevent partial segregation of the metal components, and ethylene glycol was added to polymerize with the chelating agent and produce an organometallic polymer (in a molar ratio 1:2:4 with respect to nitrates solution, citric acid, and ethylene glycol, respectively). This complexation is followed by dehydration at low temperature (up to 270 ºC) and finally, thermal decomposition of the precursors at 600 ºC forms the desired structural phases (fluorite and spinel).

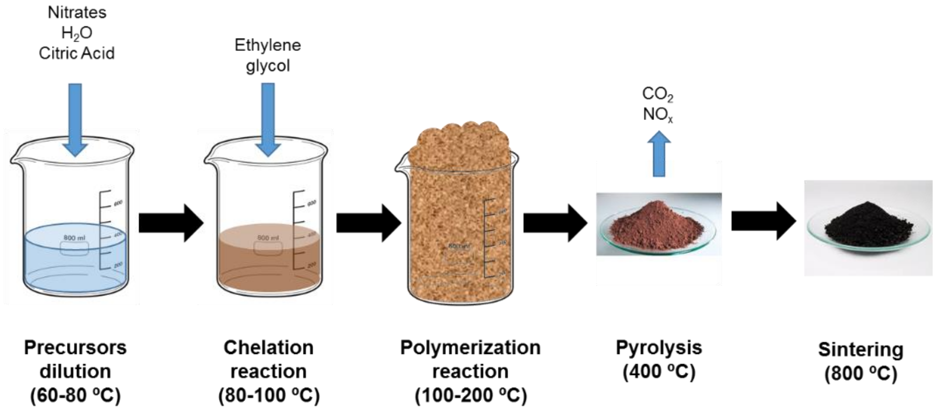
Nitrates
H_2O
Citric Acid
Ethylene glycol
CO_2
NO_x
Precursors dilution (60-80 ºC)
Chelation reaction (80-100 ºC)
Polymerization reaction (100-200 ºC)
Pyrolysis (400 ºC)
Sintering (800 ºC)

Figure 2.11: Scheme of the Pechini synthesis routine for dual-phase materials fabrication.

2.2. Material processing. Sample preparation.

2.2.1. Membranes and electrolytes.

Starting from sintered powders, membranes and electrolytes are manufactured following similar procedures, being depicted in Figure 2.12. Both the membranes and the electrolytes consist of flat dense disks with a diameter about 15 mm. In order to assure a good homogeneity during the sintering process, starting powders are ball-milled in an acetone-powder-zirconia balls dispersion for 12-15 hours thus reducing and homogenizing the particle size. The ball mill uses 3 mm diameter zirconia balls and turn at 50 rpm. After the milling, the powders are separated from the balls and dried. Finally, homogenous powders with particle size distribution of 200-400 μm re obtained by sieving through steel sieves of the referred mesh size.

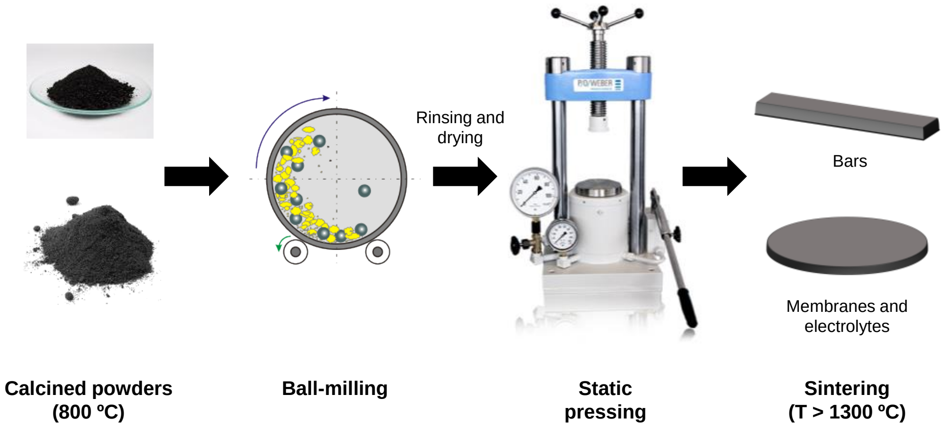

Figure 2.12: Main steps for the fabrication of membranes, electrolytes and rectangular probes.

A 26 mm diameter steel die is used to uniaxially press the material at 125 MPa during 3 minutes. Afterwards, the green disk is sintered at high temperature in order to densify the specimen. The temperature and time of the process depend on the material. Permeation measurements are performed on 15 mm diameter and 500~900 μm thick disks. This dimensions are achieved by grinding by sandpaper. In some cases both disk sides were screen printed by 15-30 μm of a catalytic layer (metals, MIECs or composite materials) in order to improve the surface catalytic behaviour. Electrolytes present same dimensions than membranes, as well as porous layers deposited by screen-printing forming the electrodes, thus being characterized during Electrochemical Impedance Spectroscopy (EIS) experiments.

2.2.2. Production of LSCF porous supports by freeze-casting.

Porous supports were prepared by ice-templating using the freeze-casting technique. A slurry containing the ceramic powder (40-50 wt%), water (30-40 wt%) as solvent, a polyacrylate-based dispersing agent (1-4 wt%) and polyethylene glycol (1-4 wt%) is stirred for 24 hours to get a good particle distribution. The slurry is then poured into Teflon mold to get a sample of 1 cm height and cooled using copper rod cooled by liquid nitrogen. After complete freezing, the sample is removed from the mold and ice crystals are sublimated by freeze drying at -53ºC and reduced pressure during 24 hours using a Scanvac commercial freeze dryer. The sample is then pre-sintered at 1200ºC under air during 6 hours to get a green porous support easy to handle for screen printing. Both heating and decreasing ramps are 20 hours.

For producing an asymmetric membrane a gas-tight LSCF top layer is then coated by screen printing upon the side of the porous support facing the copper rod during the freezing step. The slurry used for the coating contains in the 50:50 weight ratio the LSCF powder and a binder (6 wt% ethylcellulose in terpineol). Similar procedure is followed for depositing a 60NFO-40CTO top layer. For both cases, the final sintering step is realized at 1400ºC under air during 6 hours. The final diameter of the sample is 14 mm and the final thickness of 1 mm is adjusted by grinding the porous support.

2.2.3. Rectangular bars.

Ceramic powders are conformed as rectangular probes for performing electrochemical tests as DC-conductivity. After rinsing and drying, rectangular bars with dimensions 4x0.4x0.2 cm^3 are obtained by uniaxial pressing from the sintered powders (Figure 2.12) at 125 MPa during 1 minute and subsequently sintered 5 hours at 1350 ºC in air.

2.2.4. Catalytic layer/Electrode deposition.

Porous layers with thicknesses in the range of 15-30 μm were deposited on membranes surface for improving surface exchange reactions and therefore enhancing oxygen permeation. The deposition of these layers was conducted by screen-printing method. Same procedure was followed for attaching porous electrodes on CGO electrolytes and thus studying surface electrochemistry of porous layers by EIS.

By means of screen-printing technique it is possible to produce films with thicknesses of 10-100 μm in an economical and simple way. This method consists of applying an ink made of the ceramic powder, an organic binder (ethyl cellulose) and a plasticizer (terpineol). For obtaining this ink the aforementioned elements are mixed and subsequently refined in a three-roll mill forming a uniform slurry. Then, the slurry is printed on the membrane or electrolyte surface by means of a 9 mm diameter mesh thus developing the catalytic layer or the electrode, respectively. With this screen-printing step a 15 μm layer is deposited. For producing thicker layers it is only necessary repeating the process once the latter layer has been dried (after 1 hour at 80 ºC), or using another mesh with appropriate sieve. Finally, the deposited layers are sintered at high temperature. This process is depicted in Figure 2.13.

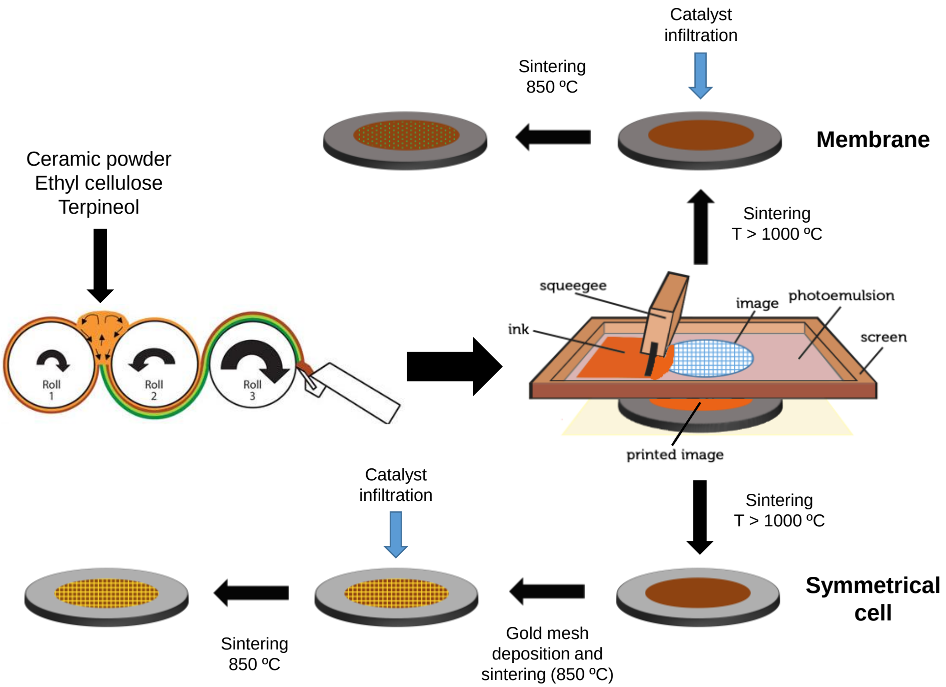
Catalyst infiltration
Sintering 850 ºC
Membrane
Ceramic powder
Ethyl cellulose
Terpineol
Sintering T > 1000 ºC
squeegee
ink
image
photoemulsion
screen
Roll 1
Roll 2
Roll 3
printed image
Catalyst infiltration
Sintering T > 1000 ºC
Symmetrical cell
Sintering 850 ºC
Gold mesh deposition and sintering (850 ºC)

Figure 2.13: Main steps for the deposition of catalytic layers on membranes (upper route) and deposition of electrodes on CGO electrolytes (lower route).

For the production of electrodes in symmetrical cells it is also needed the deposition of gold meshes on electrodes surfaces for contacting the current collector. This gold mesh is deposited by screen-printing using a gold paste that is dried and sintered at 850 ºC during 2 hours.

Both catalytic layers and electrodes were activated by infiltration of catalyst precursors (nitrates) and subsequently sintered at temperatures above 850 ºC for obtaining the desired phase.

2.3. Structural characterization.

2.3.1. Scanning Electron Microscopy.

Scanning electron microscopy (SEM) allows for high-resolution imaging of surfaces by using high-energy electrons (1.5-20 KeV) generated by a heated tungsten filament. The SEM has a magnification up to 10^6x and great depth of field. For that purpose, an incident beam of monochromatic electrons causes a secondary emission across the sample surface, which is collected to form an image of the surface. The quality and contrast obtained in the image depends mainly on the conductivity and surface topography of the sample. By detecting different emissions of the sample, it is possible to obtain diverse contrast images, *i.e.*, backscattered electrons (BSE), Auger electrons (AES) and Energy dispersive x-ray spectroscopy

(EDS). BSE causes different contrast subjected to the atomic number, Z, of the elements, so changes in composition can be distinguished; EDS is a qualitative and quantitative chemical microanalysis technique to characterize the elemental composition of the volume analysed. It is performed in conjunction with a SEM, but uses the X-rays that are emitted from the sample due to the electron beam. The combination of SEM with EDS allows the analysis of the sample morphology and the composition of the different phases that are present. The minimum detection limits are about 0.1 weight percent, depending on the element and matrix.

Conducting materials that allow the transport of the incident beam electrons do not need any handling of the sample. However, for poor conductors or insulators a conducting layer that does not modify the topography needs to be added. This is achieved by coating the sample in vacuum with Au or graphite (for EDS) using a sputter coater.

Two SEM devices were used on the characterizations, namely the Jeol JSM 6300 and Jeol JSM 5410, both with an acceleration voltage of 20 kV. The EDS microanalyses were carried out with a detector from Oxford Instruments. The Software INCAEnergy/Wave served for the interpretation of the X-ray patterns obtained. More recently, a ZEISS Ultra55 field emission SEM (FE-SEM) has been also used.

2.3.2. X-Ray Diffraction.

Very high temperatures (> 1000 ºC) have been used throughout this thesis for the production of metallic oxides. Such high temperatures assure the formation of crystalline compounds and therefore they can be analysed by means of X-ray diffraction (XRD) technique [4].

There is a characteristic XRD pattern for every crystalline substance that can be used for its identification. XRD measurements are based on the physical principle that a monochromatic X-ray beam with a wavelength λ comes into contact with the crystalline material at a particular angle. The diffraction is produced only when the distance travelled by the rays reflected from successive planes differs by a complete number of wavelengths. As shown in Figure 2.14, the diffracted angle from the family of crystallographic planes ($h\ k\ l$) has a value of 2θ, which is employed to determine the distance between layers of atoms in a sample using the Bragg's law.

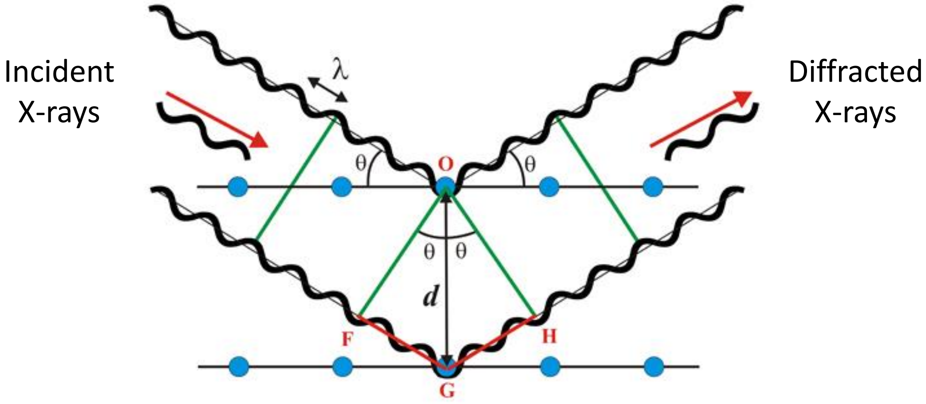

$$n \cdot \lambda = 2 \cdot d \cdot sen(\theta)$$

Figure 2.14: Bragg's Law. Diffraction of X-rays on a crystalline material. Image extracted from [5].

A PANalytical Cubix fast diffractometer, using CuKα1 radiation (λ = 1.5406 Å) and an X′ Celerator detector in Bragg−Brentano geometry was used for the identification of the crystalline phases. XRD patterns recorded in the 2θ range from 10º to 90° were analyzed using X'Pert Highscore Plus software.

XRD has been used during the realization of the present thesis for the determination of the phase purity of the manufactured compounds and the presence of impurities and secondary phase, as well as the study of the degradation of membranes after permeation tests. Furthermore, this technique has been used for studying the structural stability of materials exposed to harsh environments (e.g. CO_2, SO_2 and reducing atmospheres) by comparing XRD results of the materials before and after exposure.

2.3.4. Raman spectroscopy.

Information about the structure and properties of molecules forming ceramic materials can be obtained by using Raman spectroscopy. This information is obtained from the vibrational transitions of molecules. Raman vibrational bands are characterized by their frequency (energy), intensity, and band shape (environment of bonds). Depending on the masses of the atoms, their geometric arrangement and the strength of chemical bonds different frequencies will be obtained [6]. Therefore, observing anomalies in the position, intensity and shape of the bands it is possible to detect structural and compositional changes.

Raman spectra were measured with a Renishaw inVia Raman spectrometer equipped with a Leica DMLM microscope and a 514-nm Ar+ ion laser as an excitation source. A x50 objective of 8-mm optical length was used to focus the depolarized laser beam on a spot of about 3 μm in diameter. The Raman scattering was collected with a charged coupled device (CCD) array detector.

2.4. Thermal analysis.

2.4.1. Thermo-gravimetry (TG).

Several processes such as decomposition, dehydration, or oxidation/reduction reactions, are indicative of chemical and thermal stability of materials. These processes are accompanied by a mass change. Therefore by means of TG technique it is possible to study materials stability. The thermobalance registers the mass changes undergone by the sample as a function of temperature, time and atmosphere. The TG is combined with DTA (Differential Thermal Analysis), which records exothermic or endothermic processes that enclose transformations in the material when compared with an inert reference material. DTA is mainly used for studying transitions, chemical reactions, adsorption, crystallisation, melting and sublimation.

In the current study, the thermobalance was used to monitor changes in the oxygen non-stoichiometry, to ensure the complete decomposition of precursors (carbonates, nitrates and polymers) and to test mass changes of the material in the reaction against CO_2. The TG/DTA analysis was performed on Mettler-Toledo StarE equipment, which has different gases available, such as synthetic Air (21 vol% O_2 and 79 vol% N_2), N_2 and 5% CO_2/air. The powders were analysed in these atmospheres in the temperature range from room temperature to 1000 ºC, with heating and cooling rates of 10 ºC/min.

2.5. Electrochemical characterization.

2.5.1. DC total electrical conductivity.

Electrical conductivity measurements based on the standard four-point DC technique were performed on the studied samples for the conductivity characterization under different pO_2 atmospheres at different temperatures.

Four electric contacts made of silver and silver paste are applied on sintered samples consisting of rectangular bars. An electrical current is imposed through the sample using the external contacts, whereas the potential gradient is measured between the inner contacts (Figure 2.15).

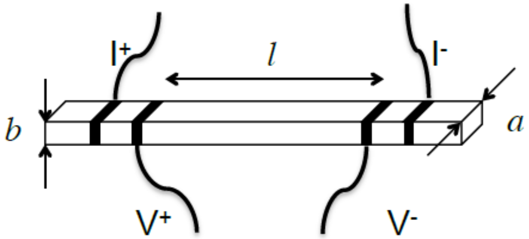

Figure 2.15: Four-point configuration for DC conductivity measurements.

The resistance (R) is obtained from Ohm's Law (E = I·R), which once corrected by the section (*a*·*b*) and the distance between the contacts (*l*), yields the total conductivity (σ_{total}) of the material (in $S \cdot cm^{-1}$):

$$\sigma_{total} = \frac{l}{a \cdot b} \cdot \frac{1}{R} \tag{2.1}$$

The conductivity measurements are thermally activated and were analysed on the basis of Arrhenius behaviour

$$\sigma\ (T) = \frac{A}{T} \cdot \exp\left(\frac{-E_a}{k \cdot T}\right) \tag{2.2}$$

The activation energy (E_a) is extracted from the slope of the graphs. Once the highest temperature (800 ºC) was reached, the samples were stabilized for two hours in order to warrantee the high-temperature reduction state corresponding to the specific pO_2.

Resistance measurements are not obtained from a single value V-I, but from the slope of several V-I points when small intensity ranges are applied. A programmable current source (Keithley 2601) supplies the constant current and a sixteen channel multimeter (Keithley 3706) detects the voltage drop. The use of gases with different O_2 contents (Linde calibrated gas mixtures checked by an YSZ oxygen sensor) allowed the determination of the material's conductivity type, *i.e.* ionic, electronic or mixed ionic-electronic.

2.5.2. Electrochemical Impedance Spectroscopy (EIS).

By means of DC conductivity it is possible to determine the conductivity type of a given material, nevertheless this technique does not provide information about the processes limiting this conductivity. These processes can be related with the transport within the material (grain and grain boundary) or with processes taking place in the reaction media (gas diffusion, surface exchange reactions, adsorption…).

All these processes can be determined by using EIS, as well as the total conductivity. During EIS tests a small sinusoidal current (or voltage) is passed through the sample, thus measuring the phase shift and amplitude, or real and imaginary parts, of the resulting voltage/current signal. Depending on the rate limiting process the material response will be different, as a result, it will be possible to determine which process prevails under the tested conditions.

Analogously to Ohm's law, for EIS the impedance (*Z*) can be expressed by the equation:

$$E = I \cdot Z \tag{2.3}$$

Writing the voltage excitation signal as function of time

$$E_t = E_0 \sin(\omega t) \tag{2.4}$$

Where E_t is the voltage at a t time, E_0 is the amplitude of the signal and ω is the radial frequency. In a linear system, the current response signal (I_t) is shifted in phase φ with different amplitude (I_0):

$$I_t = I_0 \sin(\omega t + \varphi) \tag{2.5}$$

Therefore, the impedance can be written as

$$Z = \frac{E_0 \sin(\omega t)}{I_0 \sin(\omega t + \varphi)} = Z_0 \cdot \frac{\sin(\omega t)}{\sin(\omega t + \varphi)} \tag{2.6}$$

And finally expressing the impedance as a complex function with real and imaginary parts

$$Z(\omega) = Z_0 \exp(i\varphi) = Z_0 \cdot \exp(cos\varphi + isin\varphi) \tag{2.7}$$

EIS data analysis is typically made by graphical representation and modelling to an electrical equivalent circuit that allows the physical interpretation of the single characteristics. Nyquist-plot represents real (Z') and imaginary (Z") part of impedance values, whose spectra have a semicircle shape, as shown in Figure 2.16. The high frequency intercept (for ω→∞) with the real axis represents the purely ohmic resistance, R_0 of the cell, whereas the intercept at the lower frequency (for $\omega \rightarrow 0$) represents the differential resistance, which can be obtained from the corresponding I-U characteristic at the given operating point. The difference between the low and high frequency intercept is the polarisation resistance (R_p) of the cell that is the sum of each single polarisation resistance caused by the loss mechanisms inside the cell.

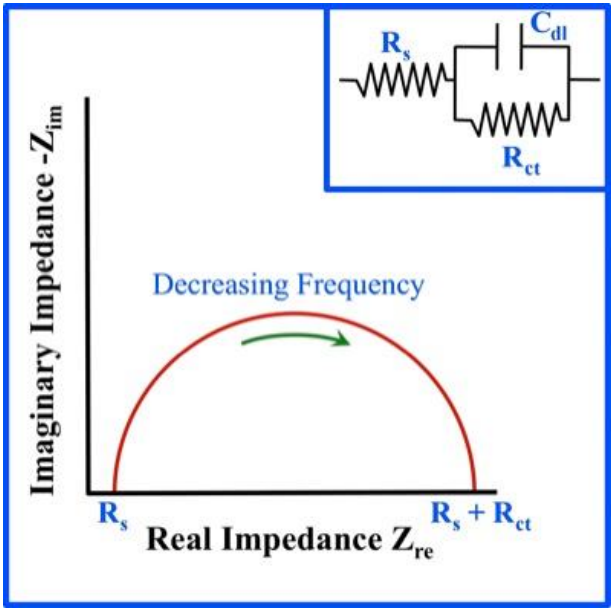

Figure 2.16: Impedance results as function of the imaginary and real impedance. Inset represents the equivalent electrical circuit fitting for the EIS measurement response.

Electrodes in symmetrical cells were tested by EIS in two-point configuration. Input signal was 0 V DC – 20 mV AC amplitude signal in the 0.01 – $3 \cdot 10^5$ Hz frequency range. This signal was generated by a Solartron 1470E and a 1455A FRA module equipment. EIS measurements were performed in the 800-900 ºC range, under different atmospheres (N_2, CO_2) at different pO_2 (5% to 21% O_2). In all the cases, the total flow remained constant (100 $ml \cdot min^{-1}$). Zview™ 2 fitting programme was employed to analyze the impedance spectra.

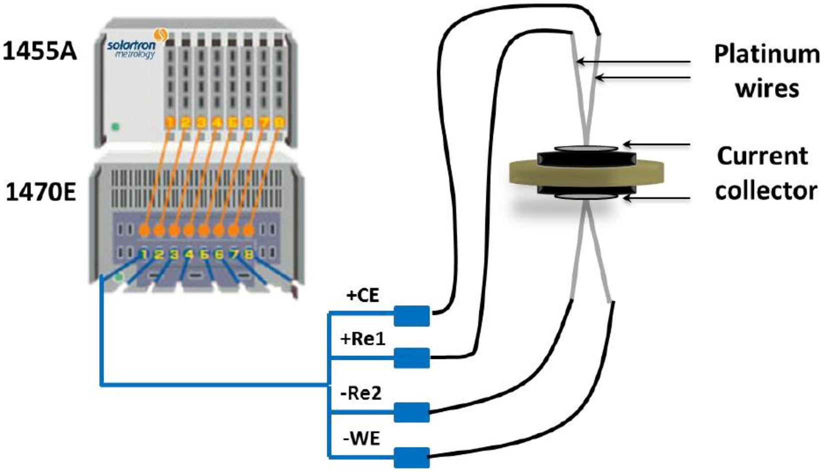

Figure 2.17: Connections between the Solartron equipment 1470E and 1455A module, with the electrochemical cell.

2.6. Membrane performance characterization.

2.6.1. Experimental set-up. Planar membranes.

A fully-automatized test bench was available for the conduction of oxygen permeation tests. This test bench, named as PH2 Reactor, was entirely designed and assembled by the personnel of the *Instituto de Tecnología Química*, thus being properly adapted to the experimental requirements of the present thesis.

The test bench lay-out is given in Figure 2.18. As can be seen, the experimental set-up follows a 4-end configuration, thus presenting two inlets and two outlets. The two gas inlets correspond to the feed (CG1 and CG2) and sweep streams (CG3, CG4 and CG5), whereas the retentate and permeate are the two outlet streams (VENT). The gas supply was done by means of five mass-flow controllers (indicated as CG). Therefore, it was possible to induce several atmospheres and gradients. Gases such as synthetic air, O_2, He, N_2, H_2, and Ar are directly supplied from the pipeline distribution system available in the ITQ facilities. Other gases including CH_4, C_2H_6 and different mixtures of CO_2 can be fed from gas cylinders connected to the bench.

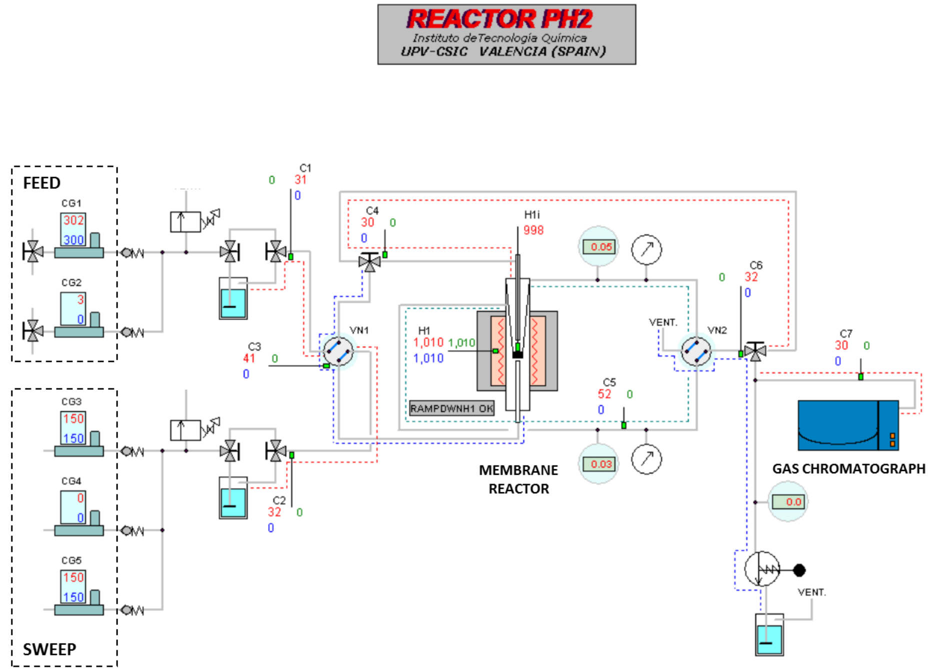
REACTOR PH2
Instituto de Tecnología Química
UPV-CSIC VALENCIA (SPAIN)
FEED
CG1
302
300
CG2
3
0
CG3
150
150
CG4
0
0
CG5
150
150
SWEEP
C1
0
31
0
C2
32
0
0
C3
41
0
0
C4
30
0
0
H1i
998
0.05
0.03
VN1
H1
1,010
1,010
1,010
RAMPDWNH1 OK
MEMBRANE
REACTOR
C5
52
0
0
VENT.
VN2
C6
0
32
0
C7
30
0
0
GAS CHROMATOGRAPH
0.0
VENT.

Figure 2.18: PH2 Reactor control program Front Panel.

The membrane reactor where the oxygen permeation studies were carried out consisted of a lab-scale quartz reactor as the one depicted in Figure 2.19. Synthetic air (21%, v/v O_2), mixtures of O_2 in N_2/He or pure oxygen were fed into the oxygen-rich chamber, while argon, CO_2 or hydrocarbons (CH_4, C_2H_6) were used as the sweep gas on the permeate side. Both streams were fed at atmospheric pressure. Inlet gases were preheated in order to ensure the correct gas temperature for contact with the membrane surface. This is particularly important when high gas flow rates are employed. All streams were individually mass flow controlled. The temperature was measured by a thermocouple attached to the membrane. A PID controller maintained temperature variations within 2 ºC of the set point. The samples consisted of 15 mm diameter disk-shaped gastight membranes and membrane gas leak-free conditions were achieved by using O-rings consisting of gold or tailored alloys. The permeate was analyzed at steady state by online gas chromatography using a micro-GC Varian CP-4900 equipped with Molsieve5A, Pora-Plot-Q glass capillary, and CP-Sil modules. Membrane gas leak-free conditions were ensured by continuously monitoring the nitrogen concentration in the product gas stream. An acceptable sealing was achieved when the ratio between the oxygen leak flow and the oxygen flux was lower than 1%. The data reported throughout the present thesis were achieved at steady state after 1 h in the reaction stream. Each GC analysis was repeated three times to minimize the analysis error. The experimental analytical error was below 0.5%.

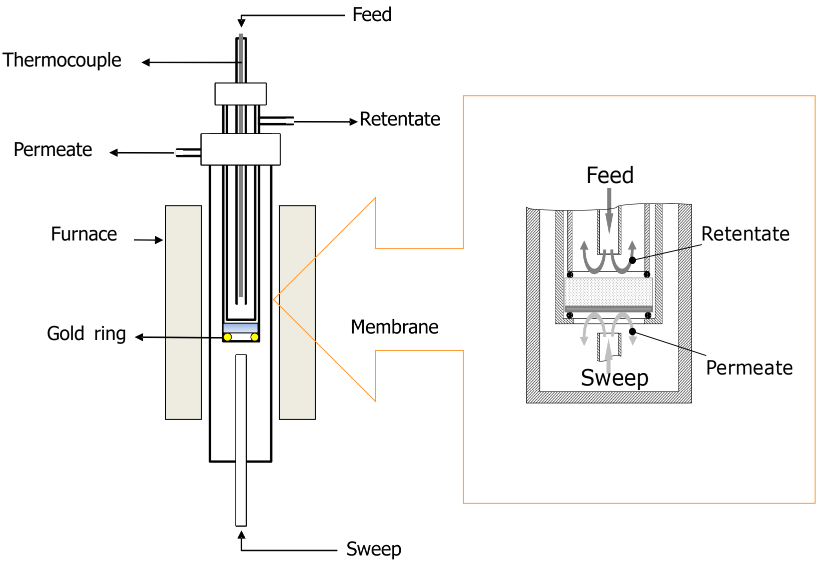

Figure 2.19: Experimental setup permeation scheme. The membrane is pressed by a spring sited in the lid.

2.6.2. Experimental set-up. Capillary membranes.

For the testing of membranes presenting tubular geometries it was necessary to build a new experimental set-up specifically for this kind of tests. As can be seen in Figure 2.20, the capillary membrane is placed inside a tubular quartz reactor. This reactor presents a porous quartz frit on the bottom. The function of this frit is for permitting the placement of a silicon carbide (SiC) packed-bed when conducting catalytic reactions. To ensure isothermal conditions (the used furnace has an isothermal zone of 30 mm), only the last 30 mm of the capillary were set available for permeating. There are several options for passivating a membrane and then avoiding it to permeate. One example is by screen-printing the target surface with gold paste, as performed by Caro et al. [7]. Nevertheless, for our case we considered covering the capillary with a quartz tube with an inner diameter close to the capillary outer diameter and closing the two ends, thus avoiding any sweep gas to be in contact with membrane surface and subsequently imposing permeation. The use of this system requires placing a packed-bed for sustaining the quartz tube.

Feed gas consisting of O_2/N_2 mixtures is introduced in the system through a thin dense alumina tube that, carrying the gas to the bottom end of the capillary. At this point, the feed gas flows through the space between the alumina tube and the capillary inner surface, occurring the permeation in a 30 mm section. Retentate gas, after circulating through the passivated membrane section, exits from the reactor to vent. As the temperature at the feed/sweep gas inlet zone is no higher than 80 ºC then commercial tube fitting solutions have been used for stanching the conductions and thus avoiding leaks from/to reactor. Therefore, even at room temperature it has been possible to check capillary and system gas tightness.

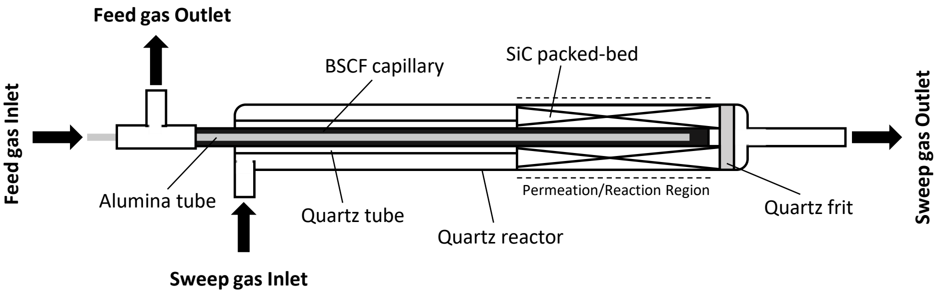
Feed gas Outlet
BSCF capillary
SiC packed-bed
Feed gas Inlet
Sweep gas Outlet
Alumina tube
Quartz tube
Permeation/Reaction Region
Quartz frit
Quartz reactor
Sweep gas Inlet

Figure 2.20: Simplified diagram of the lab-scale reactor for the conduction of capillary membrane studies.

Sweep gas or reactant gas (consisting in Argon or CH_4/Ar dilutions, respectively) is fed into the reactor, flowing in the first tract over the quartz tube without occurring permeation nor reaction, and then through the packed-bed section where the permeation/reaction occurs. After crossing a highly porous quartz frit, the permeate/products stream exits from the reactor and is analysed by an on-line GC. The conduction connecting quartz reactor and GC analyser is conveniently heated during reaction tests, thus avoiding product condensation after exiting the reactor. Reactor temperature is controlled by using a thermocouple attached to the quartz frit.

A more comprehensive detail about the permeation/reaction region delimited by the packed-bed is given in the cross-section view depicted in Figure 2.21.

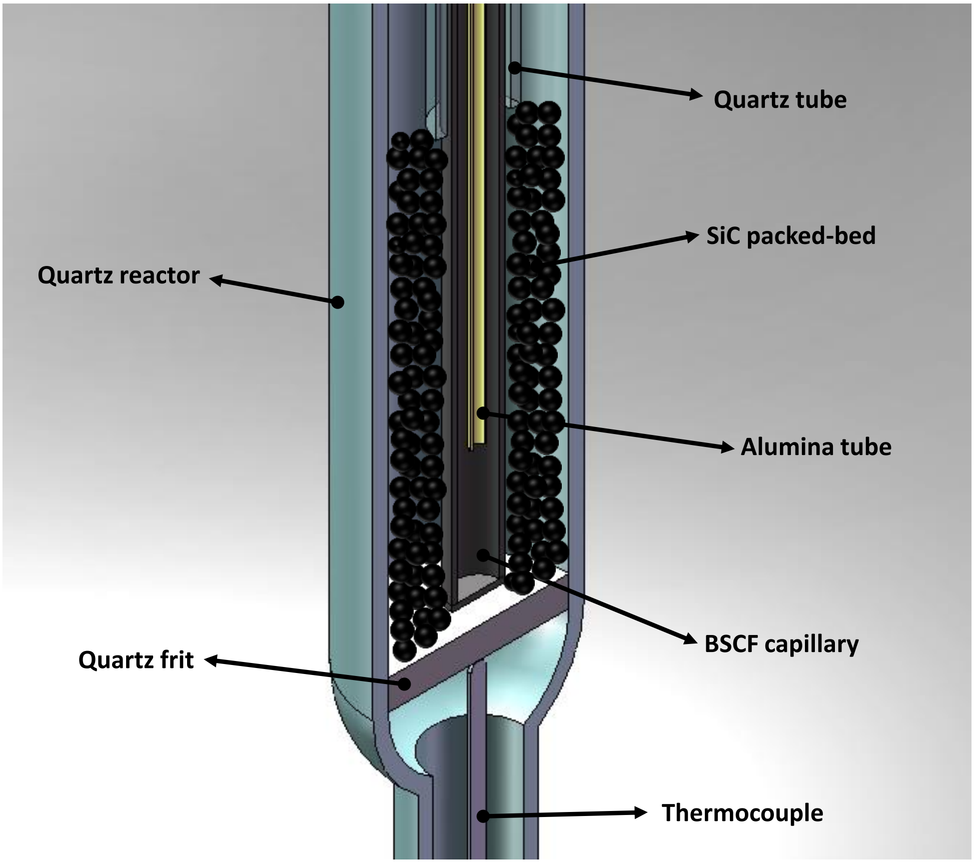
Quartz tube
SiC packed-bed
Quartz reactor
Alumina tube
BSCF capillary
Quartz frit
Thermocouple

Figure 2.21: Schematic description of the experimental set-up considered for performing tests on BSCF capillaries.

2.6.3. Oxygen flux calculation.

Oxygen concentration is calculated from the O_2 signal area and its response factor, previously calibrated. Total permeation is calculated as the product of O_2 concentration and sweep flow. Permeation flux ($ml \cdot min^{-1} \cdot cm^{-2}$) is extracted from the oxygen flux and the effective area ($A_{effective}$) of the membrane by the following equation:

$$J(O_2) = \%O_{2,permeate} \cdot \frac{Q_{sweep}}{A_{effective}} \tag{2.8}$$

Oxygen related to minor leaks is removed taking into account the presence of N_2 in the permeate stream. Therefore, permeating oxygen ($\%O_{2,\ permeate}$) is calculated from the expression:

$$\%O_{2,permeate} = \%O_{2,GC} - \left(\frac{0.21}{0.79} \cdot \%N_{2,GC}\right) \tag{2.9}$$

Where $\%O_{2,GC}$ and $\%N_{2,GC}$ are the percentages of oxygen and nitrogen measured by the GC in the permeate, respectively.

In the cases where methane or ethane are used as sweep gas, equation 2.8 is not valid for calculating permeation since permeating oxygen may react with it yielding compounds such as CO, CO_2, H_2, C_2H_6, C_2H_4, C_3H_8, C_3H_6, and C_3H_4. From GC measurements it is possible to determine concentration of every compound in the permeate stream, thus applying carbon mass balances. Therefore, $J(O_2)$ can be calculated with the equation:

$$\begin{aligned} J(O_2) = \Bigg(& \%O_{2,GC} + \frac{\%CO_{GC}}{2} + 2 \cdot \%CO_{2,GC} + \%C_2H_{4,GC} + \frac{\%C_2H_{6,GC}}{2} + 2 \\ & \cdot \%C_3H_{4,GC} + \frac{3}{2} \cdot \%C_3H_{6,GC} + \%C_3H_{8,GC} \\ & - \left(\frac{0.21}{0.79} \cdot \%N_{2,GC}\right)\Bigg) \cdot \frac{Q_{sweep}}{A_{effective}} \end{aligned} \tag{2.10}$$

2.6.4. Conversion, selectivity and yield calculation.

When conducting chemical reactions on Catalytic Membrane Reactors (CMR), parameters such as conversion (*X*), selectivity (*S*) and yield (*Y*) are determined for evaluating the reaction performance. In the present thesis, two reactions have been carried out: Oxidative Coupling of Methane (OCM) and Oxidative De-Hydrogenation of Ethane (ODHE). In this section, the equations for the determination of these parameters are presented.

$$X = \frac{F_R^{in} - F_R^{out}}{F_R^{in}} \cdot 100 \tag{2.11}$$

$$S_i = \frac{n_i \cdot F_i^{out}}{F_R^{in} - F_R^{out}} \cdot 100 \tag{2.12}$$

$$Y_i = 0.01 \cdot X_{CH4} \cdot S_i \tag{2.13}$$

Where *i* includes all the species with carbon atoms in the permeate gas stream, *R* stands for the reactant gases (i.e. methane or ethane) *F* is the flow rate of the species expressed in mol·min^{-1} and n_i is the number of carbon atoms of component *i*.

Furthermore, for the case of ODHE ethylene productivity (in ml·min^{-1}·cm^{-2}) is also determined by the equation

$$Ethylene\ productivity = \frac{Y_{C2H4} \cdot Q_{C2H6}^{in}}{A_{effective}} \tag{2.14}$$

Where Y_{C2H4} is the C_2H_4 yield and Q_{C2H6}^{in} is the initial C_2H_6 flow rate (in ml·min^{-1}). For determining the maximum theoretical productivity it is assumed a full C_2H_6 conversion with a 100% selectivity towards C_2H_4 formation, resulting in $Y_{C2H4} = 1$, thus considering the following expression:

$$Maximum\ theoretical\ productivity = \frac{Q_{C2H6}^{in}}{A_{effective}} \tag{2.15}$$

2.7. References.

[1] P.M. P, Method of preparing lead and alkaline earth titanates and niobates and coating method using the same to form a capacitor, Google Patents, 1967.

[2] E.M. Sabolsky, S. Razmyar, K. Sabolsky, Microstructural, electrical, and mechanical characterization of Bi2Cu0.1V0.9O5.35 (BICUVOX) ceramics fabricated from co-precipitated precursor powders, Journal of Materials Science, 48 (2013) 733-743.

[3] H. Luo, K. Efimov, H. Jiang, A. Feldhoff, H. Wang, J. Caro, CO2-Stable and Cobalt-Free Dual-Phase Membrane for Oxygen Separation, Angewandte Chemie International Edition, 50 (2011) 759-763.

[4] T. Ishihara, Perovskite Oxide for Solid Oxide Fuel Cells, Springer US2009.

[5] M. Martínez-Ripoll, Crystallography-Cristalografía. http://www.xtal.iqfr.csic.es/Cristalografia/parte_05_5-en.html.

[6] P. Larkin, Infrared and Raman spectroscopy, 2011.

[7] O. Czuprat, M. Arnold, S. Schirrmeister, T. Schiestel, J. Caro, Influence of CO2 on the oxygen permeation performance of perovskite-type BaCoxFeyZrzO3−δ hollow fiber membranes, Journal of Membrane Science, 364 (2010) 132-137.

3. PERMEATION STUDIES ON BSCF MEMBRANES

3. Permeation studies on BSCF membranes.

3.1. Introduction.

Amongst all mixed ionic-electronic conductive materials, oxygen transport membranes based on $Ba_{1-x}Sr_xCo_{1-y}Fe_yO_{3-d}$ compositions are probably the most studied and those presenting the highest oxygen fluxes. From the first works on BSCF membranes conducted in the early 2000s by Shao et al. [1], obtaining oxygen fluxes of 1.4 $ml\cdot min^{-1}\cdot cm^{-2}$, researchers efforts have made possible a progressive improvement of $J(O_2)$ until reaching an impressive flux of 67.7 $ml\cdot min^{-1}\cdot cm^{-2}$ on an 60 μm-thick asymmetric membrane [2]. The main strategies conducted for the optimization of the oxygen fluxes have been focused on the thickness reduction [3-9]. For that aim, membrane thicknesses have been reduced as much as possible, though very thin structures become brittle and it is necessary the use of porous supports that ensure the mechanical robustness of the membrane assembly. Studied thin supported membranes have demonstrated an improvement in oxygen permeation, in spite of this, the obtained fluxes have resulted to be lower than the predicted by Wager equation (Equation 1.5). This is mainly due to the fact that Wagner's theory is only valid for bulk diffusion, not taking into account surface exchange reactions occurring on membrane surface that limit oxygen permeation for thin membranes below the characteristic thickness (L_C) [10]. Therefore, by reducing membrane thickness below L_C no significant gain in $J(O_2)$ is obtained and other optimization strategies should be addressed. That would be the case of membrane surface modification, by means of which surface specific area and surface kinetics can be substantially improved, thus enhancing oxygen permeation [2, 8, 11].

In addition to the production of oxygen, OTMs have a very important application in the conduction of several reactions within the chemical industry. This is mainly due to the gain in process efficiency and simplicity and to the achievement of higher yields of products of interest if OTMs are used as oxygen suppliers in such processes. Despite BSCF membranes can be affected by a limited stability under reducing environments, some studies suggest a promising application of BSCF-based membranes for the conduction of chemical reactions such as OCM and ODHE [12, 13].

Furthermore, for industrial applications that are being proposed or even demonstrated, BSCF-based materials are considered in a number of prototypes and demonstrative plants [14-16]. Such industrial applications require a large surface areas for providing the oxygen, typically in the range of 10-1000 TPD. For achieving such oxygen volumes the use of membrane architectures presenting high compactness is needed, being the most considered options the planar stacks and the tubular modules [17, 18].

Therefore, this Chapter is focused on the development of $Ba_{0.5}Sr_{0.5}Co_{0.8}Fe_{0.2}O_{3-\delta}$ planar disk-shaped membranes with different thicknesses, thus studying the role of this parameter in the processes related with the oxygen permeation. Moreover, it was also considered the addition of a porous BSCF support for the case of thinner membranes in the range of 20-60 μm, also analyzing the effect of such structures in the diffusion of the gas and eventually in the oxygen permeation. Addition of catalytic layers was also considered for oxygen fluxes optimization and for the conduction of studies on the Oxidative De-Hydrogenation of Ethane (ODHE) for the production of ethylene. Finally, a study on membranes presenting different geometries (i.e. tubular geometry), BSCF capillaries were considered for the production of oxygen and for the production of ethylene by means of the Oxidative Coupling of Methane (OCM).

3.2. Planar membranes.

For this study focused on planar BSCF membranes several cases and architectures were considered. Monolithic membranes presenting different thicknesses ranging from 0.75 to 0.16 mm and asymmetric membranes consisting of 20-60 μm thick membranes supported on porous BSCF substrates. Moreover the addition of catalytic layers was also considered with the aim of improving oxygen permeation, especially at low temperatures.

3.2.1. Membrane microstructure.

Monolithic membranes with thicknesses of 0.75 and 0.38 mm were produced as explained in 2.2.1 starting from BSCF commercial powders (Treibacher Industrie, Austria), by sintering at 1100 ºC during 5 hours in air. 0.16 mm-thick membranes were provided by Fraunhofer Institute for Ceramic Technologies and Systems (IKTS), being also produced by sintering at 1100 ºC. As can be seen in Figure 3.22, an as sintered BSCF membrane presents a high bulk density in both surface and fracture cross-section. Some occlusive porosity is observed in the cross-section not exceeding a pore size of 1-2 microns. Despite of this, bulk density is around 95%, so membrane gas tightness can be ensured. In Figure 3.22a can be observed a distribution of BSCF grains on surface with sizes in the range of 10-40 μm.

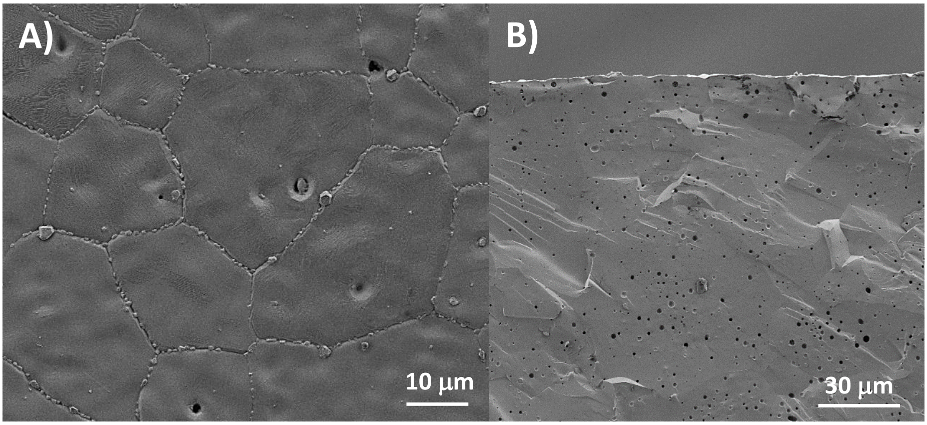

Figure 3.22: SEM images corresponding to a 0.38 mm-thick BSCF membrane a) Surface microstructure and b) fracture cross-section.

Asymmetric all-BSCF membranes comprising a supported thin-film were supplied by Forschungzentrum Jülich. Both membrane and porous support were manufactured by tape casting technique using commercial BSCF powder (Treibacher Industrie). The procedure followed for membranes fabrication is the same than the described by Baumann et al. in this publication [2]. Once tape was casted and dried, disk-shaped samples were cut out of the green tape. Both membrane and porous support were sintered at 1100 ºC in air for 3 hours.

Figure 3.23 shows a fractured cross-section of an as fabricated asymmetric membrane. In both pictures a) and b) membrane architecture can be easily identified, with the dense thin BSCF layer on the top and the porous support on the bottom. Despite the fact that two supported membranes with thicknesses of 20 and 60 μm were considered for the permeation study, only the 20 μm-thick case is depicted in the figure. In Figure 3.23a a close-up view of the cross-section is provided. As can be seen in Figure 3.23b, the dense BSCF layer has a thickness around 15-20 μm and a porosity of ca. 5%. This existing porosity is not affecting the membrane gas tightness since there is no connection among the pores. Neither cracks nor pinholes are neither observed all along the membrane. Regarding the porous support, it presents a thickness of 735 μm and a porosity of nearly a 40%. Pore sizes are in the range of 10-15 μm and are well interconnected throughout all the substrate, thus constituting good paths for the gas diffusion to the membrane.

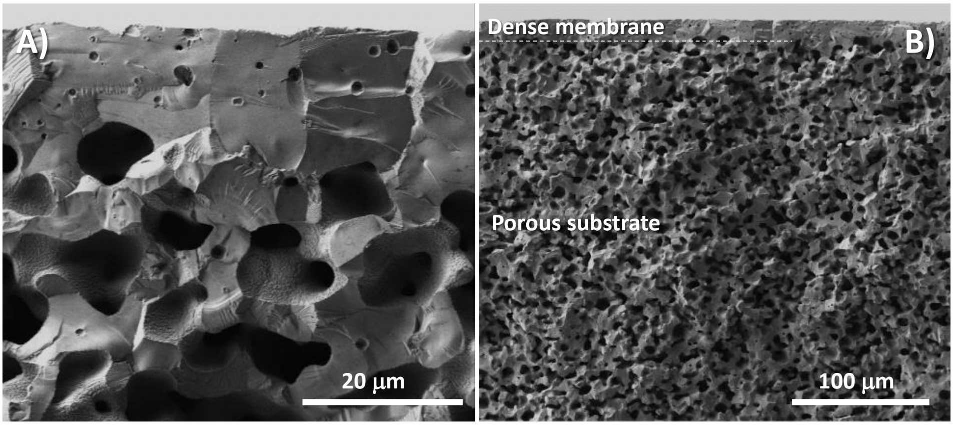

Figure 3.23: Fracture cross-sections (SEM images) of 20 μm-thick supported BSCF membranes.

3.2.2. Oxygen permeation: thickness variation.

The oxygen permeation performance of the membranes considered in the present work was studied in the temperature range of 1000-600 ºC when feeding synthetic air (300 ml·min^{-1}) and sweeping with Argon (300 ml·min^{-1}). The comparison of the obtained fluxes has permitted to study the dependence of the membrane thickness on the permeation as well as the influence of porous substrates supporting of asymmetric membranes.

Figure 3.24a depicts the oxygen fluxes of the considered membranes in dependence of thickness in the range 1000-600 ºC. As can be seen, all the membranes adjust to a two-fold Arrhenius behavior. Two different regions can be distinguished, presenting different apparent activation energies (E_a) at high (1000-800 ºC) and low temperature (800-600 ºC). In the high temperature region all the membranes present similar E_a around 45 kJ·mol^{-1}, whereas in the low temperature region it can be observed an increase in E_a values as thickness is decreased, being the 20 μm-thick asymmetric membrane that presenting the highest value. This could be ascribed to a stronger limitation of surface processes in the oxygen permeation at low temperatures affecting especially to thin membranes. With regard to the obtained $J(O_2)$, the highest value corresponds to the thinnest membrane, achieving 10.25 ml·min^{-1}·cm^{-2} at 1000 ºC. At the same temperature, the 60 μm-thick membrane yields 6.9 ml·min^{-1}·cm^{-2} whereas the 0.75 monolithic membrane permeates 4.6 ml·min^{-1}·cm^{-2}. Attending to these results and considering Wagner equation, much higher oxygen fluxes would be expected by decreasing the thickness from 0.75 mm down to 0.02 mm (i.e. 37.5 times). The observed only 2-fold improvement can be explained with the fact that despite the reduction in the thickness there are some other parameters influencing oxygen permeation beyond temperature, thickness and pO_2 gradient (main terms describing $J(O_2)$ in Wagner's equation).

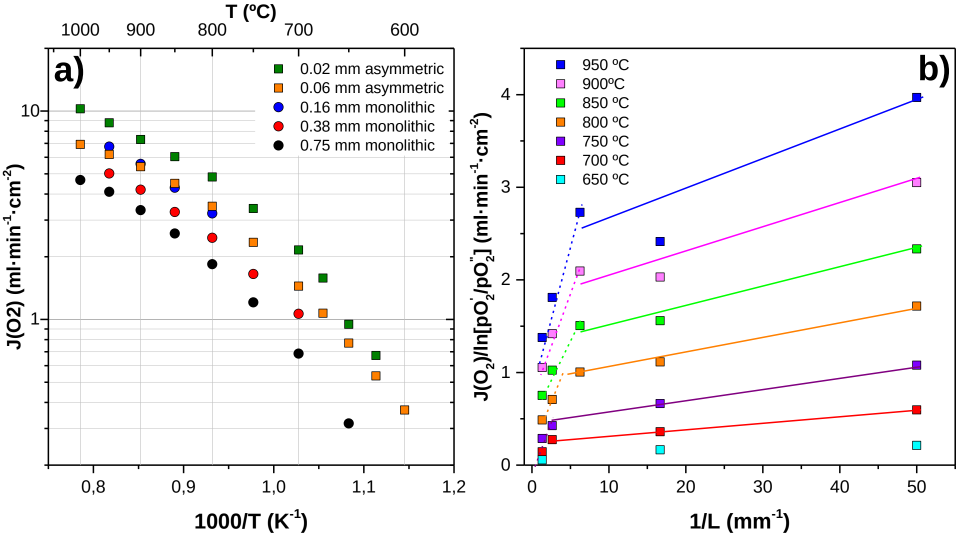

Figure 3.24: a) Oxygen permeation in dependence of temperature for various BSCF membranes. b) Oxygen permeation in dependence of membrane thickness. Q_{feed} = 300 ml·min^{-1}, Q_{sweep} = 300 ml·min^{-1}.

Table 3.2: Apparent activation energy (E_a) (kJ·mol^{-1}) derived from Figure 3.24 J(O_2) measurements for the different activated.

Membrane	Thickness (mm)	Ea (kJ·mol^{-1})	
		High T region	Low T region
Asymmetric	0.02	42.4 (± 0.5)	114.7 (± 8.3)
Asymmetric	0.06	36.7 (± 2.5)	95.9 (± 1)
Monolithic	0.16	50.7 (± 2.1)	--
Monolithic	0.38	47.9 (± 3.2)	72.9 (± 0.1)
Monolithic	0.75	45.3 (± 3.7)	87.8 (± 5.8)

One of these processes explaining the low improvement would be the surface exchange limitation occurring at thicknesses below the L_C. Therefore by decreasing membrane thickness below these values a lower permeation gain than the predicted by Wagner's equation would be obtained, since surface processes are predominantly limiting oxygen permeation. As Wagner's equation predicts an inverse linear dependence of $J(O_2)$ to membrane thickness (Eq 1.5), then by representing $J(O_2)/ln[pO_2'/pO_2'']$ vs $1/L$ it is possible to determine a bulk diffusion limitation for those values fitting a straight line intersecting the origin [19]. From the representation of the results in Figure 3.24b, only the monolithic membranes fit the linear behavior associated to a bulk diffusion limitation, whereas 20-60 μm-thick supported membranes present a deviation from this tendency thus being influenced by the surface exchange at all the temperatures. Regarding the 160 μm-thick case, it seems to be more limited by surface reactions as temperature is decreased below 900 ºC.

Another process that can affect negatively membranes performance is gas polarization concentration occurring nearby permeate side surface. This phenomenon is typical of high permeating materials like BSCF, occurring when having high permeation rates and can take place in both sides of the membrane: in the feed side due to a depletion of the gas, or in the permeate side due to an inefficient release (desorption) of the permeated O_2 molecules to the sweep stream [19]. In both situations $J(O_2)$ is dramatically affected due to a reduction of the oxygen partial pressure gradient (ΔpO_2) across the membrane. Whereas at feed side this situation is solved via pO_2 increase (feed gas pressurization) at permeate side the procedure is the contrary: pO_2 reduction. One effective way to diminish local pO_2 at permeate side is by means of sweep flow increase, promoting in this way both the desorption of the permeated O_2 molecules on the surface and avoiding any accumulation of those desorbed, as depicted in the model included in Figure 3.25 (right). The latter is confirmed by the results observed in Figure 3.25, where sweep flow was varied at 950 ºC for all the considered membranes. As can be seen, by increasing sweep flow rates $J(O_2)$ is significantly improved. Attending to the results, thinner membranes are more affected by polarization concentration with progressive improvements in $J(O_2)$ up to 750 ml·min^{-1}. On the contrary, thicker monolithic membranes show a stabilization of fluxes above 200 ml·min^{-1} thus not presenting any significant improvement beyond this flow rate (optimal sweeping). From the observation of this behavior it is clear that by decreasing membrane thickness the oxygen bulk diffusion is largely increased, however this high permeation also needs high sweeping force for alleviating the accumulation of O_2 on permeate surface. Therefore, under the test conditions used for Figure 3.24 the supported membranes would be working below their optimal point and significantly influenced by polarization concentration resistance.

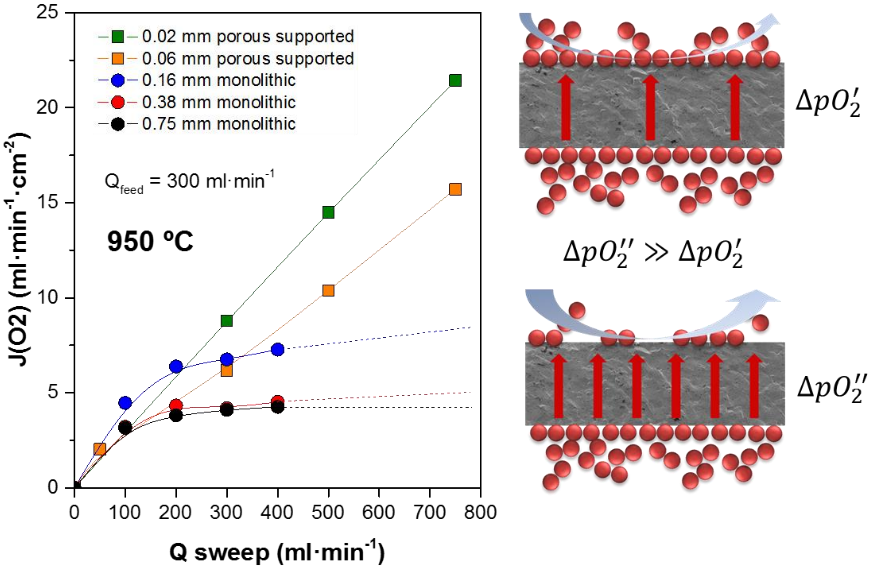

Figure 3.25: Sweep flow variation effect on oxygen permeation for different thick membranes at 950 ºC (left) and graphical description of the polarization concentration phenomena over permeate side surface (right).

Finally, another parameter that can affect the oxygen permeation performance in the supported membranes is the porous support itself. As previously suggested by Baumann et al. in their permeation model for asymmetric membranes [2], the addition of a porous support to the membrane architecture also implies an additional resistance for the oxygen permeation. Following this permeation model, two simplified models describing the gas diffusion and permeation of oxygen for the monolithic 160 µm-thick and the porous supported 60 µm-thick membranes have been represented in Figure 3.26. Then, for the two considered cases several resistances appear to affect oxygen permeation:

- Concentration polarization (R_{CP})
- Surface exchange reactions (R_S)
- Oxygen ions diffusion through bulk and grain boundaries (R_{BULK})
- Molecular diffusion of O_2 through porous support (R_{SUPP})

From the observation of the diagram it is clear that, despite the lower thickness of the supported membrane, the whole membrane assembly exceeds the thickness of the 160 µm-thick monolithic membrane. This fact adds a new resistance to the process (R_{SUPP}) that could counteract the lower thickness and thus the lower R_{BULK} for the asymmetric membrane. This, in combination with the polarization concentration discussed above, could explain the small $J(O_2)$ differences between 60 µm and 160 µm-thick membranes observed in Figure 3.24, where, despite the decrease in thickness, no gain in permeation is obtained.

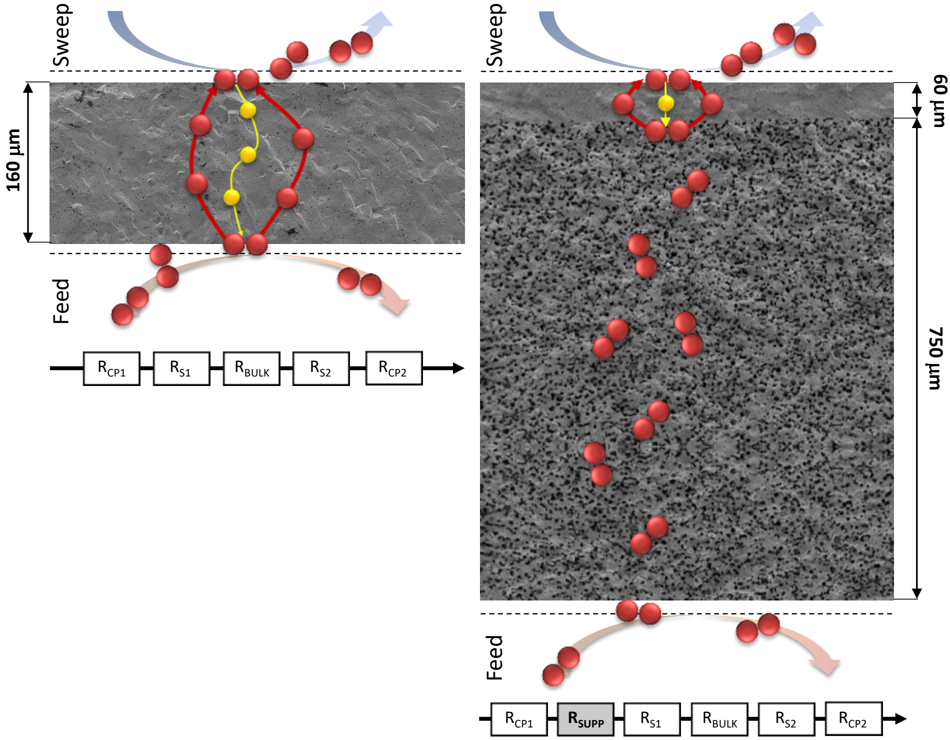

Figure 3.26: Simplified model of the gas diffusion and oxygen permeation in monolithic (left) and supported (right) membranes.

Once analysed the main parameters influencing oxygen permeation, it was intended to optimize the oxygen fluxes by inducing the most suitable conditions for alleviating the known resistances. For that aim, the thinner cases (20 and 60 µm-thick membranes) were tested when feeding with pure oxygen and when sweeping with a high argon flow rate of 750 ml·min^{-1}. Thus, R_{CP1} and R_{SUPP} would be diminished by the use of pure O_2, whereas R_{BULK} and R_{CP2} would also be by the thickness reduction and the high sweeping, respectively.

Figure 3.27 shows the permeation results of supported membranes under the aforementioned conditions. Air feeding results have also been added for a better comparison of the use of pure O_2 feeding. An impressing improvement in the performance is obtained when using O_2 as feed, thus obtaining oxygen fluxes of 88 and 92 ml·min^{-1}·cm^{-2} at 1000 ºC for the 60 µm and 20 µm membranes, respectively. Under such conditions even at low temperatures very high $J(O_2)$ are achieved, with 3.5 ml·min^{-1}·cm^{-2} at only 600 ºC. Another significant fact is the lower difference between fluxes for both membranes when feeding with O_2. That could be related with a R_{BULK} alleviation due to a higher availability of O_2 to be incorporated and thus a higher diffusion can be performed.

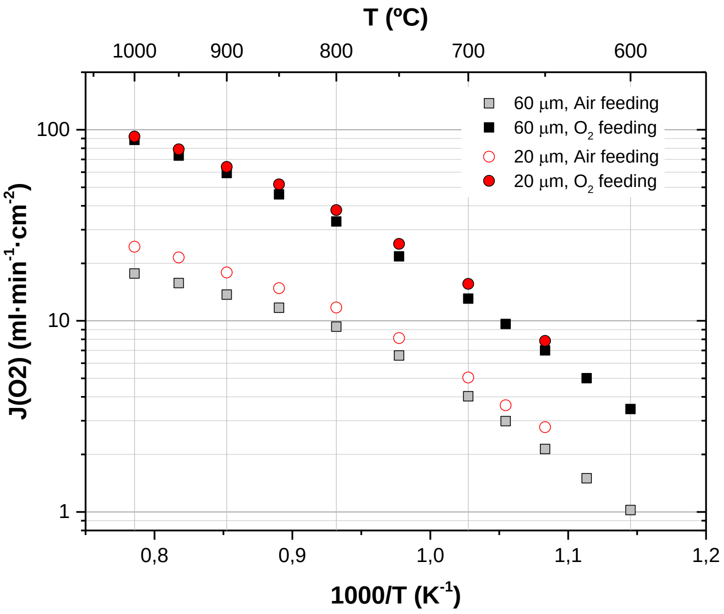

Figure 3.27: Oxygen permeation dependence with temperature for the thin supported BSCF membranes. Tests performed using Air or pure O_2 feeding (300 ml·min^{-1}) and Argon sweeping (750 ml·min^{-1}).

3.2.3. Oxygen permeation: catalytic activation.

Influence of catalytic layer on monolithic membranes

A study on the activation of monolithic membranes was performed. Three cases were considered for a 160 μm-thick membrane: (i) no catalytic deposition (bare), (ii) catalytic deposition on sweep side, and (iii) catalytic deposition in both feed and sweep sides. Catalytic layers consisted in 15 μm-thick porous BSCF layers sintered at 1050 ºC for 2 hours. Tests have been carried out in the range of temperatures 1000-750 ºC, using air as feed (300 ml·min^{-1}) and argon as sweep (300 ml·min^{-1}).

Figure 3.28 shows two fracture cross sections of a BSCF bare surface (A) and a membrane surface coated with a BSCF layer (B). As can be seen, activated surface presents a ca. 15 μm-thick porous layer over the dense membrane. In contrast to bare surface, catalytically activated side presents a higher specific surface area due to the surface modification. This will ensure the availability of a higher number of active sites for oxygen reactions thus improving oxygen permeation.

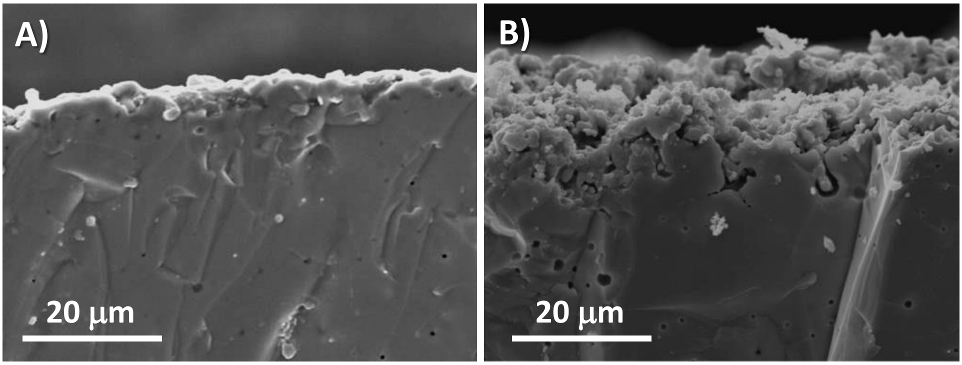

Figure 3.28: Fracture cross-sections (SEM images) of BSCF membranes without (A) and with (B) a BSCF catalytic layer.

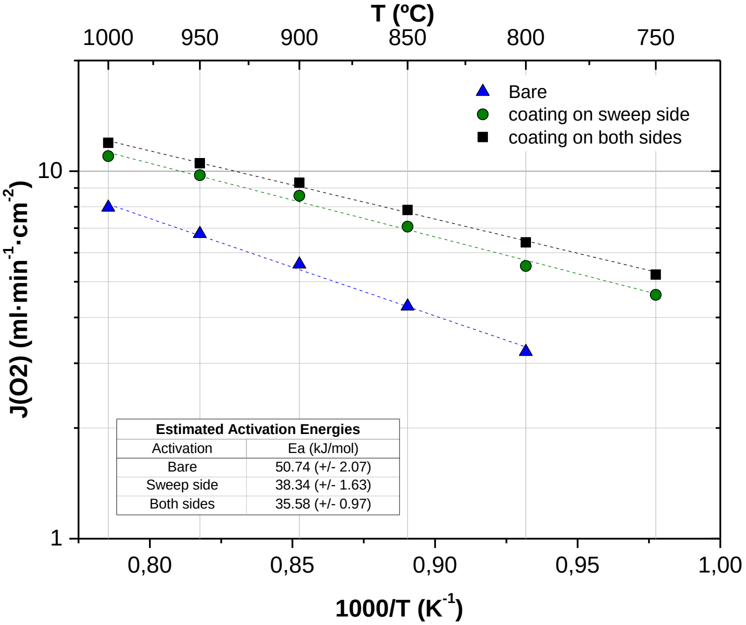

Estimated Activation Energies

Activation	Ea (kJ/mol)
Bare	50.74 (+/- 2.07)
Sweep side	38.34 (+/- 1.63)
Both sides	35.58 (+/- 0.97)

Figure 3.29: $J(O_2)$ variation in dependence of temperature for activated/non-activated monolithic BSCF membranes. Synthetic air (pO_2 = 0.21 atm) as feed, Argon as sweep. Q_{air}, Q_{sweep} = 300 ml·min^{-1}.

Results in Figure 3.29 clearly show that oxygen permeation improves when activating membranes, with an improvement at 1000 ºC from 7.97 to 10.99 ml·min^{-1}·cm^{-2} if activated only sweep side, and reaching 12 ml·min^{-1}·cm^{-2} if both membrane sides are activated. This better performance is maintained all along the temperature range. Bulk diffusion is expected to be the main limiting step above 800 ºC for a 160 µm-thick membrane, according to that such a significant improvement would not be expected when adding a catalytic layer. Nevertheless, the fact that activated cases present lower activation energies than the bare one points out that some limitation of surface reaction is taking place for the considered system at high temperature region [20]. Additionally, porous layer addition can also improve gas flow dynamics nearby membrane surface, thus promoting turbulences and subsequently facilitating the desorption of O_2 molecules at sweep side.

Catalytic activation of asymmetric membranes

Unlike monolithic membranes, porous supported membranes can only be catalytically activated by porous layer deposition at dense layer side. The strategy that was followed for the activation of 60 μm-thick membranes is the deposition of porous layers on the sweep side. Similarly to monolithic membranes, porous layers with thicknesses of 15 μm were added by means of screen-printing technique and subsequently sintered for 2 hours. Three different catalytic layers were considered: (i) a BSCF layer including a graphite pore former in the ink and sintered at 1050 ºC, (ii) a BSCF layer with pore former and 5% wt. Ag in the ink and (iii) a BSCF layer with pore former and 5% wt. Pd in the ink. The two latter layers were sintered at 950 ºC for minimizing coarsening phenomena and thus having a better dispersion and morphology of the metal nanoparticles. The preparation of the slurries containing Ag and Pd was done by incipient wetness impregnation of BSCF powder with an aqueous solution of catalysts precursors (nitrates). After impregnation and drying, powders were calcined at 500 ºC thus obtaining the metal oxides. The final step consists of the slurry preparation, performed as described in section 2.2.4. of the present Thesis with the only difference that the pore former (graphite) was added in this step.

Pore former was included in the slurries with the aim of improving layer porosity and thus increasing surface specific area and optimizing the gas diffusion media for the release of permeated oxygen. Ag and Pd have been selected for the activation of the powders due to their known promoting activity in the reduction of oxygen and subsequently in the improvement of oxygen permeation [20-23].

Table 3.3: Catalytic activation conducted on BSCF asymmetric membranes.

Catalytic layer	thickness (μm)	Sintering T (ºC)
BSCF_PF	15	1050
BSCF_PF + 5% Ag	15	950
BSCF_PF + 5% Pd	15	950

The microstructure of a membrane activated with a BSCF porous layer including 5% wt. Pd is shown in Figure 3.30. A layer thickness of 15 μm is confirmed by the SEM pictures, however due the low amount of Pd nanoparticles and the presumably small size of these (in the range of nanometers) it was not possible to make a proper identification of the catalyst dispersion.

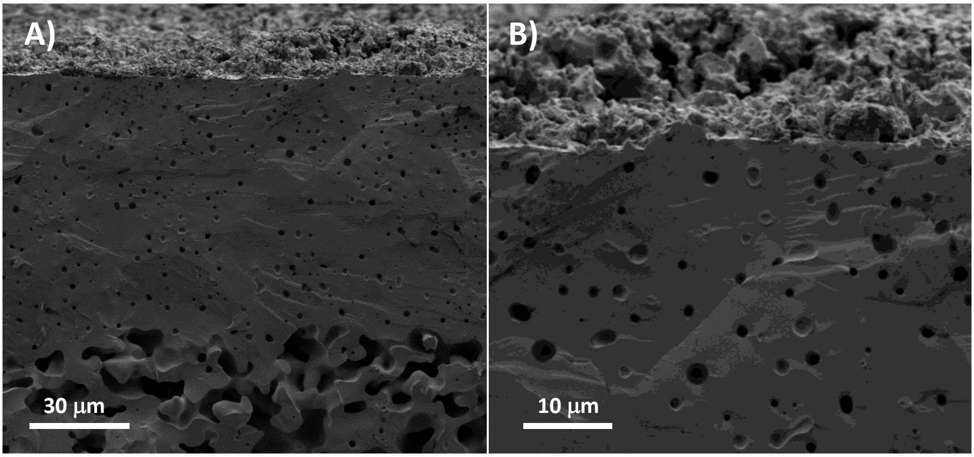

Figure 3.30: SEM cross section images of a BSCF_PF + 5% Pd activated membrane.

The oxygen permeation of the considered membranes was studied in dependence of temperature by performing a variation in the range 1000-600 ºC (950-600 ºC for the Ag, Pd activated membranes). Aiming to minimize concentration polarization resistance at permeate side, a very high sweep flow of 750 ml·min^{-1} was used. Results depicted in Figure 3.31 show that addition of a catalytic layer improves $J(O_2)$ at all the temperatures, obtaining a maximum oxygen flux of 24 ml·min^{-1}·cm^{-2} at 950 ºC for the membrane activated with BSCF + 5% wt. Pd. In fact, the activation with this catalyst shows the best results, evidencing a very enhancing role of Pd nanoparticles in the oxygen surface reactions. In return, Ag activation shows similar results than the case activated with only a porous BSCF layer, although at lower temperatures the performance seems to be slightly better.

Attending to the activation energies (E_a), three different regions are observed for all the membranes: 1000-850 ºC (High T), 850-700 ºC (Intermediate T) and 700-600 ºC (Low T). The E_a values obtained from Figure 3.31 results are presented in Table 3.4. In the high temperature region, the estimated E_a present similar values for all the considered cases, only the activation with BSCF + 5% Ag seems to present a lower value. When decreasing the temperature the effect of catalytic activation becomes more evident, with 59 kJ·mol^{-1} for the bare case and values of 48-38 kJ·mol^{-1} for the activated membranes. This is more significant in the low temperature region, where E_a decreases from 96 kJ·mol^{-1} for the bare case to 75 kJ·mol^{-1} for the membrane activated with BSCF + 5% Pd. This fact evidences the important role of membrane catalytic activation for the improvement of surface reactions and subsequently the permeation performance at low temperatures.

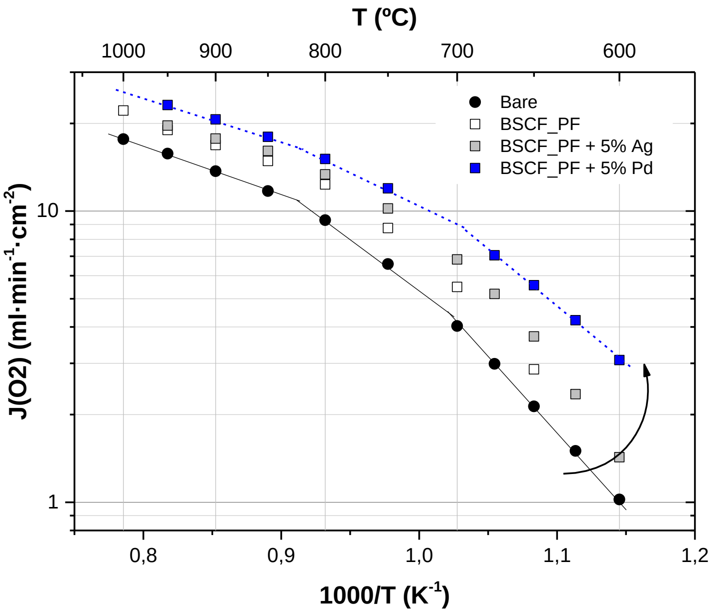

Figure 3.31: Oxygen permeation in dependence of temperature and different catalytic coatings applied on a 60 μm-thick supported BSCF membrane. Tests performed under Air/Ar gradient (300 ml·min^{-1} Air, 750 ml·min^{-1} Argon).

Table 3.4: Apparent activation energy (E_a) (kJ·mol^{-1}) derived from Figure 3.31 $J(O_2)$ measurements for the different activated membranes.

	E_a (kJ·mol^{-1})		
	High T region	Medium T region	Low T region
Bare	32.4 (± 0.8)	59.9 (± 5.6)	95.9 (±1)
BSCF_PF	31.8 (±2)	48.6 (±7)	84.1 (±6)
BSCF_PF + 5% Ag	22.9 (±1)	48.6 (±5)	101.7 (±6)
BSCF_PF + 5% Pd	28.5 (±1)	38.5 (±2)	74.6 (±2)

In order to obtain the highest possible $J(O_2)$, the best operating conditions were selected, i.e. a pure oxygen feed (pO_2' = 1 bar) with a feed flow of 300 ml·min^{-1} and an Argon sweep flow of 750 ml·min^{-1}. Therefore, R_{CP1} and R_{SUPP} are diminished due to the high pO_2 at feed side, and so R_{S2} and R_{CP2} due to the catalytic activation and the high sweeping, respectively. Under such conditions an unprecedented oxygen peak flow of 98 ml·min^{-1}·cm^{-2} was reached for the BSCF + 5% Pd activated membrane at 950 ºC. This value is the highest $J(O_2)$ ever reported for an OTM, and demonstrates the importance of the catalytic activation for oxygen permeation improvement, even at high temperatures. With regard to the fluxes obtained at low temperature, a nearly 2-fold improvement is reached at 600 ºC when activating with a BSCF + 5% Pd catalytic layer, achieving an impressing O_2 flux of 6.5 ml·min^{-1}·cm^{-2}.

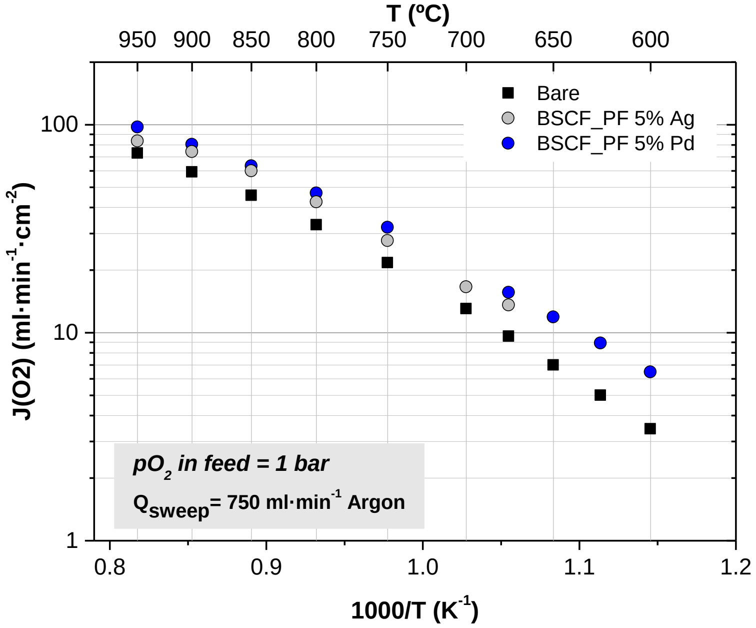

Figure 3.32: Oxygen permeation in dependence of temperature and different catalytic coatings applied on a 60 μm-thick supported BSCF membrane. Tests performed under Air/Ar gradient (300 ml·min^{-1} Air, 750 ml·min^{-1} Argon).

3.2.4. Oxidative De-Hydrogenation of Ethane (ODHE) on BSCF membrane reactors[5].

Light olefins, especially ethylene and propylene, are the most important basic petrochemicals used to produce other valuable base products, for example, polyethylene and copolymers, ethylene oxide, acetaldehyde, and higher linear olefins and alcohols. These light olefins are produced mainly by thermal or catalytic cracking. The state of the art is an ethane conversion of 69% at 78% of ethylene selectivity, implying a ethylene yield of 54% per pass [24]. These conventional methods have some drawbacks: 1) the product mixture is rather complex thus requiring significant effort for downstream processing; 2) thermal cracking is highly endothermic, causing elevated energy costs; and 3) coke is formed under reaction conditions, being necessary frequent discontinuations for reactor clean-up [25]. One possible alternative to overcome these disadvantages is the oxidative dehydrogenation of ethane (ODHE), previously presented in 1.5.3 (reaction R6). Advances in selective oxidation of hydrocarbons have been broadly studied in recent decades [24, 26-30]. Two parallel alternatives have been followed: 1) obtaining a highly active and selective catalyst, and 2) the development of convenient reactor technologies for effective and safe reactor operation.

---

[5] The study here presented has been published in ChemSusChem journal under the title “Ethylene Production by ODHE in Catalytically Modified $Ba_{0.5}Sr_{0.5}Co_{0.8}Fe_{0.2}O_{3-\delta}$ Membrane Reactors”. DOI**:** 10.1002/cssc.201100747

An attractive intensification process for the selective oxidation of hydrocarbons integrates a catalytic reactor and a gas separation membrane, thus constituting a system called Catalytic Membrane Reactor (CMR). The membrane selected for such a configuration can be, for example, an oxygen-permeable MIEC dense membrane [24, 27-39]. This kind of CMR has several benefits regarding the sustainable production of commodity chemicals, that is, reducing unit/process volume, safe operation (explosion limits), higher productivity and catalytic performance, and energy saving due to integrated oxygen separation, higher conversion per part, and minimization of downstream fractioning and recycling.

MIEC membranes are a very appealing option for conducting ODHE reactions in CMRs. Lattice O^{2-} present in permeate side surface can be used for conducting the dehydrogenation of ethane, thus forming ethylene and H_2O. However, other side reactions can take place, resulting in the formation of CO, H_2, CO_2, C_3 and higher hydrocarbons leading to coke generation. For avoiding (or minimizing) this side reactions it is then necessary to address catalytic strategies, in order to obtain high ethylene selectivities. MIEC materials, and specially BSCF, are themselves catalytically active for the ODHE reaction [30, 35, 37, 40], therefore it would be possible to increase the ethylene yield by using a proper catalyst on the membrane surface.

A BSCF catalytic layer was considered for the analysis of the effect of textural properties and the thickness of the porous catalyst layer. The porosity of the catalytic layer in a modified MIEC MR is an important issue that principally determines the catalytic activity and, to a lesser degree, the selectivity. Such behaviour can be attributed to 1) an increase of the available catalytic surface area and 2) an improvement of gas exchange due to fast removal of ethylene and minimization of side reactions. Therefore, the porous microstructure of the catalytic layer could have an important role in the catalytic performance of MIEC MR, in particular, when the reaction involves interaction between gas-phase molecules and lattice oxygen, such as in the ODHE reaction. Figure 3.33 shows SEM images of a fracture cross section for three catalytic layers of BSCF after the ODHE reaction test. The catalytic layer depicted in Figure 3.33b shows higher porosity achieved by the incorporation of graphite into screen-printing ink (Aldrich) with platelet morphology (diameter of several tens of microns). The addition of graphite (5 wt%) aimed to the promotion of macroporosity for fast oxygen gas transport. The porosity of the catalytic layers was optimized by using graphite as a pore former in the screen-printing ink. Different thicknesses of the catalyst layer were used in these ODHE experiments: 13 (Figure 3.33b) and 26 μm (Figure 3.33c).

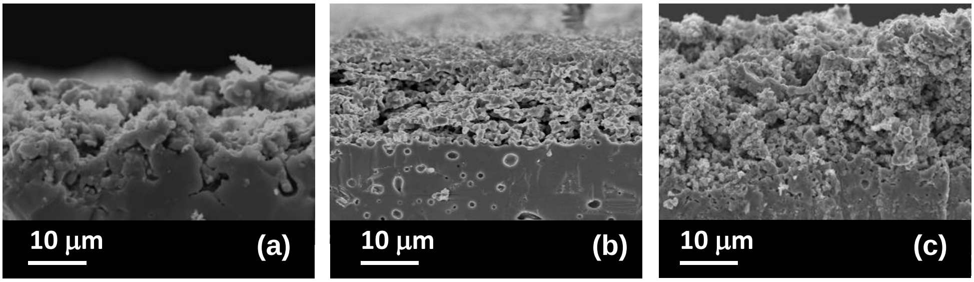

Figure 3.33: SEM images of the fracture cross section of the BSCF catalytic layer on BSFC membranes after a catalytic test. a) 12 μm thickness, b) the addition of a pore former to the screen-printing ink; 13 μm thickness, c) the addition of a pore former to the screen-printing ink; 26 μm thickness.

The effect of layer porosity on catalytic performance was studied. The ODHE tests were carried out under the same experimental conditions in different catalytic BSCF MRs. Figure 3.34 compares the results obtained in the ODHE tests when considering a bare membrane with a polished surface as a reference MR and two modified MRs with catalytic layers of BSCF with different porosities. As aforementioned, the oxygen species (O^{2-}) are transported through the BSCF membrane from the feed side to the reaction side, where they react quickly with C_2H_6 on the catalyst surface before recombination to form O_2. This membrane process makes it possible to reach higher ethylene selectivity due to complete control over the contact mode of hydrocarbons, oxygen, and the catalyst active sites. The use of a porous catalytic layer with higher macroporosity has produced an increase in the ethylene yield (up to $Y_{C2H4} \approx 81$ %). The presence of macroporosity also enhanced $J(O_2)$ through the membrane, as clearly proven when using only argon as the sweep gas. This improvement may be ascribed to the larger surface area for oxygen exchange and better gaseous oxygen transport through the porous coating [2, 41]. As a consequence, the rise in Y_{C2H4} could be related to higher $J(O_2)$ through the membrane, the larger surface area available on the catalytic coating, and improved gas transport through the coating.

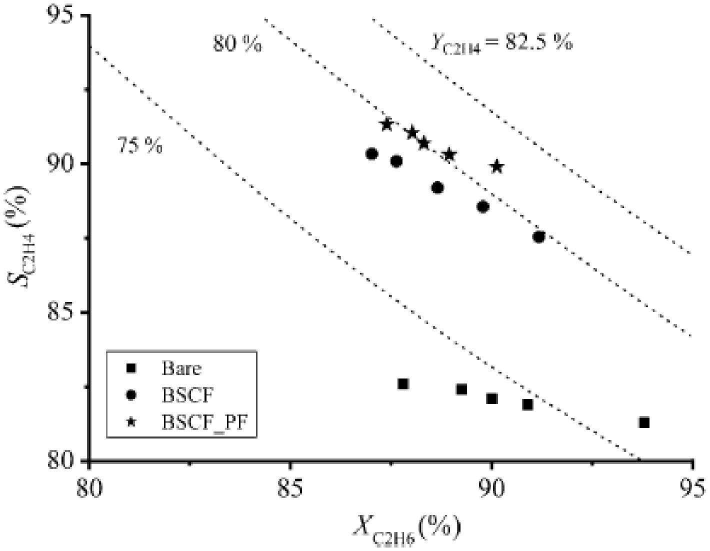

Figure 3.34: Ethylene selectivity versus ethane conversion for experiments performed with BSCF MRs. Different porosities of the catalytic layer were considered. T=850 ºC, ethane diluted with argon, $Q_{Reaction\ side}$=400 ml·min^{-1}, $Q_{Feed\ side}$=210 ml·min^{-1} (pO_2=0.04 atm).

The thickness of the catalytic layer may affect the oxygen permeation process, increasing gas diffusion resistance through this porous layer, especially at lower temperatures. A value of $J(O_2) \approx 1$ ml·min^{-1}·cm^{-2} was reached at 750 ºC in the MR with a catalytic layer of 13 μm, and $J(O_2) \approx 0.8$ ml·min^{-1}·cm^{-2} was obtained with a 26 μm catalytic layer. Likewise, the thickness of the catalytic layer, that is, the amount of catalyst used in the reaction, would affect the catalytic ODHE performance. A thicker catalyst layer (Figure 3.35b) had a positive effect on the catalytic activity of the MR because ethane conversion increases with increasing residence time (Figure 3.35a). However, a shorter residence time involves a lower probability of secondary reaction, such as oxidation or oligomerization, of the ethylene produced, so selectivity increases. A combination of these effects caused a slight decrease in Y_{C2H4} when reducing the thickness of the catalytic layer while leaving the reaction conditions unchanged (Figure 3.35b). From the results shown in the inset of Figure 3.35b, it can be inferred that the variation in the layer thickness results in a slight increase in catalytic activity (conversion), but does not alter selectivity.

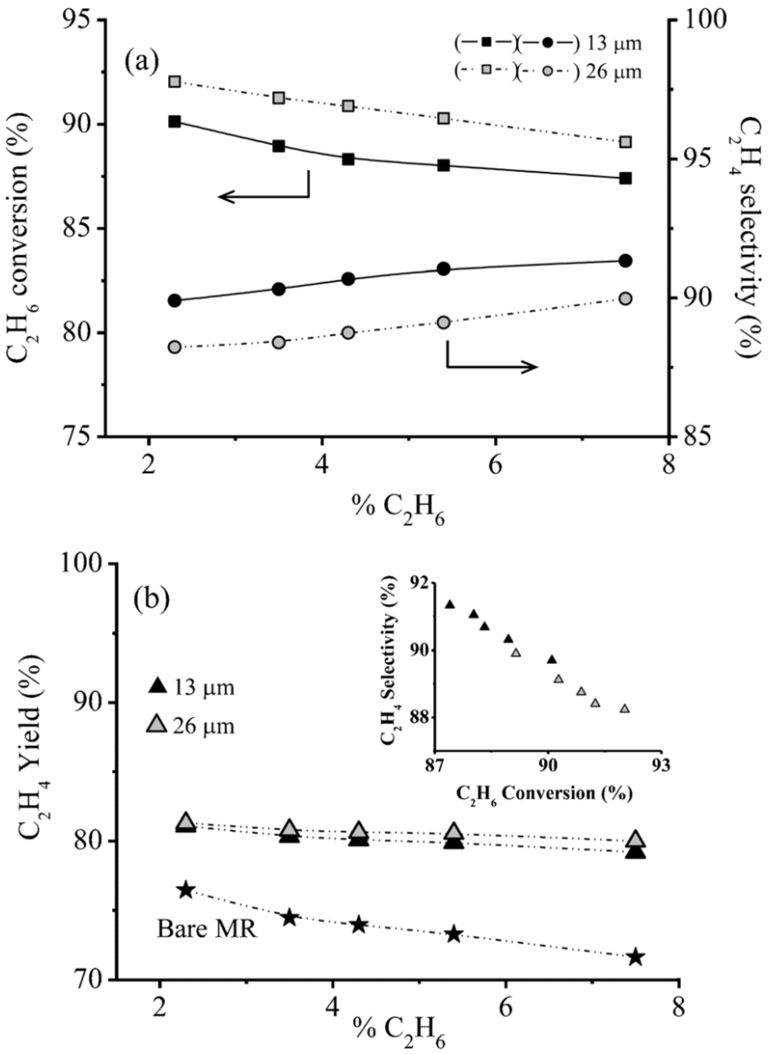

Figure 3.35: Catalytic performance of the modified BSCF MRs in the ODHE reaction as a function of the thickness of the catalytic layer: 13 and 26 µm. a) Ethane conversion and ethylene selectivity; b) ethylene yields obtained in BSCF MRs. T=850 ºC, ethane diluted with argon, $Q_{Reaction\ side}$=400 ml·min^{-1}, $Q_{Feed\ side}$=210 ml·min^{-1} (pO_2=0.04 atm).

Figure 3.36 summarizes the catalytic results from previous works published on the ODHE reaction when using perovskite type ceramic MRs along with all results obtained in this work. Mirodatos and co-workers reported an ethylene yield of 75%, with a MR using disk-shaped MIEC (BSCF) membrane modified with Pd nanoclusters and 73% Y_{C2H4} when the membrane surface was activated by using a thin layer of V/MgO; in both cases, at 777 ºC and using 25% v/v of C_2H_6 in the feed stream [37]. Akin and Lin reported an ethylene yield of 56% (per pass) with a dense tubular ceramic MR made of $Bi_{1.5}Y_{0.3}SmO_3$ (fluorite structure) at 875 ºC and

10% C_2H_6 in the feed stream [31]. Yang et al. reported an ethylene selectivity of 80% at 84% ethane conversion by using a dense MIEC (BSCF) as the membrane in a co-fed reactor [30]. Caro et al. investigated the ODHE by using a dense perovskite hollow-fiber membrane of $BaCo_xFe_yZrZO_{3-\delta}$ using a standard commercial dehydrogenation catalyst (Actisorb 410, S_dchemie, Cr_2O_3 on Ca aluminate). They obtained an ethylene yield of 43% and ethylene selectivity of 67% at 725 ºC and 30% v/v of C_2H_6 in the feed stream [42]. Wang et al. reported an ethylene selectivity of 67.4% at 80% ethane conversion by using dense MIEC (BSCF) as the membrane at 850 ºC and 10% v/v of C_2H_6 in the feed stream [40].

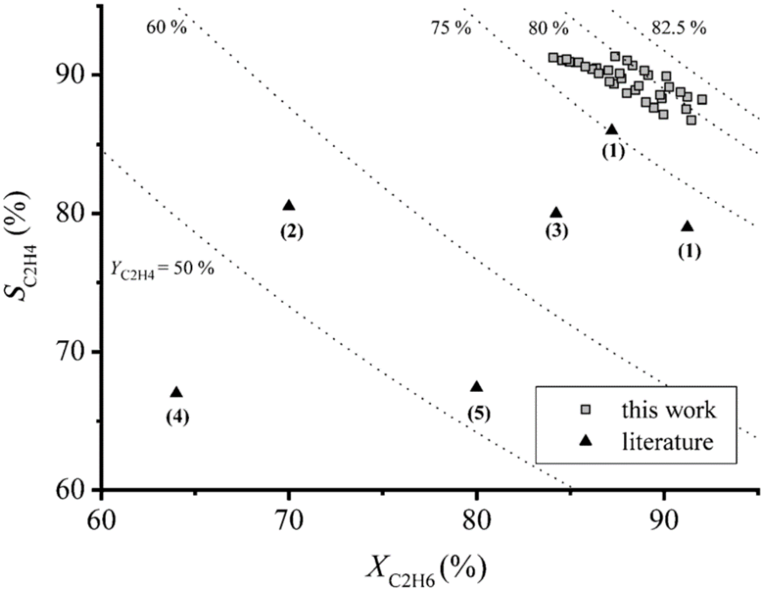

Figure 3.36: Catalytic performance of the modified BSCF MR in the ODHE reaction in terms of ethylene selectivity as a function of ethane conversion. Data for various catalytic dense MRs reported in literature: 1) Mirodatos et al. [37]; 2) Akin and Lin [31]; 3) Yang et al. [30]; 4) Caro et al. [42]; 5) Wang et al. [40]

In these works, there is a wide dispersion with regard to the temperature of the reaction, catalysts, and reactor configuration. The higher ethylene yield obtained in this study with catalytically modified MRs can be ascribed to a combination of following aspects: 1) high activity as a result of the high temperature and oxygen species diffusing through the membrane; 2) control of oxygen dosing and a low concentration of molecular oxygen in the gas phase; 3) the improved catalytic activity of the porous layers, due to the enlarged surface area (regarding the bare membrane), which influences both the hydrocarbon reaction kinetics and oxygen permeation; and 4) suitable fluid dynamics, which enables appropriate feed contact with the membrane and the rapid removal of products.

Finally, catalytic tests at 850 ºC using much higher ethane concentrations in the feed stream were conducted on a membrane coated with a BSCF layer with macroporosity. Figure 3.37 shows ethylene productivity as a function of ethane concentration, as well as the corresponding ethylene selectivity and ethane conversion values. Very high ethylene productivities can be achieved when high ethane concentrations and high gas flow rates (Q_{feed} =400 ml·min^{-1}) are employed. This high productivity is possible due to 1) the high ethylene selectivity reached at high conversions and 2) the relatively high conversion degrees attained at high ethane concentrations in the feed. Moreover, the contribution of a gas-phase dehydrogenation reaction at 850 ºC and suitable fluid dynamics in the reaction chamber, which enables the rapid evacuation of reaction products, are also very beneficial in this case. The stability of the catalytic MR operation was assessed for several days and no major degradation was observed. This short-term stability is ascribed to 1) the low coke formation rate combined with concomitant oxygen permeation and 2) negligible membrane carbonation caused by the low stability of alkali-earth carbonates above 800 ºC and low CO_2 concentration, although BSCF materials are not stable under these operating conditions for long periods mainly due to Ba and Sr carbonation [43].

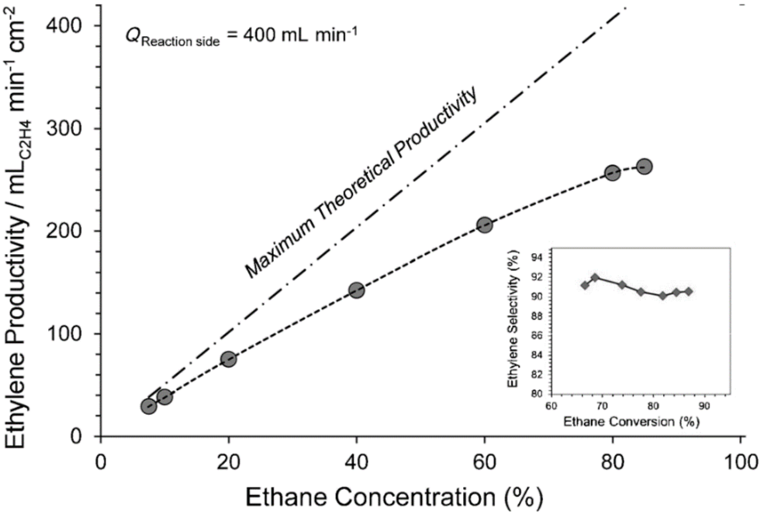

Figure 3.37: Catalytic tests with high ethane concentrations in the feed stream. Ethylene productivity obtained with the catalytic coating and ethylene selectivity versus ethane conversion (inset) are shown. T=850 ºC, ethane diluted with argon, QReaction side=400 ml·min^{-1}.

3.3. Tubular membranes.

Planar and tubular geometries are the most considered options for the manufacturing of Oxygen Transport Membrane reactors. At laboratory scale flat disk-shaped membranes are the preferred choice mainly due to their ease of fabrication and the low material amount that is required. Nevertheless, amongst tubular geometries, the particular case of hollow fiber membranes presents a big interest mainly due to their larger surface area/volume ratio in comparison with planar geometries, thus leading to higher oxygen flows in comparison with planar membranes.

Table 3.5 lists some of the most important features that both geometries present. Concerning the experimentation at laboratory scale, planar membranes can be more easily fabricated (isostatic pressing, see section 2.2.1 of the present Thesis) using little amounts of powder (in the range of 1.5-2 grams). On the contrary, tubular membranes are typically produced by more complicated methods such as thermoplastic extrusion [44], slip casting [45, 46] and spinning-phase inversion [47] (although BSCF tubes were also produced by isostatic pressing within OXYCOAL-AC project activities[6]), also requiring higher amounts of materials and further steps. In spite of these and other cons, the use of tubular membranes is of big interest in the construction of OTM modules oriented to practical applications. The main reason is the better mechanical properties of tubular architectures, thus permitting the use of higher pressurized feeding and subsequently yielding to a gain in the performance [48].

Table 3.5: Pros and cons of OTMs depending on the geometry for laboratory scale applications.

Geometry	Advantages	Disadvantages
Planar	Easy manufacturing Low material required Easy to handle Not subjected to T gradients	Difficult sealing Lower performance
Tubular	High surface area/volume ratio Higher $J(O_2)$ per volume Easier sealing	Difficult manufacturing High amount of material required Large T gradients along membranes Difficult to handle

3.3.1. Capillary membrane description.

For the permeation and reaction studies performed in the present section BSCF capillaries provided by Fraunhofer Institute for Ceramic Technologies and Systems (IKTS) have been used.

BSCF capillaries were manufactured by plastic extrusion as described in [48], obtaining tubes with a length of 220 mm, an outer diameter of 3.25 mm and an inner diameter of 2.55 mm, resulting in a wall thickness of 0.35 mm. The capillaries were closed at one side for a dead end oxygen separation. The capillary closing was made by joining a flat small disk by reactive air brazing [49]. Due to this procedure for closing the tubes, temperatures above 950 ºC are not recommended for working with these membranes.

---

[6] http://processnet.org/processnet_media/11_25h_Kaletsch-p-1768.pdf

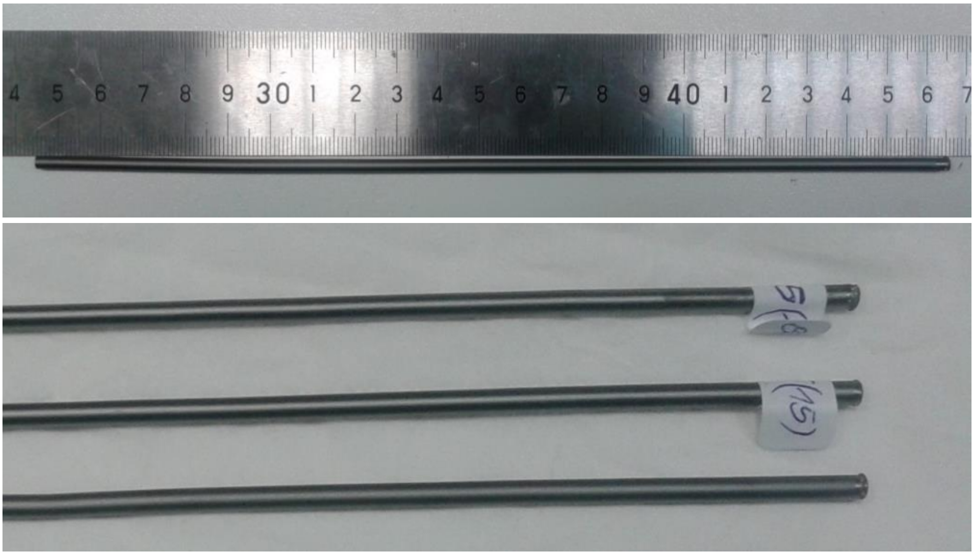

Figure 3.38: BSCF capillaries used during permeation/reaction characterization. Dead end closing detailed in picture below.

SEM observation of fresh samples indicates a good bulk density, only presenting the typical 1-2 μm BSCF occlusive porosity and some isolated larger voids that do not compromise membrane tightness.

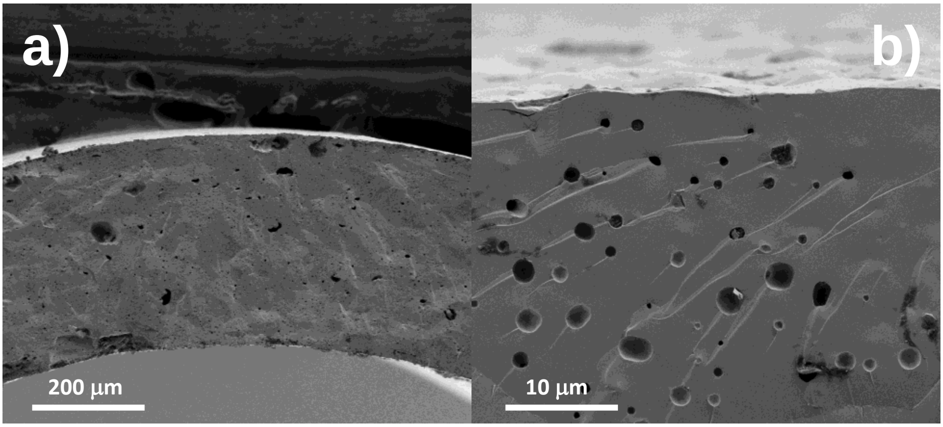

Figure 3.39: SEM cross-section views of a BSCF capillary.

3.3.2. Oxygen permeation.

A BSCF capillary was tested under clean conditions (Argon sweeping) in the temperature range 550-900 ºC. The maximum temperature of 900 ºC was not surpassed due to the silver brazing used for the bottom end close of the tube. As the melting point of Ag is 960 ºC then it was decided to operate a lower temperatures. In addition to the study of permeation in dependence of temperature it was also performed some tests when varying pO_2 in sweep side (by sweep flow variation) and in feed side.

Left Figure 3.40 depicts the $J(O_2)$ evolution with temperature for different sweep flows when feeding with synthetic air. A maximum oxygen flow rate of ca. 13 ml·min^{-1} is obtained at 900 ºC with a sweep of 500 ml·min^{-1} of Argon. As can be seen, sweep flow increase presents a more significant effect in the $J(O_2)$ improvement at higher temperatures. At these temperatures there is a higher O^{2-} diffusion through the bulk and due to the local pO_2 reduction ascribed to the high sweep used, a higher pO_2 gradient across the membrane is generated, subsequently resulting in higher $J(O_2)$. On the contrary, at lower temperatures no important rise in $J(O_2)$ are observed, with oxygen flow rates of ca 0.1 ml·min^{-1} at 600 ºC.

Variation of pO_2 in feed stream evidences the big potential of the achievable oxygen fluxes in BSCF capillaries (right Figure 3.40), producing more than 30 ml·min^{-1} O_2 for a single capillary with a length of only 3 cm when feeding with 1 bar O_2 (equivalent to a 5 bar-pressurized synthetic air feed stream). This permeation value is achieved at 900 ºC, but even at only 550 ºC oxygen fluxes of ca. 2 ml·min^{-1} are obtained with a pure oxygen feeding.

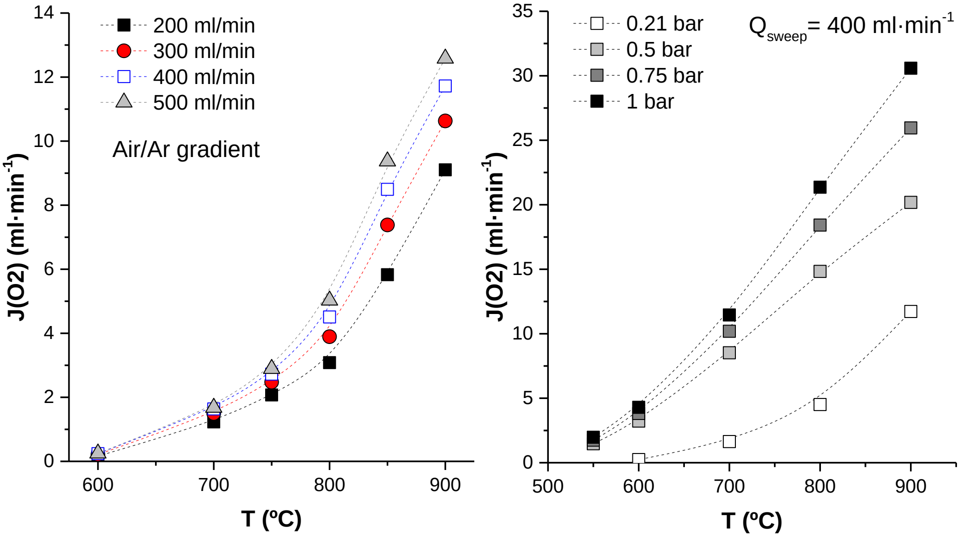

Figure 3.40: Oxygen permeation dependence with temperature when varying sweep flow rates (left) and pO_2 in feed stream (right). Q_{feed} = 200 ml·min^{-1}.

Due to the high surface area/volume relation that present OTM capillary configurations one of their most important features is the capability of separating big O_2 volumes from the feed stream. With the data obtained from the permeation tests it is possible to calculate the degree of O_2 extracted from the feed gas by only dividing the obtained $J(O_2)$ in ml·min^{-1} with the flow of the O_2 contained in the feed stream. Then, the following expression yields the O_2 separation degree for the different tested conditions

$$\%O_2^{sep} = \frac{J(O_2)}{X_{O2}^{feed} \cdot Q_{feed}} \tag{3.1}$$

In the table below are shown the percentages of the oxygen extracted from the feed stream corresponding to the data depicted in Figure 3.40. The highest separation degree is achieved at 900 ºC and 500 ml·min^{-1} sweeping when feeding with synthetic air, with nearly a 30% separation of the oxygen contained in the feed. As can be seen in Table 3.6, the separation degree is improved when operating at higher temperatures and sweep flow rates at pO_2 in feed = 0.21 bar, being this related with the higher $J(O_2)$ under these conditions. When varying pO_2 in feed, the best results below 800 ºC are obtained when feeding with pO_2 = 0.5 bar, decreasing the separation degree at higher pO_2. The presented values show the enormous potential of this kind of geometries and material in the construction of OTM modules for the supply of O_2.

Table 3.6: Percentage of oxygen separated from feed stream through the BSCF capillaries for different tested conditions. Q_{sweep} variation was performed when feeding with pO_2 = 0.21 bar. pO_2 in feed variation was carried out when sweeping with 400 ml·min^{-1} Ar.

T (ºC)	**O_2 separation (%)**							
	Q sweep				*pO_2 in feed*			
	200 ml/min	*300 ml/min*	*400 ml/min*	*500 ml/min*	*0.21 bar*	*0.5 bar*	*0.75 bar*	*1 bar*
900	21,68	25,31	27,91	29,96	27,91	20.18	17.3	15.29
850	13,88	17,58	20,22	22,31	20,22			
800	7,34	9,27	10,74	11,97	10,74	14.83	12.28	10.68
750	4,93	5,89	6,48	6,88	6,48			
700	2,93	3,56	3,9	4	3,9	8.52	6.79	5.73
600	0,39	0,51	0,57	0,59	0,57	3.23	2.54	2.15
550						1.47	1.16	0.99

Finally a comparison of the performance of a planar disk-shaped membrane and the capillary is provided in Figure 3.42. Since the capillary membrane presents a wall thickness of ca. 0.35 mm, a 0.38 mm-thick planar membrane has been considered for this evaluation. Oxygen fluxes have been expressed in ml·min^{-1}·cm^{-2} then making a more suitable comparison of the permeation. Attending to the results shown in Figure 3.42 the planar membrane presents a better performance than the capillary, especially as temperature is decreased. Since both membranes present the same formulation and similar thickness, then similar performance would be expected. Nevertheless, some issues can explain this deviation:

- Planar membrane is fed with 300 ml·min^{-1} of synthetic air, whereas the capillary is fed with only 200 ml·min^{-1}.
- For the capillary has been considered a surface area of 3.14601 cm^{-2}, corresponding to the exposed area of the 3 cm long tube, also considering the bottom end cap closing the tube. Attending to the flow dynamics during permeation depicted in Figure 3.41, this surface would not be swept in the same way than the rest of the capillary, probably presenting some dead volumes leading to a bad sweeping and subsequently to a diminution in the effective surface area.
- SiC packed bed wrapping the BSCF capillary could reduce effective surface area due to the SiC grains (d_p = 0.4-0.6 mm) adhered to the membrane surface, as depicted in Figure 3.41.

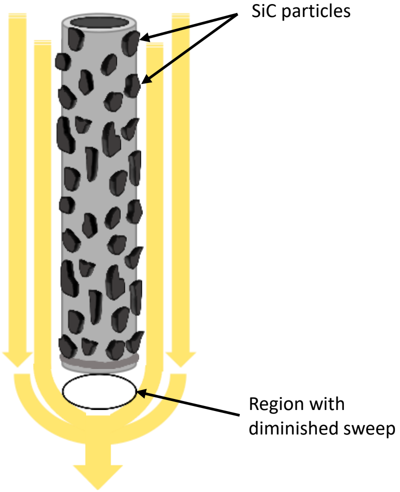

Figure 3.41: Graphic representation of the SiC particles reducing the effective surface area for oxygen permeation.

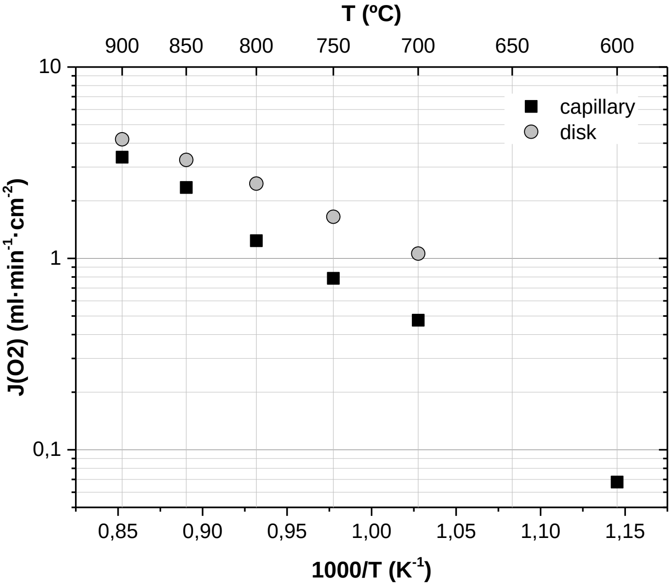

Figure 3.42: Comparison of the oxygen permeation corresponding to a capillary and a planar disk-shaped membranes. Flow conditions for capillary: $Q_{feed} = 200$ ml·min^{-1}, $Q_{sweep} = 300$ ml·min^{-1}. Flow conditions for disk: $Q_{feed} = 300$ ml·min^{-1}, $Q_{sweep} = 300$ ml·min^{-1}.

3.3.3. Oxidative Coupling of Methane.

As is has been described in section 3.2.5 of the present chapter, there is a big interest in the production of light olefins, especially ethylene. In addition to the production of ethylene by means of ODHE, CMRs can also be used for obtaining ethylene and ethane from the oxidative coupling of methane (OCM).

The direct conversion that yields to ethylene production from methane involves a dehydrogenation for forming $CH_3^{\bullet}$ active species. Since CH_4 is a very stable molecule, then methane activation for the coupling requires breaking a strong C-H bond (ca. 439 kJ·mol^{-1}); therefore, high temperatures are needed, despite some catalysts can lower the reaction temperature down to 800 ºC. Issues such as thermodynamic limitation for CH_4 conversion, low C_2 selectivities and important catalysts deactivation due to coke formation, make by now OCM practically and commercially inviable. The techno-economical threshold for considering OCM as commercially available is set at 30% C_2 yield per single-pass [50].

Nevertheless, CMRs present some features that can help overcoming these drawbacks. One of the main aspects is that permitting OTM to dose the O_2 in a controlled manner. This can be done by tuning parameters such as temperature, pO_2 at feed side, residence time and space velocity modification by reactant gas stream flow variation, etc. Therefore, by adjusting conveniently the CH_4/O_2 stoichiometry the complete oxidation of CH_4 to CO_x can be avoided and then higher C_2 selectivities can be achieved.

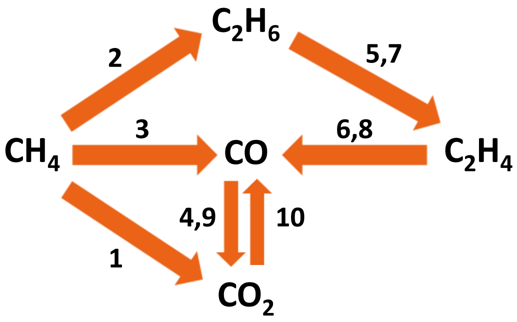

1) $CH_4 + 2O_2 \rightarrow CO_2 + 2H_2O$
2) $2CH_4 + 0.5O_2 \rightarrow C_2H_6 + H_2O$
3) $CH_4 + O_2 \rightarrow CO + H_2O + H_2$
4) $CO + 0.5O_2 \rightarrow CO_2$
5) $C_2H_6 + 0.5O_2 \rightarrow C_2H_4 + H_2O$
6) $C_2H_4 + 2O_2 \rightarrow 2CO + 2H_2O$
7) $C_2H_6 \rightarrow C_2H_4 + H_2$
8) $C_2H_4 + 2H_2O \rightarrow 2CO + 4H_2$
9) $CO + H_2O \rightarrow CO_2 + H_2$
10) $CO_2 + H_2 \rightarrow CO + H_2O$

Figure 3.43: Simplified reaction scheme of a kinetic model for OCM. Adapted from Stansch et al. [51]

During the past years several research groups have performed OCM reactions by considering different OTM materials and geometries, as well as catalysts for improving the reaction towards C_2 formation. In the table below some of the most interesting developments are summarized. As can be seen, tubular geometries are the preferred for conducting OCM in CMRs, with a special emphasis in the use of catalysts, what in the most of the cases improve C_2 selectivity. Amongst all the considered cases, the best results have been obtained by Othman et al., reaching a C_2 yield of 39% on a LSCF hollow fiber activated with $Bi_{1.5}Y_{0.3}Sm_{0.2}O_{3-\delta}$ catalyst.

Table 3.7: C_2 selectivities and yields for different OCM studies conducted on CMRs.

Material	T (ºC)	Geometry	Catalyst	S_{C2} (%)	Y_{C2} (%)	Reference
$Bi_{1.5}Y_{0.3}Sm_{0.2}O_{3-3}$	900	tubular	--	54	35	[52]
BSCF	850	tubular	La-Sr/CaO	66	15	[12]
BSCF	900	disk	La-Sr/CaO	65	18	[53]
LSCF	950	hollow fiber	--	43.8	15.3	[54]
LSCF	975	hollow fiber	$SrTi_{0.9}Li_{0.1}O_3$	40	21	[55]
LSCF	900	hollow fiber	$Bi_{1.5}Y_{0.3}Sm_{0.2}O_{3-\delta}$	79	39	[56]
BCFZ	800	hollow fiber	Mn-Na_2WO_4/SiO_2	50	17	[57]
BCGCF	850	tubular	Na-W-Mn	67.4	34.7	[58]

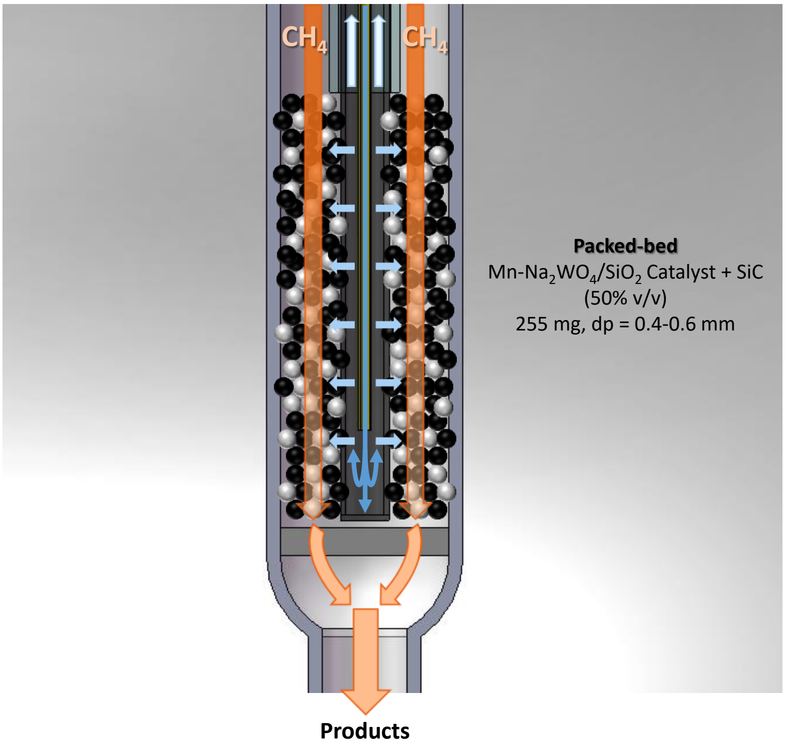

Figure 3.44: Schematic representation of the experimental set used for the OCM tests.

An OCM study has been performed on a BSCF capillary activated with a Mn-Na_2WO_4/SiO_2 catalyst. This catalyst has been selected since it is considered as a reference case within OCM works, showing a high methane conversion as well as C_2 selectivity and catalyst stability [59-61]. The experimental set-up used for this study is the same than the one considered for the oxygen permeation studies on the BSCF capillary. A packed-bed consisting of 255 mg of Mn-Na_2WO_4/SiO_2 catalyst (d_p = 0.4-0.6 mm) and SiC grains in a relation 50% v/v was considered as reaction media for the OCM. The capillary exposed area was approximately 3.5 cm^2, corresponding to a capillary length of 3 cm. The contact of the rest of the capillary with the reactant gases was avoided by placing a quartz tube above the packed-bed all along the capillary. This quartz tube presented an inner diameter of 3.75 mm, being sufficient for wrapping completely the BSCF capillary. Top and bottom inlets of the tube were blocked, thus avoiding the reactant gases to be in contact with the membrane. This was done mainly for performing the OCM tests in the 3 cm-long isothermal zone of the used furnace, thus ensuring a constant temperature in all the reaction media.

The OCM experiments were performed at 900 ºC, feeding with 200 $ml \cdot min^{-1}$ of synthetic air (or O_2/N_2 mixtures) in the inner side of the capillary. Mixtures of CH_4/Ar were used as reactant gas, varying the flows in the range of 50-600 $ml \cdot min^{-1}$. In order to study OCM reaction performance, the methane conversion (X_{CH4}), C_2 selectivity (S_{C2}) and yield (Y_{C2}) were determined. Concerning the oxygen permeation, it was obtained by means of a carbon balance as described in the section 2.6.3 of the present Thesis. All this parameters were calculated by previously determining gas species compositions of the product stream from online GC analysis.

3.3.4.1. Space velocity variation.

In order to determine the effect of reactant gas flow rate in the production of ethylene and ethane a variation study in the range of 50-600 $ml \cdot min^{-1}$ was done. Gas flow rates in this range have been expressed as Gas Hourly Space Velocity (GHSV) in $ml \cdot h^{-1} \cdot g_{cat}^{-1}$

$$GHSV = \frac{Q_{CH4}}{g_{cat}} \tag{3.2}$$

where Q_{CH4} is the flow rate (in $ml \cdot h^{-1}$) of methane and g_{cat} are the grams of catalyst loaded in the packed-bed reactor. GHSV is a useful parameter for quantifying the reactor volumes of feed can be treated in a unit time, taking also into account the catalyst load. During this experiment synthetic air was fed through the inner side of the capillary whereas a stream of 10% CH_4 in Argon was circulating through the packed-bed. As can be seen in Figure 3.45 methane conversion progressively decreases when increasing space velocity. Regarding C_2 selectivity it has a maximum of 26% at ca. 4.700 $ml \cdot h^{-1} \cdot g^{-1}$ after which becomes stabilized at 20% when increasing gas flow rate. The highest C_2 yield is achieved at 2.350 $ml \cdot h^{-1} \cdot g^{-1}$ with a yield of 13.5 % at a methane conversion of 60%. GHSV increase also affects methane oxidation towards CO_2 formation, since S_{CO2} decreases from 58% down to 20%. However, CO generation is barely affected by space velocity variation, maintaining during all the test a selectivity value around 10-5%. The only parameter that is improved by GHSV increase is the oxygen permeation, reaching a value of 7 ml·min^{-1}·cm^{-2} at 14.000 ml·h^{-1}·g^{-1} (600 ml·min^{-1}). Nevertheless, this improvement in *J(O$_2$)* is mainly ascribed to unreacted O_2.

The progressive decrease of X_{CH4} with GHSV can be explained with the fact that at higher space velocities and lower residence times, reactions leading to the oxidation of CH_4 are not favored, hence less methane is converted and less products are obtained, and so a high amount of O_2 keeps unreacted in the stream. On the other hand, low GHSV involve higher S_{CO2}, due to a higher CH_4 oxidation degree towards CO_2 at higher residence times. As the main interest of this reaction is the production of C_2 then the most suitable conditions would be set at low GHSV, in the range of 1.000-6.000 ml·h^{-1}·g^{-1}.

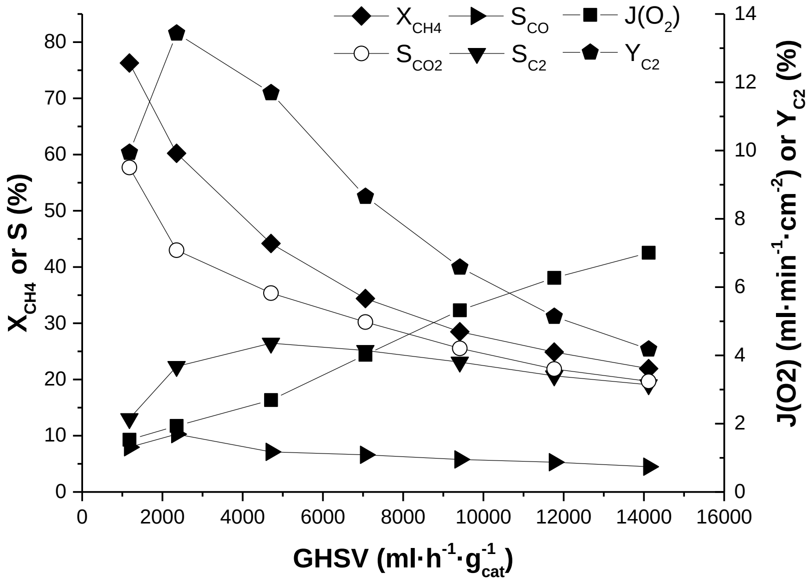

Figure 3.45: Effect of the variation of space velocity on the methane conversion, products selectivity, C_2 yield and oxygen permeation.

Figure 3.46 represents the yields of the reaction products for different methane conversions at 900 ºC. Methane conversion was varied by varying GHSV. As can be seen, there is a maximum for C_2 at conversions between 50-70%, with Y_{C2} above 13%. This yield value is similar to those obtained for BSCF tubular membranes depicted in Table 3.7, nevertheless C_2 selectivities obtained in those studies are much higher than the obtained in the present work. That could be a sign that the catalyst requires some modifications for improving its selectivity towards C_2 generation. On the other hand, increasing X_{CH4} also implies higher Y_{CO2}, meaning that complete CH_4 oxidation produces mostly CO_2 as product. Coke formation has been also estimated, presenting yield values between 12-16% (selectivities varied from 20 to 55%).

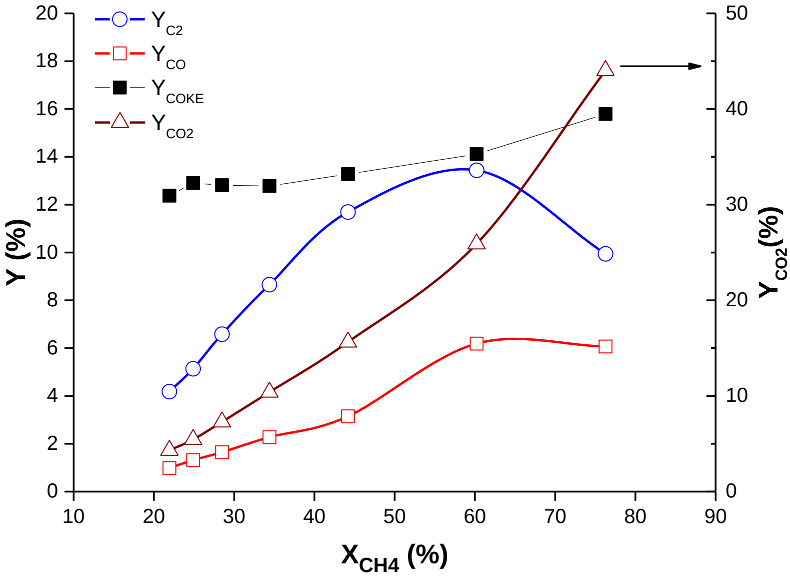

Figure 3.46: Product yields in dependence of methane conversion.

3.3.4.2. CH_4 content in reactant gas stream variation.

As well as GHSV, the influence of CH_4 content in the reactant gas stream was also studied. This was done for studying system performance under different CH_4/O_2 ratios. Considering a constant reactant gas flow rate of 100 ml·min^{-1}, CH_4 content was varied in the range of 10%-95% when using a synthetic air feeding (200 ml·min^{-1}).

As can be seen in Figure 3.47, CH_4 content variation barely affects products selectivity, with a slight decrease in the values as CH_4 is increased. This differs from other studies results where it was observed a S_{C2} improvement when increasing CH_4 under similar conditions [12]. More significant is the decrease in X_{CH4} at higher CH_4 percentages. Therefore, the reaction system cannot convert higher CH_4 volumes into products, thus diminishing methane conversion and subsequently C_2 yield, that presents a maximum at 10% CH_4. With regard to $J(O_2)$, an improvement from 2 to 4 ml·min^{-1}·cm^{-2} has been obtained when increasing CH_4 content from 10 to 95%.

Maybe this is caused by a large reactor chamber volume, being produced the OCM reactions in a region near the membrane surface.

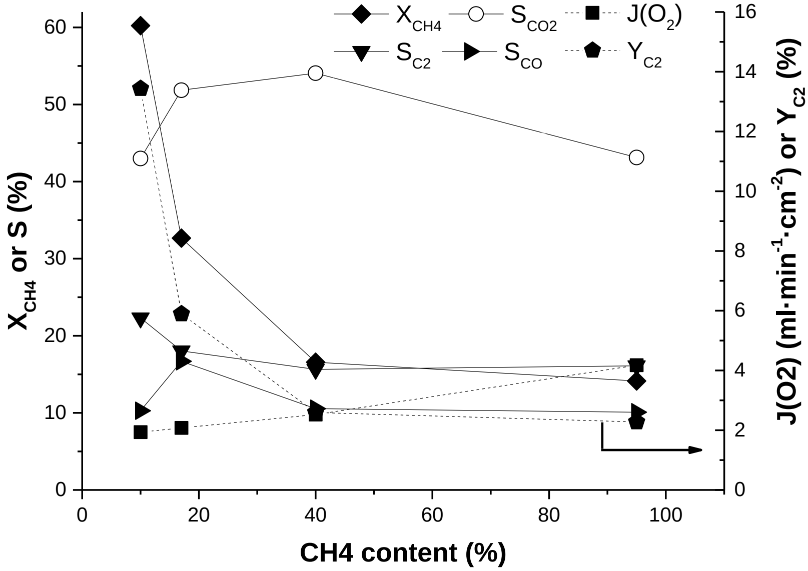

Figure 3.47: Effect of the variation of CH_4 content in reactant gas stream on the methane conversion, products selectivity, C_2 yield and oxygen permeation.

3.3.4.3. Parametric study for Y_{C2} maximization.

After GHSV and CH_4 variation tests, it was performed a broad parametric study varying GHSV and pO_2 in feed stream. This was done in order to determine the optimal conditions for conducting OCM reactions on the considered system for Y_{C2} maximization. Parameters such as X_{CH4}, S_{C2}, Y_{C2}, $J(O_2)$ and C_2H_4/C_2H_6 ratio were analysed. As previously mentioned, for considering OCM as economically viable, single-pass Y_{C2} and S_{C2} have to be above 30 and 90%, respectively [50]. CH_4 concentration was maintained at 10%, since under this condition maximum Y_{C2} was obtained. For this parametric study GHSV was varied between 2,353 and 7,059 ml·h^{-1}·g^{-1} (100-300 ml·min^{-1}), whereas pO_2 in feed was varied in the range 0.05-1 bar. All the tests were conducted at a temperature of 900 ºC and with a feed flow rate of 200 ml·min^{-1}. The results obtained from this study are listed in Table 3.8. From these data, several contour plots displaying $J(O_2)$, X_{CH4}, S_{C2} and Y_{C2} have been built and will be discussed below.

Table 3.8: Results of the parametric study conducted on BSCF capillaries at 900 ºC, 10% CH_4 in the reaction stream.

GHSV ($ml·h^{-1}·g^{-1}$)	pO_2 feed (bar)	$J(O_2)$ ($ml·min^{-1}·cm^{-2}$)	X_{CH4} (%)	S_{C2} (%)	Y_{C2} (%)	C_2H_4/C_2H_6
2353	**0.05**	0.58	27.01	15.35	4.15	0.91
4706	**0.05**	0.77	22.68	16.52	3.75	0.63
7059	**0.05**	0.9	20.16	16	3.23	0.51
2353	**0.1**	0.97	38.59	20.63	7.96	1.59
4706	**0.1**	1.25	31.95	21.87	6.99	1.04
7059	**0.1**	1.68	26.89	20.36	5.47	0.76
2353	**0.21**	1.93	60.22	22.31	13.44	3.08
4706	**0.21**	2.69	44.19	26.45	11.69	1.65
7059	**0.21**	4.02	34.4	25.15	8.65	1.08
2353	**0.5**	4.78	84.85	8.95	7.6	9.62
4706	**0.5**	7.36	58	18.6	10.79	2.5
7059	**0.5**	10.45	44.01	20.61	9.07	1.52
2353	**0.75**	8.93	92.75	4.01	3.72	5.76
4706	**0.75**	11.69	62.87	17	10.69	2.91
7059	**0.75**	15.18	46	20.57	9.46	1.69
2353	**1**	11.67	99.94	0	0	0
4706	**1**	15.59	66.55	15.34	4.59	3.21
7059	**1**	18.74	49.51	19.2	7.34	1.83

Figure 3.48 shows the oxygen fluxes in dependence of pO_2 in feed and GHSV. As can be seen, higher $J(O_2)$ are obtained when increasing both pO_2 and GHSV, with a peak value of 18.74 $ml·min^{-1}·cm^{-2}$ at 1 bar O_2 and 7,059 $ml·h^{-1}·g^{-1}$. This is due to the high pO_2 gradients across the membrane that are produced when using high oxygen concentration in the feed and high sweep flow rates in the sweep side.

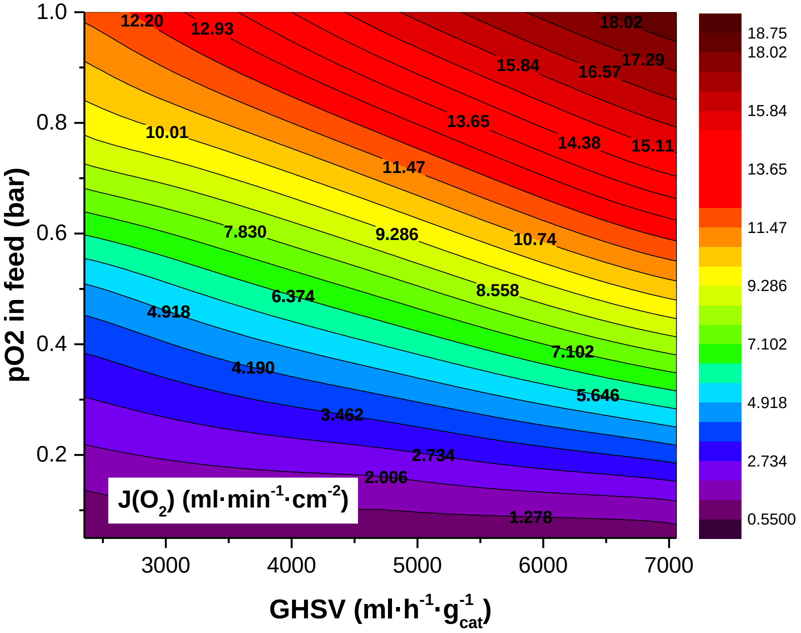

Figure 3.48: Contour plot displaying $J(O_2)$ (in ml·min^{-1}·cm^{-2}) when varying pO_2 in feed and GHSV.

In order to perform a more visual representation of the most relevant parametric study results (i.e. X_{CH4}, S_{C2} and Y_{C2}), these have been represented in dependence of $J(O_2)$ and GHSV. Thus providing a better picture of the reaction conditions, since oxygen fluxes give a magnitude of the O_2 dosage for conducting the OCM reaction.

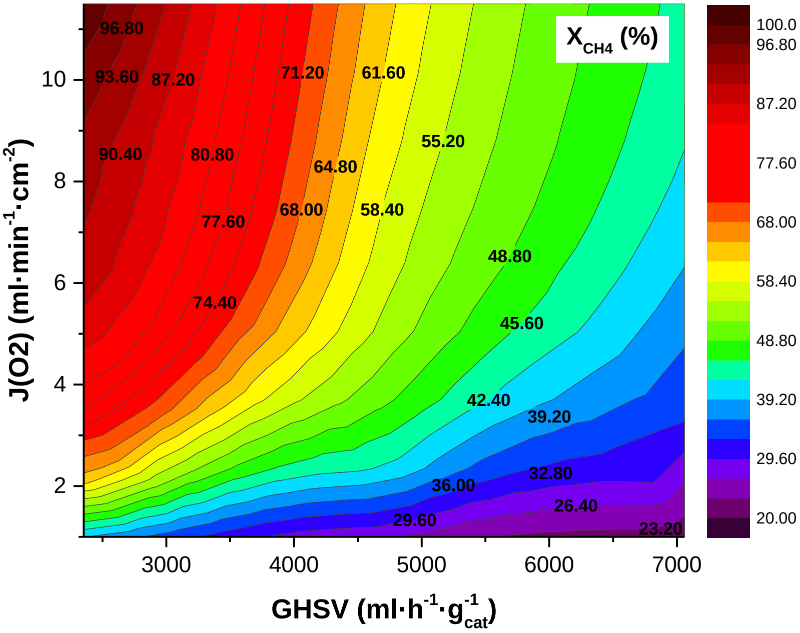

Figure 3.49: Contour plot displaying X_{CH4} (%) when varying GHSV and J(O_2).

Figure 3.49 depicts the results for X_{CH4}. As can be seen, the higher CH_4 conversions are reached when having higher O_2 fluxes at lower space velocities (2,353 ml·h^{-1}·g^{-1}) for the reactant gas stream, with a maximum value of 99.94%. On the other hand, a minimum conversion value of 20.16% is reached at a permeation of 0.9 ml·min^{-1}·cm^{-2} at 7,059 ml·h^{-1}·g^{-1}. Then it is clear that low space velocities and high O_2 fluxes favour CH_4 conversion.

Nevertheless, higher C_2 selectivities are reached at intermediate GHSV and *J(O_2)* values between 2 and 3 ml·min^{-1}·cm^{-2}, with a maximum value of 26.45% at 4,706 ml·h^{-1}·g^{-1} and 2.69 ml·min^{-1}·cm^{-2} O_2 (Figure 3.50). It is worth to mention the fact that at high *J(O_2)* and low space velocities the S_{C2} experiences a dramatic drop, even falling down to 0% at 11,67 ml·min^{-1}·cm^{-2} O_2 and 2,353 ml·h^{-1}·g^{-1}. This is maybe related with the fact that with a higher presence of O_2 in the reaction chamber and a low space velocity, CH_4 is mainly oxidized to CO_X thus diminishing C_2 selectivity.

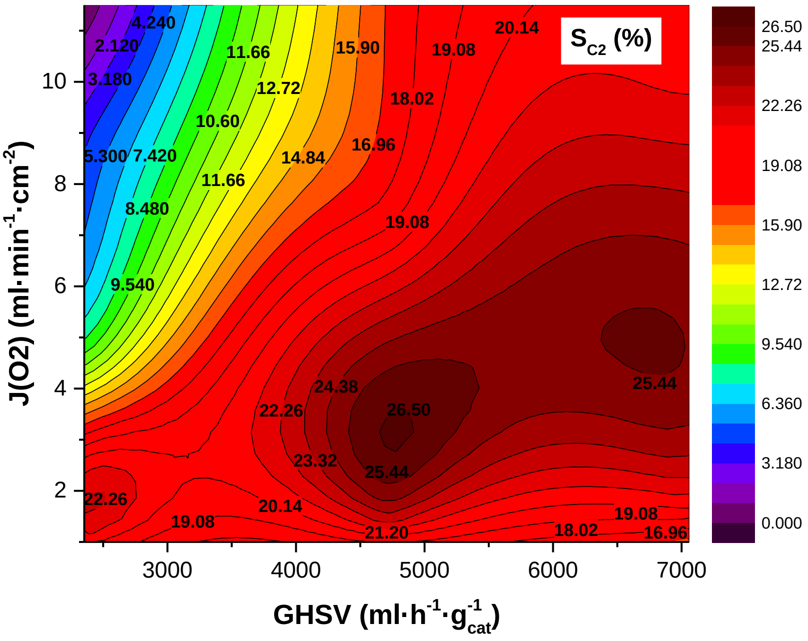

Figure 3.50: Contour plot displaying S_{C2} (%) when varying GHSV and J(O_2).

With regard to C_2 yield, a maximum value of 13.5% is obtained when supplying 1.93 ml·min^{-1}·cm^{-2} O_2 at a GHSV of 2,353 ml·h^{-1}·g^{-1} (Figure 3.51). Despite having higher S_{C2} at higher space velocities, the fact that X_{CH4} experiences a sharp decrease when increasing GHSV also affects negatively Y_{C2} at this given $J(O_2)$. Nevertheless, from the contour plot it can be observed a region (in red) where Y_{C2} is above 10%. As the plot is constructed from fitting of discrete data points (Table 3.8), further testing would allow the determination of additional maximum points in this region.

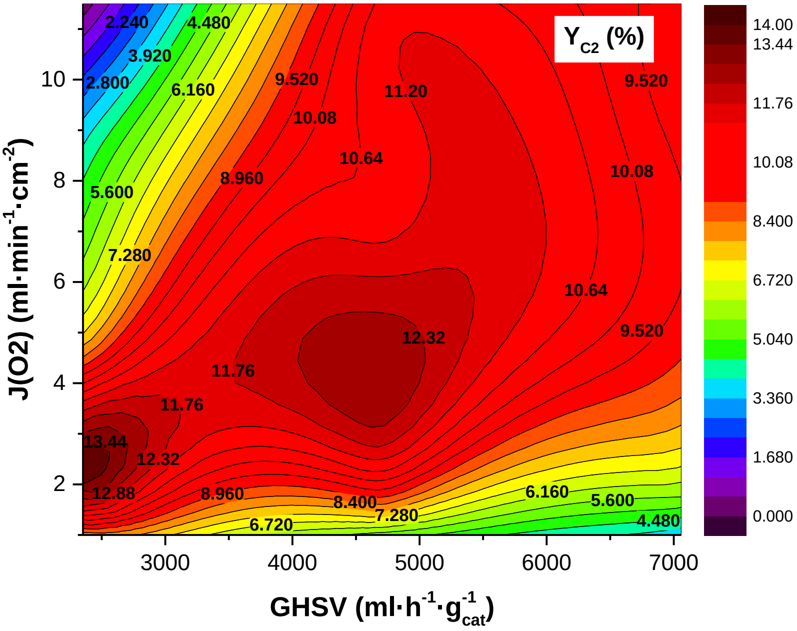

Figure 3.51: Contour plot displaying Y_{C2} (%) when varying GHSV and J(O_2).

As ethylene is the main product of interest in the OCM reaction, is always useful to study C_2H_4/C_2H_6 relation for determining both the effectiveness of a catalyst and the best conditions for maximizing ethylene production. From the observation of Figure 3.52 it is clear that maximization of C_2H_4 production with regard to C_2H_6 is obtained when supplying O_2 at a rate of ca. 5 ml·min^{-1}·cm^{-2} and at low space velocities (2,353 ml·h^{-1}·g^{-1}), resulting in a C_2H_4/C_2H_6 relation of nearly 10. This value can be considered as very high, since typical values for some co-feed and CMR are in the range of 1.5-4 [62-64]. With regard to similar studies performed on tubular

BSCF membranes, the obtained C_2H_4/C_2H_6 ratio presents a similar value than the obtained by Wang et al. with a relation of 12.45 at 900 ºC [12].

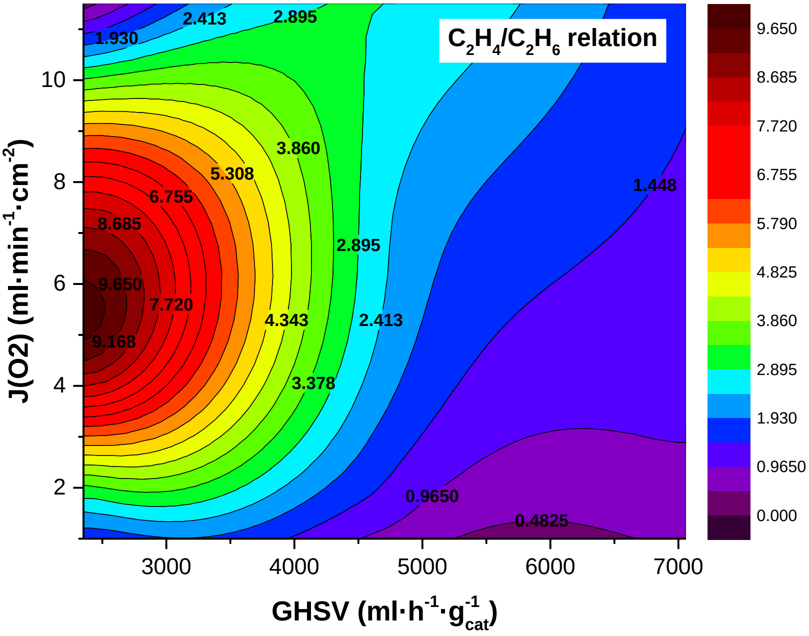

Figure 3.52: Contour maps displaying C_2H_4/C_2H_6 relation when varying GHSV and $J(O_2)$.

3.3.4.4. Post-mortem analysis.

BSCF capillary was observed by SEM before and after OCM reaction conduction in order to check how the induced conditions affected membrane microstructure and architecture. As it can be observed in Figure 3.53b, exposed surface to methane environment has resulted significantly affected after test. An evident surface degradation of the membrane caused by the highly reducing environments during OCM tests have produced a grain decomposition all over exposed surface. Nevertheless, this degradation is only taking place at the surface, since in the cross section view no signs of structure decomposition or secondary phase formation are observed.

XRD measurements performed on both fresh and OCM-tested samples are shown in Figure 3.54. In both samples there is a presence of Co_3O_4, corresponding to the small clear grains in Figure 3.53a. As can be seen, only small differences between the two patterns can be observed, with a relative diminution in some peaks in the tested sample. Despite the evident morphological changes in the tested capillary, the fact that XRD is not showing a substantial change in material structure can be attributed to BSCF is only degraded in a very thin outer layer, as can be observed in Figure 3.53c. Therefore, and due to the penetration of the XRD radiation, the structure changes would be not properly shown by these techniques.

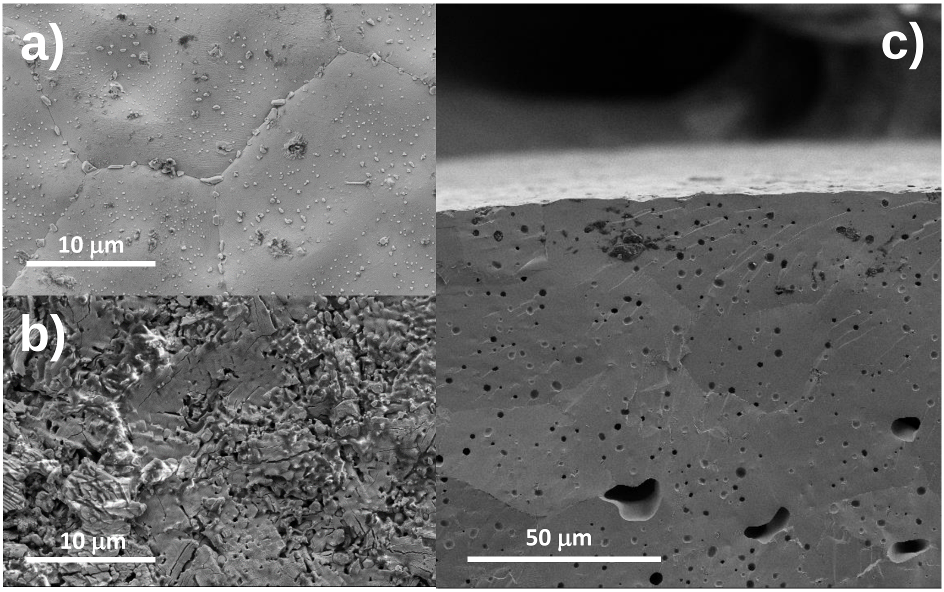

Figure 3.53: SEM images of (a) surface of a fresh BSCF capillary, (b) surface of an OCM-tested BSCF capillary, and (c) reaction side cross-section view of a BSCF capillary after OCM test.

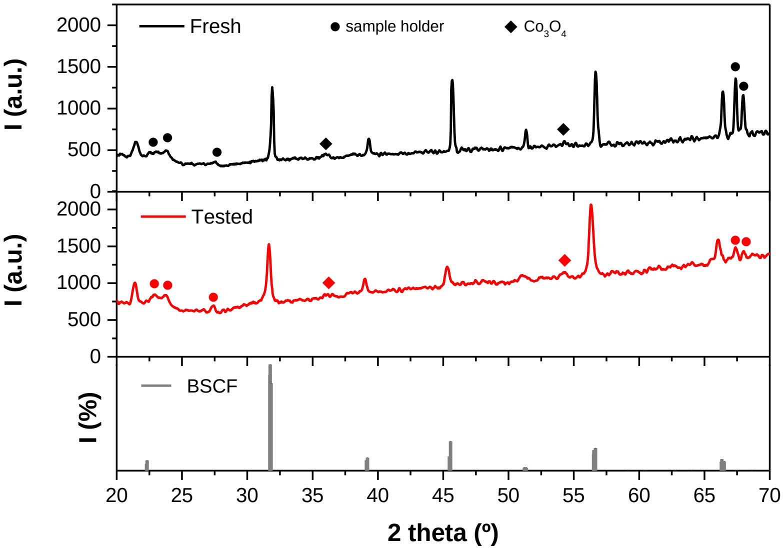

Figure 3.54: XRD patterns of fresh and OCM-tested BSCF capillaries compared to BSCF structure.

3.4. Conclusions.

Several Oxygen Transport Membranes with $Ba_{0.5}Sr_{0.5}Co_{0.8}Fe_{0.2}O_{3-\delta}$ composition have been developed and tested throughout this Chapter. Aspects such as membrane thickness and catalytic activation were studied for the case of disk-shaped planar membranes. A first evaluation of the role of membrane thickness in the oxygen permeation was performed, determining that the reduction of this parameter produces an increase in the permeation. Nevertheless, this observed improvement resulted to be lower than the predicted by Wagner equation for the case of thinner membranes. It was found that by lowering the membrane thickness the contribution of surface exchange processes to the permeation process becomes more important (Figure 3.24b) especially as temperature is decreased. Furthermore, the addition of porous substrates in asymmetric membranes seems to imply an additional resistance affecting the oxygen permeation, thus lowering the expected performance for thin membranes. Then, a strategy focused on the development of porous supports with low resistance for gas diffusion should be addressed for further optimization of $J(O_2)$ in thin asymmetric membranes.

The effect of surface catalytic activation was also studied for both monolithic and asymmetric membranes. For the case of 160 μm-thick monolithic membranes it was found that oxygen permeation improves when activating membranes, with an improvement at 1000 ºC from 7.97 to 10.99 $ml\cdot min^{-1}\cdot cm^{-2}$ if activated only sweep side, and reaching 12 $ml\cdot min^{-1}\cdot cm^{-2}$ if both membrane sides are activated. This demonstrates the importance of catalytic activation via membrane surface modification as a strategy for $J(O_2)$ optimization. A similar study was carried out by activating 60 μm-thick asymmetric membranes with porous catalytic layers on sweep side. Activation with BSCF backbones including Pd and Ag nanoparticles as catalytic promoters produced an $J(O_2)$ improvement in all the tested temperature range (1000-600 ºC), with a more significant enhancement of the fluxes in the low T region with a 3-fold improvement at 600 ºC with respect to the bare case. The latter proves the beneficial effect of catalytic activation for the boosting of surface exchange reactions limiting oxygen permeation at low temperature. In order to obtain the highest possible $J(O_2)$, oxygen permeation was measured under an O_2/Argon gradient, with a sweep flow rate of 750 $ml\cdot min^{-1}$. Under such conditions an unprecedented oxygen peak flux of 98 $ml\cdot min^{-1}\cdot cm^{-2}$ was reached for the BSCF + 5% Pd activated membrane at 950 ºC. This value is the highest $J(O_2)$ ever reported for an OTM under these conditions.

Oxidative dehydrogenation of ethane has been studied at 850 °C on a CMR based on mixed ionic–electronic conducting membranes made of BSCF. The porosity and thickness of the catalytic layer was studied. The use of a disk-shaped membrane in the reactor avoided the direct contact of molecular O_2 and hydrocarbons, and consequently, a high C_2H_4 yield of ca. 81% was reached. Such high ethylene yields were obtained when using a membrane catalytic coating based on BSCF, including macropores produced by the inclusion of a graphite pore former in the screen-printing ink. Furthermore, high productivity values were achieved when high C_2H_6 concentrations (up to 85 % in Ar) in the sweep stream were employed. These interesting results can be ascribed to a combination of 1) high activity due to high temperature and active O_2 species diffusing through the membrane; 2) the possibility of controlling the supply of O_2 and a low concentration of molecules in the gas phase; and 3) suitable fluid dynamics, which permitted proper feed contact with the membrane and the fast removal of C_2H_4 formed.

Finally, a study focused on capillary BSCF membranes with tubular geometry was conducted. An oxygen permeation study varying temperature, pO_2 in feed stream and sweep flow rate evidenced the big potential of the achievable oxygen fluxes in BSCF capillaries. More than 30 $ml \cdot min^{-1}$ O_2 were produced with a single BSCF capillary (0.35 mm wall thickness) with a length of only 3 cm when feeding with 1 bar O_2. This permeation value is achieved at 900 ºC, but even at only 550 ºC oxygen fluxes of ca. 2 $ml \cdot min^{-1}$ were obtained with a pure O_2 feeding. The separation degree of the O_2 contained in the feed stream was also determined. At 900 ºC, and under an Air/Argon gradient it was possible to extract nearly a 30% of the O_2 contained in the feed, thus showing the big potential of this kind of geometries for its consideration in the construction of OTM modules for the supply of O_2. Furthermore, Oxidative Coupling of Methane was carried out on a CMR consisting of a BSCF capillary activated with a packed bed containing a Mn-Na_2WO_4/SiO_2 catalyst. A broad study for determining the best conditions for C_2 production was performed at 900 ºC. GHSV, pO_2 in feed and CH_4 content were varied, obtaining a Y_{C2} of 13.5% at 2,353 $ml \cdot h^{-1} \cdot g^{-1}$ with a CH_4 conversion of 60% when using a reactant stream consisting of 10% CH_4 in Argon. Furthermore, a parametric study varying GHSV and pO_2 in feed stream was conducted. This was done with the aim of determining the optimal conditions for performing OCM reactions on the considered system. From the obtained results it was observed that the best conditions for reaching higher C_2 yields are met for an oxygen supply of ca. 2 $ml \cdot min^{-1} \cdot cm^{-2}$ at low space velocities (2,353 $ml \cdot h^{-1} \cdot g^{-1}$). Nevertheless, other parameters such as C_2 selectivity presented a maximum (ca. 26.5%) when dosing higher $J(O_2)$ of 2.7 $ml \cdot min^{-1} \cdot cm^{-2}$ at gas space velocities of 4,706 $ml \cdot h^{-1} \cdot g^{-1}$. The conduction of these experiments has been performed as a proof-of-concept, hence several aspects regarding the design of the experimental set-up should be improved. Despite the acceptable results, higher S_{C2} and Y_{C2} would be expected. From the observation of the system, this lower performance could be related with the concept used for the catalytic activation (i.e. catalytic packed bed). Since OCM reaction is expected to occur near membrane surface (where O^{2-} is provided), the catalyst particles relatively “far” from the membrane surface would be working in an inefficient manner, as well as molecular O_2 mainly present in this far region will react mainly with CH_4 to form CO_x, thus lowering reaction performance. Therefore, other alternatives for membrane catalytic activation such as porous catalytic layer deposition by dip coating can be considered for further investigation on this topic, as well as some changes in the reactor design for minimizing the regions where O_2 can present a predominant presence yielding to complete CH_4 oxidation towards CO_x. In spite of this, it has been demonstrated the big potential of CMRs based on BSCF capillaries for the conduction of OCM, mainly due to an important feature such as the possibility of dosing O_2 feed to the reaction in a controlled manner.

3.5. References.

[1] Z. Shao, W. Yang, Y. Cong, H. Dong, J. Tong, G. Xiong, Investigation of the permeation behavior and stability of a $Ba_{0.5}Sr_{0.5}Co_{0.8}Fe_{0.2}O_{3-\delta}$ oxygen membrane, Journal of Membrane Science, 172 (2000) 177-188.

[2] S. Baumann, J.M. Serra, M.P. Lobera, S. Escolastico, F. Schulze-Kueppers, W.A. Meulenberg, Ultrahigh oxygen permeation flux through supported Ba0.5Sr0.5Co0.8Fe0.2O3-delta membranes, Journal of Membrane Science, 377 (2011) 198-205.

[3] W.K. Hong, G.M. Choi, Oxygen permeation of BSCF membrane with varying thickness and surface coating, Journal of Membrane Science, 346 (2010) 353-360.

[4] A. Ghadimi, M.A. Alaee, A. Behrouzifar, A.A. Asadi, T. Mohammadi, Oxygen permeation of $Ba_xSr_{1-x}Co_{0.8}Fe_{0.2}O_{3-\delta}$ perovskite-type membrane: Experimental and modeling, Desalination, 270 (2011) 64-75.

[5] A. Behrouzifar, A.A. Asadi, T. Mohammadi, A. Pak, Experimental investigation and mathematical modeling of oxygen permeation through dense Ba0.5Sr0.5Co0.8Fe0.2O3-delta (BSCF) perovskite-type ceramic membranes, Ceramics International, 38 (2012) 4797-4811.

[6] F. Schulze-Kuppers, S. Baumann, W.A. Meulenberg, D. Stover, H.P. Buchkremer, Manufacturing and performance of advanced supported Ba0.5Sr0.5Co0.8Fe0.2O3-delta (BSCF) oxygen transport membranes, Journal of Membrane Science, 433 (2013) 121-125.

[7] P. Niehoff, S. Baumann, F. Schulze-Kuppers, R.S. Bradley, I. Shapiro, W.A. Meulenberg, P.J. Withers, R. Vassen, Oxygen transport through supported Ba0.5Sr0.5Co0.8Fe0.2O3-delta membranes, Separation and Purification Technology, 121 (2014) 60-67.

[8] Q.Y. Jiang, K.J. Nordheden, S.M. Stagg-Williams, Oxygen permeation study and improvement of $Ba_{0.5}Sr_{0.5}Co_{0.8}Fe_{0.2}O_x$ perovskite ceramic membranes, Journal of Membrane Science, 369 (2011) 174-181.

[9] A.V. Kovalevsky, A.A. Yaremchenko, V.A. Kolotygin, A.L. Shaula, V.V. Kharton, F.M.M. Snijkers, A. Buekenhoudt, J.R. Frade, E.N. Naumovich, Processing and oxygen permeation studies of asymmetric multilayer Ba0.5Sr0.5Co0.8Fe0.2O3-delta membranes, Journal of Membrane Science, 380 (2011) 68-80.

[10] A.J.B. H.J.M Bouwmeester, Chapter 14: Dense ceramic membranes for oxygen separation, in: P.J.G.a.H.J.M. Bouwmeester (Ed.) CRC Handbook of Solid State Electrochemistry, CRC Press, Boca Raton, 1997.

[11] J.H. Park, E. Magnone, J.P. Kim, S.H. Choi, Oxygen permeation performance of Ba0.5Sr0.5Co0.8Fe0.2O3-delta membrane after surface modification, Korean J. Chem. Eng., 29 (2012) 235-242.

[12] H. Wang, Y. Cong, W. Yang, Oxidative coupling of methane in $Ba_{0.5}Sr_{0.5}Co_{0.8}Fe_{0.2}O_{3-\delta}$ tubular membrane reactors, Catalysis Today, 104 (2005) 160-167.

[13] M.P. Lobera, M. Balaguer, J. Garcia-Fayos, J.M. Serra, Rare Earth-doped Ceria Catalysts for ODHE Reaction in a Catalytic Modified MIEC Membrane Reactor, Chemcatchem, 4 (2012) 2102-2111.

[14] E.M. Pfaff, A. Kaletsch, C. Broeckmann, Design of a Mixed Ionic/Electronic Conducting Oxygen Transport Membrane Pilot Module, Chemical Engineering & Technology, 35 (2012) 455-463.

[15] J.C.D. da Costa, S. Smart, J. Motuzas, S. Liu, D. Zhang, State of Art (SOTA) Report on Dense Ceramic Membranes for Oxygen Separation from Air, Australian National Low Emissions Coal Research & Development (ANLEC R&D), Brisbane, 2013.

[16] D.D. Athayde, D.F. Souza, A.M.A. Silva, D. Vasconcelos, E.H.M. Nunes, J.C. Diniz da Costa, W.L. Vasconcelos, Review of perovskite ceramic synthesis and membrane preparation methods, Ceramics International, 42 (2016) 6555-6571.

[17] A.L.L. Repasky J.M., Stein V.E., Armstrong P.A., Foster E.P., ITM Oxygen technology: scale-up toward clean energy applications, International Pittsburgh Coal Conference 2012, 2012.

[18] C.F. Miller, J. Chen, M.F. Carolan, E.P. Foster, Advances in ion transport membrane technology for Syngas production, Catalysis Today, 228 (2014) 152-157.

[19] J. Sunarso, S. Baumann, J.M. Serra, W.A. Meulenberg, S. Liu, Y.S. Lin, J.C.D. da Costa, Mixed ionic-electronic conducting (MIEC) ceramic-based membranes for oxygen separation, Journal of Membrane Science, 320 (2008) 13-41.

[20] P.F. Haworth, S. Smart, J.M. Serra, J.C. Diniz da Costa, Combined investigation of bulk diffusion and surface exchange parameters of silver catalyst coated yttrium-doped BSCF membranes, Physical Chemistry Chemical Physics, 14 (2012) 9104-9111.

[21] C. Yacou, J. Sunarso, C.X.C. Lin, S. Smart, S. Liu, J.C. Diniz da Costa, Palladium surface modified La0.6Sr0.4Co0.2Fe0.8O3−δ hollow fibres for oxygen separation, Journal of Membrane Science, 380 (2011) 223-231.

[22] A. Leo, S. Liu, J.C. Diniz da Costa, The enhancement of oxygen flux on Ba0.5Sr0.5Co0.8Fe0.2O3−δ (BSCF) hollow fibers using silver surface modification, Journal of Membrane Science, 340 (2009) 148-153.

[23] A. Egger, W. Sitte, Enhanced oxygen surface exchange of La2NiO4+delta by means of a thin surface layer of silver, Solid State Ionics, 258 (2014) 30-37.

[24] M.M. Bhasin, Is True Ethane Oxydehydrogenation Feasible?, Topics in Catalysis, 23 (2003) 145-149.

[25] H. Zimmermann, R. Walzl, Ethylene, Ullmann's Encyclopedia of Industrial Chemistry, Wiley-VCH Verlag GmbH & Co. KGaA2000.

[26] M.M. Bhasin, J.H. McCain, B.V. Vora, T. Imai, P.R. Pujadó, Dehydrogenation and oxydehydrogenation of paraffins to olefins, Applied Catalysis A: General, 221 (2001) 397-419.

[27] T. Blasco, J.M.L. Nieto, Oxidative dyhydrogenation of short chain alkanes on supported vanadium oxide catalysts, Applied Catalysis A: General, 157 (1997) 117-142.

[28] F. Cavani, N. Ballarini, A. Cericola, Oxidative dehydrogenation of ethane and propane: How far from commercial implementation?, Catalysis Today, 127 (2007) 113-131.

[29] R.K. Grasselli, Advances and future trends in selective oxidation and ammoxidation catalysis, Catalysis Today, 49 (1999) 141-153.

[30] W. Yang, H. Wang, X. Zhu, L. Lin, Development and Application of Oxygen Permeable Membrane in Selective Oxidation of Light Alkanes, Topics in Catalysis, 35 (2005) 155-167.

[31] F.T. Akin, Y.S. Lin, Selective oxidation of ethane to ethylene in a dense tubular membrane reactor, Journal of Membrane Science, 209 (2002) 457-467.

[32] H.J.M. Bouwmeester, Dense ceramic membranes for methane conversion, Catalysis Today, 82 (2003) 141-150.

[33] C.M. Chen, D.L. Bennett, M.F. Carolan, E.P. Foster, W.L. Schinski, D.M. Taylor, ITM Syngas ceramic membrane technology for synthesis gas production, in: B. Xinhe, X. Yide (Eds.) Studies in Surface Science and Catalysis, Elsevier2004, pp. 55-60.

[34] J.-A. Dalmon, A. Cruz-López, D. Farrusseng, N. Guilhaume, E. Iojoiu, J.-C. Jalibert, S. Miachon, C. Mirodatos, A. Pantazidis, M. Rebeilleau-Dassonneville, Y. Schuurman, A.C. van Veen, Oxidation in catalytic membrane reactors, Applied Catalysis A: General, 325 (2007) 198-204.

[35] M. Pilar Lobera, S. Escolastico, J.M. Serra, High Ethylene Production through Oxidative Dehydrogenation of Ethane Membrane Reactors Based on Fast Oxygen-Ion Conductors, Chemcatchem, 3 (2011) 1503-1508.

[36] A. Machocki, A. Denis, Simultaneous oxidative coupling of methane and oxidative dehydrogenation of ethane on the Na+/CaO catalyst, Chemical Engineering Journal, 90 (2002) 165-172.

[37] M. Rebeilleau-Dassonneville, S. Rosini, A.C. van Veen, D. Farrusseng, C. Mirodatos, Oxidative activation of ethane on catalytic modified dense ionic oxygen conducting membranes, Catalysis Today, 104 (2005) 131-137.

[38] Z. Shao, H. Dong, G. Xiong, Y. Cong, W. Yang, Performance of a mixed-conducting ceramic membrane reactor with high oxygen permeability for methane conversion, Journal of Membrane Science, 183 (2001) 181-192.

[39] H. Wang, C. Tablet, T. Schiestel, J. Caro, Hollow fiber membrane reactors for the oxidative activation of ethane, Catalysis Today, 118 (2006) 98-103.

[40] H.H. Wang, Y. Cong, W.S. Yang, Continuous oxygen ion transfer medium as a catalyst for high selective oxidative dehydrogenation of ethane, Catalysis Letters, 84 (2002) 101-106.

[41] J.M. Serra, V.B. Vert, M. Betz, V.A.C. Haanappel, W.A. Meulenberg, F. Tietz, Screening of A-Substitution in the System A0.68Sr0.3Fe0.8Co0.2O3 − δ for SOFC Cathodes, Journal of The Electrochemical Society, 155 (2008) B207-B214.

[42] O. Czuprat, S. Werth, S. Schirrmeister, T. Schiestel, J. Caro, Olefin Production by a Multistep Oxidative Dehydrogenation in a Perovskite Hollow-Fiber Membrane Reactor, ChemCatChem, 1 (2009) 401-405.

[43] J. Yi, M. Schroeder, High temperature degradation of Ba0.5Sr0.5Co0.8Fe0.2O3-delta membranes in atmospheres containing concentrated carbon dioxide, Journal of Membrane Science, 378 (2011) 163-170.

[44] M. Salehi, E.M. Pfaff, A. Kaletsch, T. Graule, F. Clemens, B. Grobéty, Manufacturing of Tubular Dead-End Membranes by Continuous Thermoplastic Extrusion, International Journal of Applied Ceramic Technology, 12 (2015) E13-E18.

[45] M.B. Choi, D.K. Lim, S.Y. Jeon, H.S. Kim, S.J. Song, Oxygen permeation properties of BSCF5582 tubular membrane fabricated by the slip casting method, Ceramics International, 38 (2012) 1867-1872.

[46] Y.W. Zhang, F.L. Zeng, C.C. Yu, C.Z. Wu, W.Z. Ding, X.G. Lu, Fabrication and characterization of dense BaCo0.7Fe0.2Nb0.1O3-delta tubular membrane by slip casting techniques, Ceramics International, 41 (2015) 1401-1411.

[47] H. Wang, C. Tablet, T. Schiestel, J. Caro, Hollow fiber membrane reactors for the oxidative activation of ethane, Catalysis Today, 118 (2006) 98-103.

[48] M. Schulz, U. Pippardt, L. Kiesel, K. Ritter, R. Kriegel, Oxygen permeation of various archetypes of oxygen membranes based on BSCF, AIChE Journal, 58 (2012) 3195-3202.

[49] K.M. Erskine, A.M. Meier, S.M. Pilgrim, Brazing perovskite ceramics with silver/copper oxide braze alloys, Journal of Materials Science, 37 (2002) 1705-1709.

[50] B.L. Farrell, V.O. Igenegbai, S. Linic, A Viewpoint on Direct Methane Conversion to Ethane and Ethylene Using Oxidative Coupling on Solid Catalysts, ACS Catalysis, 6 (2016) 4340-4346.

[51] Z. Stansch, L. Mleczko, M. Baerns, Comprehensive Kinetics of Oxidative Coupling of Methane over the La2O3/CaO Catalyst, Industrial & Engineering Chemistry Research, 36 (1997) 2568-2579.

[52] F.T. Akin, Y.S. Lin, Oxidative coupling of methane in dense ceramic membrane reactor with high yields, AIChE Journal, 48 (2002) 2298-2306.

[53] L. Olivier, S. Haag, C. Mirodatos, A.C. van Veen, Oxidative coupling of methane using catalyst modified dense perovskite membrane reactors, Catalysis Today, 142 (2009) 34-41.

[54] X. Tan, K. Li, Oxidative Coupling of Methane in a Perovskite Hollow-Fiber Membrane Reactor, Industrial & Engineering Chemistry Research, 45 (2006) 142-149.

[55] X. Tan, Z. Pang, Z. Gu, S. Liu, Catalytic perovskite hollow fibre membrane reactors for methane oxidative coupling, Journal of Membrane Science, 302 (2007) 109-114.

[56] N.H. Othman, Z. Wu, K. Li, An oxygen permeable membrane microreactor with an in-situ deposited Bi1.5Y0.3Sm0.2O3−δ catalyst for oxidative coupling of methane, Journal of Membrane Science, 488 (2015) 182-193.

[57] O. Czuprat, T. Schiestel, H. Voss, J. Caro, Oxidative Coupling of Methane in a BCFZ Perovskite Hollow Fiber Membrane Reactor, Industrial & Engineering Chemistry Research, 49 (2010) 10230-10236.

[58] S. Bhatia, C.Y. Thien, A.R. Mohamed, Oxidative coupling of methane (OCM) in a catalytic membrane reactor and comparison of its performance with other catalytic reactors, Chemical Engineering Journal, 148 (2009) 525-532.

[59] S.-B. Li, Oxidative Coupling of Methane over W-Mn/SiO2 Catalyst, Chinese Journal of Chemistry, 19 (2001) 16-21.

[60] S. Jašo, S. Sadjadi, H.R. Godini, U. Simon, S. Arndt, O. Görke, A. Berthold, H. Arellano-Garcia, H. Schubert, R. Schomäcker, G. Wozny, Experimental investigation of fluidized-bed reactor performance for oxidative coupling of methane, Journal of Natural Gas Chemistry, 21 (2012) 534-543.

[61] H.R. Godini, A. Gili, O. Görke, U. Simon, K. Hou, G. Wozny, Performance Analysis of a Porous Packed Bed Membrane Reactor for Oxidative Coupling of Methane: Structural and Operational Characteristics, Energy & Fuels, 28 (2014) 877-890.

[62] C.B. Alcock, J.J. Carberry, R. Doshi, N. Gunasekaran, Methane Coupling Reaction on Oxide Solid Solution Catalysts, Journal of Catalysis, 143 (1993) 533-538.

[63] K. Omata, O. Yamazaki, K. Tomita, K. Fujimoto, Oxidative coupling of methane on an ABO3 type oxide with mixed conductivity, Journal of the Chemical Society, Chemical Communications, (1994) 1647-1648.

[64] Y. Zeng, Y.S. Lin, Oxygen permeation and oxidative coupling of methane in yttria doped bismuth oxide membrane reactor, Journal of Catalysis, 193 (2000) 58-64.

4. PERMEATION STUDIES ON LSCF MEMBRANES

4. Permeation studies on LSCF membranes

4.1. Introduction.

Amongst perovskite type materials, $La_{1-x}Sr_xCo_{1-y}Fe_yO_{3-\delta}$ (LSCF) has received great interest due to their high *J(O₂)* and excellent stabilities, especially in CO_2-containing environments [1-8]. Moreover, in the last years, MIEC membranes are focusing a growing interest for their implementation in oxyfuel-based power plants [9-14]. As it has been previously indicated in Chapter 1, oxygen permeation depends on several factors like material composition [15], powder preparation method [16], sintering temperature [17, 18], membrane shape [19] and thickness. Regarding to the thickness, different models of ionic transport in the oxide based on Wagner equation show that the flux is proportional to the inverse of the membrane thickness and several investigations have found that reducing membrane thickness results in higher oxygen fluxes [1, 8, 20-24] up to a limit, when other mass transport or surface kinetic phenomena start controlling the permeation process. Therefore, there is a growing interest in the development of supported membranes, since for practical application high $J(O_2)$ are a must. For achieving sufficiently high fluxes membrane thickness should be in the range of several microns (10-50 μm). As a consequence of such a thin structures, the thin membranes must be supported on porous substrates in order to warranty the mechanical stability and integrity, particularly in the case of planar membranes [11, 25-30].

Thin and ultra-thin MIEC layers are deposited over porous supports, preferably consisting of the same material, thus avoiding thermal expansion incompatibilities that would lead to membrane cracking. In this case an additional function of the porous MIEC support structure is enlarging the surface area of the membrane and then serving as a coarse activation to facilitate oxygen exchange reactions.

This chapter is focused on the preparation and characterization of asymmetric LSCF membranes deposited on porous LSCF supports. Two techniques such as tape casting and freeze casting have been considered for manufacturing thin supported LSCF membranes. Further, a systematic study of the membrane operation variables has been carried out: temperature; sweep gas flow; oxygen partial pressure in feed; and CO_2 content in sweep stream. Finally, the influence of these variables on the oxygen flux has been determined. Furthermore, the effect of the application of an activation layer on the membrane surface (permeate side) has been investigated.

4.2. Tape-cast supported LSCF membranes[7].

4.2.1. Characterization of the membrane assembly microstructure.

The asymmetric all-LSCF membranes used in the conduction of this study were supplied by Forschungszentrum Jülich. Membranes were manufactured by inverse tape casting technique as described in [31]. After sintering at 1200 °C for 5 h, a homogeneous membrane layer thickness of 30 µm and a support thickness of 630 µm were achieved, as shown in Figure 4.55a and b. The porosity remaining after sintering for the membrane layer is 4% while the pores are closed. The support layer has a porosity of 39% while the support porosity is open and very well connected, whereby a percolating network for gas exchange between the membrane surface and feed gas compartment is formed, as confirmed by gas permeability measurements. The gas tightness of the bare membranes was confirmed by measuring the He leak, revealing values of 5-$6 \cdot 10^{-5}$ mbar·l·cm^{-2}·s^{-1}. Figure 4.55c presents the membrane with an activation layer composed of porous LSCF. This catalytic layer was deposited by screen-printing technique, as described in chapter 2.2.4. The screen printing ink consisted of LSCF powder prepared by the Pechini method and subsequently sintered at 1000 ºC, moreover graphite (Aldrich) was used as pore former in the ink. The printed layer was sintered at 1060 ºC, thus obtaining a catalytic layer with an open microstructure and a homogeneous thickness of about 20 µm. Furthermore, the porous layer proved to be stable during the whole high-temperature oxygen permeation measurement.

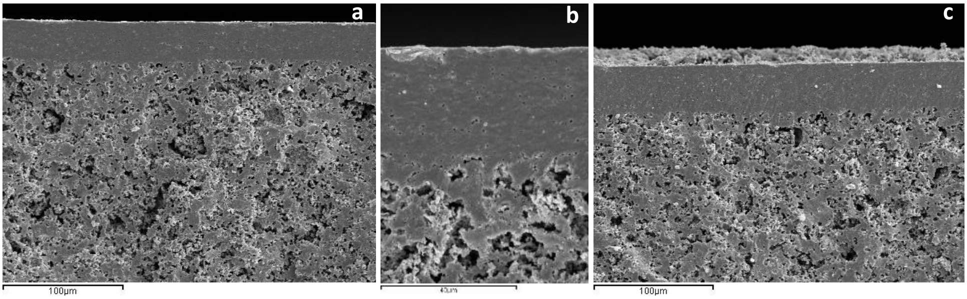

Figure 4.55: Fracture cross sections (SEM images) of the two membranes before oxygen permeation measurement: (a and b) bare, (c) with porous activation layer.

4.2.2. Effect of sweep gas flux on the oxygen permeation.

Figure 4.56 presents the oxygen permeation flux obtained for asymmetric LSCF membrane as a function of temperature (1000 - 750 ºC) and the sweep gas flow rate (300 – 750 ml·min^{-1}). The oxygen fluxes achieved in this temperature range are around 5-10 times higher than the fluxes obtained for monolithic membranes (0.8 mm) [32]. However, a higher improvement (20-fold) was expected by just

---

[7] The study here presented has been published in the Journal of Membrane Science under the title "Oxygen permeation through tape-cast asymmetric all-$La_{0.6}Sr_{0.4}Co_{0.2}Fe_{0.8}O_{3-\delta}$ membranes". http://doi.org/10.1016/j.memsci.2013.07.030

considering the effect of thickness reduction on the bulk transport, as postulated by Wagner's equation (Equation 1.5).

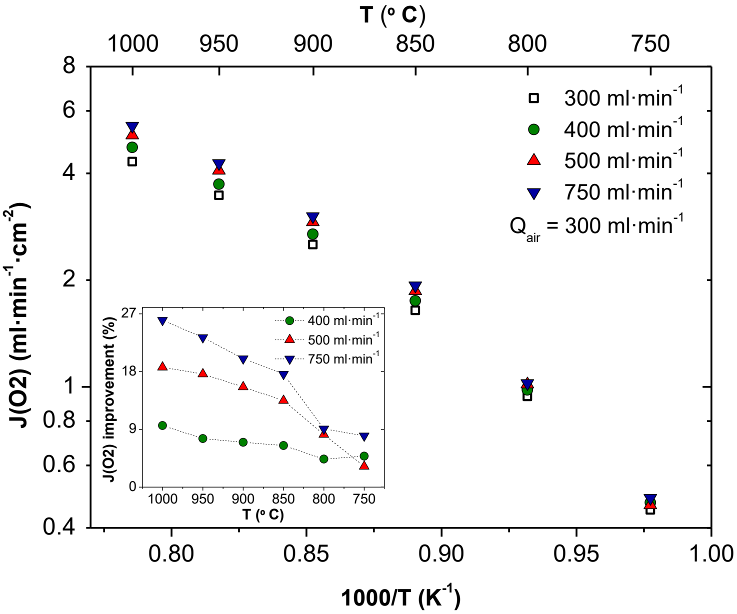

Figure 4.56: Variation of oxygen flux as a function of temperature and sweep gas flow rate. The feed consisted of synthetic air. (Inset: relative oxygen flux improvement in % with respect to Q_{Ar} = 300 ml·min^{-1}).

The oxygen flux is strongly influenced by the magnitude of the applied sweep gas flow rate and this effect is ascribed principally to two coupled effects: (i) the improvement of the fluid dynamics in the permeate chamber, which allows reducing concentration polarization resistance and therefore decreasing substantially the local pO_2 at the membrane surface; and (ii) the increase in the driving force, caused by the higher dilution of the permeated oxygen, which is particularly important for the used planar geometry and the specific setup geometry [33]. Oxygen flux rises from 4.32 to 5.44 ml·min^{-1}·cm^{-2} when the sweep flow rate is increased from 300 to 750 ml·min^{-1} at 1000 ºC. This improvement is more important at high temperatures when the permeation fluxes are higher and therefore the oxygen gas diffusion in the permeate chamber becomes more critical [28]. Accordingly, when using 750 ml·min^{-1} argon as sweep, $J(O_2)$ is improved up to 26% at 1000ºC with respect to the values measured at 300 ml·min^{-1} argon, whilst the relative improvement decreases down to 8% at 750 ºC. A less important improvement in the flux is reached when using 400 ml·min^{-1} argon, for this case $J(O_2)$ improves 9.6% at 1000ºC, going down to 4.8% at 750 ºC. Summing up, the overall oxygen permeation is strongly improved by increasing the sweep gas flow rate and temperature.

Table 4.9: Apparent activation energy (E_a) (kJ·mol^{-1}) derived from J(O_2) measurements for different sweep gas flow rates and pO_2 in feed stream (Q_{feed} = 300 ml·min^{-1})

Membrane Type	Q_{Ar} (ml·min^{-1})	E_a (High T)	Ea (Low T)	Ea (High T)	Ea (Low T)
		pO_2 = 0.21 atm		pO_2 = 1 atm	
asymmetric	300	72	123	119	146
asymmetric	400	77	123	--	--
asymmetric	500	78	131	121	149
asymmetric	750	80	131	122	152
monolithic	300	89	119	--	--

Regarding the thermal activation of the permeation process under the applied operating conditions, a two-fold Arrhenius behavior is observed, distinguishing two regions in the plot (Figure 4.56): one in the range 1000-850ºC and other in the range 850-750ºC. Table 4.9 summarizes the E_a values calculated for the different argon flow rates. As a reference, the E_a corresponding to the oxygen permeation through a monolithic 800 µm-thick membrane is added in Table 4.9. As inferred from the asymmetric membrane data, increasing sweep flow rate gives rise to slightly higher apparent activation energies (E_a) at both temperature regions, tough the effect on E_a is lower with regard to the effect observed on oxygen flux magnitude. The nature of processes limiting the oxygen permeation rate at these temperatures (1000-750ºC) does not seem to be significantly influenced by sweep gas flow rate, since no important variation in E_a is observed. A plausible explanation is to consider that, in this temperature range (≥750 ºC), oxygen permeation is mainly limited by oxygen ions diffusing through the perovskite bulk and grain boundary, and gas transport in the porous substrate (air membrane side). Indeed, the rise in the sweep gas flow rate (> 300 ml(STP)·min^{-1}) does not affect ionic transport mechanism, while the observed permeation improvement is due to the reduction in pO_2 on the permeate side. This explanation is supported by the similar E_a magnitude observed for the permeation through the asymmetric and the monolithic membrane. The obtained activation energies are in agreement with E_a literature values for the case of monolithic LSCF membranes, presenting values in the range of 103-140 kJ·mol^{-1} at 900-700ºC [4].

Figure 4.57 presents the oxygen permeation results in an Arrhenius arrangement when pure oxygen was used as feed gas instead of air and the sweep gas flow rate was varied. As for the case when air was fed, the rise in the sweep gas flow rate induces a substantial improvement in the permeation flux, specifically at 1000ºC oxygen flux increases from 11.88 to 13.22 ml·min^{-1}·cm^{-2} when the sweep flow rate is varied in the range 300-750 ml·min^{-1}. Additionally, this effect on the flux is less pronounced with decreasing temperatures, e.g. a relative improvement of around 3% is observed at 750 ºC (see Figure 4.57 Inset).

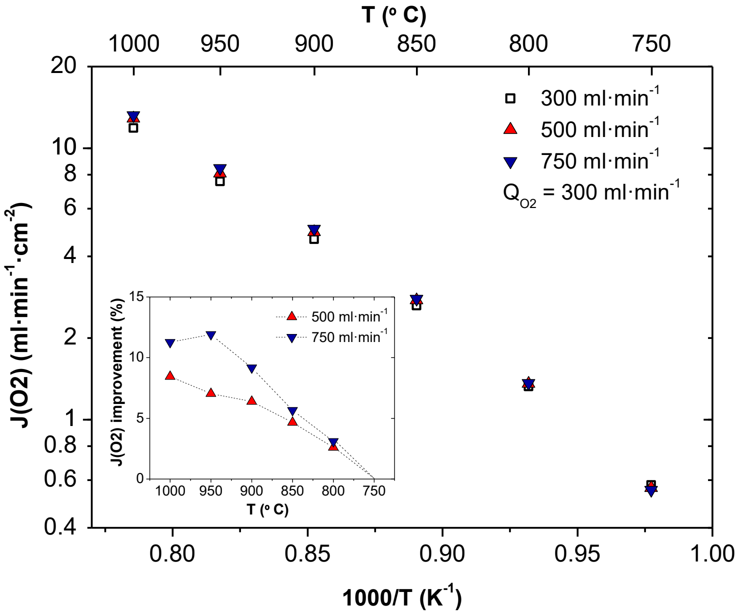

Figure 4.57: Variation of oxygen flux as a function of temperature and sweep gas flow rate. The feed consisted of pure oxygen. (Inset: relative oxygen flux improvement in % with respect to Q_{Ar} = 300 ml·min^{-1}).

4.2.3. Effect of oxygen partial pressure in feed on the oxygen permeation.

Further analysis of Figure 4.57 reveals that the use of pure oxygen as feed on the porous side of the membrane has a tremendous effect on the permeation flux magnitude and this is again ascribed to two coupled effects: (i) the higher imposed driving force (pO_2 gradient) across the membrane; and (ii) the strongly improvement of gaseous diffusion of molecular oxygen through the support pore systems by neglecting the presence of N_2 in the gas feed. In order to shed further light on the limiting steps related to the porous substrate, a series of new experiments were carried out. Specifically, the pO_2 and the type of inert gas (N_2 or He) diluting oxygen in the feed stream were varied (Figure 4.58), while, sweep and feed gas flow rates were maintained at 300 ml·min^{-1}. pO_2 variation was done by using a mixture of helium and oxygen in the following range: 0.21, 0.5 and 0.75 atm. Moreover, the temperature range was broadened (1000-600 ºC) in this study.

With regard to the nature of the diluting gas, using helium instead of nitrogen allows improving the permeation flux in whole temperature range (Figure 4.58). This effect is particularly important at the highest and lowest temperatures. The improvement is attributed to the faster diffusion of oxygen in helium in the porous substrate, which in turn increases the overall oxygen concentration on the membrane surface, and stems from the higher gas diffusivity (and Knudsen transport) and the lower gas viscosity of the feed. In the temperature range (1000-750 ºC), the better gaseous diffusion makes it possible to increase the pO_2 at the membrane surface and, assuming that the permeation is limited by the ambipolar *bulk* diffusion, the flux is increased due to higher driving force. On the other hand, a distinct mechanism is expected in the low temperature range. Specifically, gas surface exchange is typically the limiting step for supported thin-films made of fast mixed conductors [34] and this situation is again suggested for the present membrane, as it will be experimentally supported in the next section (4.3.4). In this case, the rise in the local pO_2 on the membrane surface (and attached porous LSCF structure) may have a direct effect on the (rate limiting) exchange kinetics, typically following a $pO_2^{0.5}$ dependency [35].

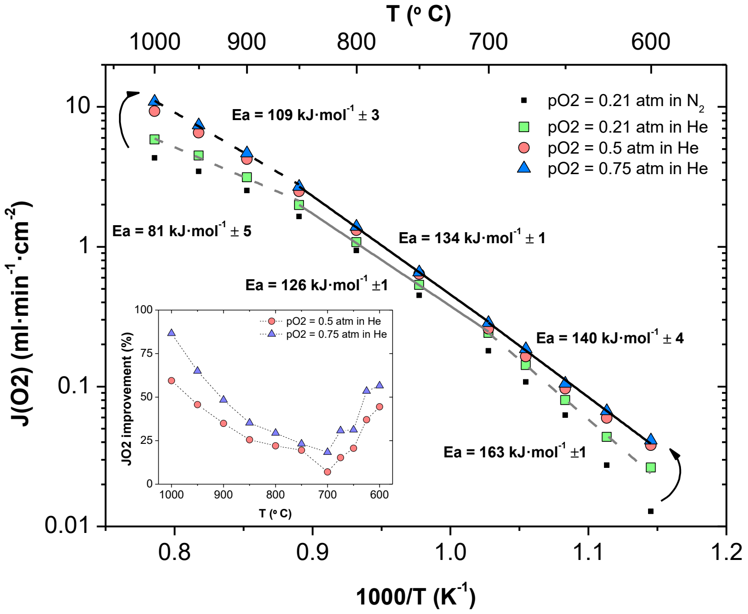

Figure 4.58: Oxygen permeation flux as a function of temperature and feed stream composition. (Q_{sweep} = 300 ml·min^{-1} Argon). Inset: Relative improvement (with respect to pO_2 = 0.21 atm in He results) of the oxygen flux as a function of temperature and pO_2 in the feed (Q_{sweep} = 300 ml·min^{-1} Argon).

Regarding the effect of pO_2 in the feed inlet, the pO_2 increase leads to higher oxygen fluxes. At 1000 ºC the following fluxes are obtained for the diverse pO_2 considered (0.21, 0.5, 0.75 and 1 atm): 5.85, 9.33, 10.92 and 11.87 ml·min^{-1}·cm^{-2}, respectively. The highest improvement in flux is observed when pO_2 is increased from 0.21 to 0.5 atm (+3.48 ml·min^{-1}·cm^{-2}) while the other consecutive pO_2 steps yield lower differences (+1.59 and +0.95 ml·min^{-1}·cm^{-2}, respectively). These asymptotic effect may be related to the fact that at pO_2=0.5 atm, the concentration polarization in the porous media is strongly alleviated and the use of higher pO_2 (above 0.5 atm) has principally an effect on the driving force and in a less extent on the accumulation of inert gas molecules.

The thermal evolution of flux (Figure 4.58) reveals a three-fold Arrhenius behavior for the measurement at pO_2=0.21 atm for this temperature range, whilst the flux presents a two-fold Arrhenius behavior for higher pO_2 in feed. The three regions observed for the three-fold system (pO_2=0.21 atm) are: high temperature (1000-850 ºC), intermediate temperature (850-700 ºC) and low temperature (700-600 ºC), and the corresponding activation energies are displayed in Table 4.10. This complex thermal behavior implies that three different processes (or a balanced mix of processes) are controlling the oxygen permeation for each given temperature range. On the other hand, when increasing pO_2 in feed, the activation energies in the medium and low temperature regions get a similar magnitude, approaching values ca. ~134 kJ·mol^{-1}.

Table 4.10: Apparent activation energy (E_a) (kJ·mol^{-1}) derived from oxygen permeation measurements using different feed gas compositions ($Q_{feed, sweep}$ = 300 ml(STP)·min^{-1})

pO_2 (atm) in feed side	**E_a (High T)**	**E_a (Intermediate T)**	**E_a (Low T)**
0.21 (in N_2)	74	128	178
0.21 (in He)	81	126	163
0.75 (in He)	109	134	140
1	118	146	144

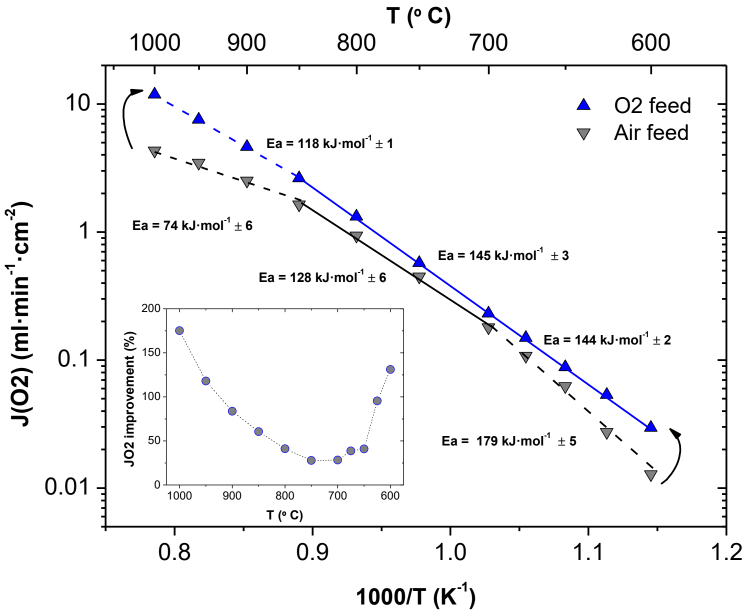

Figure 4.59: Thermal evolution of the oxygen flux in a wider temperature range (1000 - 600ºC) in air and pure oxygen. (Q_{sweep} = 300 ml·min^{-1} Argon). Inset: Relative improvement (with respect to pO_2 = 0.21 atm in N_2 results) of the oxygen flux as a function of temperature and pO_2 in the feed.(Q_{sweep} = 300 ml·min^{-1} Argon.)

In summary, the three-fold Arrhenius behavior can be associated with the following controlling processes, in agreement with the model suggested (Figure 4.60) previously for the permeation through asymmetric BSCF membranes [28]:

(1) High temperature range: bulk diffusion (R_{BULK}) through the dense film principally controls the permeation although the gas diffusion in the porous substrate ($R_{SUPPORT}$), gas transport in the permeate chamber (R_{CP2}) and surface exchange (R_{S1-2}) are also partly limiting the permeation. The magnitude of each resistance may depend on the specific operating conditions.

(2) Medium temperature range: bulk diffusion is controlling although the activation energy notably rises as a consequence of the phase transition in the perovskite structure from cubic (high temperature) to rhombohedral (lower temperatures), as inferred from XRD results in air summarized in Figure 4.61. However, the phase transition extent and temperature may depend on the specific pO_2 and this could be the reason for the progressive rise of E_a in the higher temperature range with increasing pO_2 by trend stabilizing the rhombohedral phase. In this temperature range, the magnitude of the resistances related to gaseous transport appears to be much lower than R_{BULK}.

(3) Low temperature range: the limiting step is the surface exchange reaction at both sides of the membrane (R_{S1-2}), being very positively influenced by increasing the oxygen partial pressure or by the catalytic activation (section 4.2.4).

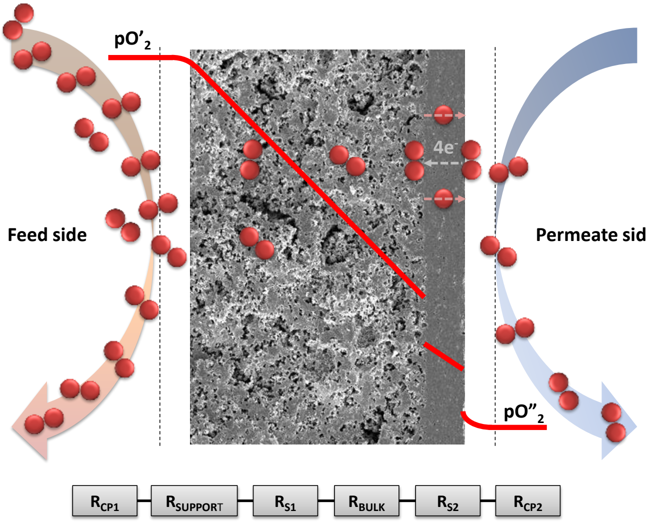

Figure 4.60: Concentration profiles across the asymmetric membrane thickness and the corresponding model resistances.

The insets in Figure 4.58 and Figure 4.59 show the relative improvement achieved by changing the feed pO_2 as a function of temperature (with respect to pO_2 = 0.21 atm in N_2 case). Oxygen flux could be improved up to ca. 180% at 1000ºC and pO_2 = 1 atm, whereas an improvement of ca. 60% was obtained at the same temperature when pO_2 in feed was 0.5 atm. The relative flux improvement decreases with temperature for all the cases down to 700ºC, when a minimum is reached; then, $J(O_2)$ improvement increases again as temperature drops. This behavior arises from the progressive changes in the controlling steps at high and intermediate (*bulk diffusion*) and low (*surface exchange kinetics*) temperatures, and the fact that these processes are strongly influenced by the pO_2 gradient across the membrane. Additionally, bulk diffusion is affected by changes in the perovskite symmetry. The minimum in $J(O_2)$ improvement is reached (700ºC) within the transition region from the bulk diffusion control to surface exchange control.

Figure 4.61 shows the evolution of the perovskite symmetry in air as a function of temperature. A phase transition is observed for LSCF at temperatures above 850 ºC [36]. The change in the crystal symmetry implies changes in ions position, and consequently affects the oxygen vacancy concentration and mobility, and ultimately the ionic conductivity. Accordingly, this change in the phase symmetry may be responsible for the change in the activation energy observed during the permeation tests.

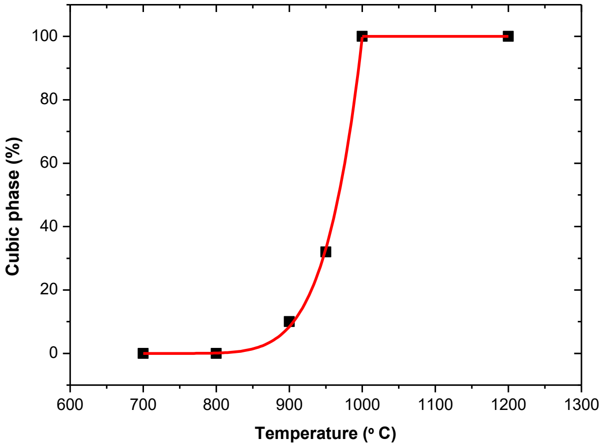

Figure 4.61: LSCF phase transition (rhombohedral ↔ cubic symmetry) as a function of temperature: Percentage of the cubic perovskite in the material as calculated from HT-XRD experiments in air. The line is a guide to the eye.

4.2.4. Effect of catalytic layer on the oxygen permeation.

A 15 µm thick catalytic layer was deposited over the dense membrane side in order to enhance oxygen permeation (Figure 4.55c). This surface modification was done via screen-printing using a pore former in the ink. The catalyst consisted of fine-grained LSCF powder. After membrane coating, the deposited catalytic layer was sintered for 2 hours at 1060ºC.

The membrane activation allows achieving higher oxygen permeation fluxes, as previously observed [8, 28, 37, 38]. This improvement is noteworthy higher at low temperatures and this fact confirms that surface exchange process is the limiting step in the permeation at temperatures below 700 ºC. Figure 4.62 shows the permeation results (in Air/Ar gradient) for the temperature range from 600 to 1000 ºC. The reached flux improvement at 600ºC is about. 300% with respect to bare membrane, whilst at 1000ºC the improvement is only 24%. This slight improvement reflects the low extent (R_{S2}) of surface exchange at high temperatures, where bulk diffusion is the major limiting step. The same behavior can be observed in Figure 4.63, which displays the evolution of oxygen permeation for the bare and activated membranes when using pure oxygen as feed. A peak oxygen flux of 13.3 ml·min^{-1}·cm^{-2} is reached at 1000ºC for the activated membrane.

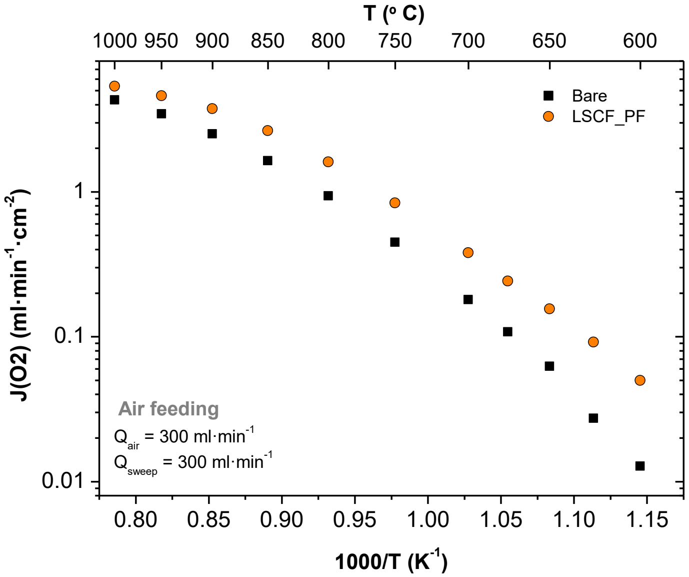

Figure 4.62: Effect of the catalytic surface activation: Thermal evolution of the permeation flux for the bare and activated membrane using air as feed and argon as sweep gas. Q_{air}*=300 ml·min*$^{-1}$*,* Q_{sweep}*=300 ml·min*$^{-1}$*. Logarithmic scale.*

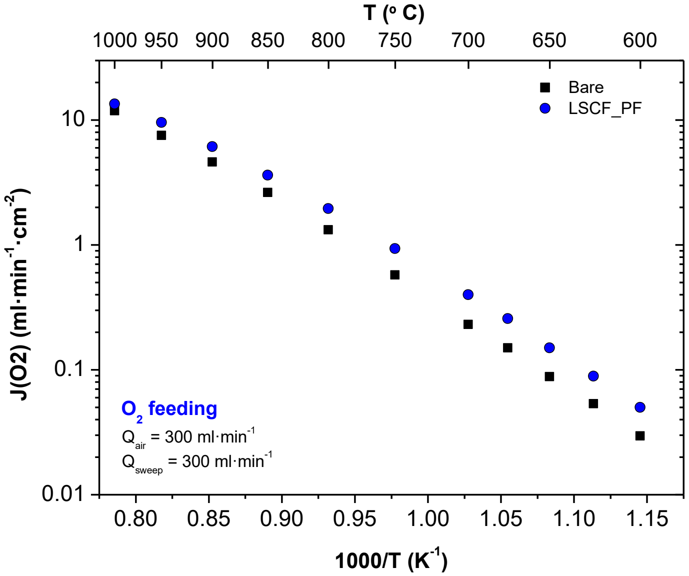

Figure 4.63: Comparison between the measured oxygen fluxes for the bare and activated membrane in dependence of temperature. Q_{O2}*=300 ml·min*$^{-1}$*,* Q_{sweep}*=300 ml·min*$^{-1}$*. Logarithmic scale.*

4.2.5. Effect of CO_2 content in sweep stream on the oxygen permeation.

Diverse tests have been carried out using different carbon dioxide concentrations in the sweep gas. This study aims to determine the effect of CO_2 in the permeation and study the membrane stability under CO_2-rich environments. The conditions were varied from a CO_2-free flow to a 100% CO_2 sweep stream at two different temperatures: 900 and 1000ºC, feeding with synthetic air (300 ml·min^{-1}) and using different mixtures Ar/CO_2 in the sweep stream (300 ml·min^{-1}).

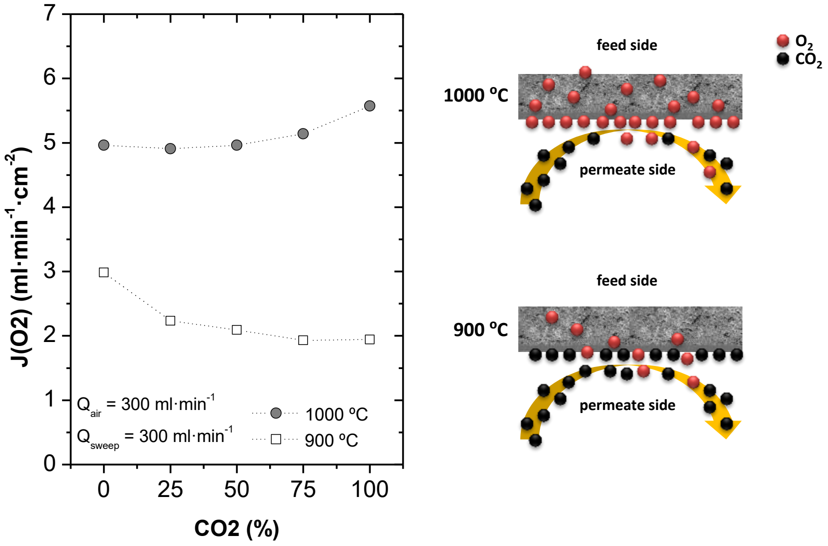

Figure 4.64: Oxygen permeation fluxes as a function of CO_2 content (in Ar) in the sweep stream.

Figure 4.64 shows the permeation results for the tested cases. At 900ºC J(O_2) decreases as carbon dioxide content is increased. A drop in *J(O_2)* (32%) is observed from 2.98 to 1.94 ml·cm^{-2}·min^{-1}, as a result of the full replacement of Ar by CO_2, although the flux does not diminishes substantially for CO_2 50%. This fall in *J(O_2)* may not be related with surface carbonation processes, since at these temperatures carbonates are not stable [39]. Moreover, TG measurements performed on Air and 5% O_2 in Air show no signs of mass gain or loss related to carbonation processes (Figure 4.65), thus LSCF can be considered as stable under the reproduced CO_2 conditions. A possible reason for explaining the *J(O_2)* decrease is the physical phenomenon of competitive adsorption of CO_2 and O_2 on actives sites of membrane surface [2, 39]. The final steps of the permeation process involve the recombination of oxygen ions to form molecular oxygen on surface active sites, the molecule desorption and then the diffusion to the sweep stream. However, when CO_2 is present in the sweep side, part of the required active sites are occupied/blocked by CO_2-species while the CO_2 coverage depends on the adsorption constant for each specific site, temperature and *p*CO_2. Competitive adsorption is usually modeled following a Langmuir adsorption model and describes the data reported in Figure 4.64 at 900 ºC. As a consequence, CO_2 adsorption results in a reduction of actives sites available for the exchange reactions, which is reflected in the drop in the permeation flux observed at 900 ºC.

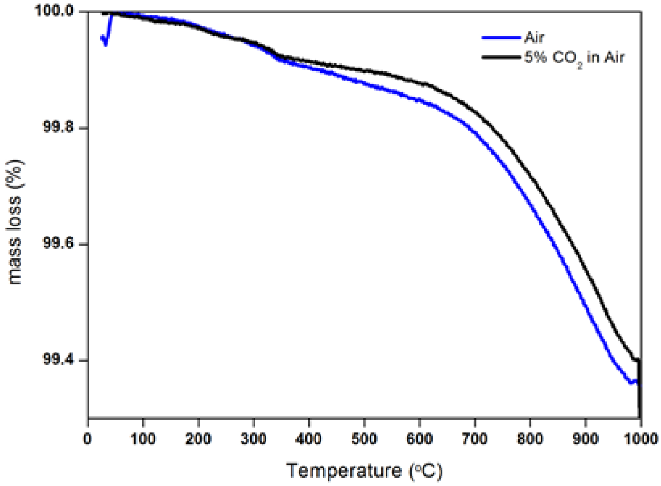

Figure 4.65: Thermogravimetric analysis of LSCF power in air and air with 5% CO_2.

The tests carried out at 1000ºC present an opposite behavior in comparison with results at 900ºC, since oxygen flux increases with carbon dioxide content. This result implies that (i) CO_2 adsorption is not limiting the number of actives sites in the exchange process, i.e. CO_2 adsorption constant strongly decreases with this temperature step changes; (ii) the positive effect of CO_2 arising from the better sweeping capacity of CO_2 with regard to Ar, which allows alleviating concentration polarization (similar effect produced by increasing the sweep gas flow rate (Figure 4.56).

The membrane remained stable under operation, including the use of CO_2 as sweep, for three weeks and the repeated thermal cycling from 1000 to 650 ºC did not cause the loss in the mechanical integrity despite the phase transition occurring at 850ºC. Moreover, the original O_2 flux obtained without CO_2 in the sweep gas was fully recovered when the membrane side was swept again using pure Ar.

4.3. Freeze-cast supported LSCF membranes[8].

4.3.1. Production of porous supports by means of freeze casting.

As indicated in the model suggested in Figure 4.60, for the case of asymmetric membranes, the characteristics of porous support play a crucial role in the permeation process. This is mainly related to the fact that a gas transport resistance (R_{SUPP}) across the porous substrate will hinder the gas diffusion to/from the membrane surface, thus limiting oxygen permeation. Therefore, production of porous supports with low gas diffusion resistance is of big interest for the improvement of the oxygen fluxes in OTMs.

Freeze-casting appears like a very interesting and innovative route for the production of supports with hierarchical porosity [40, 41]. Widely studied the last few years, mainly for bone substitution [42], it consists of freezing a liquid suspension, followed by the sublimation of the solvent under both low temperature and pressure and the final sintering of the particles for consolidation. The obtained structure is porous with oriented channels corresponding to the replica of the solvent crystals along the propagation direction of the solid-liquid interface [43]. Modifying the powder characteristics, the freezing conditions or the slurry formulation, the porosity of the sample can be tailored for the targeted requirements. The work herein presented is the first reported application of freeze casted structures for its use as porous supports for OTMs.

Porous LSCF supports were manufactured by freeze-casting technique, as explained in chapter 2.2.2. On top of freeze-casted supports, gas-tight LSCF layers were coated and subsequently sintered at 1400 ºC.

---

[8] The studies here presented have been published in the Journal of Materials Chemistry A under the title “Enhancing oxygen permeation through hierarchically-structured perovskite membranes elaborated by freeze-casting” DOI: 10.1039/C3TA14069E, and in ChemPlusChem Journal under the title “Oxygen Permeation Improvement under CO_2-Rich Environments through Catalytic Activation of Hierarchically Structured Perovskite Membranes” DOI: 10.1002/cplu.201402142.

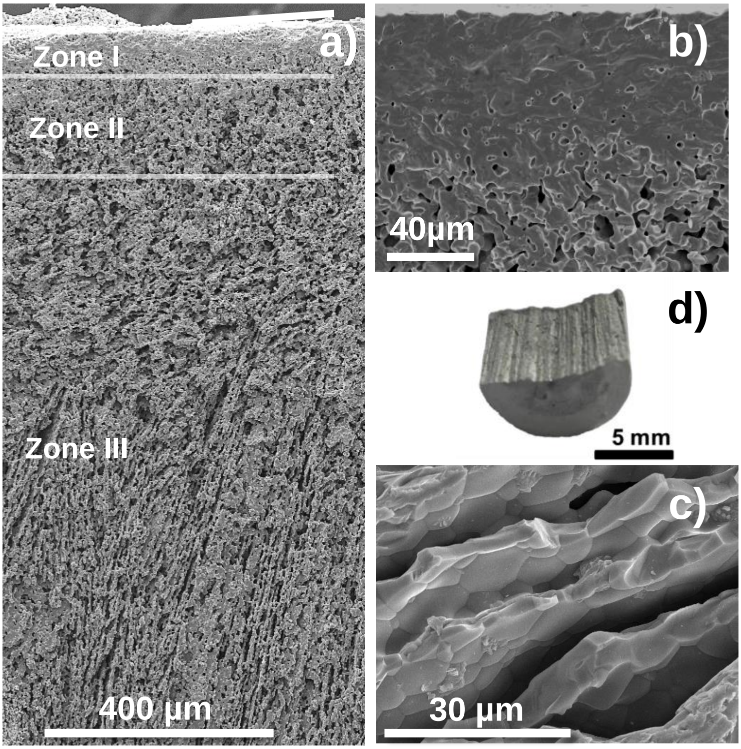

Figure 4.66: a) SEM cross-section of the LSCF asymmetric membrane b) magnified view of dense layer in Zone I section, c) oriented pores detail of Zone III and d) optical image of a fracture free-casted support monolith

The optical picture (d) of the Figure 4.66 represents a fracture of the LSCF asymmetric membrane after sintering at 1400ºC, where the unidirectional architecture of the porous support becomes visible. At the macroscopic point of view, we can note the vertical orientation of the porosity. The total porosity of the porous support is ~58%, as calculated by means of geometric measurements and comparison with the LSCF theoretical density ($\rho_{\text{theoretical LSCF}}$ = 6.33 g.cm^{-3} [44]).

Figure 4.66a shows a cross-section image of the asymmetric membrane. The porous support is composed by two regions with two distinct porous organisations (Zone II and Zone III) and a region at the top (Zone I) presenting high material density. Indeed, in the bottom of this picture we can note that the porosity is hierarchically oriented at a long range order while a second layer of about 150 µm, sandwiched between this layer and the dense top layer, presents a non-oriented and random porosity. This difference in microstructure can be related to the water solidification mechanism during the support freeze-casting process. Indeed, the solidification process takes place in two steps. The first one is related to a non-steady state period where ice nucleation is not organised and thus results in random porosity (i.e. the 150 µm layer above detailed) after freeze-drying and sintering. The second step is the ice nucleation under stationary state and along the temperature gradient and the post-formation of vertically-oriented channels [45]. The coating of the dense layer was done over the non-organized porous side of the support because it was experimentally easier to coat random porosity. Figure 4.66c depicts a close-up of the oriented channels. The spacing between two ceramic walls is about 7 µm while the walls are well densified and present an average width of 5 µm. The top-layer presents a thickness of about 30 µm with a good densification virtually with no defects (Figure 4.66b).

4.3.2. Effect of the freeze-cast porous support.

Figure 4.67 represents the O_2 permeation flux as a function of temperature for the asymmetric membrane fabricated in this study and for two membranes also tested in our laboratory: a LSCF monolithic membrane of 0.8 mm-thick prepared by uniaxial pressing and an asymmetric LSCF membrane manufactured by inverse tape casting [46]. The thickness of the dense layer of this latter is 30 µm enabling an easy comparison of the porous support effect with our membrane. The first information is that the freeze-cast membrane presents O_2 fluxes values significantly higher than the two others membranes all over the temperature range. In comparison with the monolithic membrane, the values are about (depending on the temperature) one order of magnitude higher, which is not surprising just by taking into account the effect of the membrane thickness on the permeation, as postulated by Wagner's law [35, 47]. The plots of both asymmetric membranes respond to an Arrhenius law and can be divided in three regions with distinct apparent activation energy. It indicates that the rate limiting steps in the permeation is different according to the temperature. The method of least squares was used to determine the apparent activation energy values and the related uncertainties. At low temperature, i.e. under 700ºC, the apparent activation energy is of (148±6) kJ.mol^{-1} while it decreases to (121±3) kJ.mol^{-1}in the intermediate temperature range. Finally, it reaches (78±3) kJ.mol^{-1} for temperatures higher than 800ºC, in agreement with the value of (81±5) kJ.mol^{-1} of the tape-cast membrane. The change in the energy of activation at intermediate to high temperatures can be attributed to a phase transition of the LSCF structure from cubic (at high temperature) to rhomboedral (at low temperature) [48] revealing that *bulk* ionic transport is partly controlling the permeation process. In the low temperature range, the role of the catalytic O_2 surface exchange becomes more important [1, 49] although the effect of the optimized porous system remains very important. At 900ºC, the O_2 flux of the freeze-cast membrane is 4 ml.min^{-1}.cm^{-2} and increases to 6.8 ml.min^{-1}.cm^{-2} at 1000ºC. Comparison with literature always remains complicated since (a) the O_2 permeation is dependent on the membrane microstructure and on the synthesis powder; and (b) there is not a unique single physical phenomenon controlling the permeation rate in asymmetric membranes. Indeed, several physical phenomena (solid state transport, gas phase diffusion, surface exchange) are contributing in a more or less balanced manner to the overall rate [28, 50, 51]. Results may vary by orders of magnitude like here demonstrated but we can note that these values are remarkably high since for the LSCF perovskite compound and a planar membrane configuration. Oxygen permeation values usually do not exceed the unity [52, 53], like for the bare membrane here tested, or with for example the value of

0.6 ml.min^{-1}.cm^{-2} at 1000ºC after optimization of the fabrication process reported by Zou [54, 55]. Our freeze-cast membrane yields better results than a state-of-the-art ultrathin hollow fiber membrane[56] working at 1050ºC and presenting a permeation flux of 5.77 ml.min^{-1}.cm^{-2}. [57]. These promising results are principally attributed to the beneficial contribution of the particular porous structure of membrane support [28]. Figure 4.68 depicts the evolution of the O_2 permeation flux as a function of the feed (air) flow rate and the operating temperature. For temperatures below 800ºC, the influence of the air flow rate is negligible. For a temperature of 1000ºC, the effect is noteworthy since the O_2 permeation reaches 7.3 ml·min^{-1}.cm^{-2} with a feeding flux of 300 ml·min^{-1} while it was of 5.6 ml·min^{-1}.cm^{-2} with a feeding flux of 50 ml·min^{-1}.

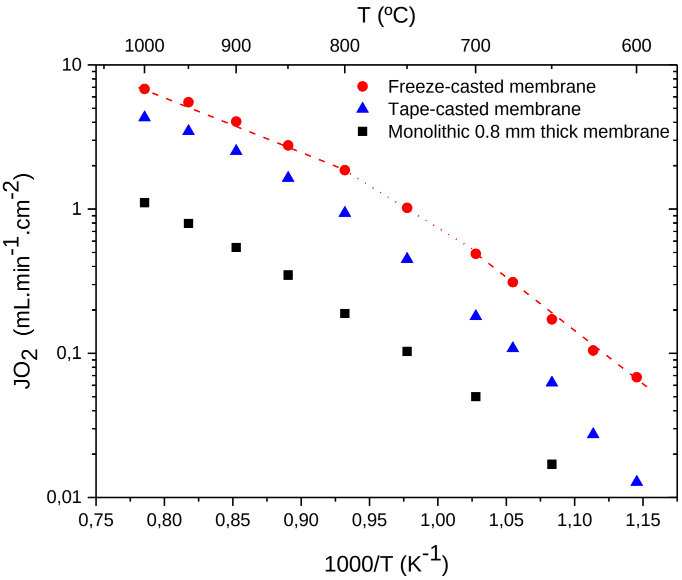

Figure 4.67: Oxygen permeation of three LSCF membranes: Square symbol: monolithic membrane, triangle symbol: asymmetric membrane developed by Jülich and circular symbol: freeze-cast asymmetric membrane. Air and sweep sides fed with 300 mL.min^{-1}.

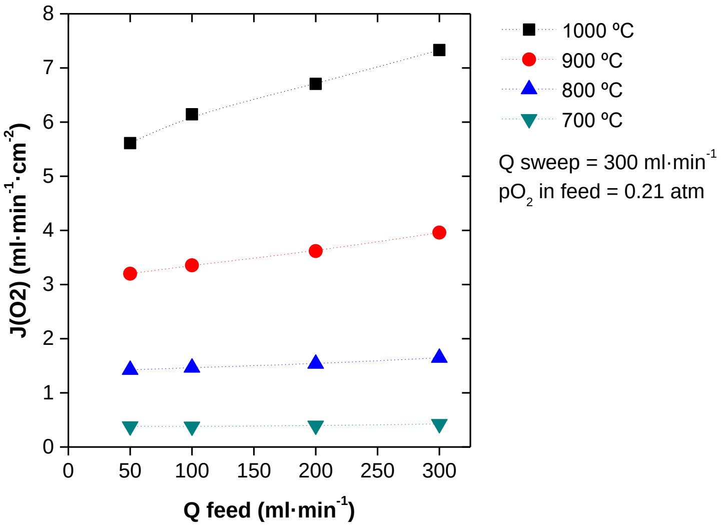

Figure 4.68: Oxygen permeation flux as a function of Q_{feed} and of the temperature for the freeze-cast asymmetric membrane .Q_{sweep} = 300 ml·min^{-1} and pO_2 in feed = 0.21 atm

A full study of the gaseous transport at high temperatures through the support has been realized for both freeze- (only the organized porosity layer) and tape-cast supports and the details are given in Figure 4.69. The transport regime in the porous support is found to be essentially related to *Knudsen* diffusion with a less important contribution of viscous flow. In the freeze-cast support, the pores are straight and highly-oriented in the flow direction, which leads to the strong increase in the gas permeance [58]. The pressure drop is very low for the porous support prepared by freeze-casting in comparison with the tape-cast one. Indeed, its pressure drop (0.59 bar·mm^{-1} with argon) at 800 ºC for an inlet flow of 400 ml·min^{-1} is three times lower than the pressure drop of the other support for an inlet flow of 50 ml·min^{-1} (1.77 bar·mm^{-1}). This result provides evidence about the important role of the hierarchical porosity of the support over the overall asymmetric membrane permeance.

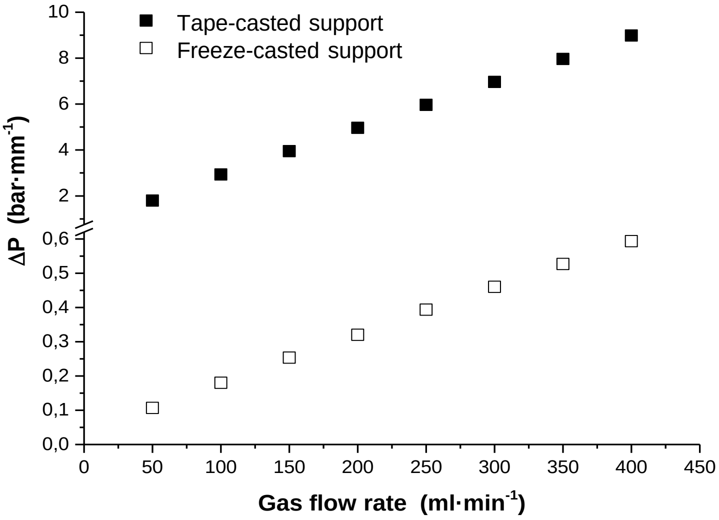

Figure 4.69: Normalized pressure drop ΔP across two porous support (filled symbol: support elaborated by tape-casting, empty symbol: support of the asymmetric membrane developed by freeze-casting) as a function of the Ar flow rate and at 900ºC.

Oxygen permeation under CO_2 conditions.

Membrane stability is a key point for up-scaling and industrial development. In particular, the chemical stability and membrane effectiveness in CO_2 at work is considered as very crucial [59] in several applications. Oxygen permeation tests consisted of a CO_2 content variation in the sweep stream by using different Ar-CO_2 mixtures in the temperature range 1000-850 ºC. Additionally, a stability test was performed at 900 ºC, maintaining during 52 hours a sweep stream composed by 50% CO_2 in Argon. During the stability test oxygen permeation was continuously measured, thus determining *J(O_2)* evolution with time under the referred conditions. Feed gas consisted of synthetic air for all the tests.

CO_2 content was varied in the range 0-100% as depicted in Figure 4.70. Permeation results show that CO_2 presence produces a slight improvement in *J(O_2)* at 1000 ºC. This effect has been previously observed for LSCF (Figure 4.64) and is ascribed to the better sweeping properties of CO_2 at very high temperatures in comparison with Ar. As can be seen, as temperature is decreased oxygen permeation is more affected by CO_2 presence, being more significant at lower T. At 850 ºC, *J(O_2)* drops from 2.5 down to 1 ml·min^{-1}·cm^{-2}. The reason for these drops is related with competitive adsorption processes between CO_2 and O_2 on membrane actives sites for oxygen permeation. CO_2 is adsorbed on LSCF surface thus hindering surface O_2 reactions. Due to CO_2 adsorption is stronger at lower temperatures then the effect is more significant when reducing T.

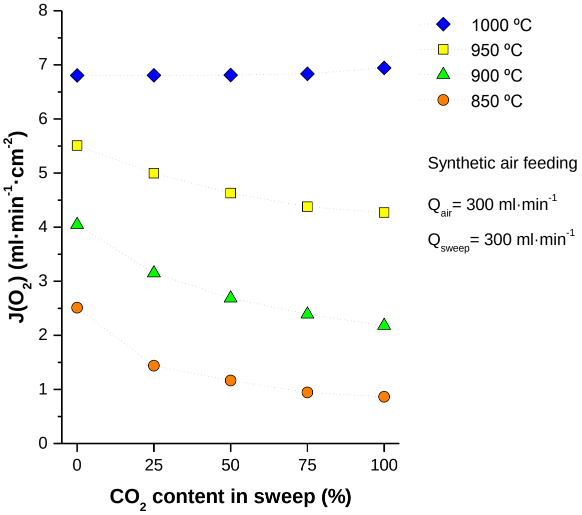

Figure 4.70: Oxygen permeation in dependence of CO_2 content in sweep stream at different temperatures.

Particularly at 850 ºC, it has been studied the JO2 evolution when increasing CO_2 content in sweep (from 0 up to 100%) and when withdrawing CO_2 from the stream. Results depicted in Figure 4.71 show that once LSCF is exposed to a full CO_2 atmosphere, initial $J(O_2)$ (2.5 ml·min^{-1}·cm^{-2}) is not recovered again under clean conditions (1.8 ml·min^{-1}·cm^{-2}) and after 12 hours there is only a slight improvement (2.1 ml·min^{-1}·cm^{-2}). Therefore, at 850 ºC, CO_2 affects LSCF performance once returned to clean conditions. This may be significant of CO_2 adsorption or carbonates formation. The latter phenomenon is unlikely since TG performed on LSCF under 5% CO_2 in Air atmosphere showed no signs of mass gain or loss different from TG measurements under Air conditions (Figure 4.65).

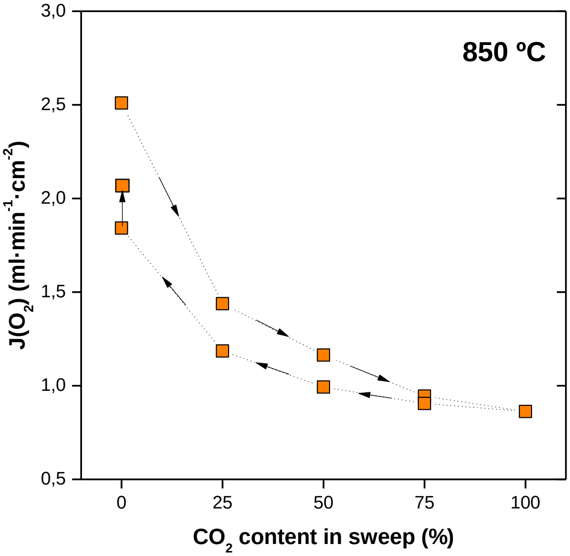

Figure 4.71: $J(O_2)$ evolution at 850 ºC when increasing and decreasing CO_2 content in sweep stream.

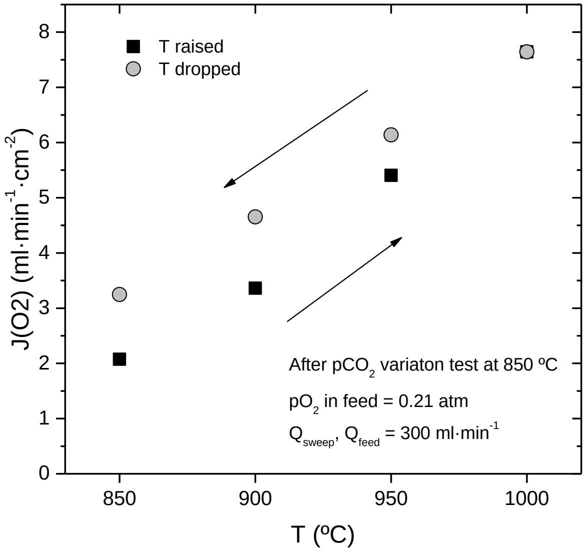

Figure 4.72: Oxygen permeation evolution when rising and dropping T after CO_2 exposure. Test carried out under Air/Argon gradient.

After CO_2 content variation test at 850 ºC, temperature was raised up to 1000 ºC and then dropped again to 850 ºC under Ar sweeping. This was done in order to observe $J(O_2)$ evolution after a thermal treatment. As can be seen in Figure 4.72,

$J(O_2)$ at 850 ºC after the thermal cycling is increased up to 3.2 ml·min^{-1}·cm^{-2} thus confirming CO_2 release from LSCF surface. Nevertheless, $J(O_2)$ is even higher than the obtained for initial conditions. This could be ascribed to a thermal activation of LSCF after Argon annealing at 1000 ºC.

Finally, it was performed a stability test at 900 ºC when exposing membrane to a 50% CO_2 containing atmosphere. Results depicted in Figure 4.73 show a significant loss in oxygen permeation when switching from Ar to CO_2. After 52 hours of continuous exposition $J(O_2)$ is stabilized. When switching back to clean conditions initial $J(O_2)$ is not recovered, despite an increasing trend is observed with time.

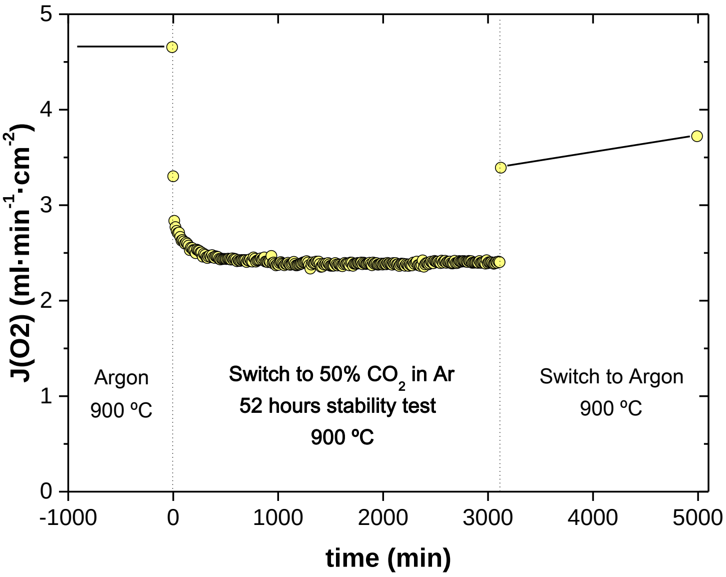

Figure 4.73: $J(O_2)$ evolution in dependence of time under 50% CO_2 at 900 ºC.

4.3.3. Effect of membrane catalytic activation.

Aiming to improve the oxygen permeation performance of the LSFC supported freeze cast system, a 30 μm thick LSCF porous catalytic layer was deposited on an all- LSFC freeze-cast membrane. As for the case explained in section 4.2.4, catalytic layer was deposited by means screen-printing method and subsequent calcination.

Microstructural study

A microscopic study of the activated freeze-cast asymmetric membrane using FE-SEM is presented in Figure 4.74. Image (a) details the top surface of the dense layer without catalytic porous layer. The layer presents homogeneous and well sintered grains with an average size of 3 µm. According to a global mapping of the surface layer, good densification is achieved. Gas tightness was confirmed prior further coating of the LSCF top porous layer by checking the absence of Helium gas pressure loss through the asymmetric membrane during 10 minutes. The surface of the as-sintered LSCF catalytic porous layer is shown on the image (b). LSCF grains are well sintered and connected and the porosity (black part of the image) is homogeneously distributed. Thus, uniform gas distribution all over the catalytic layer volume is expected. Image (c) shows a fracture cross-section of the membrane and details the interface between both dense and catalytic porous layer, revealing that the catalytic porous layer presents a thickness of 30 µm and adheres very well to the dense layer surface. Finally, image (d) depicts a cross-section of the whole asymmetric membrane consisting of (i) the top 30 µm-thick LSCF catalytic porous layer (4); (ii) the 100 µm-thick gastight LSCF layer (3) and (iii) the porous freeze-cast support. The support is composed mostly of a structure of hierarchically oriented pores (1), which are aligned perpendicular to the membrane surface, and a 300 µm-thick non-organized porous layer (2).

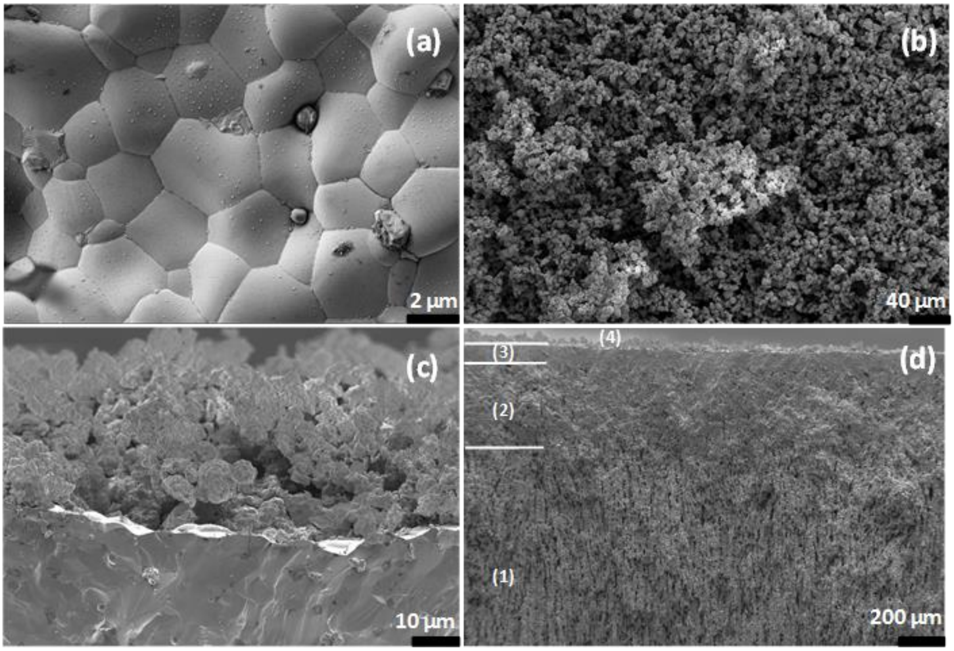

*Figure 4.74: FE-SEM images of the surface of the LSCF dense layer (**a**), of the surface of the catalytic porous LSCF layer (**b**), focus on the dense / catalytic porous layers interface (**c**) and global cross-section of the whole asymmetric membrane consisting of the vertically oriented channels porous layer (**1d**), the non-organized porous layer (**2d**), the dense LSCF layer (**3d**) and the 30 µm-thick LSCF porous catalytic layer (**4d**).*

XRD analysis was performed over the active porous top-layer membrane after sintering at 1060ºC and before permeation test. Figure 4.75 presents the patterns related to the LSCF starting powder and to both the activated membrane before and after permeation test. The porous layer is highly crystalline and corresponds only to the LSCF structure without phase modification. Further, XRD analysis of the activated freeze-cast asymmetric membrane after the oxygen permeation tests under CO_2 reveals that the LSCF crystalline structure is maintained and no new phases appeared. Nevertheless, three additional peaks with high crystallinity are observed at 38.2º, 44.3º and 64.7º (notified by * on the related pattern) and can be ascribed to cubic gold structure (JCPDS code 00-004-0784) employed as sealing ring during the permeation test. In summary, LSCF crystallinity is preserved during operating conditions and structural modification can be ruled out to the limit of the XRD analysis.

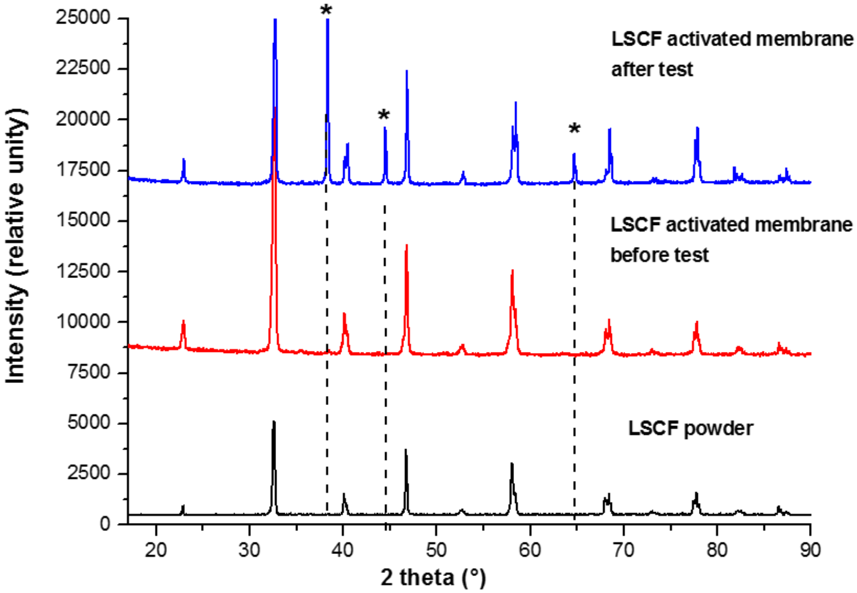

Figure 4.75: XRD patterns of the starting LSCF powder sintered, of the activated LSCF freeze-cast membrane before and after permeation and stability tests under CO_2.

Oxygen permeation: influence of pO_2 variation in feed stream

Figure 4.76 shows the temperature dependence of oxygen flux response for two different oxygen partial pressure in feed, i.e. 0.21 atm (synthetic air) and 1 atm O_2 (pure oxygen), in the range 600-1000 ºC and using argon as sweep gas. Flow rates of both feed and sweep streams were set at 300 ml·min^{-1} during the test. The permeation flux when using synthetic air exhibits a 3-fold Arrhenius behavior along the temperature range, whereas when switching to pure oxygen the flux follows a simple Arrhenius behavior. This effect was also observed for conventional tape-cast LSCF membranes (Figure 4.59) and the changes in the activation energy has been related to transitions in the permeation controlling step [60]: bulk diffusion at high and intermediate temperatures (1000-700ºC) and surface exchange reactions at low temperature (<700 ºC). If the porosity and pore structure of the membrane support is not adequate, gas polarization problems may become limiting, especially at high temperatures, when higher permeation fluxes are achieved, i.e. higher air depletion degree is reached. In Figure 4.76, the change in activation energy at 850 ºC for the 0.21 atm case may be ascribed to the phase transition in LSCF from cubic (high T) to rhombohedral (low T) [61, 62]. By assuming phase stabilization under higher arising pO_2 towards a cubic system, it is possible to explain the absence of E_a variation in the 1 atm O_2 test above 850 ºC. Furthermore, E_a differences below 700 ºC can be explained by the fact that oxygen permeation follows a pO_2^n dependence when surface kinetics controls the permeation. The highest oxygen flux is reached at 1000 ºC and 1 atm O_2 in the feed side, with a value of 16.3 $ml \cdot min^{-1} \cdot cm^{-2}$. Indeed, this value is higher than the oxygen peak flux of 13.3 $ml \cdot min^{-1} \cdot cm^{-2}$ measured in the activated tape-cast all-LSCF membrane under the same experimental conditions (Figure 4.59). If synthetic air is used as feed, a flux of 7.05 $ml \cdot min^{-1} \cdot cm^{-2}$ is obtained at 1000 ºC. The use of pure oxygen instead of synthetic air allows the improvement of $J(O_2)$ whatever the temperature. Figure 4.76 depicts the $J(O_2)$ improvement when pO_2 is raised from 0.21 to 1 atm. Accordingly, a flux improvement of 127% is reached at 1000 ºC, whereas at 600 ºC $J(O_2)$ increases up to 76% when pure oxygen is used.

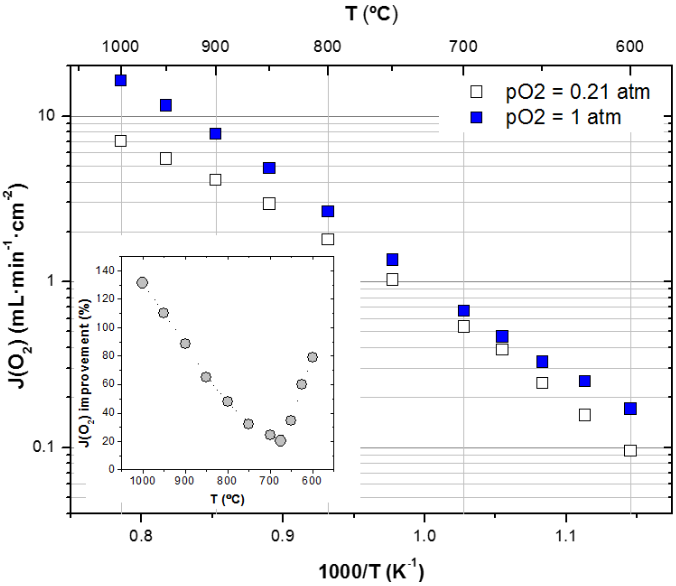

Figure 4.76: Oxygen permeation flux through the activated freeze-cast asymmetric membrane as a function of temperature and of pO_2 in the feed flow.

Membrane activation influence under CO_2-free environments

The activation of the asymmetric membrane by the coating of a porous LSCF layer on the top of the dense layer would be especially beneficial in the low temperature range where kinetics exchange is the rate limiting process. Figure 4.77 represents the effect of the porous catalytic layer over the oxygen permeation as a function of temperature. The most important improvement in $J(O_2)$ is observed for temperatures lower than 700ºC. For example, *J(O_2)* at 600ºC is improved by 54.5% thanks to the catalytic layer achieving a flux of 0.17 ml·min^{-1}·cm^{-2} with regard to the flux 0.11 ml·min^{-1}·cm^{-2} achieved with the bare membrane. For temperatures higher than 700ºC, the oxygen permeation enhancement is lower but still perceptible and around 10%.

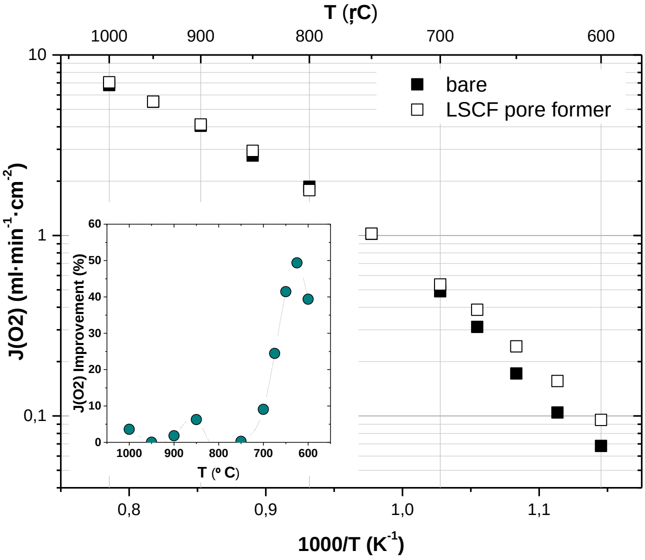

Figure 4.77: Oxygen permeation flux as a function of inverse temperature for two membranes: LSCF freeze-cast asymmetric membrane: solid symbols; activated LSCF freeze-cast asymmetric membrane: empty symbols Feed gas: 300 mL min^{-1} of air. Sweep gas: 300 mL min^{-1} of argon.

Membrane activation influence under CO_2-rich environment

Different mixtures of argon-CO_2 were considered for the study, i.e., from 100% argon to 100% CO_2 at different temperatures in the range 800-1000 ºC. The testing procedure was carried out as follows, for each given temperature the test started with a sweep stream containing 0% CO_2 (100% Ar), then increasing CO_2 content by 25% steps until 100% CO_2 was reached. Isothermal oxygen permeation was also studied in the way back, i.e. from 100% CO_2 sweep to 0% CO_2, thus analyzing the recovery behavior of the membrane when carbon dioxide is withdrawn from the gas stream.

Figure 4.78 represents *J(O_2)* as a function of CO_2 content in sweep for various temperatures (1000 ºC, 950 ºC, 900 ºC, 850 ºC and 800 ºC). Solid symbols correspond to the present activated asymmetric membrane, whereas empty symbols refer to the results obtained for the not activated membrane. The effect of varying CO_2 is similar for both membranes, i.e., at 1000 ºC CO_2 affects positively

$J(O_2)$ while at lower temperatures, as CO_2 concentration is raised, $J(O_2)$ drops down to a minimum value. Despite both bare and activated membranes show a similar response as a function of CO_2 concentration, the addition of a catalytic layer seems to grant protective features against CO_2 exposure since $J(O_2)$ drop is significantly lower for the activated membrane. The highest oxygen flux is obtained at 1000 ºC and 100% CO_2, corresponding to a value of 7.2 $ml\cdot min^{-1}\cdot cm^{-2}$. At 850 ºC, $J(O_2)$ falls from 2.9 $ml\cdot min^{-1}\cdot cm^{-2}$ to 1.6 and 1.3 $ml\cdot min^{-1}\cdot cm^{-2}$ when CO_2 content is 50% and 100%, respectively. Therefore, under representative conditions of oxycombustion, the membrane performance is affected by a permeation loss of 44.8-55.1%. Moreover, when CO_2 content in sweep was set to 0% in the way back, $J(O_2)$ was immediately recovered for all tested temperatures and even improved at certain temperatures. This reversible behavior suggests that no carbonation processes are taking place on the membrane surface otherwise $J(O_2)$ should be lower than in the starting point and the recovery may take some time. The drop in oxygen permeation upon CO_2 feeding drops could be related to the competitive adsorption between CO_2 and O_2 at the surface active sites, which leads to the slowdown of gas exchange reaction and then this step becomes rate limiting. Accordingly, the effect of adding a catalytic layer boosting surface exchange reactions is much more important under CO_2-rich environments. Figure 4.79 represents JO_2 in an Arrhenius arrangement and shows that the rise in CO_2 concentration induces the progressive increase in the activation energy (E_a), which reveals a change in the rate limiting step. Specifically, the higher E_a values are in line with surface exchange process [63-66], which become very limiting at the highest CO_2 contents. These E_a values are similar to those observed in CO_2-free conditions in the temperature range 750-600 ºC (see Figure 4.77).

Therefore, catalytic activation of LSCF freeze-cast asymmetric membrane results in an improvement in the $J(O_2)$ in all the tested T range under presence of CO_2. Moreover, the loss in oxygen fluxes due to CO_2 is lower for the case of the activated membrane, hence some protective features against CO_2 are provided by catalytic layer addition.

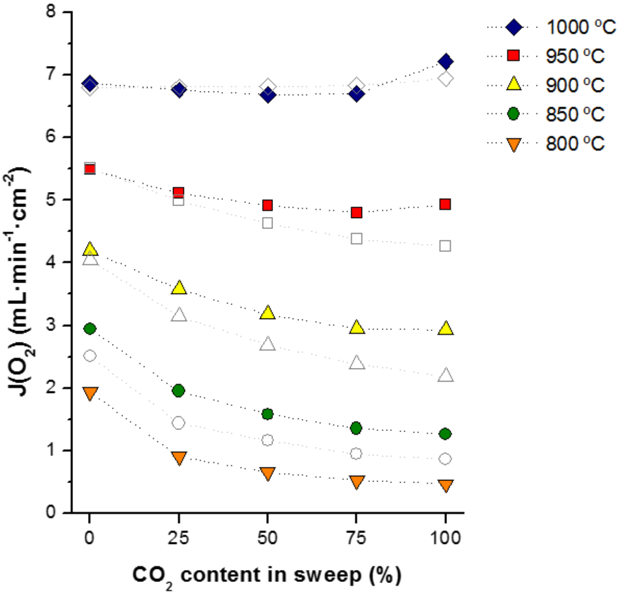

Figure 4.78: Oxygen permeation flux through the activated freeze-cast asymmetric membrane (solid symbols) and through the freeze-cast asymmetric membrane (empty symbols) as a function of temperature and of the CO_2 content in the sweep gas

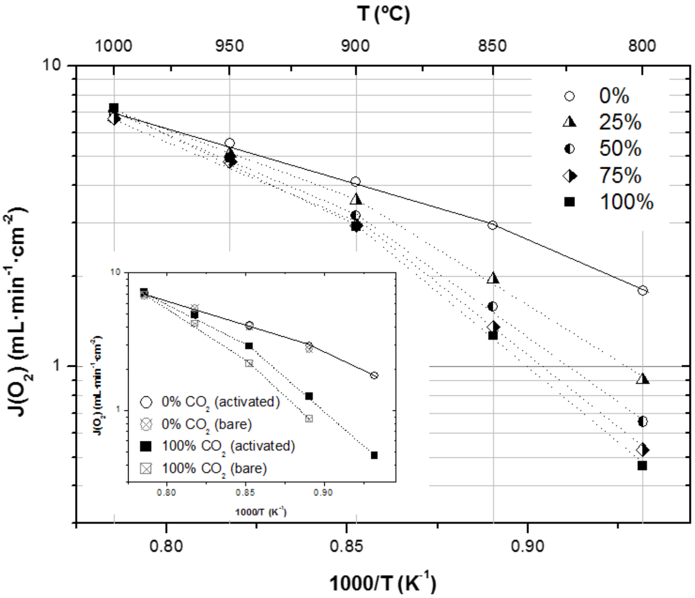

Figure 4.79: Arrhenius plot for the oxygen flux through the activated membrane for different CO_2 contents. Inset: comparison of CO_2 effect as a function of temperature for the bare and activated membranes.

Stability test

In industrial applications, OTM modules providing gas oxygen to a process should operate during extended periods of time (> 3 years). Along these periods of continuous operation, the membrane system must be capable of supplying a constant flow of oxygen, as well as not suffering excessive degradation of its mechanical integrity, which typically implies a substantial loss in $J(O_2)$. In order to assess the stability of the membrane material and architecture under *oxyfuel*-like conditions, the oxygen permeation was monitored as a function of time during 92 hours under a 50% CO_2-containing sweep gas and at 850ºC. Figure 4.80 details the evolution of $J(O_2)$ as a function of time. The activated membrane was firstly maintained under a sweep flow of 100% of argon during 3 hours to clean the membrane surface. The sweep gas was then switched to the 50% CO_2-containing flow in argon for 92 hours. After a short transient period where the O_2 flux decreases quickly, upon CO_2 introduction, from 2.8 $ml·min^{-1}·cm^{-2}$ to 1.41 $ml·min^{-1}·cm^{-2}$, the O_2 permeation slowly decreases with time during the 92 hours of test to reach the final value of 1.25 $ml·min^{-1}·cm^{-2}$. Finally, a linear degradation rate of $4.27·10^{-2}$ $ml·min^{-1}·cm^{-2}$ per day (2.96 % per day) is found for this activated freeze-cast membrane.

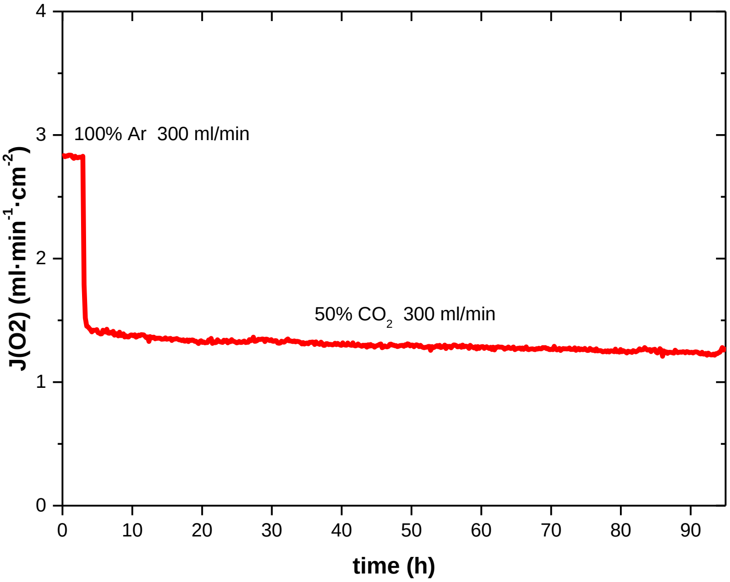

Figure 4.80: Oxygen permeation flux at 850 ºC as a function of time for the activated freeze-cast membrane under a 50% CO_2-containing flux in argon as sweep gas (total flux 300 $ml·min^{-1}$). The feed stream is composed by 300 $ml·min^{-1}$ of air.

4.4. Conclusions.

A complete permeation study on asymmetric 30 µm-thick LSCF membranes manufactured by inverse tape-casting and freeze-casting is presented. Several parameters were varied during the test in order to get a better understanding of the different processes involved in the oxygen permeation through LSCF asymmetric membranes. Specifically, temperature, sweep gas flow, oxygen partial pressure in feed, CO_2 content in sweep stream, and the catalytic membrane activation were studied.

For the LSCF tape casted membrane the increase in sweep flow rate has a very positive impact in the oxygen flux, obtaining higher improvements in the temperature range from 1000 to 850ºC. Whereas at lower temperatures, this effect becomes much less visible. The increase in the pO_2 in the feed (porous substrate side) and the use of He instead of N_2 allow increasing significantly the flux. The highest effect is observed in two different temperature ranges, i.e., 1000-850 ºC and 700-600 ºC. A phase transition in LSCF perovskite has been observed at above 850ºC (from rhombohedral to cubic symmetry), and induces a change in the activation energy related to oxygen bulk diffusion, which is the rate limiting step in this temperature range. $J(O_2)$ decreases under rich-CO_2 environments at 900ºC due to competitive adsorption between CO_2 and O_2. On the other hand, CO_2 allows improving the permeation flux at 1000 ºC due to better sweeping capability compared to Ar. Surface exchange reactions are improved by membrane catalytic activation, up to ca. 300% of $J(O_2)$ improvement at low temperatures while the effect is very small at high temperatures. A peak oxygen flux of 13.3 $ml \cdot min^{-1} \cdot cm^{-2}$ is reached at 1000ºC for the tape casted activated membrane when using O_2 as feed.

With regard to freeze casted membranes, it was enabled the optimization of the gas transport through the porous membrane support by creating a hierarchical porosity while a dense top-layer of 30 μm was coated over this support by screen printing. Permeation tests proved the beneficial effect of such porous supports over the O_2 fluxes with a maximum value of 6.8 $ml \cdot min^{-1} \cdot cm^{-2}$ at 1000 ºC. Moreover, the permeation study including thermo-chemical cycling revealed an interesting stability of the membrane. The short-term test under oxyfuel conditions in the presence of 50% CO_2 suggests that the sample was apparently stable and the O_2 flux is decreased with regard to CO_2-free operation although this effect is reversible and can be reverted upon CO_2 removal. Further stability tests for at least 3 months would be required to demonstrate the reliable operation under high-CO_2 conditions at a reasonable degradation rate.

The catalytic functionalization of a LSCF freeze-cast asymmetric membrane has been realized by coating a 30 μm-thick porous LSCF layer. Under CO_2-free operation, the beneficial effect is mostly observed in the low temperature range (< 700ºC), when gas exchange is a limiting step and the porous coating strongly enlarges the number of active sites available for oxygen exchange reactions. At 600 ºC and using air as feed, the improvement for $J(O_2)$ is estimated at 50% while a maximum oxygen permeation of 16.3 $ml \cdot min^{-1} \cdot cm^{-2}$ is reached at 1000 ºC when pure oxygen is fed, being higher than the peak flux of 13.3 $ml \cdot min^{-1} \cdot cm^{-2}$ obtained under the same conditions for the tape cast membrane.

The addition of this catalytic layer has a striking effect on the permeation rate under CO_2-rich gas atmosphere, i.e. the negative effect of CO_2 on $J(O_2)$ is alleviated, especially at 950 and 900ºC. This effect is fully and suddenly reverted upon CO_2 removal from the gas stream at any tested temperature. Further, an increase in $J(O_2)$ is observed at 1000 ºC with increasing CO_2 concentrations. Nevertheless, the influence of CO_2 over oxygen permeation over all the temperature range remains to be elucidated. In this way, in-situ characterizations for surface species detection would be really interesting and would enable to resolve the involved mechanisms on the surface membrane under CO_2-rich environments. Finally, the membrane operation was evaluated at 850 ºC under CO_2-rich sweep gas over a period of 92 hours, leading to a degradation rate of $4.27\cdot10^{-2}$ $ml\cdot min^{-1}\cdot cm^{-2}$ per day. Further improvement of the active porous layer could be achieved by dispersing an oxygen-activation catalyst, e.g., Pr, Ce, Ag or Pd, in the porous LSCF layer [21, 67].

The presented results are very promising as a first attempt of such asymmetric membranes, especially those based on freeze-cast supports. Nevertheless, such a membrane configuration deserves further development for optimization. First of all, a material with higher intrinsic conductivities and/or stability could be selected. The modification of the freeze-casting protocol could lead to a better control of the porosity while other coating techniques could be considered to minimize the thickness of the dense top-layer and thus optimize the oxygen permeation. Finally, the catalytic functionalization of the dense layer would further improve the permeation fluxes whereas the use of more chemically-robust membrane materials should be used to attain long-term stable operation in realistic oxyfuel operation gas environments.

4.5. References.

[1] A.A. Asadi, A. Behrouzifar, M. Iravaninia, T. Mohammadi, A. Pak, Preparation and Oxygen Permeation of La0.6Sr0.4Co0.2Fe0.8O3-delta (LSCF) Perovskite-Type Membranes: Experimental Study and Mathematical Modeling, Industrial & Engineering Chemistry Research, 51 (2012) 3069-3080.

[2] X. Tan, N. Liu, B. Meng, J. Sunarso, K. Zhang, S. Liu, Oxygen permeation behavior of La0.6Sr0.4Co0.8Fe0.2O3 hollow fibre membranes with highly concentrated CO2 exposure, Journal of Membrane Science, 389 (2012) 216-222.

[3] Y. Zou, W. Zhou, S. Liu, Z. Shao, Sintering and oxygen permeation studies of La0.6Sr0.4CoO2Fe0.8O3-delta ceramic membranes with improved purity, Journal of the European Ceramic Society, 31 (2011) 2931-2938.

[4] T.T. Norton, Y.S. Lin, Transient Oxygen Permeation and Surface Catalytic Properties of Lanthanum Cobaltite Membrane under Oxygen-Methane Gradient, Industrial & Engineering Chemistry Research, 51 (2012) 12917-12925.

[5] Y. Teraoka, Y. Honbe, J. Ishii, H. Furukawa, I. Moriguchi, Catalytic effects in oxygen permeation through mixed-conductive LSCF perovskite membranes, Solid State Ionics, 152 (2002) 681-687.

[6] B. Zydorczak, Z. Wu, K. Li, Fabrication of ultrathin La0.6Sr0.4Co0.2Fe0.8O3-delta hollow fibre membranes for oxygen permeation, Chemical Engineering Science, 64 (2009) 4383-4388.

[7] X.Y. Tan, Y.T. Liu, K. Li, Preparation of LSCF ceramic hollow-fiber membranes for oxygen production by a phase-inversion/sintering technique, Industrial & Engineering Chemistry Research, 44 (2005) 61-66.

[8] H. Kusaba, Y. Shibata, K. Sasaki, Y. Teraoka, Surface effect on oxygen permeation through dense membrane of mixed-conductive LSCF perovskite-type oxide, Solid State Ionics, 177 (2006) 2249-2253.

[9] M. den Exter, J.F. Vente, D. Jansen, W.G. Haije, Viability of mixed conducting membranes for oxygen production and oxyfuel processes in power production, in: J. Gale, H. Herzog, J. Braitsch (Eds.) Greenhouse Gas Control Technologies 92009, pp. 455-459.

[10] S. Engels, F. Beggel, M. Modigell, H. Stadler, Simulation of a membrane unit for oxyfuel power plants under consideration of realistic BSCF membrane properties, Journal of Membrane Science, 359 (2010) 93-101.

[11] M.P. Lobera, J.M. Serra, S.P. Foghmoes, M. Søgaard, A. Kaiser, On the use of supported ceria membranes for oxyfuel process/syngas production, Journal of Membrane Science, 385–386 (2011) 154-161.

[12] R. Castillo, Thermodynamic analysis of a hard coal oxyfuel power plant with high temperature three-end membrane for air separation, Applied Energy, 88 (2011) 1480-1493.

[13] W.G. Haije, S.C. Kluiters, R.W. van den Brink, D. Jansen, Systems and materials for mixed ionic electronic conducting membranes in integrated oxyfuel combustion systems, in: J. Gale, C. Hendriks, W. Turkenberg (Eds.) 10th International Conference on Greenhouse Gas Control Technologies2011, pp. 996-1001.

[14] X. Zhu, H. Liu, Y. Cong, W. Yang, Novel dual-phase membranes for CO2 capture via an oxyfuel route, Chemical Communications, 48 (2012) 251-253.

[15] J.W. Stevenson, T.R. Armstrong, R.D. Carneim, L.R. Pederson, W.J. Weber, Electrochemical properties of mixed conducting perovskites La(1-x)M(x)Co(1-y)Fe(y)O(3-delta) (M=Sr,Ba,Ca), Journal of the Electrochemical Society, 143 (1996) 2722-2729.

[16] M. Ikeguchi, Y. Yoshino, K. Kanie, M. Nomura, E. Kikuchi, M. Matsukata, Effects of preparation method on oxygen permeation properties of SrFeCo0.5Ox membrane, Separation and Purification Technology, 32 (2003) 313-318.

[17] Z. Pingying, R. Ran, C. Zhihao, G. Hongxia, S. Zongping, J.C.D. da Costa, L. Shaomin, Significant effects of sintering temperature on the performance of La0.6Sr0.4Co0.2Fe0.8O3-delta oxygen selective membranes, Journal of Membrane Science, 302 (2007) 171-179.

[18] S. Baumann, F. Schulze-Kuppers, S. Roitsch, M. Betz, M. Zwick, E.M. Pfaff, W.A. Meulenberg, J. Mayer, D. Stover, Influence of sintering conditions on

microstructure and oxygen permeation of Ba0.5Sr0.5Co0.8Fe0.2O3-delta (BSCF) oxygen transport membranes, Journal of Membrane Science, 359 (2010) 102-109.

[19] M. Schulz, U. Pippardt, L. Kiesel, K. Ritter, R. Kriegel, Oxygen permeation of various archetypes of oxygen membranes based on BSCF, Aiche Journal, 58 (2012) 3195-3202.

[20] W.K. Hong, G.M. Choi, Oxygen permeation of BSCF membrane with varying thickness and surface coating, Journal of Membrane Science, 346 (2010) 353-360.

[21] P.F. Haworth, S. Smart, J.M. Serra, J.C. Diniz Da Costa, Combined investigation of bulk diffusion and surface exchange parameters of silver catalyst coated yttrium-doped BSCF membranes, Physical Chemistry Chemical Physics, 14 (2012) 9104-9111.

[22] H. Wang, C. Tablet, J. Caro, Oxygen production at low temperature using dense perovskite hollow fiber membranes, Journal of Membrane Science, 322 (2008) 214-217.

[23] T. Schiestel, M. Kilgus, S. Peter, K.J. Caspary, H. Wang, J. Caro, Hollow fibre perovskite membranes for oxygen separation, Journal of Membrane Science, 258 (2005) 1-4.

[24] P. Haworth, S. Smart, J. Glasscock, J.C.D. da Costa, High performance yttrium-doped BSCF hollow fibre membranes, Separation and Purification Technology, 94 (2012) 16-22.

[25] O. Buechler, J.M. Serra, W.A. Meulenberg, D. Sebold, H.P. Buchkremer, Preparation and properties of thin La1-xSrxCo1-yFeyO3-delta perovskitic membranes supported on tailored ceramic substrates, Solid State Ionics, 178 (2007) 91-99.

[26] J. Gurauskis, Ø.F. Lohne, H.L. Lein, K. Wiik, Processing of thin film ceramic membranes for oxygen separation, Journal of the European Ceramic Society, 32 (2012) 649-655.

[27] X. Chang, C. Zhang, Y. He, X. Dong, W. Jin, N. Xu, A Comparative Study of the Performance of Symmetric and Asymmetric Mixed-conducting Membranes, Chinese Journal of Chemical Engineering, 17 (2009) 562-570.

[28] S. Baumann, J.M. Serra, M.P. Lobera, S. Escolastico, F. Schulze-Kueppers, W.A. Meulenberg, Ultrahigh oxygen permeation flux through supported Ba0.5Sr0.5Co0.8Fe0.2O3-delta membranes, Journal of Membrane Science, 377 (2011) 198-205.

[29] F. Schulze-Küppers, S. Baumann, W.A. Meulenberg, D. Stöver, H.P. Buchkremer, Manufacturing and performance of advanced supported Ba0.5Sr0.5Co0.8Fe0.2O3−δ (BSCF) oxygen transport membranes, Journal of Membrane Science, 433 (2013) 121-125.

[30] M. Lipinska-Chwalek, J. Malzbender, A. Chanda, S. Baumann, R.W. Steinbrech, Mechanical characterization of porous Ba0.5Sr0.5Co0.8Fe0.2O3−d, Journal of the European Ceramic Society, 31 (2011) 2997-3002.

[31] I. Garcia-Torregrosa, M.P. Lobera, C. Solis, P. Atienzar, J.M. Serra, Development of CO2 Protective Layers by Spray Pyrolysis for Ceramic Oxygen Transport Membranes, Advanced Energy Materials, 1 (2011) 618-625.

[32] J.M. Gozalvez-Zafrilla, A. Santafe-Moros, S. Escolastico, J.M. Serra, Fluid dynamic modeling of oxygen permeation through mixed ionic-electronic conducting membranes, Journal of Membrane Science, 378 (2011) 290-300.

[33] J. Sunarso, S. Baumann, J.M. Serra, W.A. Meulenberg, S. Liu, Y.S. Lin, J.C.D. da Costa, Mixed ionic-electronic conducting (MIEC) ceramic-based membranes for oxygen separation, Journal of Membrane Science, 320 (2008) 13-41.

[34] H. Bouwmeester, A. Burggraaf, Dense Ceramic Membranes for Oxygen Separation, Handbook of Solid State Electrochemistry, CRC Press1997.

[35] B.X. Huang, R.W. Steinbrech, S. Baumann, J. Malzbender, Creep behavior and its correlation with defect chemistry Of La0.58Sr0.4Co0.2Fe0.8O3-delta, Acta Materialia, 60 (2012) 2479-2484.

[36] C. Yacou, J. Sunarso, C.X.C. Lin, S. Smart, S. Liu, J.C. Diniz da Costa, Palladium surface modified La0.6Sr0.4Co0.2Fe0.8O3−δ hollow fibres for oxygen separation, Journal of Membrane Science, 380 (2011) 223-231.

[37] J. Serra, V. Vert, O. Buchler, W. Meulenberg, H. Buchkremer, IT-SOFC supported on mixed oxygen ionic-electronic conducting composites, Chemistry of Materials, 20 (2008) 3867-3875.

[38] V.B. Vert, J.M. Serra, Study of CO2 stability and electrochemical oxygen activation of mixed conductors with low thermal expansion coefficient based on the TbBaCo3ZnO7+delta system, Journal of Power Sources, 196 (2011) 4270-4276.

[39] M. Klotz, I. Amirouche, C. Guizard, C. Viazzi, S. Deville, Ice Templating—An Alternative Technology to Produce Micromonoliths, Advanced Engineering Materials, 14 (2012) 1123-1127.

[40] S. Deville, E. Saiz, R.K. Nalla, A.P. Tomsia, Freezing as a path to build complex composites, Science, 311 (2006) 515-518.

[41] B.-H. Yoon, W.-Y. Choi, H.-E. Kim, J.-H. Kim, Y.-H. Koh, Aligned porous alumina ceramics with high compressive strengths for bone tissue engineering, Scripta Materialia, 58 (2008) 537-540.

[42] S. Deville, Freeze-casting of porous ceramics: A review of current achievements and issues, Advanced Engineering Materials, 10 (2008) 155-169.

[43] Y. Liu, S.-I. Hashimoto, H. Nishino, K. Takei, M. Mori, T. Suzuki, Y. Funahashi, Fabrication and characterization of micro-tubular cathode-supported SOFC for intermediate temperature operation, Journal of Power Sources, 174 (2007) 95-102.

[44] A. Lasalle, C. Guizard, E. Maire, J. Adrien, S. Deville, Particle redistribution and structural defect development during ice templating, Acta Materialia, 60 (2012) 4594-4603.

[45] J.M. Serra, J. Garcia-Fayos, S. Baumann, F. Schulze-Küppers, W.A. Meulenberg, Oxygen permeation through tape-casted asymmetric all-

La0.6Sr0.4Co0.2Fe0.8O3-δ membranes, Journal of membrane Science, 447 (2013) 297-305.

[46] A. Chroneos, B. Yildiz, A. Tarancon, D. Parfitt, J.A. Kilner, Oxygen diffusion in solid oxide fuel cell cathode and electrolyte materials: mechanistic insights from atomistic simulations, Energy & Environmental Science, 4 (2011) 2774-2789.

[47] T.V. Aksenova, M.V. Anan'ev, L.Y. Gavrilova, V.A. Cherepanov, Phase equilibria and crystal structures of solid solutions in the system LaCoO3-delta-SrCoO2.5 +/-delta-SrFeO3-delta-LaFeO3-delta, Inorganic Materials, 43 (2007) 296-300.

[48] X.Y. Tan, K. Li, Modeling of air separation in a LSCF hollow-fiber membrane module, Aiche Journal, 48 (2002) 1469-1477.

[49] A. Behrouzifar, A.A. Asadi, T. Mohammadi, A. Pak, Experimental investigation and mathematical modeling of oxygen permeation through dense Ba0.5Sr0.5Co0.8Fe0.2O3−δ (BSCF) perovskite-type ceramic membranes, Ceramics International, 38 (2012) 4797-4811.

[50] J. Caro, 3.01 - Basic Aspects of Membrane Reactors, in: D. Editor-in-Chief: Enrico, G. Lidietta (Eds.) Comprehensive Membrane Science and Engineering, Elsevier, Oxford, 2010, pp. 1-24.

[51] P. Zeng, R. Ran, Z. Chen, H. Gu, Z. Shao, J.C.D. da Costa, S. Liu, Significant effects of sintering temperature on the performance of La0.6Sr0.4Co0.2Fe0.8O3−δ oxygen selective membranes, Journal of Membrane Science, 302 (2007) 171-179.

[52] S. Lee, K.S. Lee, S.K. Woo, J.W. Kim, T. Ishihara, D.K. Kim, Oxygen-permeating property of LaSrBFeO3 (B=Co, Ga) perovskite membrane surface-modified by LaSrCoO3, Solid State Ionics, 158 (2003) 287-296.

[53] Y. Zou, W. Zhou, S. Liu, Z. Shao, Sintering and oxygen permeation studies of La0.6Sr0.4Co0.2Fe0.8O3−δ ceramic membranes with improved purity, Journal of the European Ceramic Society, 31 (2011) 2931-2938.

[54] C.Y. Tsai, A.G. Dixon, Y.H. Ma, W.R. Moser, M.R. Pascucci, Dense perovskite, La 1-xA′ xFe 1-yCo yO 3-δ (A′ = Ba, Sr, Ca), membrane synthesis, applications, and characterization, Journal of the American Ceramic Society, 81 (1998) 1437-1444.

[55] C.-G. Fan, W. Liu, Y.-B. Zuo, Z.-Q. Deng, X.-X. Huang, C.-S. Chen, Thermal and oxygen-permeable properties of SrCo0.8Fe0.2O3-Œ¥ and SrCo0.8Fe0.1Sn0.1O3-Œ¥ ceramic membranes, Wuji Cailiao Xuebao, 21 (2006) 1141-1146.

[56] B. Zydorczak, Z. Wu, K. Li, Fabrication of ultrathin La0.6Sr0.4Co0.2Fe0.8O3–δ hollow fibre membranes for oxygen permeation, Chemical Engineering Science, 64 (2009) 4383-4388.

[57] Y. Guo, M. Bessaa, S. Aguado, M.C. Steil, D. Rembelski, M. Rieu, J.-P. Viricelle, N. Benameur, C. Guizard, C. Tardivat, P. Vernoux, D. Farrusseng, An all porous solid oxide fuel cell (SOFC): a bridging technology between dual and single chamber SOFCs, Energy & Environmental Science, (2013).

[58] M. Schulz, R. Kriegel, A. Kaempfer, Assessment of CO2 stability and oxygen flux of oxygen permeable membranes, Journal of Membrane Science, 378 (2011) 10-17.

[59] J.M. Serra, J. Garcia-Fayos, S. Baumann, F. Schulze-Küppers, W.A. Meulenberg, Oxygen permeation through tape-casted asymmetric all-La0.6Sr0.4Co0.2Fe0.8O3-δ membranes, Journal of membrane Science, Submitted (2013).

[60] S. Baumann, J.M. Serra, M.P. Lobera, S. Escolástico, F. Schulze-Küppers, W.A. Meulenberg, Ultrahigh oxygen permeation flux through supported Ba0.5Sr0.5Co0.8Fe0.2O3−δ membranes, Journal of membrane Science, 377 (2011) 198-205.

[61] B.X. Huang, R.W. Steinbrech, S. Baumann, J. Malzbender, Creep behavior and its correlation with defect chemistry of La0.58Sr0.4Co0.2Fe0.8O3−δ, Acta Materialia, 60 (2012) 2479-2484.

[62] M. Pilar Lobera, S. Escolastico, J. Garcia-Fayos, J.M. Serra, Ethylene Production by ODHE in Catalytically Modified Ba0.5Sr0.5Co0.8Fe0.2O3-delta Membrane Reactors, Chemsuschem, 5 (2012) 1587-1596.

[63] E.N. Armstrong, K.L. Duncan, D.J. Oh, J.F. Weaver, E.D. Wachsman, Determination of Surface Exchange Coefficients of LSM, LSCF, YSZ, GDC Constituent Materials in Composite SOFC Cathodes, Journal of the Electrochemical Society, 158 (2011) B492-B499.

[64] E. Bucher, W. Sitte, Long-term stability of the oxygen exchange properties of (La,Sr)(1-z)(Co,Fe)O3-delta in dry and wet atmospheres, Solid State Ionics, 192 (2011) 480-482.

[65] C.C. Kan, H.H. Kan, F.M.I. Van Assche, E.N. Armstrong, E.D. Wachsman, Investigating oxygen surface exchange kinetics of La(0.8)Sr(.20)MnO(3-delta) and La(0.6)Sr(0.4)Co(0.2)Fe(0.8)O(3-delta) using an isotopic tracer, Journal of the Electrochemical Society, 155 (2008) B985-B993.

[66] J.M. Serra, V.B. Vert, O. Büchler, W.A. Meulenberg, H.P. Buchkremer, IT-SOFC supported on mixed oxygen ionic-electronic conducting composites, Chemistry of Materials, 20 (2008) 3867-3875.

5. OXYGEN PERMEATION ON AN ASYMMETRIC CGO-Co MEMBRANE

5. Oxygen permeation on an Asymmetric CGO-Co membrane.

5.1. Introduction.

Electric power generation is mainly produced by means of the combustion of fossil fuel (representing a 68.1%), being coal the main exploited source for that purpose with a 41.6% [1]. Such a high percentage of fossil fuel utilization in our large electricity demanding society generated a CO_2 emission of 31,102.3 Mtons in 2010 [2], existing forecasts saying that this amount will be increased up to 40,226 Mtons in 2040 [1]. Since it is well-known by the scientific community that CO_2 is the gas emission that most contributes to the greenhouse effect, from the last two decades increasingly restrictive policies have been draft, limiting CO_2 gas emissions and promoting processes and technologies for avoiding carbon dioxide to be released to the atmosphere. Most interesting technologies aiming to fit these requirements are focused on conducting strategies for carbon dioxide capture and sequestration, known as Carbon Capture and Storage (CCS) technologies. In order to make easier and cheaper to capture CO_2 from a combustion exhaust gas stream, the latter has to contain primarily CO_2 and H_2O, what is not possible if air is used in the combustion (since CO and NOx will also be formed). Thus, to assure a complete combustion leading to CO_2 and H_2O, O_2 or a N_2-free gas must be used as comburent, by means of the Oxyfuel combustion process.

The use of Oxyfuel combustion technology presents a significant drawback regarding the oxygen supply. Since oxygen is currently produced at large scale by cryogenic air separation, is not economically viable neither the integration of air separation units in the most of existing power plants, nor oxygen provision from commercial suppliers in such a high volumes. For solving this situation, materials like Oxygen Transport Membranes (OTM) have been taken into account. Due to OTM are materials consisting of metallic oxides presenting MIEC properties and O_2 can permeate through their ceramic lattice in the ionic form O^{2-}, therefore it is possible to deliver pure oxygen directly to the combustion chamber and thus achieve a complete combustion. OTM membranes presenting higher oxygen permeation rates are those with perovskite formula $ABO_{3-\delta}$, comprising alkali-earth metal cations in the A-position. However, these materials are very prone to carbonation under CO_2-rich environments, making them unsuitable for Oxyfuel applications due to their chemical and mechanical instability.

Amongst oxygen transport materials, lanthanide substituted ceria materials present a combination of high oxygen-ion mobility and chemical compatibility with water and carbon dioxide at high temperatures. A few reports have studied gadolinium doped ceria ($Ce_{0.9}Gd_{0.1}O_{1.95-\delta}$, CGO) oxygen permeability characteristics for syngas and oxyfuel applications [3, 4] and for oxygen separation [5], obtaining very promising results. However, due to the fact that CGO membranes present low electronic conductivity, there is a big interest in improving its oxygen permeability by means of the use of CGO in dual-phase structures, being combined with pure electronic conducting materials and thus, obtaining higher permeation rates; several studies have been conducted on this matter [6-12]. Other strategies consist of the use of ultra-thin CGO membranes aiming to improve oxygen permeation by means of thickness reduction under reducing environments [3, 4], or considering the deposition of a CGO protective layer on a perovskite membrane [13].

The present chapter is focused on studying the oxygen permeation features of a thin-film $Ce_{0.9}Gd_{0.1}O_{1.95-\delta}$ membrane with 2 mol.% of Cobalt (for the improvement of electronic conductivity) supported on a porous CGO substrate and activated with Pd nanoparticles on dense membrane surface, determining the influence of temperature, sweep gas flow and oxygen partial pressure at feed side. Moreover, it has been studied permeation response under CO_2-containing atmospheres and under reducing environments (presence of methane in the sweep stream).

5.2. Membrane assembly microstructure.

The studied asymmetric CGO membrane was supplied by Risø National Laboratory for Sustainable Energy. This membrane was prepared by means of tape casting, lamination and subsequent co-sintering and cutting. The slurries for the tape casting of the porous support and the membrane were prepared by ball milling in ethanol a CGO powder from Rhodia S.A. (France), a PVB based binder system and a polyethylene imine (PEI, branched, M.W. 10,000, 99% Alfa Aesar) as a dispersant. As a sintering aid and for providing some electronic conductivity it was added 2 mol.% of Co nitrate (cobalt(II) nitrate hexahydrate, 97.7% min, Alfa Aesar) after drying in a desiccator to remove excess water. For the promotion of porosity in the CGO support, it was used about 5% vol.% graphite (V-UF1, 99.9, Graphit Kropfmühl AG, Germany) in the slurry for tape casting. Once tape casted the layers of both the thin film CGO membrane and the porous CGO support, these were combined by lamination by applying heat and pressure on to the tubes between two rolls. Round membranes of about 34 mm diameter were stamped out from the green membrane tapes before sintering. In a binder removal step the organics were removed by a very slow de-bindering profile to avoid damage of the structure. Subsequently, the structure was sintered in air at 1300 °C for 2 h. Finally, the sintered membrane structures were laser-cut to the final dimensions (diameter of 15 mm).

A microstructural characterization was performed on a fresh tape cast CGO membrane by means of Scanning Electron Microscopy. Figure 5.81a, c and d presents some fracture cross sections where the membrane assembly can be clearly identified. Figure 5.81a shows the dense membrane layer on top of the porous substrate. As can be seen, a very high density of this layer has been achieved, with no presence of pores or cracks all along the layer. This fact is confirmed by Figure 5.81b, corresponding to a top view of the dense layer. A distribution of completely-packed CGO grains is depicted, with grain sizes between 200 nm and 1 μm. Alike the cross section, no holes and pinholes were observed, thus ensuring an optimal gas tightness of the membrane (confirmed by a He-leak test). From SEM images it has been determined a thickness of ca. 38 μm for the dense CGO layer and 337 μm for the porous support. Regarding the porous substrate, a porosity in the range of 20-25% has been estimated from image analysis with ImageJ software. Pores size ranges from 0.5 to 3 mm approximately being apparently well interconnected although some of the pores appear isolated.

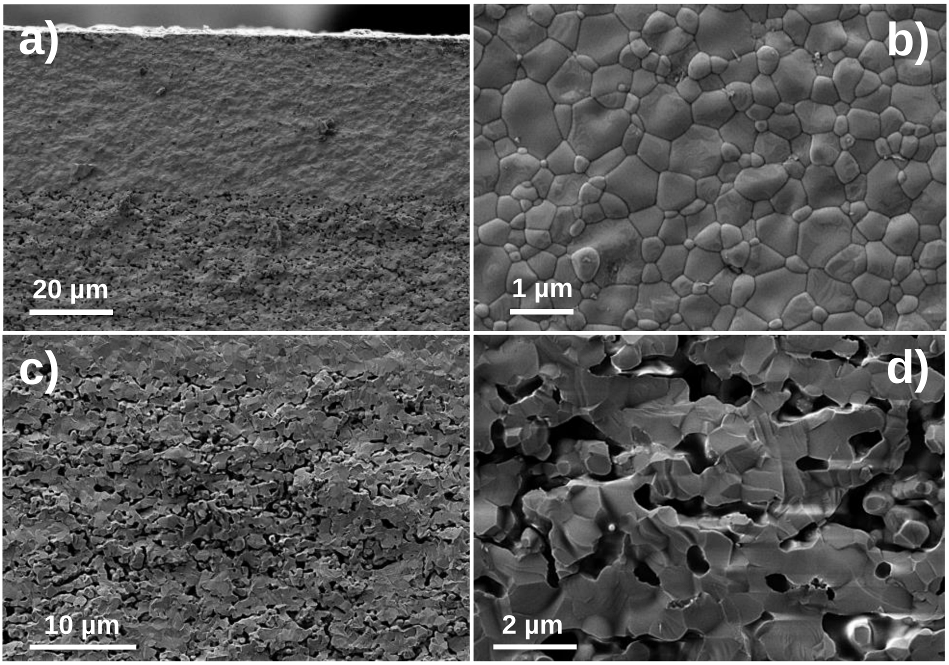

Figure 5.81: SEM images of an as fabricated asymmetric CGO membrane: a) Membrane fracture cross section. b) Surface of CGO dense top layer. c) and d) Fracture cross section details of the porous support.

XRD measurements performed on a fresh asymmetric membrane confirmed the composition of the membrane to be completely formed by CGO, not presenting any secondary phase or impurities, as can be seen in Figure 5.82.

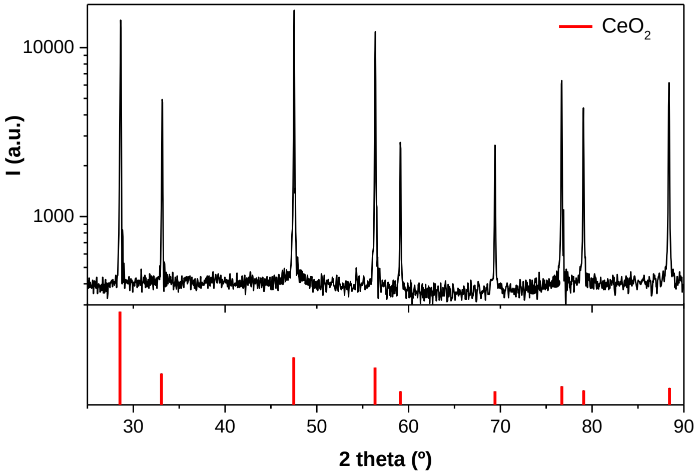

Figure 5.82: XRD pattern of an as-fabricated asymmetric CGO membrane.

5.3. Oxygen permeation tests.

For the conduction of permeation tests it was considered a CGO asymmetric membrane as previously shown in the microstructural characterization. Due to the lower membrane thickness and the expected poor performance of CGO in terms of oxygen fluxes, it was decided to speed surface reactions by means of catalytic activation. This activation consisted of the addition of Pd nanoparticles by dropping onto membrane surface a 1 M dilution containing a Pd precursor (Pd nitrate dyhidrate). After deposition, the catalytic coating was dried at 80 ºC during 1 hour and final sintering was produced in-situ once the membrane was located in the experimental set for the conduction of oxygen permeation tests.

5.3.1. Temperature and sweep gas dependence.

Figure 5.83 depicts the oxygen permeation dependence with temperature (1000-750 ºC) for the asymmetric CGO membrane when using synthetic air as feed stream (300 ml·min^{-1}) and when considering different environments by using diverse sweep gases: Argon, CO_2 and 10% CH_4 in Argon (300 ml·min^{-1}). For the case of Argon sweeping an oxygen flux of ca. 0.35 ml·min^{-1}·cm^{-2} is obtained at 1000 ºC, at lower temperatures $J(O_2)$ drops down to 0.1 and 0.025 ml·min^{-1}·cm^{-2} at 900 and 750 ºC, respectively.

With regard to the membrane performance under other sweep environments, results show an increase in oxygen fluxes when sweeping with CO_2 thus obtaining 0.47 ml·min^{-1}·cm^{-2} O_2 at 1000 ºC, with smaller but similar improvements at 950 and 900 ºC. Despite CO_2 would be expected to cause $J(O_2)$ drops due to carbonates formation on membrane surface and due to competitive adsorption between CO_2 and O_2 on surface actives sites, it has been observed that oxygen permeation improves when switching from Ar to CO_2 for the considered membrane. This effect has been previously observed for the case of the asymmetric LSCF membrane studied in Chapter 4. Alike this case, these improvements can be ascribed to a better sweeping properties of CO_2 at high temperatures (>900 ºC) and the lack of interaction between CO_2 and CGO for the formation of carbonates.

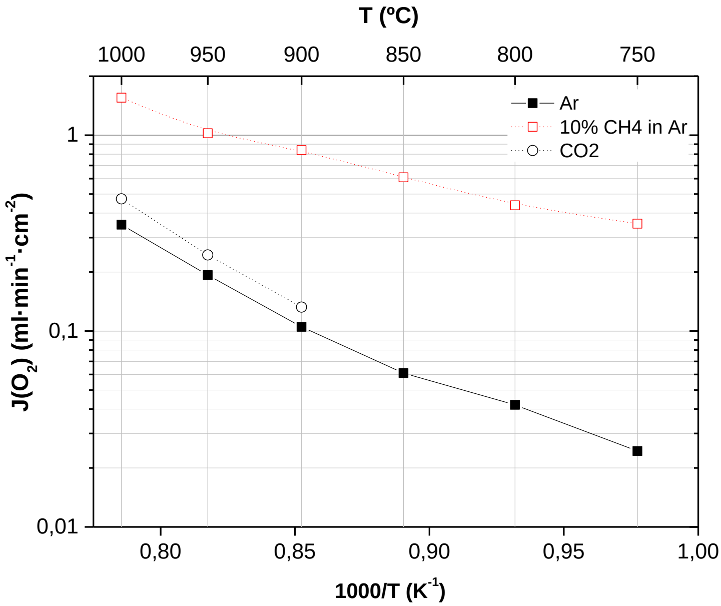

Figure 5.83: Oxygen permeation in dependence of temperature under different sweep environments: Ar, CO_2 and 10% CH_4 in Ar (300 ml·min^{-1}). Synthetic air feeding for all the cases (300 ml·min^{-1})

One of the handicaps of CGO membranes regarding oxygen permeation is the lack of electronic conductivity, mainly under oxidizing environments. This low electronic conductivity leads to poor oxygen fluxes through membrane, despite its good ionic conductivity in such conditions. One way for improving electronic conductivity, and consequently the oxygen permeation, is the use of reducing atmospheres (e.g. methane, hydrogen…). The basis of this phenomenon is the fact that reduced species in the membrane lattice (partial reduction of Ce^{+4} to Ce^{+3}) increase n-type electronic conductivity and thus ambipolar conductivity [4]. Another effect that improves oxygen permeation by the use of reducing sweep gases as methane is the reduction of pO_2 at permeate side in comparison with Argon. This reduction in pO_2 results in a higher pO_2 gradient through membrane thus increasing driving force and eventually implying a gain in $J(O_2)$ [14]. Some authors also relate oxygen permeation improvement in MIEC membranes with some surface modifications under reducing atmospheres leading to an increase of surface specific area and a change in surface catalytic properties [15]. For the present case, we considered a sweep gas consisting of 10% CH_4 diluted in Argon. Under such conditions the oxygen permeation increases significantly from 0.35 to 1.55 ml·min^{-1}·cm^{-2} at

1000 ºC, and from 0.1 to 0.8 ml·min^{-1}·cm^{-2} at 900 ºC. Therefore, the $J(O_2)$ enhancement of CGO membranes by reducing atmospheres induction is proven.

5.3.2. Effect of oxygen partial pressure in feed stream.

Oxygen permeation flux through MIEC membranes is directly related to oxygen partial pressure, as described in Wagner equation. From this equation, it is clear that the more the difference between pO_2 at feed and sweep sides the higher the oxygen permeation. Therefore, increasing oxygen partial pressure at feed side will yield higher oxygen permeation rates.

During these tests, sweep and feed fluxes were maintained at 300 ml·min^{-1}, varying only the oxygen partial pressure in the feed stream. This variation was done by using a mixture of helium and oxygen, considering the following pO_2: 0.21, 0.5 and 0.75 atm. As already demonstrated in a LSCF asymmetric membrane (Chapter 4, section 4.2.3) using helium as diluting gas instead of nitrogen, improves diffusion through porous support; this fact is related with He low molecular size, since blocking of the pores is not produced and oxygen has more paths to diffuse through material. The effect of using He instead of N_2 (synthetic air) is shown in Figure 5.84, obtaining higher oxygen fluxes in all over the range when switching to helium (solid symbols). At 1000 ºC oxygen flux when diluting in He was 0.57 ml·min^{-1}·cm^{-2}, 0.1 ml·min^{-1}·cm^{-2} more than when diluting with N_2. This difference was of ca. 0.06 ml·min^{-1}·cm^{-2} at 850 ºC; despite the fact of being a lower difference in absolute terms it is an improvement of 60% in $J(O_2)$ only if switching from nitrogen to helium as diluting gas. The latter is a sign of the limiting porosity of the support.

The highest obtained oxygen flux correspond to the conditions of pure oxygen feeding (pO_2 = 1 atm), with a value of 1.2 ml·min^{-1}·cm^{-2} at 1000ºC. In this way, switching oxygen partial pressure to 1 atm resulted in an increase of 2.5 times the $J(O_2)$ at 0.21 atm. At 700ºC, oxygen fluxes corresponding to pO_2 between 0.5-1 atm, were in the range 0.16-0.21 ml·min^{-1}·cm^{-2}, quite far from the 0.03 ml·min^{-1}·cm^{-2} measured at the same temperature when feeding with 21% O_2 in N_2. As can be seen in Figure 5.84, oxygen fluxes for each given temperature in the range 1000-700ºC are represented versus pO_2 in the feed side; two main conclusions can be formulated from the observed results: (i) higher pO_2 in feed side yield higher oxygen permeation fluxes, and (ii) at higher temperatures, pO_2 increasing results in higher $J(O_2)$ improvement. This is in agree with Wagner equation, since oxygen fluxes improve more with pO_2 in the high T region due to the bulk diffusion limitation. Consequently, oxygen permeation tests carried out at 700ºC would be limited by surface exchange processes, given that increasing pO_2 at feed side hardly improves $J(O_2)$ even if using pure oxygen.

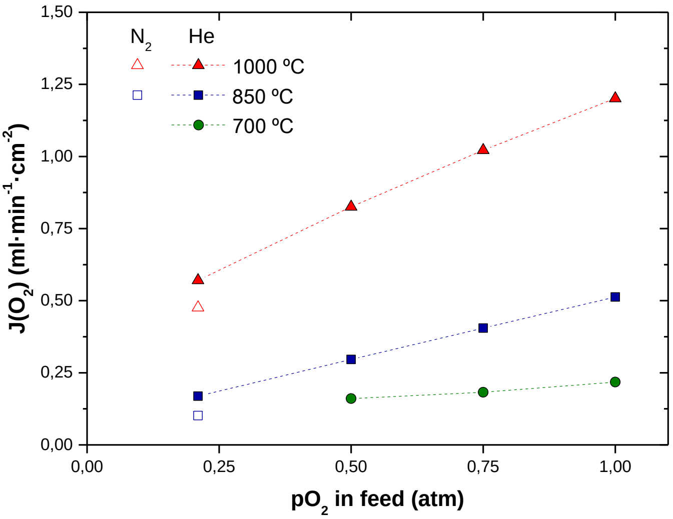

Figure 5.84: Oxygen permeation dependence on pO_2 in feed stream at different temperatures. Fill symbols correspond to O_2/He mixtures whereas void symbols correspond to O_2/N_2 mixtures.

5.3.3. Effect of CO_2 content in sweep stream.

Tests using different CO_2 concentrations in sweep stream have been carried out in order to study permeation response under CO_2 environments. Conditions were varied from a CO_2-free flux to a 100% CO_2 sweep stream. This study was done at three different temperatures: 900, 950 and 1000ºC, feeding with synthetic air (300 ml·min^{-1}) and using different mixtures Ar/CO_2 in the sweep stream (300 ml·min^{-1}).

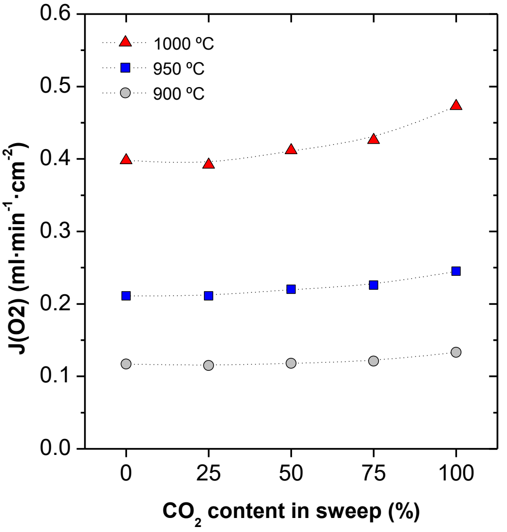

Figure 5.85: Oxygen fluxes in dependence of CO_2 content in sweep stream at different temperatures- Air feeding (300 ml·min^{-1}).

Figure 5.85 depicts the permeation results for the three given temperatures. Highest permeation values belong to 1000ºC tests, as observed in previously performed tests. Regarding CO_2 content in sweep stream, oxygen fluxes improve as CO_2 percentage is raised. Main processes causing oxygen flux decrease when working under CO_2 environments are related with membrane surface carbonation (mainly attributed to the interaction with alkaline earth metal elements in membrane structure [16-18], not present in the studied CGO membrane) and O_2-CO_2 surface competitive adsorption [19]. The first is not expected to occur due to carbonates are not stable at the considered temperatures, as well as there are no chemical elements in CGO structure able to react with CO_2 to form carbonates, so they are not formed. Competitive adsorption between CO_2 and O_2 is more reliable to occur under the considered conditions, however taking into account the observed results it is clear that such a process is not taking place in the considered temperature range. Moreover, CO_2 presence in sweep stream seems to enhance oxygen permeation, increasing even more at both high CO_2 concentration and temperature. $J(O_2)$ increases from 0.39 to 0.47 ml·min^{-1}·cm^{-2} at 1000 ºC when switching from 0 to 100% CO_2 content in sweep, resulting in an improvement of ca. 18.85%. At lower temperatures (950 and 900ºC) this effect is less marked. Once dismissed any significant interaction between CO_2 and surface membrane as the abovementioned carbonation and competitive adsorption processes, it can be assumed that the improving effect it is only depending on the sweep gas flow properties, as previously seen for LSCF membranes in Chapter 4. Thus, neglecting CO_2 side effects not occurring in CGO membrane at 1000-900ºC, CO_2 should have better sweeping properties than Argon, resulting in a more efficient O_2 desorption from membrane surface or/and lower oxygen partial pressure in permeate side, and consequently in higher pO_2 gradients.

5.3.4. Effect of CH_4 content in sweep stream.

In addition to the study performed with the use of a reducing sweep gas in section 5.3.1 of the present Chapter, it has also been considered the evaluation of the oxygen permeation of CGO membrane when exposed to more reducing environments. It is well-known that CGO is a good ionic conductor, but presenting poor electronic conductivity under oxidizing conditions. Nevertheless, when exposed to reducing environments the electronic conductivity increases substantially. This is due to the partial reduction of Ce^{+4} to Ce^{+3}, and due to the increase of the pO_2 gradient. Under such conditions, higher oxygen fluxes are obtained [4]. Therefore, CH_4 content in the sweep stream was varied at 1000 ºC by using different dilutions of CH_4 in Argon (10%, 25%, 50% and 75% of CH_4).

If a significant 5-fold rise improvement in $J(O_2)$ was observed when adding 10% CH_4 (Figure 5.83), then the increase in the CH_4 content enabled to reach much higher oxygen fluxes. Figure 5.86 illustrates clearly this effect, with the achievement of a maximum $J(O_2)$ of 7.8 $ml \cdot min^{-1} \cdot cm^{-2}$ when using a 75% CH_4 in Ar sweep gas. This obtained value corresponds to a 22-fold improvement in the oxygen permeation at 1000 ºC and establishes a good scenario for the application of CGO membranes in the conduction of chemical reactions where CH_4 is participating, such as Partial Oxidation of Methane for the production of syngas, or Oxidative Coupling of Methane for obtaining ethylene.

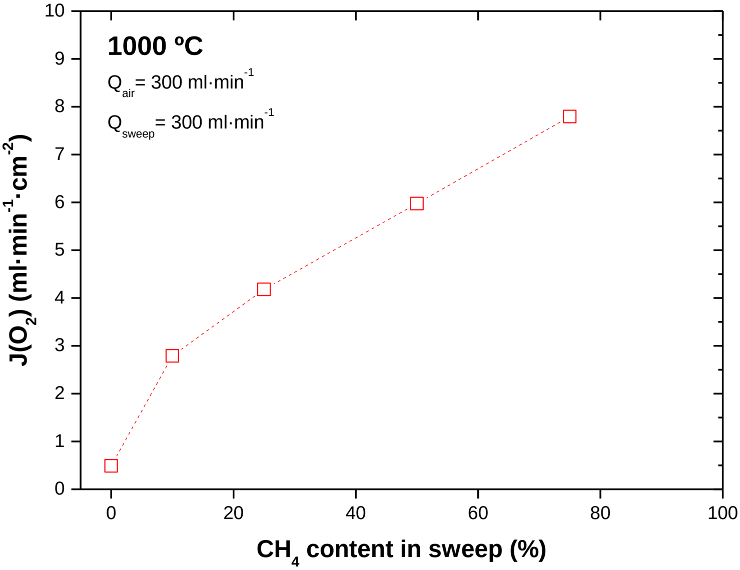

Figure 5.86: Oxygen permeation in dependence of methane content in the sweep stream (300 ml·min^{-1}) at 1000 ºC. Synthetic air as feed gas (300 ml·min^{-1}).

5.3.5. Carbon dioxide stability test.

Asymmetric CGO membrane has been proven not to be affected by working under high CO_2 environments at high temperatures (1000-900ºC), even improving its performance, as observed in point 5.3.3. To characterize broadly CO_2 poisoning resistance of the considered membrane it is very interesting to perform a stability test at lower temperatures, thus confirming whether the membrane is able to work under conditions of industrial application (e.g. oxyfuel processes) without suffering neither chemical or mechanical degradation and nor any loss of yield. A stability test procedure that has successfully demonstrated protective properties of some coatings over CGO membranes when exposed to CO_2 is already described in the following publications [4, 13]. This procedure consists of expositing a membrane to a stream consisting of 15% CO_2 in argon in the sweep side, maintaining this atmosphere during a period of 48 hours at 750ºC. Then, gas sweep is switched to pure argon and temperature is set at 650ºC, afterwards $J(O_2)$ is measured in two consecutive steps, first rising temperature from 650 to 1000ºC, and then back from 1000 to 650ºC, as can be seen in figure below.

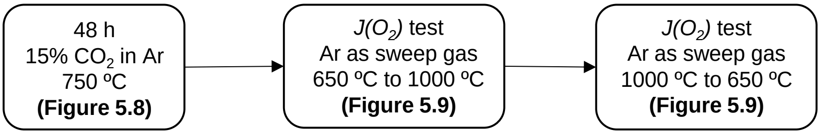

Figure 5.87: Experimental procedure for the CO_2 stability. Synthetic air feeding (300 $ml \cdot min^{-1}$) in all the steps.

Experimental data from these tests is plotted in Figure 5.88 and Figure 5.89. Results in Figure 5.88 correspond to a 48 hours in 15% CO_2 constant $J(O_2)$ monitoring. As can be observed, there is a high dispersion in measured fluxes during all test, due mainly to the complexity of determining accurately $J(O_2)$ values when having such a low permeation fluxes (ca. 0.01-0.02 $ml \cdot min^{-1} \cdot cm^{-2}$), so a high error (ca. ±30%) is present in the available data. Considering averaged data in fractions of 120 minutes, after 48 hours oxygen flux dropped freom 0.022 to 0.018 $ml \cdot min^{-1} \cdot cm^{-2}$ thus evidencing a slight loss of permeation under CO_2 atmosphere at 750ºC. Taking this into account, Pd-activated surface membrane has probably been influenced by CO_2 presence in a way that oxygen permeation is diminished. This statement is confirmed by the results shown in Figure 5.89, where data corresponding to temperature rising and decreasing test are plotted. As abovementioned, after 48 hours of CO_2 stability test sweep gas was switched to pure Ar and temperature was dropped to 650 ºC. Figure 5.89 shows that oxygen permeation is lower in the T-increase test than in the T-decrease test. There are significant differences when comparing oxygen fluxes before and after heating up to 1000ºC, at 650ºC $J(O_2)$ presents a value of 0.007 and 0.013 $ml \cdot min^{-1} \cdot cm^{-2}$ before and after proceeding with test, respectively. It is clear then, that CO_2 is affecting Pd-activated CGO membrane, improving to higher oxygen fluxes after setting system at 1000ºC. The point from where $J(O_2)$ are coincident is above 900ºC, so in case any species lowering oxygen permeation have been formed during CO_2

stability test they should be decomposed or reacted into another when exceeding 900ºC. Another explanation could be related with a catalyst evolution after testing.

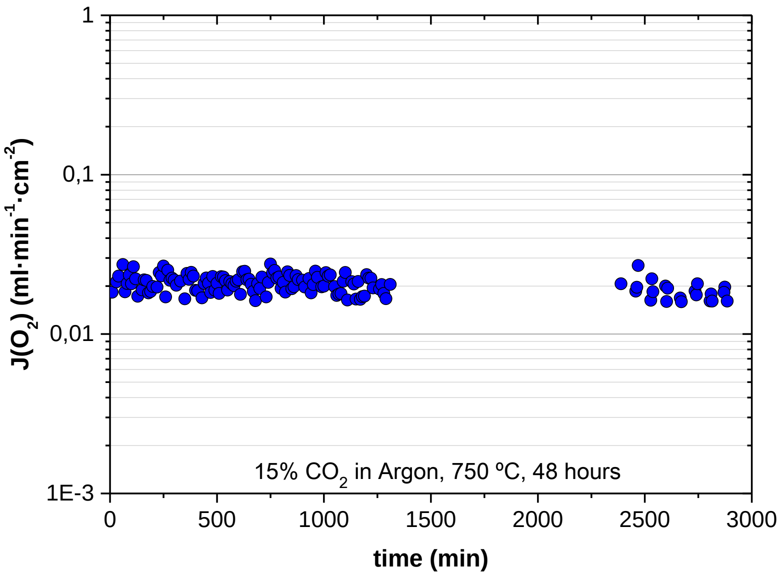

Figure 5.88: Oxygen permeation evolution with time under Air/15% CO_2 in Ar gradient at 750 ºC.

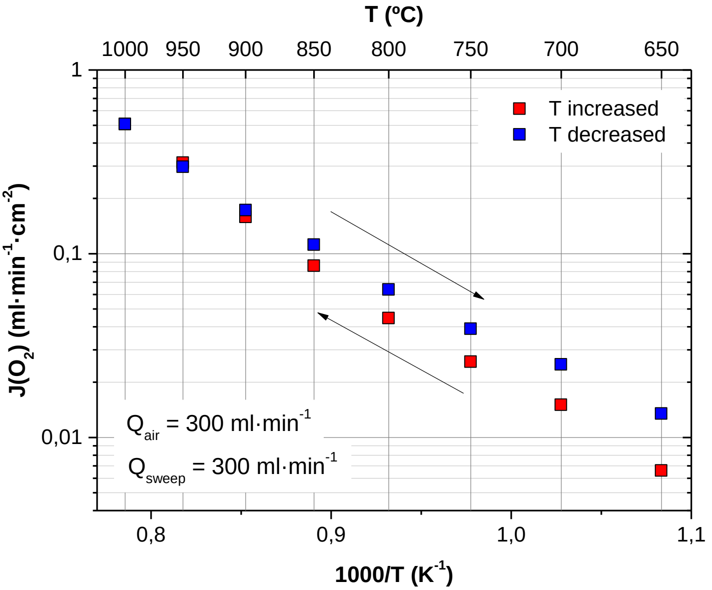

Figure 5.89: Effect of increasing temperature in $J(O_2)$ after 48 hours exposition under 15% CO_2 in Argon.

Aiming to elucidate the effect of the exposure to CO_2 at 750 ºC, an analytical characterization was carried on a CGO powder of nanometric particle size presenting the same formulation as membrane, with an addition of Pd catalyst by impregnation (from a palladium nitrate dilution) trying to achieve similar proportions as for the coating deposited on membrane permeate-side surface (i.e. a 5% wt. Pd). This Pd-impregnated CGO powder was exposed during 48 hours to a 15% CO_2 in Ar stream at 750 ºC in a packed bed reactor, reproducing this way the conditions given in the oxygen permeation test. After CO_2 exposure, the characterization consisted of X-Ray diffraction and Raman analysis of the sample before and after CO_2 treatment.

Regarding to XRD results depicted in Figure 5.90, sample before treatment presents a peak corresponding to Pd-O at 34.05º (★), whereas it disappears in XRD after treatment, then presenting only peaks of metallic Pd^0 (◆). Thus, it would mean that (i) Palladium di-nitrate used as Pd precursor is converted into PdO when temperature is above 800ºC, and (ii) Palladium (II) oxide is reduced into metallic Pd when exposed to CO_2.

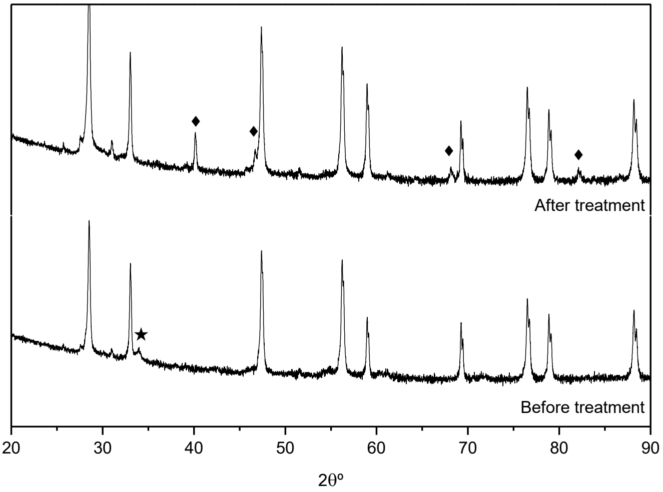

Figure 5.90: XRD measurements before and after CO_2 annealing during 48 hours at 750 ºC.

Before treatment Raman spectra in Figure 5.91 shows a band at 463.4 cm^{-1} belonging to the Raman active F_{2g} mode vibration of CeO_2 [20, 21], a band at 567 cm^{-1} attributed to oxygen vacancies and at 650 cm^{-1} [22] a strong band corresponding to the Pd-O bond [23]. After treatment results evidence Pd-O bond disappearance, probably due to PdO reduction into Pd, since it is not possible to detect Pd-Pd bonds by means Raman spectroscopy.

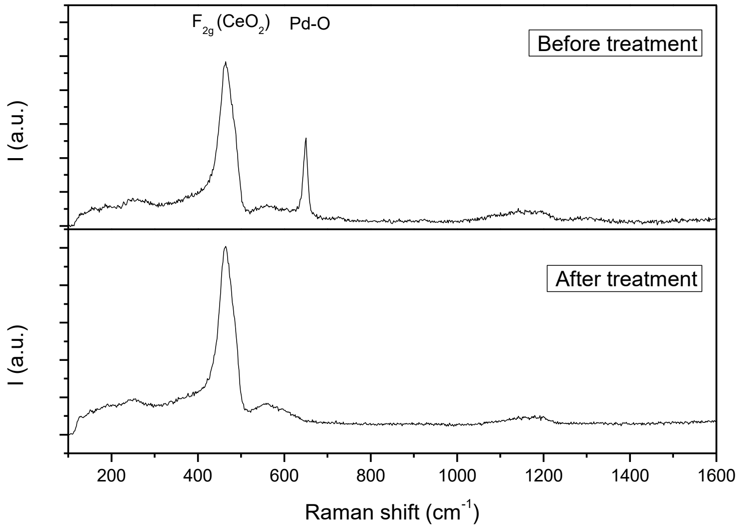

Figure 5.91: Raman spectra of CGO-Pd powder before and after CO_2 annealing.

From the results observed in XRD and Raman characterization it is clear that PdO particles are present after sintering and under clean conditions, getting reduced in presence of CO_2 to metallic Pd at 750 ºC. One of the reasons for explaining the lower permeation values when catalyst is in the form of Pd particles could be related with the better catalytic properties of PdO in the conduction of oxygen surface reactions, as well as change in the dispersion and morphology of the catalyst after CO_2 exposition at high temperatures.

Finally, a post-mortem characterization of the membrane was performed by means XRD and SEM. In Figure 5.92a and b are shown surface images of an as-fabricated and a spent Pd-activated CGO membranes, respectively. As-fabricated membrane was only subjected to air environment during catalyst sintering, whereas tested membrane was exposed to CO_2 and CH_4-containig atmospheres. As can be seen, in the non-tested membrane there is a dispersion of Pd particles covering ca. 20% of membrane surface, with particle sizes of <200 nm membrane surface presents a degradation in the form of 0.5-1 μm holes. Nevertheless, these holes are only affecting membrane surface, since cross-section shown in Figure 5.92c belonging to the same membrane does not present any degradation sign. The surface degradation can be related with a CGO reduction during CH_4 experiment leading to a grain expansion phenomena and eventually to the release of some surface grains. Another reason could be ascribed to the degradation and release of some Pd nanoparticles during the conduction of the tests. Observing Figure 5.92b it can be also distinguished the dispersion and morphology of the deposited Pd nanoparticles (light gray grains). As can be seen the most of the particles present sizes between 200 and 500 nm, although there are larger particles reaching up to

1 μm size. Pd particles dispersion is quite homogeneous and presents a surface coverage of ca. 10% as estimated with ImageJ software. The presence of this big Pd particles could be due to the coalescence of small particles with the time on stream during tests, as observed by Yacou et al. in the case of Pd-activated LSCF hollow fibres [24]. Furthermore, XRD measurements performed on the spent membrane and depicted in Figure 5.92d shows no evidence of secondary phases generated from CGO reaction after testing, only presence of Au peaks belonging to the sealing system employed for achieving leak-free conditions.

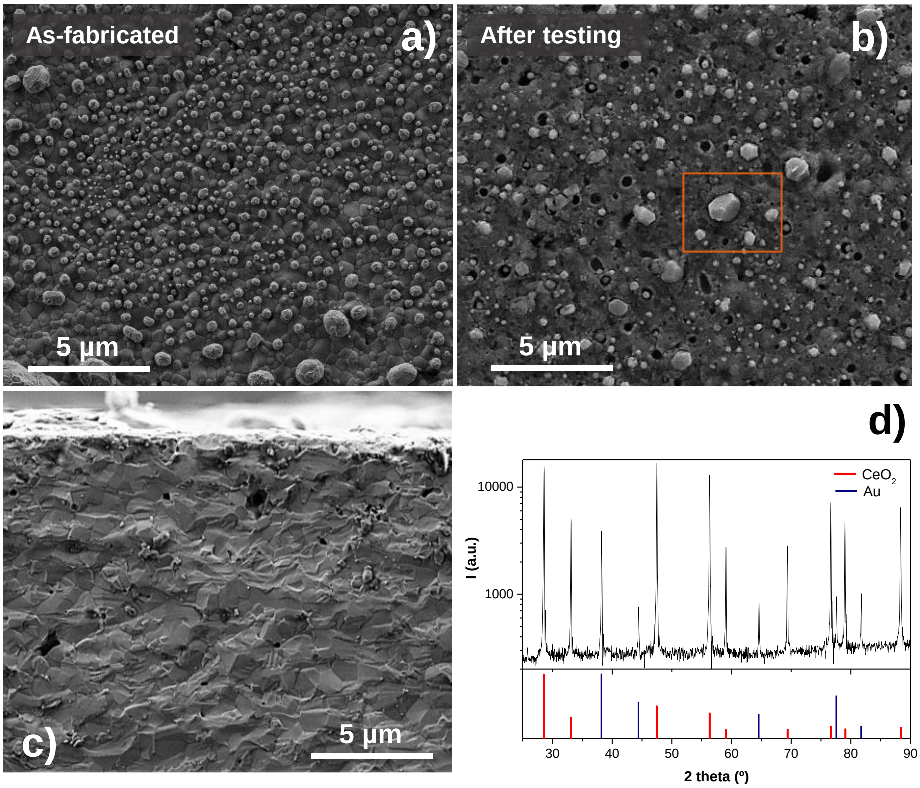

Figure 5.92: a) Surface SEM image of an as-fabricated CGO membrane, b) surface and c) cross section pictures of a Pr-activated CGO membrane after test. d) XRD measurement of CGO membrane after test.

An EDS analysis conducted on a group of Pd nanoparticles (area inside box in Figure 5.92b) is displayed in Figure 5.93. From these results is confirmed that light gray nanoparticles observed on membrane surface are composed by Pd, corresponding the rest of the material to CGO.

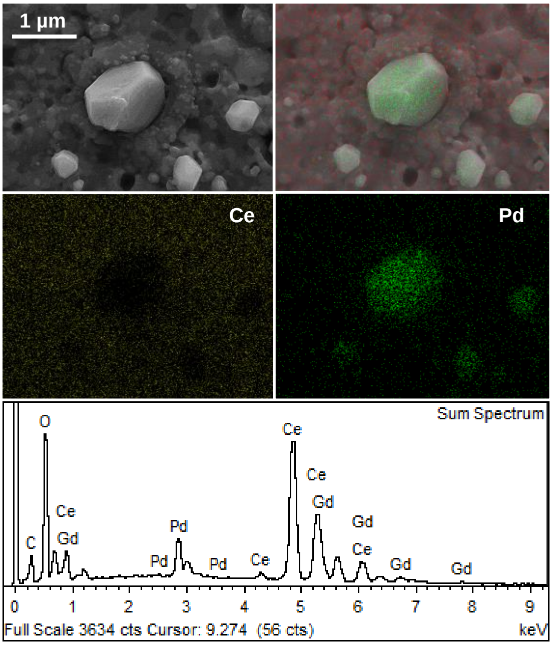

Figure 5.93: EDS mapping analysis performed on Pd particles.

5.4. Conclusions.

A 40 μm thick CGO + 2 mol.% Co supported membrane has been selected for studying its performance as oxygen membrane for the production of oxygen under oxyfuel conditions and for the conduction of chemical reactions involving CH_4. For improving oxygen permeation a well-known active element as Pd has been deposited on membrane surface. A first evaluation of the asymmetric membrane confirmed a good membrane density with total absence of pores that can affect membrane gas tightness. This microstructural study also allowed the evaluation of the membrane assembly and the quantification of support porosity, resulting in a value of 20-25%.

Regarding oxygen permeation, it was studied membrane behavior under different gradients. For the case of Argon sweeping an oxygen flux of ca. 0.35 $ml{\cdot}min^{-1}{\cdot}cm^{-2}$ was obtained at 1000 ºC, whereas 0.47 and 1.55 $ml{\cdot}min^{-1}{\cdot}cm^{-2}$ were obtained when sweeping with CO_2 and 10% CH_4 in Ar, respectively. Oxygen partial pressure variation in feed side resulted in the obtaining of 1.2 $ml{\cdot}min^{-1}{\cdot}cm^{-2}$ at 1000 ºC when pure O_2 is used. CO_2 content effect on membrane performance was also studied, resulting in a beneficial effect of CO_2 sweeping at 1000 ºC and a lack of negative influence at lower temperatures. With the use of highly reducing atmospheres by increasing CH_4 content in sweep stream it has been obtained an outstanding $J(O_2)$ of 7.8 $ml{\cdot}min^{-1}{\cdot}cm^{-2}$ when using a 75% CH_4 in Ar sweep gas, corresponding to a 22-fold improvement in the oxygen permeation at 1000 ºC. Finally, a stability test conducted in the presence of CO_2 showed a slight $J(O_2)$

decrease at 750 ºC after 48 hours of continuous exposure. A T rising and T dropping test under clean conditions (Air/Ar gradient) after CO_2 stability test revealed a different response of the membrane at the same T after heating at 1000 ºC, thus pointing a change in membrane when exposed to CO_2.

Microstructural analysis of the tested membrane showed a good dispersion of Pd catalyst and a surface degradation that only affects membrane morphology in the very outer layer, not observing any degradation in the membrane assembly leading to a membrane breakage.

From the observed results CGO supported membranes could be considered as suitable for their use on applications with harsh environments (CO_2 and reducing atmospheres) due to the high stability features that have been shown. Nevertheless, oxygen fluxes are still very low for practical applications and further work on the catalytic activation, thickness reduction and assembly optimization would be required.

5.5. References.

[1] OECD, Electricity Generation, OECD Publishing.

[2] I.E. Agency, CO2 Emissions from Fuel Combustion 2012, OECD Publishing.

[3] A. Kaiser, S. Foghmoes, C. Chatzichristodoulou, M. Søgaard, J.A. Glasscock, H.L. Frandsen, P.V. Hendriksen, Evaluation of thin film ceria membranes for syngas membrane reactors—Preparation, characterization and testing, Journal of Membrane Science, 378 (2011) 51-60.

[4] M.P. Lobera, J.M. Serra, S.P. Foghmoes, M. Søgaard, A. Kaiser, On the use of supported ceria membranes for oxyfuel process/syngas production, Journal of Membrane Science, 385–386 (2011) 154-161.

[5] H.J. Park, G.M. Choi, Oxygen permeability of gadolinium-doped ceria at high temperature, Journal of the European Ceramic Society, 24 (2004) 1313-1317.

[6] V.V. Kharton, A.V. Kovalevsky, A.P. Viskup, A.L. Shaula, F.M. Figueiredo, E.N. Naumovich, F.M.B. Marques, Oxygen transport in Ce0.8Gd0.2O2−δ-based composite membranes, Solid State Ionics, 160 (2003) 247-258.

[7] I. Kagomiya, T. Iijima, H. Takamura, Oxygen permeability of nanocrystalline Ce0.8Gd0.2O1.9–CoFe2O4 mixed-conductive films, Journal of Membrane Science, 286 (2006) 180-184.

[8] B. Wang, J. Yi, L. Winnubst, C. Chen, Stability and oxygen permeation behavior of Ce0.8Sm0.2O2−δ–La0.8Sr0.2CrO3−δ composite membrane under large oxygen partial pressure gradients, Journal of Membrane Science, 286 (2006) 22-25.

[9] J.S. Yoon, M.Y. Yoon, E.J. Lee, J.-W. Moon, H.J. Hwang, Influence of Ce0.9Gd0.1O2&#xa0;−&#xa0;δ particles on microstructure and oxygen

permeability of Ba0.5Sr0.5Co0.8Fe0.2O3&#xa0;−&#xa0;δ composite membrane, Solid State Ionics, 181 (2010) 1387-1393.

[10] M.B. Choi, S.Y. Jeon, H.J. Hwang, J.Y. Park, S.J. Song, Composite of Ce0.8Gd0.2O2&#xa0;−&#xa0;δ and GdBaCo2O5&#xa0;+&#xa0;δ as oxygen separation membranes, Solid State Ionics, 181 (2010) 1680-1684.

[11] H. Luo, H. Jiang, K. Efimov, F. Liang, H. Wang, J. Caro, CO2-Tolerant Oxygen-Permeable Fe2O3-Ce0.9Gd0.1O2-δ Dual Phase Membranes, Industrial & Engineering Chemistry Research, 50 (2011) 13508-13517.

[12] H. Luo, K. Efimov, H. Jiang, A. Feldhoff, H. Wang, J. Caro, CO2-Stable and Cobalt-Free Dual-Phase Membrane for Oxygen Separation, Angewandte Chemie International Edition, 50 (2011) 759-763.

[13] I. Garcia-Torregrosa, M.P. Lobera, C. Solis, P. Atienzar, J.M. Serra, Development of CO2 Protective Layers by Spray Pyrolysis for Ceramic Oxygen Transport Membranes, Advanced Energy Materials, 1 (2011) 618-625.

[14] Z. Shao, G. Xiong, H. Dong, W. Yang, L. Lin, Synthesis, oxygen permeation study and membrane performance of a Ba0.5Sr0.5Co0.8Fe0.2O3−δ oxygen-permeable dense ceramic reactor for partial oxidation of methane to syngas, Separation and Purification Technology, 25 (2001) 97-116.

[15] T.T. Norton, Y.S. Lin, Transient Oxygen Permeation and Surface Catalytic Properties of Lanthanum Cobaltite Membrane under Oxygen-Methane Gradient, Industrial & Engineering Chemistry Research, 51 (2012) 12917-12925.

[16] J.X. Yi, S.J. Feng, Y.B. Zuo, W. Liu, C.S. Chen, Oxygen permeability and stability of Sr0.95Co0.8Fe0.2O3-delta in a CO2- and H2O-containing atmosphere, Chemistry of Materials, 17 (2005) 5856-5861.

[17] J. Yi, M. Schroeder, T. Weirich, J. Mayer, Behavior of Ba(Co, Fe, Nb)O3-delta Perovskite in CO2-Containing Atmospheres: Degradation Mechanism and Materials Design, Chemistry of Materials, 22 (2010) 6246-6253.

[18] A.A. Yaremehenko, V.V. Kharton, M. Avdeev, A.L. Shaula, F.M.B. Marques, Oxygen permeability, thermal expansion and stability of SrCo0.8Fe0.2O3-delta-SrAl2O4 Composites, Solid State Ionics, 178 (2007) 1205-1217.

[19] A. Yan, B. Liu, Y. Dong, Z. Tian, D. Wang, M. Cheng, A temperature programmed desorption investigation on the interaction of Ba0.5Sr0.5Co0.8Fe0.2O3−δ perovskite oxides with CO2 in the absence and presence of H2O and O2, Applied Catalysis B: Environmental, 80 (2008) 24-31.

[20] W.H. Weber, K.C. Hass, J.R. McBride, Raman study of CeO_{2}: Second-order scattering, lattice dynamics, and particle-size effects, Physical Review B, 48 (1993) 178-185.

[21] S. Wang, W. Wang, J. Zuo, Y. Qian, Study of the Raman spectrum of CeO2 nanometer thin films, Materials Chemistry and Physics, 68 (2001) 246-248.

[22] M. Guo, J. Lu, Y. Wu, Y. Wang, M. Luo, UV and Visible Raman Studies of Oxygen Vacancies in Rare-Earth-Doped Ceria, Langmuir, 27 (2011) 3872-3877.

[23] L. Meng, A.-P. Jia, J.-Q. Lu, L.-F. Luo, W.-X. Huang, M.-F. Luo, Synergetic Effects of PdO Species on CO Oxidation over PdO-CeO2 Catalysts, Journal of Physical Chemistry C, 115 (2011) 19789-19796.

[24] C. Yacou, J. Sunarso, C.X.C. Lin, S. Smart, S. Liu, J.C. Diniz da Costa, Palladium surface modified La0.6Sr0.4Co0.2Fe0.8O3−δ hollow fibres for oxygen separation, Journal of Membrane Science, 380 (2011) 223-231.

6. COMPOSITE OTMs FOR OPERATION IN CO_2/SO_2-RICH GAS ENVIRONMENTS

6. Composite oxygen-transport membranes for operation in CO_2/SO_2-rich gas environments.

6.1. Introduction.

Throughout the present thesis several materials such as BSCF, LSCF and CGO have been studied, determining its performance under application environments for the production of oxygen and the conduction of some chemical reactions (OCM and ODHE). The present chapter is focused specifically on the study of materials for oxyfuel applications where atmospheres containing CO_2 and SO_2 can be met.

As it has been widely commented, OTM are typically made of MIEC ceramic oxides, being the most studied compounds the already characterized perovskites $Ba_{0.5}Sr_{0.5}Co_{0.8}Fe_{0.2}O_{3-\delta}$ (BSCF) and $La_{0.6}Sr_{0.4}Co_{0.2}Fe_{0.8}O_{3-\delta}$ (LSCF). BSCF and LSCF are the materials presenting the highest oxygen fluxes [1, 2]; however, under oxyfuel flue gas conditions (CO_2, H_2O and traces of SO_2) they suffer a dramatic drop in oxygen permeation, as well as a loss in chemical and mechanical stability leading to a material failure, especially for the case of BSCF and under SO_2-containing atmospheres [3-7]. This instability is due to the presence of alkaline-earth elements in the material structure due to carbonation and sulfating reactions taking place [8, 9]. Hence, for practical applications it is necessary to use stable materials delivering high oxygen permeating rates, even when exposed SO_2 and CO_2-containing environments at high temperatures (ca. 850 ºC). Fluorite materials like CGO present good stability behavior when are in contact with these environments, nevertheless as resulted from chapter 5 study, the lack of enough mixed conductivity leads to yield low oxygen permeation values.

Gathering all these pointed features (i.e. stability and high permeation) in one single material is a very challenging issue. Dual-phase composite materials comprising two different crystalline materials, each one providing a specific conductivity (electronic or ionic), is a very interesting option for obtaining membranes with enough mixed conductivity and stability under the referred conditions. The considered configurations for composite membranes are ceramic-metal (*cermet*) [10] [11] [12] and ceramic-ceramic (*cercer*) [13] [14] [15].

Cermet composites consist of a metal (typically Au, Ag, Pd and Pt) providing the electronic conductivity and a ceramic phase presenting high ionic conduction properties. Main drawbacks such as lack of catalytic activity towards oxygen exchange reactions, difficult in the formation of percolative pathways, thermal expansion coefficient mismatch and, specially, the high costs related to the use of noble metals, make these materials as not suitable for their use as OTMs in practical applications [16-18]. On the other hand, *cercer* materials are less affected by these limitations, thus being more suitable for constituing oxygen separation membranes. Besides the transport properties and the costs, other requirements have to be taken into account: (i) both phases must be stable not reacting with each other, and (ii) both compounds must present similar Thermal Expansion Coefficients (TEC) in order to ensure mechanical stability. According to this strategy, several compounds such as fluorites, perovskites, spinels and rocks salts have been combined in dual-phase structures; being an example of this the recent works developed on spinel-fluorite [19-22], perovskite-fluorite [23-25] and doped ZnO with fluorite [26]. These composite systems have exhibited material stability and promising oxygen permeation under oxyfuel-like conditions. Amongst these compositions, one of the most interesting is the consisting of Co-free spinel Fe_2NiO_4 and Gd-doped ceria [27].

Therefore, this chapter focuses on the development spinel-fluorite composites made of Fe_2NiO_4 (NFO) as electronic phase and $Ce_{0.8}Tb_{0.2}O_{2-\delta}$ (CTO) as ionic conductor, and the study of their performance under CO_2 and SO_2-containing atmospheres. The reason for choosing a Tb-doped ceria is due to the reported mixed ionic-electronic conductivity shown by this material at high pO_2 as well as its stability under CO_2-containing atmospheres [28]. With this composition it is expected an enhancement in the oxygen permeation performance, since CTO MIEC properties would allow the generation of additional electronic pathways, acting the whole composite material as an electronic conductor. A first evaluation of fluorite phase content and its dependence on oxygen permeation is presented. Moreover, balanced composite 50%$NiFe_2O_4$ – 50%$Ce_{0.8}Tb_{0.2}O_{2-\delta}$ is in-depth studied under mimicked oxyfuel process conditions, determining oxygen permeation performance and material stability after an extended period of time on-stream under CO_2 and SO_2-containing atmospheres. Furthermore, a catalytic study on dual-phase membrane activation has been performed in order to determine the catalysts presenting best activity for conducting oxygen permeation under oxyfuel conditions. Finally, a thin NFO-CTO membrane was deposited on a porous LSCF freeze-cast support, in order to optimize membrane performance and thus trying to reach oxygen fluxes near the techno-economic targets defined for practical applications, i.e. in the range of 5-10 $ml \cdot min^{-1} \cdot cm^{-2}$ [29].

6.2. Oxygen permeation and stability of dual-phase bulk membranes[9].

6.2.1. Microstructural characterization.

The XRD patterns of NFO-CTO composites at room temperature are shown in Figure 6.94. All diffraction peaks can be assigned to those of the reported NFO cubic spinel (also depicted in the graph for comparison) and CeO_2 fluorite.[30] With increasing CTO phase contents, a slight rise in the intensity of the fluorite peaks can also be observed. The absence of any secondary phases containing elements from NFO or CTO confirms the selective formation of the phases via a one-pot route and their compatibility in the whole temperature range. The cell parameters computed from the patterns do not change significantly for the different composite compositions, indicating that there are not differences in preparation.

---

[9] The study here presented has been published in ChemSusChem journal under the title “Dual-Phase Oxygen Transport Membranes for Stable Operation in Environments Containing Carbon Dioxide and Sulfur Dioxide” DOI: 10.1002/cssc.201500951

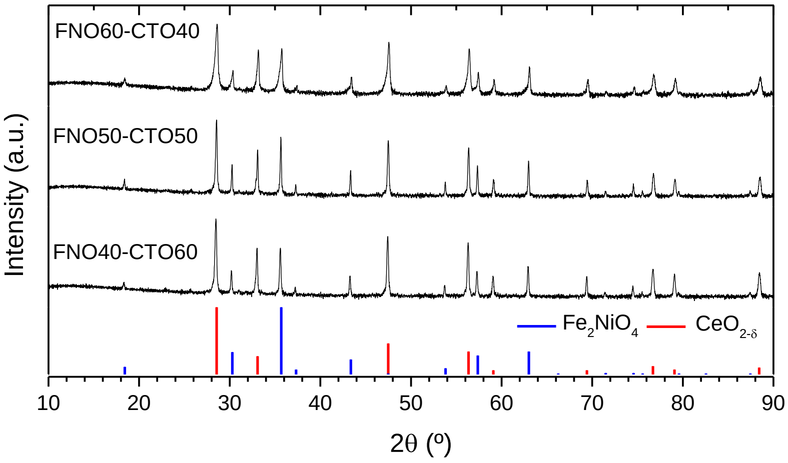

Figure 6.94: XRD patterns of NFO-CTO composite membranes at room temperature compared with CeO_2 fluorite and Fe_2NiO_4 spinel structure.

SEM analysis (Figure 2) shows the structural and morphologic characteristics of the composite membranes. The membrane architecture pictured in Figure 2a reveals that the studied membranes consist of a three-layered structure formed by a 30 μm-thick porous CGO-LSM layer deposited on both sides of a bulk dense NFO-CTO membrane (only cross-section of permeate side is shown). Figure 2b presents a detailed view corresponding to the interface between these two layers on the membrane with 50/50 composition. In this BSD-SEM image, the two phases forming the composite material are clearly identifiable, i.e. NFO as dark grains indicating elements with lower atomic number and CTO as bright grains. Similarly, the two phases comprised in the porous layer can be distinguished as CGO gray grains and LSM bright small grains. No reaction interfaces are detected between catalytic layer and membrane materials, confirming proper chemical compatibility. In addition, neither reactions between the phases nor impurities on the grain boundaries are detected. In Figure 2c, BSD-SEM microstructures corresponding to different fluorite content are displayed, confirming high membrane density for all the considered compositions. Moreover, narrow grain size distribution (centered on 1 μm) and homogeneous distribution of grains can be observed.

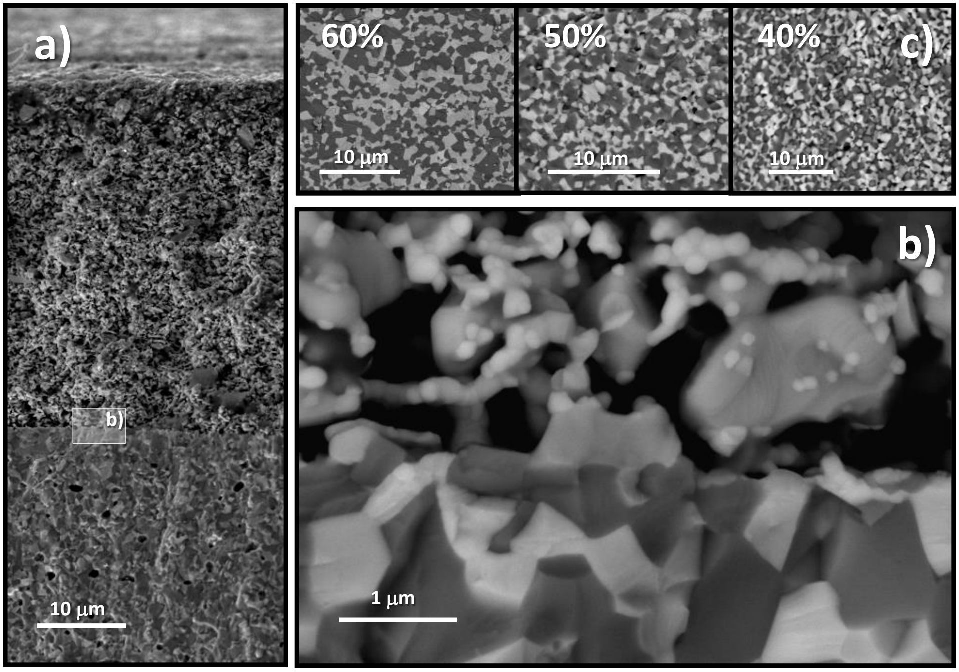

Figure 6.95: a) SEM image of the cross section corresponding to 50% NFO – 50% CTO composite. b) BSD-SEM detailed view of the interface catalytic layer-membrane on 50% NFO – 50% CTO composite. c) BSD-SEM images of composites membranes with different CTO content.

6.2.2. EC measurements.

DC-electrical conductivity results are summarized in Figure 6.96 for the different NFO/CTO volume ratios. Figure 6.96a shows the Arrhenius behavior of the composites. A maximum in total conductivity in air is found for the composition 60NFO-40CTO. The change in the slope is attributed to the influence of CTO, which after 480 °C releases oxygen on increasing temperature, consequently reduces the Tb^{4+} to Tb^{3+} and creates additional oxygen vacancies [31, 32]. The variation of apparent E_a indicates a change in the dominant conduction mechanism, which occurs at lower temperature upon increasing the CTO content.

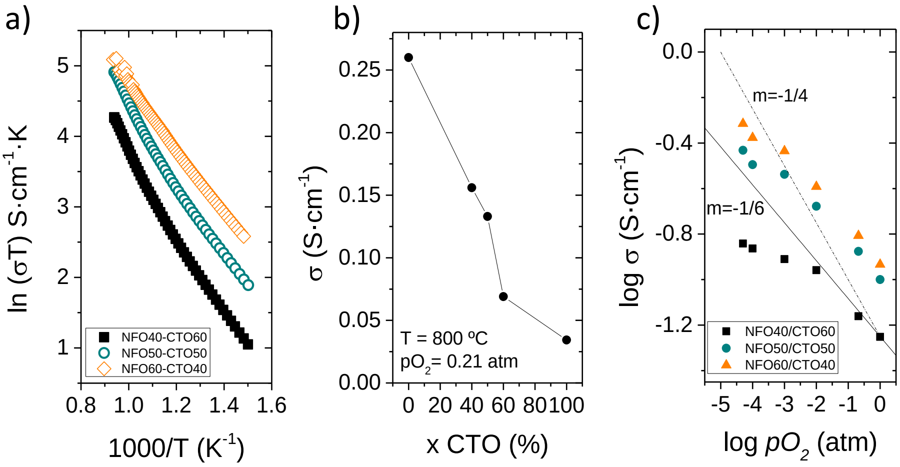

Figure 6.96: a) Arrhenius plot of the total electrical conductivity in air for the considered composite formulations. b) Total electrical conductivity in air of the NFO-CTO composites as a function of the CTO content, measured at 800 °C. c) Logarithm total electrical conductivity at 800 °C as a function of the pO_2.

Figure 6.96b represents the total conductivity in air of the composites as a function of the CTO content, measured at 800 °C. The total conductivity of the composites lies in between the values observed for pure spinel and pure fluorite, decreasing as the CTO content increases [33, 34]. Figure 6.96c presents the logarithm of the total conductivity for different compositions at 800 °C, measured as a function of pO_2. The value of the electrical conductivity in a mixed ionic electronic conductor depends on the balance of the charge carriers of different nature that dominate the conduction process. The plot shows the enhancement in conductivity as the pO_2 decreases, attributed to the increase of n-type electronic conductivity of NFO due to the reduction of Fe^{3+} to Fe^{2+} in the inverse spinel [35]. The conductivity-pO_2 behavior deviates from the -1/4 slope expected for n-type electronic conductors, and the higher the CTO content, the greater the deviation. At 800 °C most of the Tb^{4+} is reduced to Tb^{3+} and the CTO behaves as a pure ionic conductor, whose conductivity is not influenced by the pO_2 and results in an overall less pronounced slope. Therefore, although the total conductivity decreases with the CTO content we can expect a higher ionic conductivity in the composite with 60% CTO, and ensure an electronic percolating network by the NFO increasing the ambipolar conductivity, which will be reflected in the magnitude of the oxygen permeation flux.

6.2.3. Oxygen permeation characterization.

CTO content influence on oxygen permeation

Figure 6.97a reveals the dependence of oxygen flux on temperature for the different dual-phase compositions: 40% NFO – 60% CTO, 50% NFO – 50% CTO and 60% NFO – 40% CTO, in the temperature range 1000-700 ºC. For a better comparison, $J(O_2)$ has been normalized to the thickness and permeation effective area, and then expressed in $(ml \cdot min^{-1} \cdot cm^{-2}) \cdot mm$. The highest permeation fluxes are obtained with the membrane with the highest content of the ion conducting phase (60% CTO), reaching an oxygen flux of 0.25 (ml·min^{-1}·cm^{-2})·mm at 1000 ºC. $J(O_2)$ fits a two-fold Arrhenius behavior presenting two activation energies (E_a): one in the range 1000-800 ºC and other in the range 800-700 ºC. Table 6.11 summarizes the E_a values calculated for the different dual-phase compositions. No significant changes in E_a are observed in the low temperature range when varying CTO phase volume and this suggests that surface exchange is the rate limiting step rather than bulk diffusion. In the high temperature range (1000-800 ºC), the E_a increases as CTO content is increased, as expected if the ion diffusion through the dense composite mostly controls the overall permeation process.

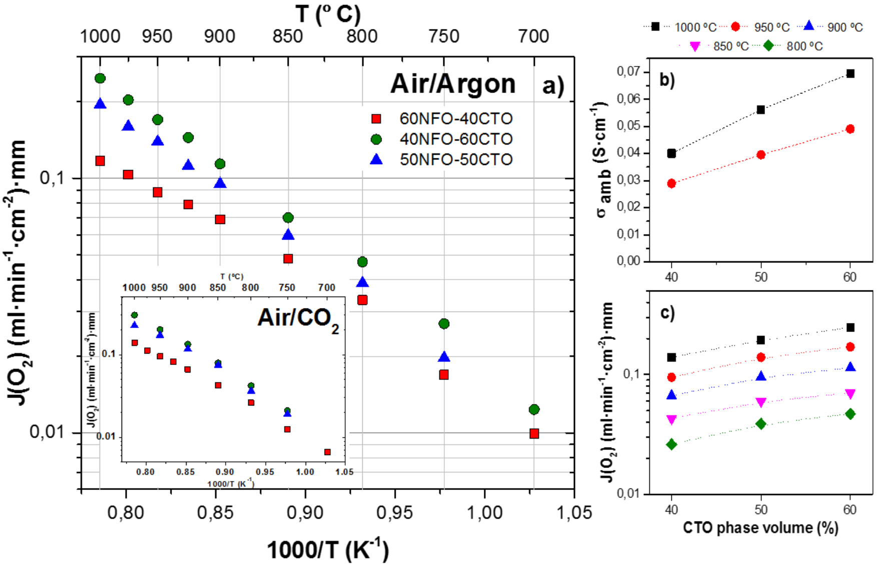

Figure 6.97: a) Oxygen permeation as a function of temperature for different membrane compositions when using 100 ml·min^{-1} synthetic air feeding and 300 ml·min^{-1} Argon sweeping. (Inset: Oxygen permeation in dependence of temperature when sweeping with CO_2.) b) Ambipolar conductivity and c) oxygen permeation in dependence of CTO content (in %) at several temperatures.

The three composite membranes were also tested under different pO_2 gradients (i.e. variation of pO_2 in feed and sweep chambers) at different temperatures. When the charge-carrier transport through the membrane interior dominates [36, 37], the ambipolar conductivity of the composites at 1000 and 950 ºC (Figure 6.97b) can be determined based on the equation:

$$\sigma_{amb} = JO_2 \cdot \frac{4^2F^2L}{RT} \cdot \left[ln \frac{pO_2'}{pO_2''} \right]^{-1}$$

where pO_2' and pO_2'' are the oxygen partial pressures at feed and sweep side, respectively, L is the membrane thickness in cm, F is Faraday's constant, T is temperature in K and $J(O_2)$ is the oxygen permeation expressed in mol·s^{-1}·cm^{-2}. As can be seen in Figure 6.97b, σ_{amb} increases with CTO content, contrarily to the total conductivity, confirming that ionic conductivity is limiting the oxygen permeation for CTO-NFO composites. Thus, higher oxygen fluxes are obtained when the ratio spinel/fluorite is lowered given that the spinel phase percolates through the membrane thickness [38, 39].

Oxygen permeation tests were also performed with pure CO_2 as sweep gas (inset of Figure 6.97a). Sweeping with Argon and CO_2 leads to a similar thermal behavior, i.e. oxygen evolution fits a 2-fold Arrhenius model for all the three membranes. However, E_a present higher values when switching to CO_2 over the whole temperature range tested, revealing a stronger influence of surface exchange steps under CO_2 atmospheres. Only 50% NFO – 50% CTO membrane presents a slight decrease in E_a at high temperatures. In the same temperature range, the thermal evolution is steeper for the 40% CTO membrane. On the other hand, the use of CO_2 improves oxygen fluxes at 1000 ºC for all the cases, achieving a $J(O_2)$ of 0.3 (ml·min^{-1}·cm^{-2})·mm for the 40% NFO – 60% CTO membrane and this beneficial effect is attributed to better fluid dynamics and thermal emissivity of CO_2 gas. In the low temperature region, similar activation energies are observed for all three membranes and this can be related to an equal CO_2 competitive adsorption limitation (gas exchange step) occurring in CGO-LSM activation layer independently of the composite formulation.

Table 6.11: Apparent activation energy (E_a) (KJ·mol^{-1}) derived from oxygen permeation measurements for different dual-phase compositions (pO_2 in feed = 0.21 atm, Q_{feed} = 100 ml(STP)·min^{-1},Q_{sweep} = 300 ml(STP)·min^{-1})

Membrane composition	Sweep gas	E_a (kJ·mol^{-1})	
		High T range	Low T range
60NFO-40CTO	Argon	70	112
	CO_2	92	126
50NFO-50CTO	Argon	91	--
	CO_2	84	136
40NFO-60CTO	Argon	95	110
	CO_2	103	127

CO_2-SO_2 effect on $J(O_2)$ in a 50NFO-50CTO membrane

An in-depth analysis of the separation performance was performed using the 50% NFO – 50% CTO membrane aiming to validate the suitability of these composite materials in operation in oxy-combustion industrial plants. Oxygen permeation tests were performed under harsh environments mimicking combustion flue gases. In a first approach, CO_2 effect on membrane performance was studied. Figure 6.98a shows $J(O_2)$ permeation results under different concentrations of CO_2 in the sweep stream (300 $ml \cdot min^{-1}$) at 1000, 850 and 750 ºC. In all cases, CO_2 content does not seem to affect negatively the oxygen permeation, even improving $J(O_2)$ at 1000 and 850 ºC. This enhancing effect associated to CO_2 sweeping has been previously observed above 900 ºC in other studies carried out on a 60% NFO-40% CTO membrane [40] and on supported LSCF membranes [2, 41]. This is mainly due to the better sweeping properties in comparison with Ar, however, it is noteworthy the observed positive effect of using CO_2 at 850 ºC (typical oxy-combustion temperature conditions), where oxygen fluxes increase from 0.11 $ml \cdot min^{-1} \cdot cm^{-2}$ at 0% CO_2 up to 0.13 $ml \cdot min^{-1} \cdot cm^{-2}$ under full-CO_2 conditions. At 750 ºC no significant variation in oxygen permeation is observed when adding CO_2 to the sweep gas, maintaining a value around 0.025 $ml \cdot min^{-1} \cdot cm^{-2}$. Under similar conditions (CO_2 sweeping at 850 ºC) and in the case of perovskite-fluorite composites, other authors have reported oxygen fluxes of 0.21 and 0.25 $ml \cdot min^{-1} \cdot cm^{-2}$ for $Ce_{0.9}Pr_{0.1}O_{2-\delta}$-$Pr_{0.6}Sr_{0.4}Fe_{0.5}Co_{0.5}O_{3-\delta}$ [21] and $Ce_{0.85}Gd_{0.1}Cu_{0.05}O_{2-\delta}$ - $La_{0.6}Ca_{0.4}FeO_{3-\delta}$ [25] membranes, respectively.

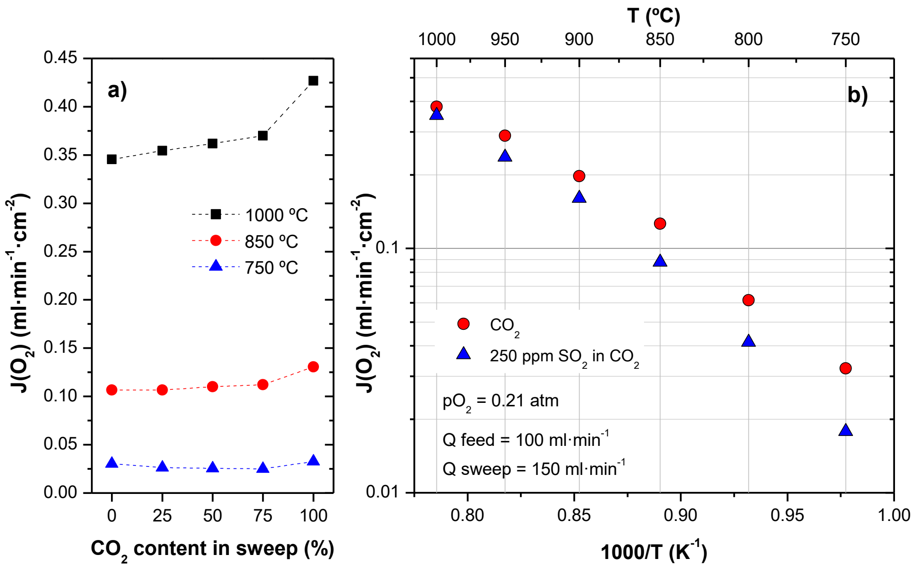

Figure 6.98: a) Oxygen permeation of 50% NFO – 50% CTO membrane as a function of CO_2 content in sweep stream (300 $ml \cdot min^{-1}$) when feeding with synthetic air (100 $ml \cdot min^{-1}$) at several temperatures. b) Oxygen permeation of 50% NFO – 50% CTO membrane in dependence of temperature when sweeping with 100% CO_2 and 250 ppm SO_2 in CO_2 (150 $ml \cdot min^{-1}$). Synthetic air feeding (100 $ml \cdot min^{-1}$).

Further tests for validating NFO-CTO composite materials in oxy-combustion applications consisted of checking membrane performance and stability in SO_2 presence. Figure 6.98b displays the oxygen permeation in dependence of temperature (1000-750 ºC) when feeding with synthetic air (100 $ml \cdot min^{-1}$) and sweeping with 100% CO_2 and 250 ppm SO_2 in CO_2 (150 $ml \cdot min^{-1}$). These results evidence a loss in permeation, being this drop more dramatic as temperature is decreased. An evolution of $J(O_2)$ as a function of time for the tests corresponding to Figure 6.5b data is given in Figure 6.99. Here, it can be seen that when adding SO_2 the oxygen permeation is decreased, being stabilized after 120 minutes of continuous exposure. Despite this reduction in oxygen permeation, $J(O_2)$ is still presenting acceptable values (0.09 $ml \cdot min^{-1} \cdot cm^{-2}$ at 850 ºC) since oxygen flux is not dropping dramatically or becoming negligible, what is the typical behavior of state-of-the-art oxygen membranes when exposed to sulphur containing environments [8, 42-44]. Moreover, when returning to clean conditions (Ar sweeping) after SO_2 exposure, $J(O_2)$ recover initial values in the most of the cases. An estimation of E_a was also done, which is given in Table 6.12. E_a values increase when adding SO_2 and CO_2 to the sweep gas on permeate side, due to the stronger limitation in the surface exchange. Indeed, this increase is related to the competitive adsorption between O_2, CO_2 and SO_2, since the two latter block oxygen active sites due to the increasing surface coverage with decreasing temperature, especially for the case of SO_2 which adsorbs very strongly with respect to O_2 and CO_2.

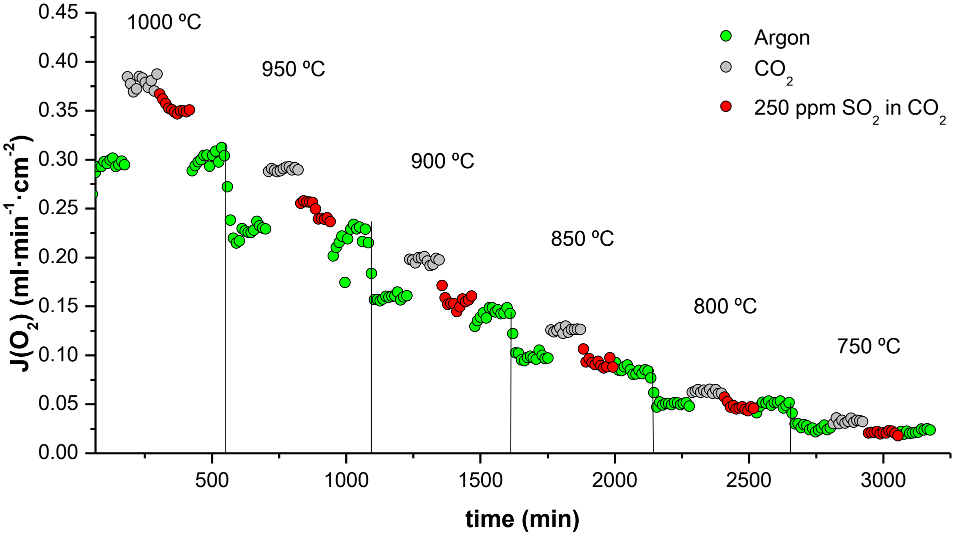

Figure 6.99: Oxygen permeation evolution with time, at different sweeping conditions and temperatures of 50% NFO -50% CTO membrane. From these results Figure 6.98b is built.

Table 6.12: Apparent activation energy (E_a) (KJ·mol^{-1}) derived from oxygen permeation measurements for different sweeping conditions (pO_2 in feed = 0.21 atm, Q_{feed} = 100 ml(STP)·min^{-1},Q_{sweep} = 150 ml(STP)·min^{-1})

Sweep used	E_a (High T range)	E_a (Low T range)
Argon	79	133
CO_2	86	137
250 ppm SO_2 in CO_2	98	140

Electrochemical impedance spectroscopy measurements performed on a 60% NFO – 40% CTO electrode (explained more in detail in section 6.3.1) confirmed unambiguously that SO_2 affects surface exchange processes since SO_2 presence enlarges dramatically the magnitude of resistive processes appearing at low frequencies, likely due to a SO_2 adsorption and blocking of active sites for oxygen evolution. In terms of oxygen permeation, this would explain the observed loss in performance. Nevertheless, when withdrawing SO_2 from the gas stream, the electrochemical performance returns to its initial state, proving that the composite material structure is not irreversibly altered upon sulfur exposure and then, the considered system is fully stable for this application.

According to the obtained results, dual-phase membrane based on 50% NFO - 50% CTO composition shows very good performance in terms of oxygen permeation when working under realistic oxy-combustion conditions. Chemical and mechanical stability, as well as constant oxygen delivering during extended periods of time, are the main issues to be fulfilled in order to consider industrial implementation of the studied membrane. Thus, further stability tests at 850 ºC were conducted. Figure 6.100a and 6.7b show $J(O_2)$ evolution with time under different sweeping conditions: Argon, 100% CO_2 and 250 ppm SO_2 in CO_2. In the stability test shown in Figure 6a, membrane was maintained during 40 hours under full-CO_2 environment, as a result oxygen flux progressively improves from 0.13 up to 0.14 ml·min^{-1}·cm^{-2}. The reason for this enhancement is not completely clear, although similar improvements with time in $J(O_2)$ under CO_2 sweeping have been also reported by several studies on composite membranes[19, 22, 26, 27, 40, 45]. This can be ascribed to a surface or/and grain boundary processes, although Yun et al. suggest the relation with an effect known as "electrode activation" [23] that can be explained by the activation of the CGO-LSM catalytic layers. When switching again to Argon sweeping, $J(O_2)$ returns to the initial value before CO_2 exposure. After performing the tests corresponding to Figure 6.98b, it was run a second stability test (Figure 6.100b) consisting of the use of the sweep gas containing CO_2 and 250 ppm of SO_2. Such conditions were maintained during 12 hours, throughout which $J(O_2)$ dropped slightly from 0.103 to 0.095 ml·min^{-1}·cm^{-2}, where it stabilized. The observed performance of the membrane when exposed to these harsh environments (i.e. no significant loss of permeation in presence of CO_2 and SO_2)

proves NFO-CTO dual-phase membrane as suitable material for its use in OTM modules for oxy-combustion applications.

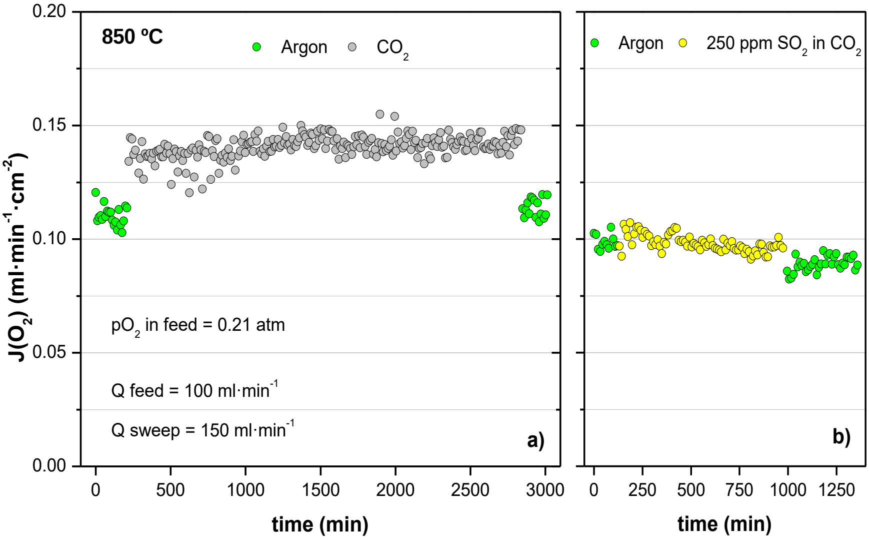

Figure 6.100: a) Oxygen permeation of 50% NFO – 50% CTO membrane at 850 ºC in function of time under Argon and CO_2 sweeping (150 ml·min^{-1}). b) Oxygen permeation of 50% NFO – 50% CTO membrane at 850 ºC in dependence of time under Argon and 250 ppm SO_2 in CO_2 sweeping (150 ml·min^{-1}).

Post-mortem analysis

Finally, XRD, BSD-SEM and EDS analysis were carried out on the spent membrane. In order to evaluate if continuous CO_2/SO_2 exposure affected membrane structure, leading to the formation of carbonates, sulfates, membrane cracks or any morphologic change indicating that composite material is not stable. BSD-SEM image in Figure 6.101a reveals no signs of secondary phases beyond the initial NFO, CTO, CGO and LSM, as well as no reaction interfaces or cracks on dense membrane. Furthermore, EDS mapping (Figure 6.101b) on the catalytic layer and the membrane support reveals the absence of sulphur species, confirming the membrane stability under the tested conditions. XRD analysis on permeate membrane side (Figure 6.101c) presents only patterns corresponding to the membrane constituent phase. The presence of additional peaks belonging to Au is due to the use of gold gaskets. With regard to another studied materials, a work carried out on doped ZnO-CGO composite showed material stability after 2 hours under 100 ppm SO_2 exposition at 850 ºC [26]. Another experiments conducted on $MnCo_{1.9}Fe_{0.1}O_4$-$Ce_{0.8}Gd_{0.2}O_{2-\delta}$ and $Cu_{0.6}Ni_{0.4}Mn_2O_4$-$Ce_{0.8}Gd_{0.2}O_{2-\delta}$ composites also demonstrated material chemical stability after a dwell time of 24 hours under 95% CO_2, 5% O_2 and 400 ppm SO_2 at 900 ºC [22]. Nevertheless, the exposed area to CO_2 and SO_2 was affected by degradation, becoming porous. Therefore, the NFO-CTO material presented in this work can be considered as one of the most promising options amongst the currently studied materials for oxyfuel applications, since chemical and mechanical stability has been proven as well as its performance in terms of oxygen permeation.

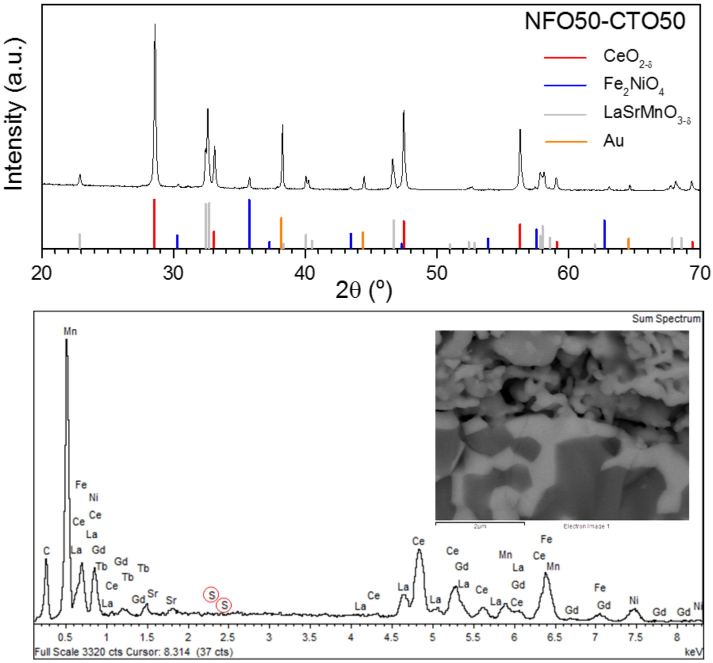

Figure 6.101: a) BSD-SEM picture corresponding to 50% NFO -50% CTO membrane interface after testing. b) EDS mapping corresponding to area depicted in Figure 5a after testing. c) XRD patterns of 50% NFO -50% CTO membrane after testing.

6.3. Catalytic study on the activation of the system 60NFO-40CTO.

Since oxygen permeation becomes limited by surface exchange reactions, especially at low temperatures and when reducing membrane thickness [46], it is possible by modifying membrane surface to achieve an improvement in oxygen fluxes [47, 48]. One of the most considered options is the addition of porous layers on membrane surfaces [1]. Proceeding with this strategy on oxygen membranes allows the enhancement in surface exchange reactions rates mainly due to the increase of surface specific area. A membrane presenting a larger active area also presents a higher number of active sites for oxygen reactions and a higher Triple Phase Boundary (TPB) length, and therefore, more sites available for O_2 molecules to be incorporated/released to/from membrane. A membrane architecture consisting of 30 μm thick porous 60NFO-40CTO layers deposited on both sides of a bulk dense 60NFO-40CTO membrane is considered for this study. Porous layers are deposited on membrane surfaces by means of screen-printing technique and subsequently calcined at 1100 ºC for 2 hours.

However, the performance of these systems will remain limited by the oxygen reaction kinetics involved in the oxygen dissociation/recombination and adsorption processes ($O_2(g) \rightarrow O_2(ad)$ and $O_2(ad) \leftrightarrow 2O^{2-} + 4e^-$). Therefore, by using suitable elements presenting redox character and adsorption properties these reactions can be boosted and thus, the oxygen permeation can be improved. Several oxides containing some lanthanides and metals meet these requirements. For this study, catalytic activation with Co, Ce, Tb, Pr, Sm, Nb, Mo, Zr and Al has been considered. Activation was carried out by dropping 2 M solutions of the element precursors (typically nitrates) on the 60NFO-40CTO porous backbone, occurring the infiltration by capillarity. Once infiltrated and dried, the samples are subsequently sintered at 850 ºC during 2 hours.

Initially, electrochemical behavior of catalytically activated 60NFO-40CTO porous backbones was studied as electrodes on symmetrical cells. These symmetrical cells consist of a CGO-Co electrolyte coated with 30 μm thick porous 60NFO-40CTO electrodes deposited on both sides (manufacturing procedure explained in sections 2.2.1 and 2.2.4). The oxygen activity under different environments representative of real oxyfuel conditions and its response in terms of impedance variation has been characterized by means of Electrochemical Impedance Spectroscopy. As explained in section 2.5.2 of the present thesis, EIS can provide information about the processes taking place in the catalytic layer (gas diffusion, surface exchange reactions, adsorption…) and processes related with the transport within the material (grain and grain boundary). Therefore, this technique can be very useful in the determination of the limiting processes under different conditions.

After the electrochemical characterization of symmetrical cells and once identified the most interesting catalysts, a similar procedure was followed on membranes, studying the effect of catalytic layer addition and the activation with catalysts in the oxygen permeation. Analogous atmospheres were considered for this study, thus determining the improving effect of adding catalytic layers.

6.3.1. Electrochemical characterization of reference case.

As aforementioned, 30 μm thick 60NFO-40CTO porous structures have been characterized as electrodes in CGO-Co symmetrical cells. 60NFO-40CTO composition was selected as reference case for the conduction of EIS experiments and for the activation of membranes due to the higher conductivity that has been obtained with this composition (Figure 6.96), that can lead to the achievement of better surface kinetics performance in comparison to the other compositions. Figure 6.102d shows a cross-section of the considered system. Electrochemical behavior was studied by EIS at 850 ºC under different environments, mimicking different situations that can be met in a membrane under realistic operation conditions. The steps followed for performing the electrochemical characterization are indicated in Table 6.13.

Table 6.13: EIS test conditions.

Step	Environment	Gas composition	Duration
1	Feed side	21% O_2 in N_2	90 minutes
2	Sweep side (clean conditions)	5% O_2 in N_2	90 minutes
3	Sweep side (oxyfuel conditions)	5% O_2 in CO_2	90 minutes
4	Sweep side (oxyfuel conditions)	250 ppm SO_2, 5% O_2 in CO_2	250 minutes
5	Sweep side (Recovery, clean conditions)	5% O_2 in N_2	10 hours

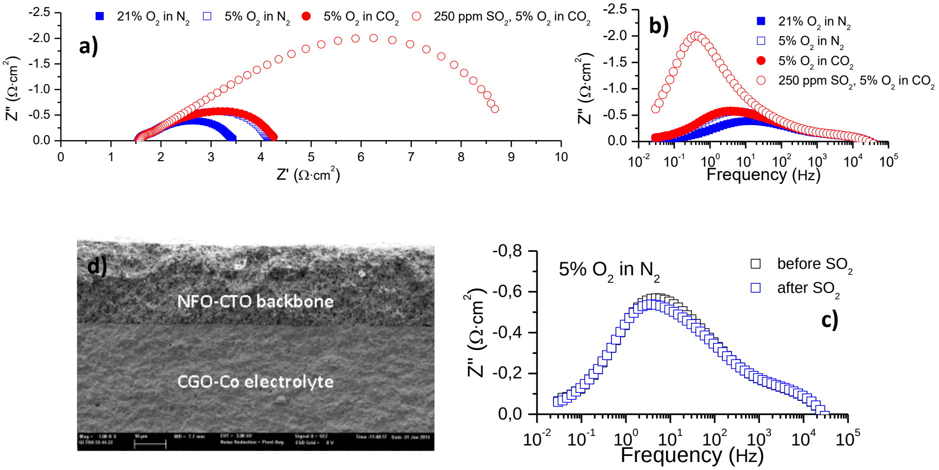

Figure 6.102: a) Nyquist plot and b) BODE plot at different gas compositions at 850 ºC for a 60NFO-40CTO electrode. c) BODE plot corresponding to electrode performance under 5% O_2 in N_2 before and after SO_2 exposure at 850 ºC. d) SEM image of the cross-section corresponding to the symmetric cell measured by means of EIS.

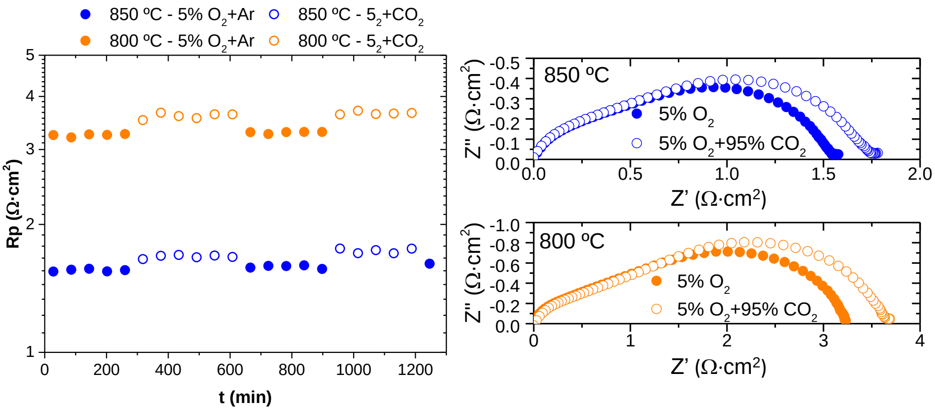

Figure 6.103: Polarization resitance (left) and Nyquist plots (right) in dependence of gas composition and temperature.

EIS results are shown in BODE and Nyquist diagrams depicted in Figures 6.8a and 6.8b, respectively. As it can be seen, lower polarization resistance (R_p) values are obtained under air feeding conditions. When decreasing O_2 content from 21% to 5% then R_p increases from 1.85 to 2.69 $\Omega\cdot cm^2$, thus confirming that higher O_2 concentrations favor oxygen surface semi-reactions. Moreover, when switching from N_2 to CO_2, only a slight increment of 0.1 $\Omega\cdot cm^2$ in R_p is observed at 850 ºC (Figure 6.103 left), this occurring at low frequencies (Figure 6.102b). Since this effect is reversible, it can be associated to CO_2 competitive adsorption on O_2 active sites. No important alterations in $J(O_2)$ would be expected according to the R_p change magnitude.

On the other hand, a dramatic change in R_p is observed when adding 250 ppm of SO_2, with a significant increase up to 7.09 $\Omega\cdot cm^2$. Furthermore, this increase is related with low frequency processes, as can be noted in Figure 6.102b. Following the same statements used for explaining the case of CO_2, the presence of SO_2 would be hindering the surface exchange reactions taking place on the oxygen active sites. The main reason can be ascribed to SO_2 adsorption and blocking of oxygen active sites on composite surface, thus inhibiting oxygen activation. Attending to the observed behavior, this adsorption would be stronger than in the case of CO_2. Nevertheless, this negative effect is also reversible and it is not affecting the composite structure since once SO_2 is withdrawn the impedance values are recovered, as can be seen in Figure 6.102c.

6.3.2. Electrochemical characterization of activated cases.

Once 60NFO-40CTO porous backbone was characterized under the application environments, the next step consisted of the catalytic activation with several elements. The aim of this activation is to determine the cases presenting best electrochemical behavior and therefore, the potential candidates for the activation of OTMs.

Different catalysts have been considered: mainly lanthanides (Ce, Pr, Sm, Tb), transition metals (Zr, Nb, Mo, Co) and other metals (Al). These catalysts were infiltrated in the electrodes using precursor dilutions of the elements. After infiltration, samples were sintered in air at 850 ºC. Figure 6.104 shows XRD patterns of reference 60NFO-40CTO case and some activated cases after infiltration and characterization. As can be seen, different element oxides are formed, no signs of carbonates nor sulfates were found in any of the backbones after EIS tests, however they could be present but below the device limit detection.

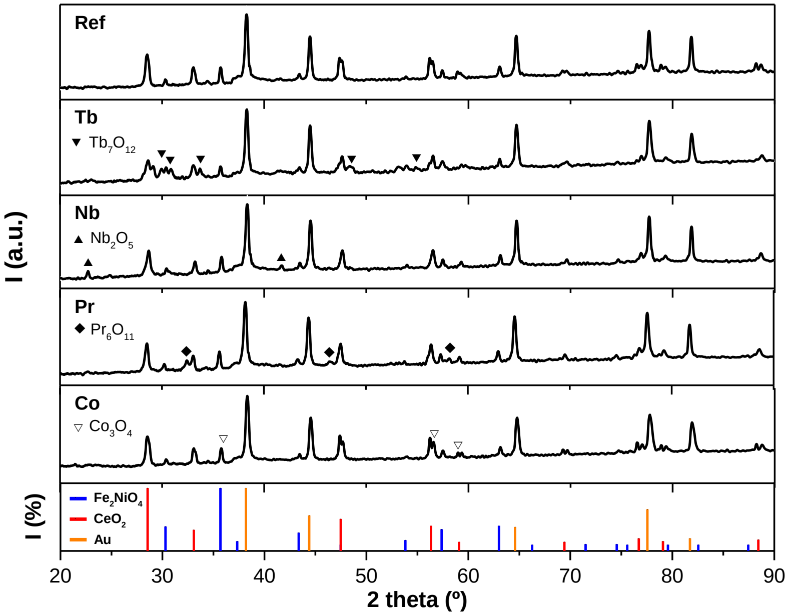

Figure 6.104: XRD patterns of some 60NFO-40CTO activated cases and a comparison with respect the not activated case (Ref). Au peaks belong to gold contacts.

The tests consisted of EIS measurements carried out at 850 ºC, like those performed for the reference case and following the steps depicted in Table 6.13. R_p values presented in Figure 6.105 correspond to the last measurement of each step.

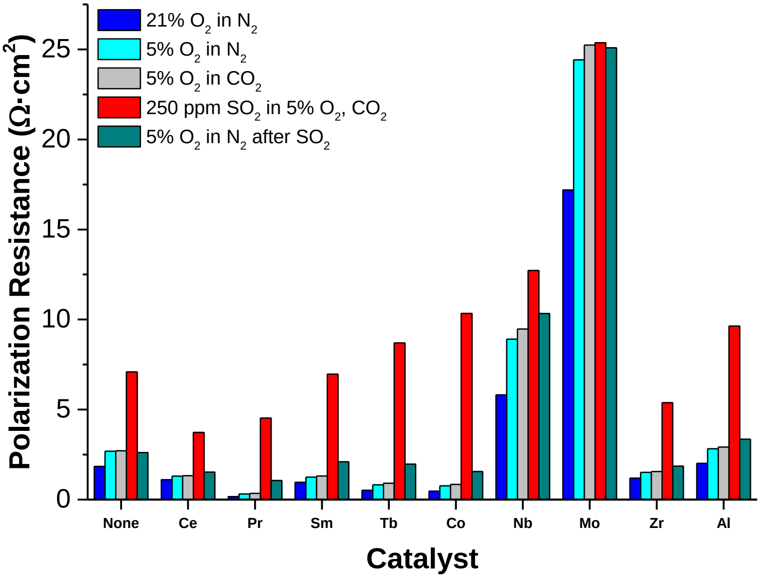

Figure 6.105: Polarization resistance values of dual-phase backbones infiltrated with different elements. Values extracted from EIS measurements performed at 850 ºC.

As can be seen in Figure 6.105, under feed side conditions (21% O_2 in N_2) almost all catalysts improved R_p values with respect to the reference case. This is specially the case of Pr, with a significant reduction in R_p. This improving effect of Pr on oxygen reduction reactions (ORR) was previously reported [49]. In this work, the authors observed an outstanding and highly stable promotion effect of ORR when infiltrating CGO-LSM cathodes with Pr nanoparticles. For our case, activation of 60NFO-40CTO with Pr produces a 10-fold improvement in R_p, with a reduction from 1.85 to 0.17 $\Omega\cdot cm^2$ at 850 ºC. Moreover, as Figure 6.106 depicts for Pr case under feed side conditions, this R_p reduction with respect to the reference case is produced by an impressing lowering of impedance values at medium and low frequencies, thus confirming the effect observed in the cited publication. Similar improvements are observed for Co, Ce, Zr, Tb and Sm activation.

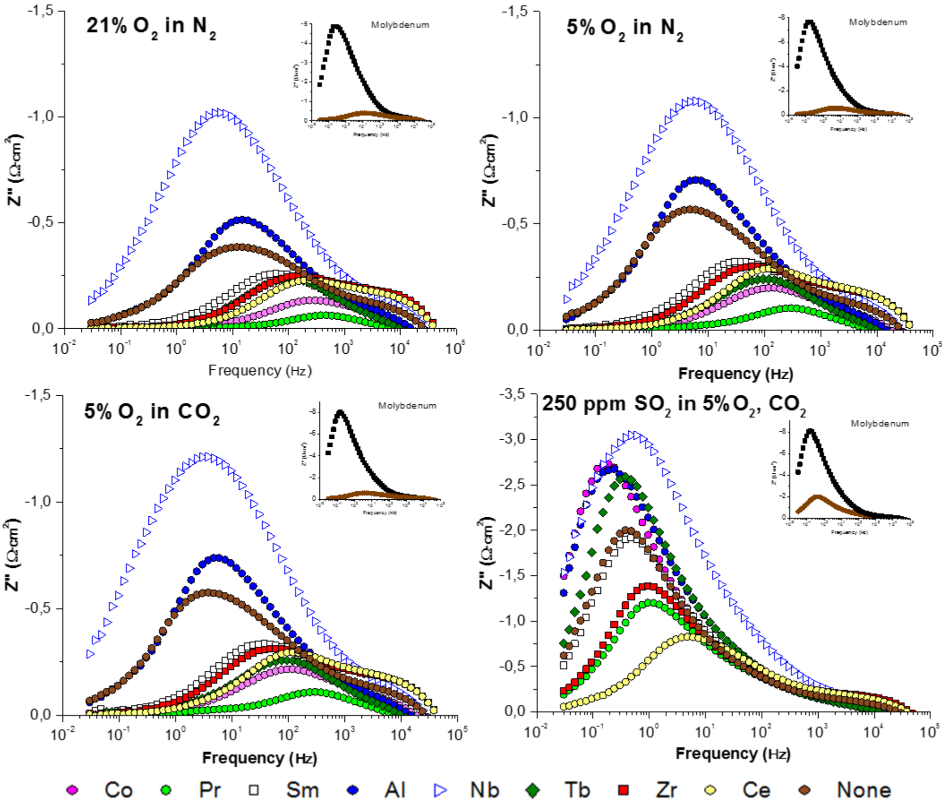

Figure 6.106: BODE plots of the different catalysts under the tested environments at 850 ºC. Molybdenum-infiltrated case is presented in Insets.

When inducing sweep side clean conditions (5% O_2 in N_2) R_p increases for all the cases due to the reduction in pO_2 and the lower availability of oxygen for conducting the oxygen reactions. Under such conditions all the catalysts excepting Al, Nb and Mo present better R_p than the reference case. Therefore, it would be expected an improvement of oxygen surface reactions in sweep side for the case of activated membranes with these catalysts. This argument is confirmed by the results shown in the corresponding BODE plot in Figure 6.106. Impedance values of Pr, Ce, Zr, Co, Sm and Tb activated cases still present lower levels than the not activated case at low frequencies. Similar behavior is found when switching to CO_2-containing atmospheres, with slight increases in R_p associated to competitive adsorption but affecting unimportantly the electrode performance.

Nevertheless, when switching to harsher conditions by means of SO_2 addition all the catalysts experience a significant worsening. Alike the reference case (Figure 6.102b) the R_p increments take place at low frequencies, establishing a direct relation between SO_2 adsorption on active sites and O_2 activity hindrance. However, SO_2 withdrawal does not produce a full recovery to the initial state.

Impedance spectra displayed in Figure 6.107 and *Rp* values in Figure 6.105 show that for all cases excepting reference and Ce-infiltrated cases initial values are not recovered after SO_2 exposure. This could be ascribed to the formation of sulfates from the active species during the SO_2 exposure and/or to SO_2 molecules that remain adsorbed on active sites after test. In the XRD measurements performed on spent samples it is not possible to identify any sulfate compound, this is probably due to the low concentration of the species that would be below the device limit detection.

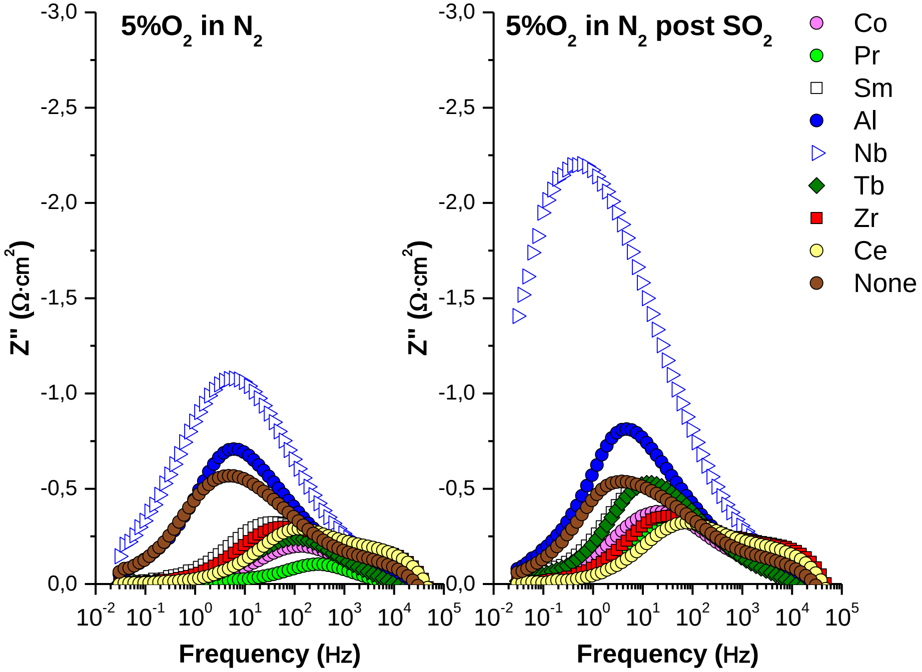

Figure 6.107: BODE plots of 5% O_2 in N_2 tests before and after SO_2 exposure.

Attending to the obtained results, the catalysts presenting better electrochemical properties regarding surface oxygen reaction under application environments are Ce and Pr, being Pr-infiltrated case more active under clean conditions and Ce-activated system presenting better performance under harsh oxyfuel environments. Therefore, Ce and Pr catalysts are very promising candidates for improving OTMs performance.

SEM analysis was conducted on some EIS tested samples. Figure 6.108 shows BSD-SEM pictures of the reference case and 60NFO-40CTO backbones activated with Pr, Ce and Al. As can be seen in Figure 6.108a, gray light grains correspond to CTO phase, whereas darker grains belong to NFO phase. A good dispersion of 50-100 nm grains can be observed. Infiltration with Pr (Figure 6.108b) produces Pr_6O_{11} nanoparticles deposited all over the backbone surface forming needle-like structures of about 500 nm. With respect to Ce activation, a predominance of light gray grains (Figure 6.108c) evidences a coverage of CeO_x particles over the composite grains forming the backbone. Al infiltration is clearly identifiable in Figure 6.108d as darker sheets of about 1 micron on some areas of the backbone. EDS analysis on these samples shown the presence of the mentioned elements in the indicated structures. No sign of S was detected in any of the samples.

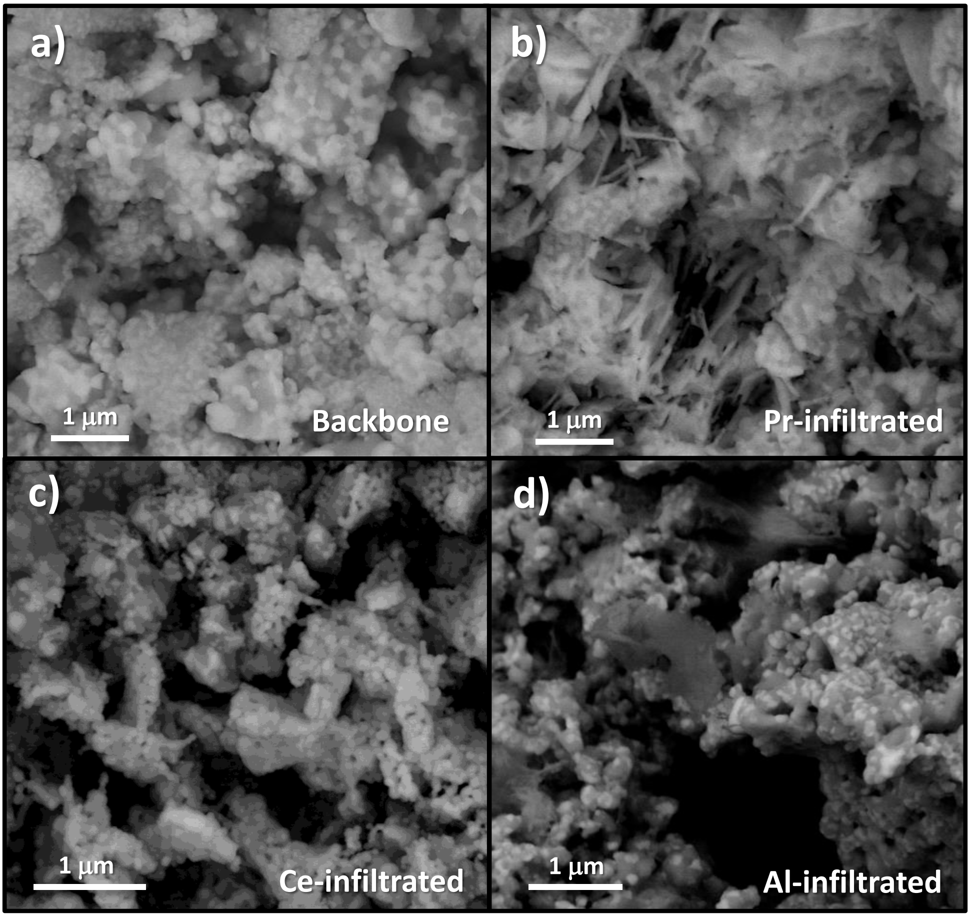

Figure 6.108: BSD-SEM pictures of different 60NFO-40CTO backbones: (a) not activated, (b) Pr-infiltrated, (c) Ce-infiltrated and (d) Al-infiltrated, after EIS tests.

6.3.3. Oxygen permeation tests.

After electrochemical characterization and once identified Ce and Pr catalysts as those yielding the best performance in terms of surface oxygen activity, a batch of coated dual-phase membranes was prepared for the conduction of oxygen permeation tests. This study was performed on bulk dense 60NFO-40CTO membranes with thicknesses in the range of 0.6-0.7 mm. 30 µm thick porous backbone structures were deposited on both sides of membranes following the procedure as described in the experimental section. Five different cases were considered for the oxygen permeation study: a bare dual-phase membrane, and four 60NFO-40CTO coated membranes. Three of these membranes were infiltrated with Ce, Pr and Al; whereas one was left without infiltration thus setting a reference case. Aluminum activation was chosen because of the observed bad oxygen surface activity during the electrochemical characterization and thus making a better correlation between EIS and $J(O_2)$ results.

In Figure 6.109a, the oxygen permeation for the five membranes is depicted versus temperature under clean conditions (Air/Ar gradient). Clearly, the addition of a porous layer improves $J(O_2)$ significantly, from 0.015 to 0.038 $(ml \cdot min^{-1} \cdot cm^{-2}) \cdot mm$ at 850 ºC, corresponding to a 2.5-fold improvement, while at 750 °C a 4-fold improvement was found. Increase of permeation by surface modification has been previously reported by several publications [2, 50]. This enhancement can be ascribed to (i) the fact that the membrane surface specific area is increased and thus additional active sites for O_2 permeation and TPBs are generated, and (ii) improvement of local gas flow dynamics, promoting turbulences and thus leading to a better access/release of O_2 to/from active sites.

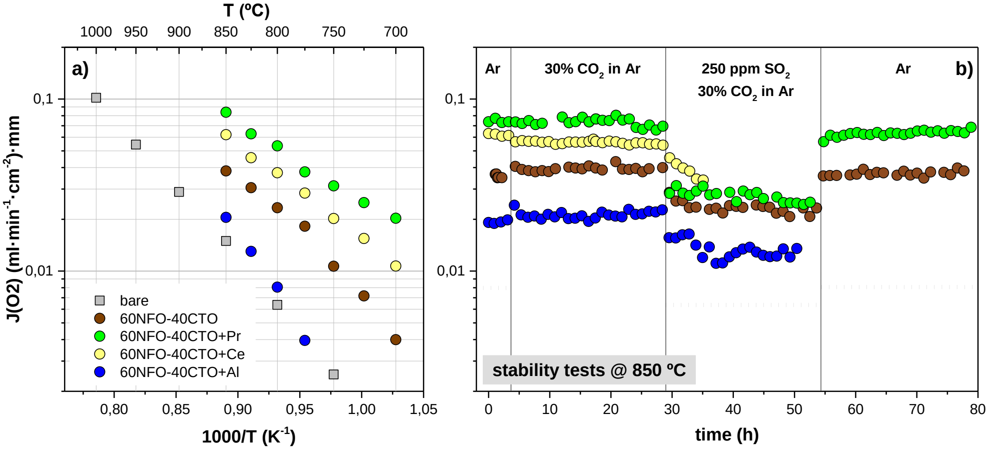

Figure 6.109: Oxygen permeation tests on bare and activated membranes. (a) Oxygen permeation in dependence of temperature under clean conditions (Air/Ar gradient). (b) Oxygen permeation as function of time under different environments at 850 ºC. For all the tests air was used as feed gas (100 $ml \cdot min^{-1}$) and mixtures of Ar as sweep gas (150 $ml \cdot min^{-1}$).

The activation with the different catalysts clearly shows an oxygen permeation promoting effect for the case of Ce and Pr, and a worsening if Al is included. Membrane activation with Pr produces a significant raise in the oxygen permeation in all the temperature range. An oxygen flux of 0.084 $(ml \cdot min^{-1} \cdot cm^{-2}) \cdot mm$ is reached at 850 ºC (ca. 6-fold improvement). At lower temperatures the positive effect of membrane activation becomes more evident with a 12.5-fold increase at 750 ºC with respect to the bare case. Lower $J(O_2)$ are obtained with Ce activation with values of 0.06 (ml·min^{-1}·cm^{-2})·mm at 850 ºC, nevertheless these values are better than those obtained with the pristine membrane. On the contrary, Al-infiltrated membrane implies a worsening in the membrane performance with respect to the reference case, obtaining fluxes of 0.021 (ml·min^{-1}·cm^{-2})·mm at 850 ºC. From the data displayed in Figure 6.109a apparent activation energies (E_a) have been estimated. For the cases including porous backbones (excepting Al infiltration) it is observed a lower dependency of $J(O_2)$ on temperature since lower E_a in the range of 90-105 kJ·mol^{-1} are obtained. For the bare and Al-infiltrated cases the values of E_a are considerably higher.

Table 6.14: Apparent activation energy (E_a) (kJ·mol^{-1}) derived from oxygen permeation measurements shown in Figure 6.109.

Catalytic layer	**T range (ºC)**	**Ea (kJ·mol^{-1})**
bare	850-750	171 (±0.25)
60NFO-40CTO	850-775	97.3 (±2)
60NFO-40CTO+Al	850-775	197.3 (±10)
60NFO-40CTO+Ce	850-700	104 (±3)
60NFO-40CTO+Pr	850-700	91.6 (±4)

In addition to the characterization under clean conditions (Air/Ar gradient) it has also been tested the performance of the membranes when exposed to harsher environments. Therefore, oxygen permeation was studied over extended times to investigate the stability of the catalytic systems (Figure 6.109b). First, membranes were maintained in Air/Ar gradient (only last 4 hours are shown in graph) prior to switching to 30% CO_2 in Ar sweeping. Synthetic air feeding was kept during all tests. After 24 hours, sweep gas was changed to 250 ppm SO_2, 30% CO_2 in Ar, keeping these conditions for another 24 hours. Finally it was switched back to Ar sweeping for monitoring membrane permeation recovery.

As can be seen in Figure 6.109b, reference case presents a stable behavior under all the conditions. Despite suffering a drop in $J(O_2)$ when adding SO_2 the initial permeation rate is fully recovered when turning back to clean conditions. These results agree completely with those observed in EIS measurements (Figure 6.105) where initial *Rp* values are achieved again after SO_2 exposure. Ce and Pr activation improve $J(O_2)$ in all conditions, showing a flat oxygen flux evolution when exposed to CO_2. Under such conditions, permeation rates of 0.07 and 0.054 (ml·min^{-1}·cm^{-2})·mm are obtained after 24 hours on-stream for Pr and Ce cases, respectively. A marked drop occurs when introducing SO_2 in the sweep, with an instantly $J(O_2)$ drop down to 0.03 (ml·min^{-1}·cm^{-2})·mm for the Pr-activated membrane. A more sustained oxygen flux decrease is observed for the case of Ce, unfortunately sealing system failed and no more data could be registered beyond 35 hours of test. Up to this point, Ce-activation seemed to present better results than Pr case under SO_2. This would be in agree with EIS results, attending to the *Rp* obtained during SO_2 tests, where Ce activation showed lower values than Pr. After 24 hours of SO_2 exposure Pr membrane $J(O_2)$ decreased slightly to 0.025 $(ml\cdot min^{-1}\cdot cm^{-2})\cdot mm$, thus improving reference case performance. The initial oxygen flux value was not entirely recovered after 24 hours under clean conditions, nevertheless $J(O_2)$ evolution seem to point a return to starting levels if test duration would have been extended. Finally, as expected from EIS characterization Al-activation implies a worsening under all the tested conditions, presenting $J(O_2)$ below the reference case. As occurred during Ce membrane tests, sealing system failed during SO_2 tests registering data only up to 50 hours.

From the oxygen permeation tests and taking into account the results obtained after EIS measurements, it is possible to perform a correlation with R_p and $J(O_2)$ values. Inverse of R_p has been represented for every catalyst in order to give an idea of the conductivity performance of the catalysts and the loss of the magnitude when switching to SO_2-containing environments. As can be seen in Figure 6.110a and b, elements improving electrode performance also produce and enhancement in $J(O_2)$ with respect to reference case. A similar relation is observed for Aluminum, with a worsening in the performance in both characterizations. Therefore, a direct relation can be observed between the two characterizations since the catalyst performing better in EIS tests under CO_2 environments is also the one yielding better oxygen permeation (Pr catalyst). In the same manner, Ce activation presents the lower R_p under SO_2 exposure as well as the higher $J(O_2)$ under the same conditions. According to this, EIS technique can be used for performing screening studies (much faster and easier than oxygen permeation tests) in order to identify the best potential candidates for OTMs activation.

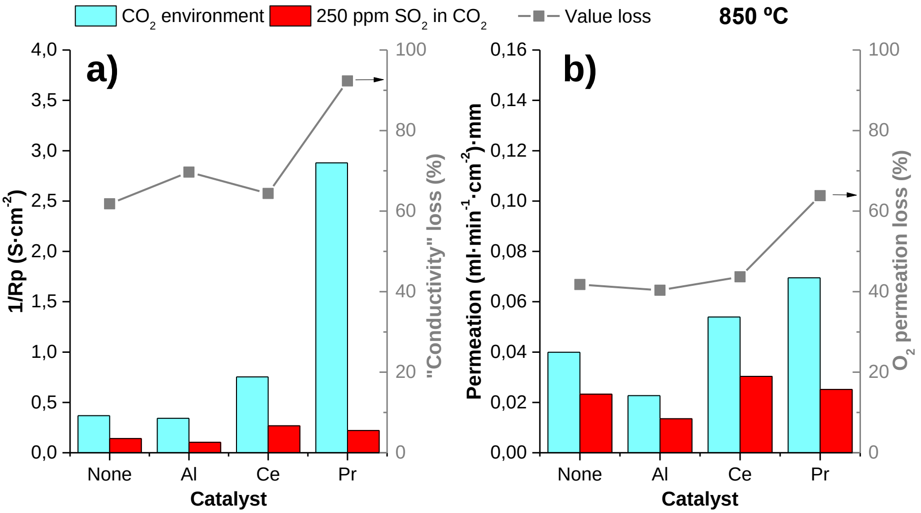

Figure 6.110: a) Inverse of polarization resistance under different environments and % value loss for every catalyst when exposing to SO_2. b) J(O_2) values under different environments and permeation loss when adding SO_2 to the sweep.

6.4. Oxygen permeation in thin supported dual-phase membranes[10].

The potential of dual-phase membranes based on 60% NFO – 40% CTO composition for providing high oxygen fluxes has been studied considering the case of thin membranes supported on a porous support.

For that aim, an 8 μm thick 60% NFO – 40% CTO membrane was deposited over a $La_{0.6}Sr_{0.4}Co_{0.2}Fe_{0.8}O_{3-\delta}$ (LSCF) porous freeze-casted support by means of screen-printing method, and subsequently sintered at 1400 ºC for 6 hours. Both the procedures for manufacturing the porous support and the membrane deposition are the same than the explained in the section 2.2.2. Production of LSCF porous supports by freeze-casting.

6.4.1. Chemical compatibility.

First the chemical compatibility between NFO-CTO (membrane) and LSCF (porous support) was analyzed. From previous studies on the chemical compatibility of NFO and CTO it is well-known the absence of reaction between these two phases. Nevertheless, the reactivity between the dual-phase components and the support material (LSCF) was evaluated by mixing both powders in a weight ratio 50:50 followed by annealing 50 hours at 1000ºC and 6 hours at 1400ºC, mimicking the membrane operating temperature and the final step of the membrane manufacture respectively. Figure 6.111 shows the XRD patterns of (i) the LSCF perovskite material; (ii) the NFO-CTO dual-phase material as synthesized by the one-pot Pechini method; and (iii) both powders mixtures annealed at high temperature. Both starting materials are well crystallized. Concerning the dual-phase material, both spinel and fluorite phases are found without any additional phases. The patterns related to the powders mixtures show peaks corresponding exclusively to the NFO-CTO and LSCF phases to the limit of XRD detection.

---

[10] The study here presented has been published in ChemSusChem journal under the title “Enhanced Oxygen Separation through Robust Freeze-Cast Bilayered Dual-Phase Membranes” DOI: 10.1002/cssc.201402324

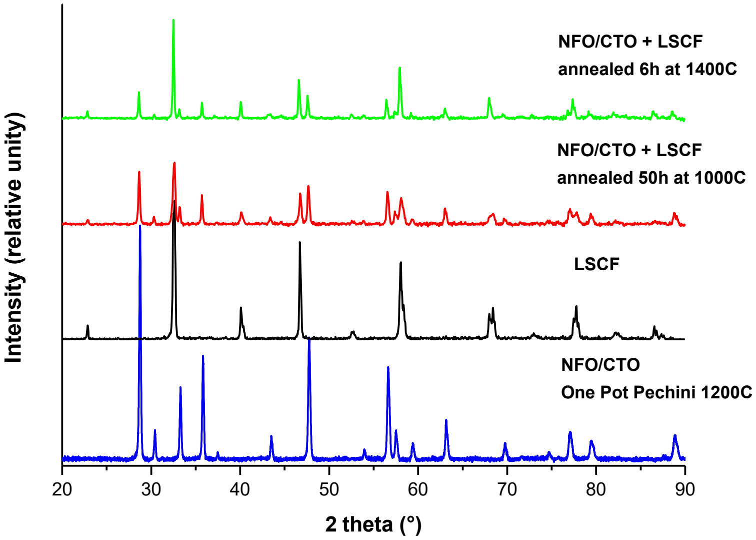

Figure 6.111: XRD patterns of the NFO/CTO dual-phase prepared by a one-pot Pechini synthesis and sintered at 1200 ºC, of the LSCF perovskite and of both mixtures of NFO/CTO and LSCF powders annealed 50 hours at 1000 ºC and 6 hours at 1400 ºC.

6.4.2. Microstructural study

Asymmetric membrane assembly was characterized by BSD SEM/EDX. As can be seen in Figure 6.112a, and as observed in the LSCF freeze-cast membranes studied in Chapter 4, three different porosity zones are easily identifiable through the support cross section view. In the lower zone (Zone III) the substrate presents vertical and well-organized pores of about 400 μm long. In Zone II the porosity is connected but non-oriented and randomly organized with a thickness of 150 μm. And finally, a 10 μm-thick LSCF layer with very low porosity is formed on top of the support (Zone Ib in Figure 6.112c). Some of this pores appear infiltrated with $NiFe_2O_4$ grains (confirmed by EDS mapping), probably occurring during the coating of the top NFO-CTO layer (Zone Ia). Concerning the composite layer, it appears well densified with no pores and defects that can be observed on its surface (Figures 14c and 14d). Moreover, both phases are homogeneously distributed and therefore, one can expect to have both electronic and ionic paths properly built through the layer.

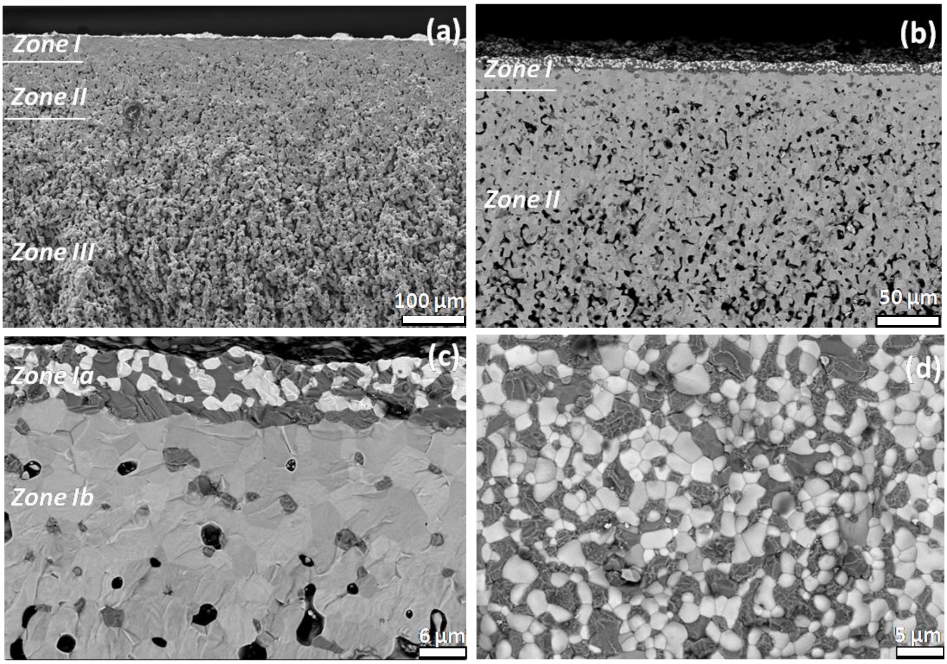

*Figure 6.112: Cross sections of the coated freeze-cast support (**a**), cross section of the non-organized porosity layer and composite dense top layer (**b**) cross section focus on the interface between the LSCF freeze-cast support and the NFO/CTO dense top-layer (**c**) and surface of NFO/CTO dense top-layer (**d**).*

Despite the absence of powder reactivity during annealing at high temperature as detailed above, XRD analysis was performed over the dense top-layer membrane after coating and sintering to verify the absence of any additional phase before oxygen permeation tests. Figure 6.113 presents the related pattern and the LSCF and NFO-CTO patterns previously detailed as comparison. We can see that the dense top-layer remains crystalline after sintering. The main peaks are related to the NFO-CTO dual-phase material. Nevertheless, we can observe the presence of peaks associated to the LSCF perovskite structure. It is explained by the depth of interaction of the X-ray beam during the analysis. Indeed, not only the top surface of the asymmetric membrane is analyzed but also part of the LSCF support. All peaks can be assigned to starting powder materials and no additional phase is detected to the limit of the XRD analysis.

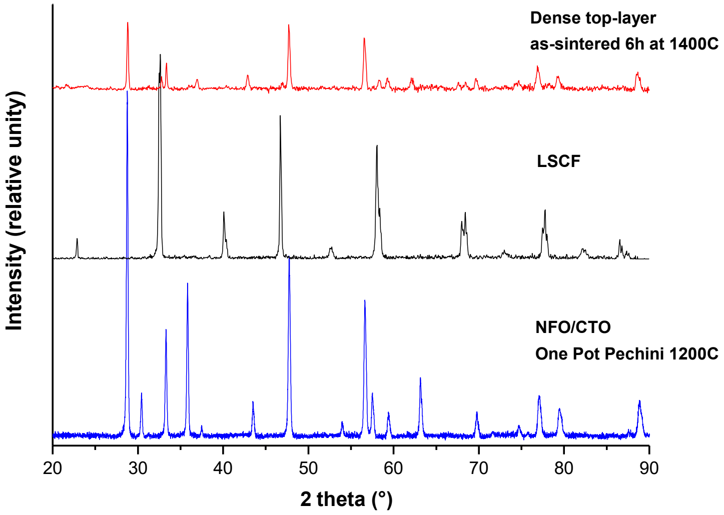

Figure 6.113: XRD patterns of the NFO/CTO dual-phase elaborated by a one-pot Pechini method and sintered at 1200 ºC, of the LSCF perovskite and of dense top-layer after sintering 6 hours at 1400 ºC.

6.4.3. Oxygen permeation tests.

The oxygen permeation of the asymmetric membrane has been evaluated as a function of temperature. As a comparison, the $J(O_2)$ for the monolithic 0.68 mm-thick 60NFO-40CTO membrane studied in section 6.2.3 of the present chapter is added to Figure 6.114. For both membranes, the feed and sweep fluxes were 300 $ml \cdot min^{-1}$ of air and argon respectively. The highest oxygen permeation flux is observed for the asymmetric membrane with more than one order of magnitude whatever the temperature. This result is not surprising just taking into account the thickness of the dense layer over the permeation flux according to the Wagner´s law [51]. As an example, the oxygen permeation flux of the freeze-cast membrane reaches 4.8 $ml \cdot min^{-1} \cdot cm^{-2}$ at 1000 ºC while it is of 0.17 $ml \cdot min^{-1} \cdot cm^{-2}$ for the monolithic membrane. $J(O_2)$ for both membranes follows an Arrhenius behavior that can be divided in two regions with change in the activation energy (E_a) at 850 ºC. In general, the freeze-cast membrane presents the lowest E_a (Table 6.15) in the whole temperature range. The important difference of oxygen permeation flux between both membranes can be explained by two reasons, (i) the thickness of the dense layer as previously explained and (ii) the beneficial effect of the freeze-cast support with hierarchical and vertically oriented porosity. Indeed, the effect of such porous support prepared by the freeze-casting technique has already been pointed out in Chapter 4 of the present thesis and in a previous paper where a full study of the gaseous transport has been realized [52]. The relatively high permeation obtained here can be explained in part by the beneficial effect of the hierarchical porous support [53].

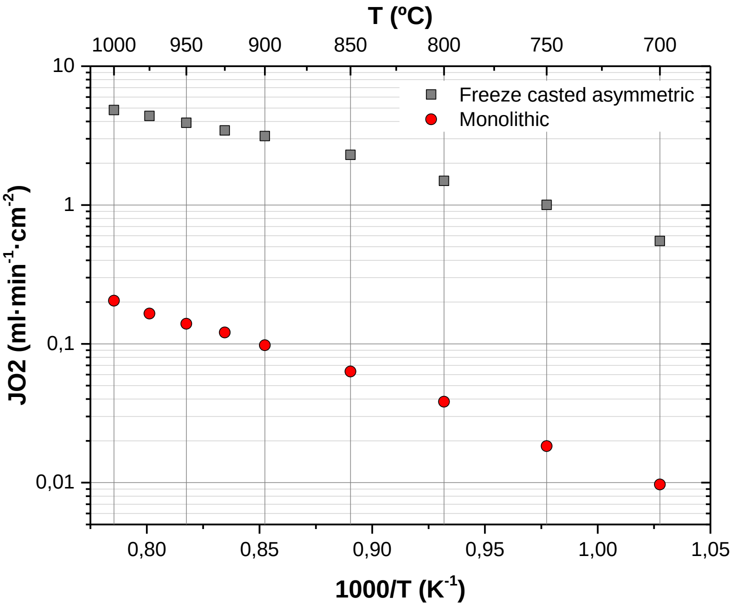

Figure 6.114: Oxygen permeation as a function of temperature for two membranes. Solid symbols: Freeze-cast membrane constituted by a LSCF support and a 8 µm 60NFO-40CTO dual phase dense top-layer. Empty symbols: Monolithic 0.68 mm thick 60NFO-40CTO dense membrane. Q_{feed} = 300 ml·min^{-1}. Q_{sweep} = 300 ml·min^{-1}.

Table 6.15: Activation energy as a function of temperature for the freeze-cast membrane and for the monolithic 0.68 mm thick 60NFO-40CTO membranes.

Membrane	**E_a (T > 850 ºC)**	**E_a (T < 850 ºC)**
Freeze-cast membrane	56.7±5	83.1±6
Monolithic membrane	69±4	97.1±16

The effect of the sweep gas flow rate was studied as a function of temperature (Figure 6.115a), a 1.5-fold improvement in the flux can be achieved at 1000 ºC by increasing the Ar flow rate from 300 to 500 ml·min^{-1}. Specifically, the flux increases from 4.8 to 7.0 ml·min^{-1}·cm^{-2} at 1000 ºC. The effect is more pronounced with increasing temperatures, i.e., when the flux is higher and concentration polarization problems are more likely to occur. Apart from the improvement in the fluid dynamics [54], a higher sweep flow rate has the additional effect of increasing the separation driving force, since the dilution of the permeated oxygen leads to an overall lower *p*O_2. Another important aspect is the use of higher pressures in the air feed in order to enlarge the oxygen production. Here, this is simulated by increasing *p*O_2 in the feed stream, as shown in Figure 6.115b. Specifically, Figure 6.115b presents the variation of *J(*O_2*)* as a function of *p*O_2 and temperature when pure CO_2 is employed as sweep gas. At high temperatures, *J(*O_2*)* increases almost proportionally to *p*O_2, achieving a peak flow of 17.4 ml·min^{-1}·cm^{-2} at 1000 ºC and *p*O_2 = 1 atm. On the other hand, at lower temperatures the influence of *p*O_2 on the JO_2 magnitude becomes lower, which is especially patent at 700 ºC. This behavior suggests a change in the rate limiting step, which may be less influence by the *p*O_2 in the feed, as for instance surface gas exchange [1, 55-57]. This observation is fully consistent with the oxygen permeation model developed by Xu et al. [58] where at low temperature, the oxygen permeation is controlled by the surface exchange at the oxygen-lean side of the membrane.

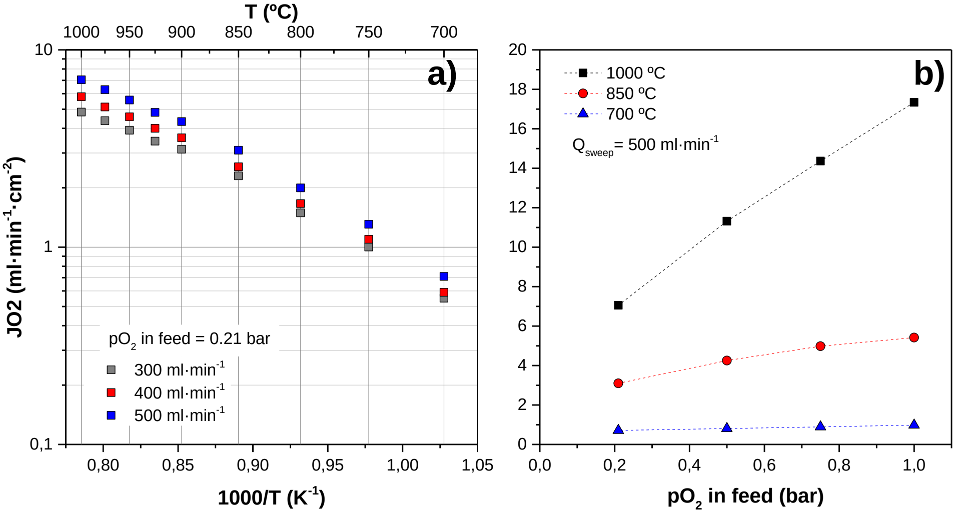

Figure 6.115: a) Oxygen permeation in dependence of temperature and sweep gas flow. Air/Ar gradient. Q_{feed} *= 300 ml·min*$^{-1}$*. b) Oxygen permeation in dependence of p*O_2 *in feed stream. Argon sweeping.* Q_{feed} *= 300 ml·min*$^{-1}$*.*

As previously detailed throughout the Thesis, the preferred *oxyfuel* scheme using membrane modules as ASU implies the recirculation of the flue gas passing through membrane module for O_2 enrichment. However, the high CO_2 content in this sweep gas could lead to the membrane deterioration via formation of carbonates [7, 59, 60]. With the aim to determine the specific effect of CO_2 on both the membrane stability and permeation, oxygen permeation was studied at four distinct temperatures as a function of the CO_2 content in the sweep gas (Figure 6.116), using a gas flow rate of 300 ml·min^{-1}. Regarding the effect of the CO_2, the increase in CO_2 content leads to the decrease in *J(*O_2*)*, for temperatures below 925ºC. At higher temperatures, the tendency is reversed with a beneficial effect of the increase in CO_2 content. Indeed at 1000 ºC, *J(*O_2*)* increases linearly with the CO_2 content and reaches 5.63 ml·min^{-1}·cm^{-2} with 100% of CO_2 in the sweep gas while it is of 4.8 ml·min^{-1}·cm^{-2} under pure inert gas. This thermo-chemical behavior can be explained as follows. At lower temperatures, the oxygen permeation could be affected by the carbonate formation and the competitive adsorption of CO_2 and O_2 on the surface of the dense layer. The latter option seems more realistic since carbonate formation over this class of composites has been shown to be unlikely [61]. This permeation loss with increasing CO_2 content is reversible as inferred from Figure 6.116, where $J(O_2)$ is plotted as a function of temperature and CO_2 content in the sweep gas during heating and cooling ramping. For the four considered temperatures, the initial $J(O_2)$ obtained for CO_2-free sweep is completely recovered after membrane exposure to CO_2, which proves that irreversible carbonation processes do not take place even at 700ºC. Further, the drop in $J(O_2)$ upon CO_2 exposure is ascribed to competitive adsorption between O_2 and CO_2, which strongly affects the gas exchange. This effect becomes more dramatic with decreasing temperatures, when exchange usually is partly limiting the overall permeation process and the exothermic CO_2 adsorption is promoted. Another interesting point is the observed hysteresis. This can be ascribed to the different kinetics existing between CO_2 adsorption and desorption over the membrane surface, the latter presenting a slower rate. In contrast to the previous behavior, a positive effect of CO_2 is observed at 1000 ºC, i.e. $J(O_2)$ increases with increasing CO_2 content in the sweep gas. This could be explained by considering (i) the smaller CO_2 adsorption constant at higher temperature, (ii) the improved sweeping gas effect of CO_2 over the adsorbed oxygen species, (iii) the particular thermal emissivity of CO_2 at very high temperatures, leading to very good thermal homogeneity over the membrane [62, 63].

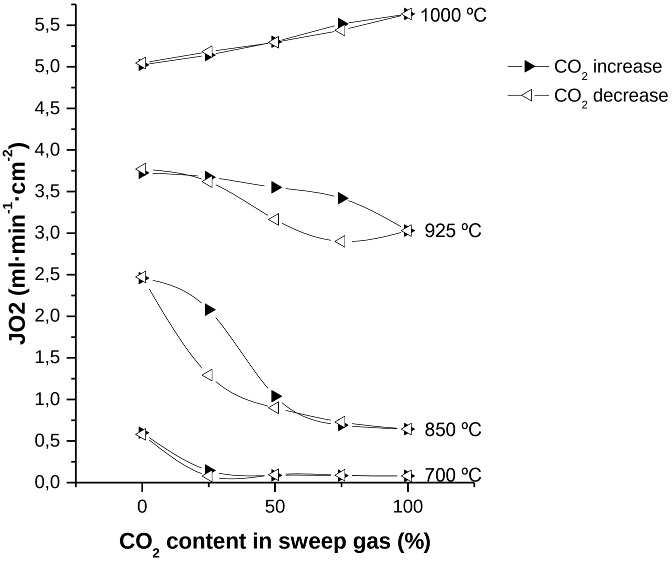

Figure 6.116: Oxygen permeation flux through the asymmetric membrane as a function of temperature and of the CO_2 content in the sweep gas.

The use of a CH_4-containing sweep gas in other practical applications [64] may result in a net increase in the separation driving force. The present membrane showed an increase of 1.5-fold in the JO_2 for all the tested temperatures when CH_4 (10% in Ar) was used as sweep (Figure 6.117). In ceria-based materials, the use of reactive/reducing gases results in the promotion of the electronic conductivity in the fluorite through the partial reduction of Ce^{4+} cations [65, 66]. The membrane remained stable under operation with CH_4 even when subjected to thermal cycling for 60 h.

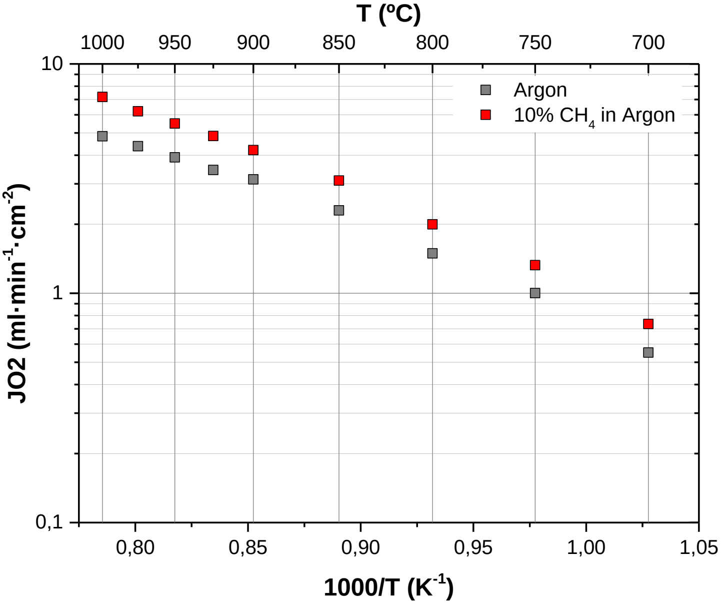

Figure 6.117: Influence of 10% of methane in the sweep gas over oxygen permeation flux through the asymmetric membrane. Feed gas: 300 ml·min^{-1} of air. Sweep gas: 300 ml·min^{-1}.

The previous evaluation of the oxygen permeation flux under CO_2 atmosphere revealed the impact over the oxygen permeation. The membrane stability with time is an essential requirement for industrial purposes. Thus, a stability test was performed under a CO_2-rich sweep gas flow mimicking the *oxyfuel* operation condition. The stability of the asymmetric freeze-cast membrane was evaluated at 950ºC during 150 hours under a sweep gas of 50% of CO_2 in argon with a total flow of 300 ml·min^{-1} while the feed stream was 300 ml·min^{-1} of air. Figure 6.118 presents the evolution of the oxygen permeation with time. The oxygen permeation remains constant during the first 40 hours of test with an average value of 4.4 ml·min^{-1}·cm^{-2}. After this period, the oxygen flux decreases linearly to reach 4.25 ml·min^{-1}·cm^{-2} during the next 110 hours of test. In average, a degradation rate of 0.024 ml·min^{-1}·cm^{-2} per day is obtained for this asymmetric membrane. In general, the membrane remained stable for 500 h during the test comprising thermal cycling and exposure to CO_2 and CH_4-rich gas environments.

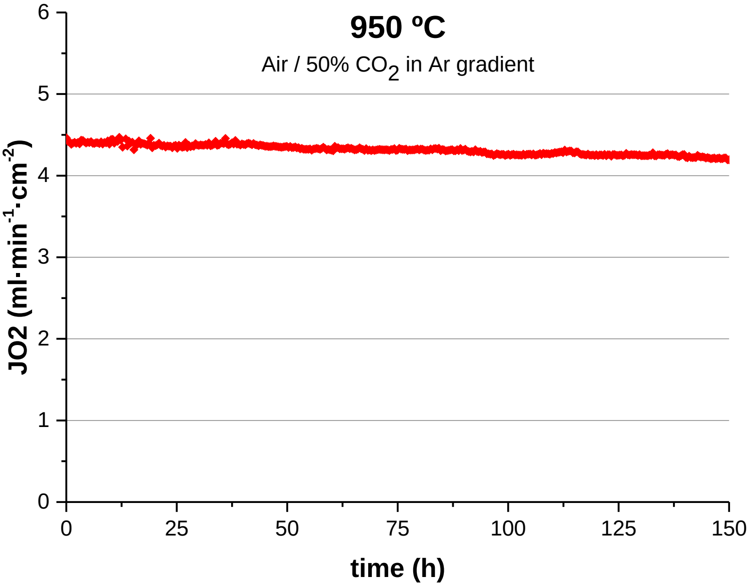

Figure 6.118: Oxygen permeation flux at 950 ºC as a function of time for the asymmetric freeze-cast membrane under a 50% CO_2-containing flux in argon as sweep gas (total flux 300 ml·min^{-1}). The feed stream is composed by 300 ml·min^{-1} of air.

6.5. Conclusions.

Dual-phase membranes based on $NiFe_2O_4$ – $Ce_{0.8}Tb_{0.2}O_{2-\delta}$ were considered for implementation in oxyfuel applications. A first evaluation of $Ce_{0.8}Tb_{0.2}O_{2-\delta}$ content and its relation with oxygen permeation was performed, determining that fluorite phase content improves the ionic conductivity while preserving enough electronic conductivity, thus enhancing the $J(O_2)$. An oxygen flux of 0.25 (ml·min^{-1}·cm^{-2})·mm at 1000 ºC was obtained for a thick self-standing membrane with 40% NFO – 60% CTO formula. Aiming to validate composite materials for their use in oxyfuel applications, an in-deep study reproducing typical process harsh conditions was performed on a 50% NFO – 50% CTO membrane. The membrane operation under high CO_2 content and SO_2 presence on sweep gas stream was evaluated. Oxygen fluxes of 0.13 and 0.09 ml·min^{-1}·cm^{-2} at 850 ºC were obtained for a 0.59 mm thick membrane under CO_2 and 250 ppm SO_2 in CO_2 sweep conditions, respectively. At 850ºC in CO_2 and 250 ppm SO_2 conditions the permeation is principally limited by surface exchange since SO_2 adsorptions dramatically affects the oxygen evolution rate. This aspect was also confirmed using electrochemical impedance spectroscopy.

Prolonged testing under CO_2 and SO_2-containing atmospheres rendered good and stable permeation results. XRD, BSD-SEM and EDS analysis on the spent membrane further confirmed material stability when exposed to oxyfuel environments.

Aiming to achieve a better understanding of oxygen surface reactions, the role of CO_2 and SO_2 on such processes and the role of several catalysts under these environments, an electrochemical study was conducted on 60NFO-40CTO composition. A first design of experiments performed by EIS determined a strong influence of SO_2 in the oxygen oxidation/reduction reactions, with significant increases in R_p. With this study it was also confirmed the 60NFO-40CTO stability after SO_2 expositions, not suffering any structural degradation and recovering the initial R_p values. Furthermore, the activation of 60NFO-40CTO porous backbones and their study by EIS allowed the identification of Ce and Pr catalysts as the most active for boosting oxygen surface reactions. All these findings were later confirmed by oxygen permeation tests on activated 60NFO-40CTO membranes. Activation of membranes with Pr catalyst yield an 6-fold improvement in $J(O_2)$ under Air/Ar gradient with respect to the reference case at 850 ºC. Moreover, Ce-activation was found to enhance up to 2 times the oxygen permeation rates when membranes were exposed to oxyfuel-like atmospheres containing 250 ppm of SO_2.

Finally, a highly-permeable and robust oxygen permeable membrane was engineered by combining an optimized composite material and a particular freeze-cast membrane architecture. The developed asymmetric ceramic membrane is composed by an original ice-templated $La_{0.6}Sr_{0.4}Co_{0.2}Fe_{0.8}O_{3-\delta}$ support with hierarchically oriented porosity and a top fully-densified bilayered coating comprising (i) a 10 µm-thick $La_{0.6}Sr_{0.4}Co_{0.2}Fe_{0.8}O_{3-x}$ layer and (ii) a top protective 8 µm-thick layer made of $NiFe_2O_4/Ce_{0.8}Tb_{0.2}O_{2-x}$. The thermo-chemical compatibility among the distinct crystalline components was proved by XRD and SEM/EDX analysis on the fully-assembled membrane. Permeation studies revealed promising oxygen permeation fluxes achieving peak values of 4.8 and 12 $ml\cdot min^{-1}\cdot cm^{-2}$ at 1000 ºC in Ar when air and pure oxygen were fed, respectively. The influence of CO_2 content in the sweep on the oxygen permeation was evaluated, showing a striking beneficial effect at temperatures above 950 ºC. At lower temperatures, a drop in the oxygen flux is observed with increasing CO_2 contents, which was reversible even at 700 ºC, and this is attributed to the detrimental competitive adsorption of CO_2 and O_2. Finally, the membrane operation was evaluated at 950 ºC under CO_2-rich sweep gas over a period of 150 hours, leading to a degradation rate of 0,024 $ml\cdot min^{-1}\cdot cm^{-2}$ per day.

The present results encourage the use of composite materials based on $NiFe_2O_4$ – $Ce_{0.8}Tb_{0.2}O_{2-\delta}$ as oxygen membranes in real-world operation conditions. Further research in the composite formulation and in the deposition of these materials as thin layers on porous supports [67] could lead the way to the achievement of higher $J(O_2)$ meeting technical feasibility requirements for their implementation as oxygen suppliers in industrial plants.

6.6. References.

[1] S. Baumann, J.M. Serra, M.P. Lobera, S. Escolastico, F. Schulze-Kueppers, W.A. Meulenberg, Ultrahigh oxygen permeation flux through supported Ba0.5Sr0.5Co0.8Fe0.2O3-delta membranes, Journal of Membrane Science, 377 (2011) 198-205.

[2] J.M. Serra, J. Garcia-Fayos, S. Baumann, F. Schulze-Kueppers, W.A. Meulenberg, Oxygen permeation through tape-cast asymmetric all-La0.6Sr0.4Co0.2Fe0.8O3 (-) (delta) membranes, Journal of Membrane Science, 447 (2013) 297-305.

[3] S. McIntosh, J.F. Vente, W.G. Haije, D.H.A. Blank, H.J.M. Bouwmeester, Oxygen stoichiometry and chemical expansion of Ba0.5Sr0.5Co0.8Fe0.2O3-delta measured by in situ neutron diffraction, Chemistry of Materials, 18 (2006) 2187-2193.

[4] S. McIntosh, J.F. Vente, W.G. Haije, D.H.A. Blank, H.J.M. Bouwmeester, Structure and oxygen stoichiometry of SrCo0.8Fe0.2O3-delta and Ba0.5Sr0.5Co0.8Fe0.2O3-delta, Solid State Ionics, 177 (2006) 1737-1742.

[5] S. McIntosh, J.F. Vente, W.G. Haije, D.H.A. Blank, H.J.M. Bouwmeester, Phase stability and oxygen non-stoichiometry of SrCo0.8Fe0.2O3-delta measured by in situ neutron diffraction, Solid State Ionics, 177 (2006) 833-842.

[6] D.N. Mueller, R.A. De Souza, T.E. Weirich, D. Roehrens, J. Mayer, M. Martin, A kinetic study of the decomposition of the cubic perovskite-type oxide BaxSr1-xCo0.8Fe0.2O3-delta (BSCF) (x=0.1 and 0.5), Physical Chemistry Chemical Physics, 12 (2010) 10320-10328.

[7] J. Yi, M. Schroeder, High temperature degradation of Ba0.5Sr0.5Co0.8Fe0.2O3-delta membranes in atmospheres containing concentrated carbon dioxide, Journal of Membrane Science, 378 (2011) 163-170.

[8] A. Waindich, A. Möbius, M. Müller, Corrosion of Ba1−xSrxCo1−yFeyO3−δ and La0.3Ba0.7Co0.2Fe0.8O3−δ materials for oxygen separating membranes under Oxycoal conditions, Journal of Membrane Science, 337 (2009) 182-187.

[9] M. Arnold, H. Wang, A. Feldhoff, Influence of CO2 on the oxygen permeation performance and the microstructure of perovskite-type (Ba0.5Sr0.5)(Co0.8Fe0.2)O3−δ membranes, Journal of Membrane Science, 293 (2007) 44-52.

[10] C.S. Chen, B.A. Boukamp, H.J.M. Bouwmeester, G.Z. Cao, H. Kruidhof, A.J.A. Winnubst, A.J. Burggraaf, Microstructural development, electrical properties and oxygen permeation of zirconia-palladium composites, Solid State Ionics, 76 (1995) 23-28.

[11] C.S. Chen, H. Kruidhof, H.J.W. Bouwmeester, H. Verweij, A.J. Burggraaf, Oxygen permeation through oxygen ion oxide-noble metal dual phase composites, Solid State Ionics, 86-88 (1996) 569-572.

[12] J. Kim, Y.S. Lin, Synthesis and oxygen permeation properties of ceramic-metal dual-phase membranes, J. Membr. Sci., 167 (2000) 123-133.

[13] W. Yang, Q. Li, X. Zhu, Y. Cong, Preparation of asymmetric biphase composite oxygen permeable membrane, Dalian Institute of Chemical Physics, Chinese Academy of Sciences, Peop. Rep. China . 2009, pp. 18pp.

[14] V.V. Kharton, A.V. Kovalevsky, A.P. Viskup, F.M. Figueiredo, A.A. Yaremchenko, E.N. Naumovich, F.M.B. Marques, Oxygen permeability and Faradaic efficiency of Ce0.8Gd0.2O2,ÄìŒ¥,ÄìLa0.7Sr0.3MnO3,ÄìŒ¥ composites, Journal of the European Ceramic Society, 21 (2001) 1763-1767.

[15] H. Luo, H. Jiang, T. Klande, Z. Cao, F. Liang, H. Wang, J. Caro, Novel Cobalt-Free, Noble Metal-Free Oxygen-Permeable 40Pr0.6Sr0.4FeO3-d/60Ce0.9Pr0.1O2-d Dual-Phase Membrane, Chemistry of Materials, 24 (2012) 2148-2154.

[16] T.J. Mazanec, T.L. Cable, J.G. Frye Jr, Electrocatalytic cells for chemical reaction, Solid State Ionics, 53–56, Part 1 (1992) 111-118.

[17] C.S. Chen, H. Kruidhof, H.J.M. Bouwmeester, H. Verweij, A.J. Burggraaf, Oxygen permeation through oxygen ion oxide-noble metal dual phase composites, Solid State Ionics, 86–88, Part 1 (1996) 569-572.

[18] C.S. Chen, A.J. Burggraaf, Stabilized bismuth oxide–noble metal mixed conducting composites as high temperature oxygen separation membranes, Journal of Applied Electrochemistry, 29 (1999) 355-360.

[19] H. Luo, H. Jiang, K. Efimov, F. Liang, H. Wang, J. Caro, CO2-Tolerant Oxygen-Permeable Fe2O3-Ce0.9Gd0.1O2-δ Dual Phase Membranes, Industrial & Engineering Chemistry Research, 50 (2011) 13508-13517.

[20] H. Luo, H. Jiang, T. Klande, Z. Cao, F. Liang, H. Wang, J. Caro, Novel Cobalt-Free, Noble Metal-Free Oxygen-Permeable 40Pr(0.6)Sr(0.4)FeO(3-delta)-60Ce(0.9)Pr(0.1)O(2-delta), Dual-Phase Membrane, Chemistry of Materials, 24 (2012) 2148-2154.

[21] F. Liang, H. Luo, K. Partovi, O. Ravkina, Z. Cao, Y. Liu, J. Caro, A novel CO2-stable dual phase membrane with high oxygen permeability, Chemical Communications, 50 (2014) 2451-2454.

[22] U. Pippardt, J. Boeer, C. Bollert, A. Hoffmann, M. Heidenreich, R. Kriegel, M. Schulz, A. Simon, Performance and Stability of Mixed Conducting Composite Membranes Based on Substituted Ceria, Journal of Ceramic Science and Technology, 5 (2014) 309-316.

[23] K.S. Yun, C.-Y. Yoo, S.-G. Yoon, J.H. Yu, J.H. Joo, Chemically and thermo-mechanically stable LSM–YSZ segmented oxygen permeable ceramic membrane, Journal of Membrane Science, 486 (2015) 222-228.

[24] J.H. Joo, K.S. Yun, J.-H. Kim, Y. Lee, C.-Y. Yoo, J.H. Yu, Substantial Oxygen Flux in Dual-Phase Membrane of Ceria and Pure Electronic Conductor by Tailoring the Surface, Acs Applied Materials & Interfaces, 7 (2015) 14699-14707.

[25] W. Fang, F. Liang, Z. Cao, F. Steinbach, A. Feldhoff, A Mixed Ionic and Electronic Conducting Dual-Phase Membrane with High Oxygen Permeability, Angewandte Chemie-International Edition, 54 (2015) 4847-4850.

[26] S. Cheng, M. Sogaard, L. Han, W. Zhang, M. Chen, A. Kaiser, P.V. Hendriksen, A novel CO2- and SO2-tolerant dual phase composite membrane for oxygen separation, Chemical Communications, 51 (2015) 7140-7143.

[27] H. Luo, K. Efimov, H. Jiang, A. Feldhoff, H. Wang, J. Caro, CO2-Stable and Cobalt-Free Dual-Phase Membrane for Oxygen Separation, Angewandte Chemie International Edition, 50 (2011) 759-763.

[28] M. Balaguer, C.-Y. Yoo, H.J.M. Bouwmeester, J.M. Serra, Bulk transport and oxygen surface exchange of the mixed ionic-electronic conductor Ce1-xTbxO2-delta (x=0.1, 0.2, 0.5), Journal of Materials Chemistry A, 1 (2013) 10234-10242.

[29] H.J.M. Bouwmeester, Dense ceramic membranes for methane conversion, Catalysis Today, 82 (2003) 141-150.

[30] Y. Rao, Z. Wang, L. Chen, R. Wu, R. Peng, Y. Lu, Structural, electrical, and electrochemical properties of cobalt-doped NiFe2O4 as a potential cathode material for solid oxide fuel cells, International Journal of Hydrogen Energy, 38 (2013) 14329-14336.

[31] M. Balaguer, C. Solis, J.M. Serra, Study of the Transport Properties of the Mixed Ionic Electronic Conductor Ce1-xTbxO2-d + Co (x = 0.1, 0.2) and Evaluation As Oxygen-Transport Membrane, Chemistry of Materials, 23 (2011) 2333-2343.

[32] M. Balaguer, C. Solis, J.M. Serra, Structural-Transport Properties Relationships on Ce(1-x)Ln(x)O(2-delta) System (Ln = Gd, La, Tb, Pr, Eu, Er, Yb, Nd) and Effect of Cobalt Addition, Journal of Physical Chemistry C, 116 (2012) 7975-7982.

[33] A. Petric, H. Ling, Electrical Conductivity and Thermal Expansion of Spinels at Elevated Temperatures, Journal of the American Ceramic Society, 90 (2007) 1515-1520.

[34] M. Balaguer, C.-Y. Yoo, H.J. Bouwmeester, J.M. Serra, Bulk transport and oxygen surface exchange of the mixed ionic–electronic conductor Ce 1− x Tb x O 2− δ (x= 0.1, 0.2, 0.5), Journal of Materials Chemistry A, 1 (2013) 10234-10242.

[35] C. Solís, S. Somacescu, E. Palafox, M. Balaguer, J.M. Serra, Particular Transport Properties of NiFe2O4 Thin Films at High Temperatures, The Journal of Physical Chemistry C, 118 (2014) 24266-24273.

[36] M.B. Choi, D.K. Lim, S.Y. Jeon, H.S. Kim, S.J. Song, Oxygen permeation properties of BSCF5582 tubular membrane fabricated by the slip casting method, Ceramics International, 38 (2012) 1867-1872.

[37] Z. Chen, Z. Shao, R. Ran, W. Zhou, P. Zeng, S. Liu, A dense oxygen separation membrane with a layered morphologic structure, Journal of Membrane Science, 300 (2007) 182-190.

[38] J.H. Joo, K.S. Yun, Y. Lee, J. Jung, C.-Y. Yoo, J.H. Yu, Dramatically Enhanced Oxygen Fluxes in Fluorite-Rich Dual-Phase Membrane by Surface Modification, Chemistry of Materials, 26 (2014) 4387-4394.

[39] J.H. Joo, K.S. Yun, C.-Y. Yoo, J.H. Yu, Novel oxygen transport membranes with tunable segmented structures, Journal of Materials Chemistry A, 2 (2014) 8174-8178.

[40] M. Balaguer, J. Garcia-Fayos, C. Solis, J.M. Serra, Fast Oxygen Separation Through SO2- and CO2-Stable Dual-Phase Membrane Based on NiFe2O4-Ce0.8Tb0.2O2-delta, Chemistry of Materials, 25 (2013) 4986-4993.

[41] C. Gaudillere, J. Garcia-Fayos, J. Serra, Enhancing oxygen permeation through hierarchically-structured perovskite membranes elaborated by freeze-casting, Journal of Materials Chemistry A, (2013).

[42] J. Gao, L. Li, Z. Yin, J. Zhang, S. Lu, X. Tan, Poisoning effect of SO2 on the oxygen permeation behavior of La0.6Sr0.4Co0.2Fe0.8O3-delta perovskite hollow fiber membranes, Journal of Membrane Science, 455 (2014) 341-348.

[43] S. Engels, T. Markus, M. Modigell, L. Singheiser, Oxygen permeation and stability investigations on MIEC membrane materials under operating conditions for power plant processes, Journal of Membrane Science, 370 (2011) 58-69.

[44] Y. Alqaheem, A. Thursfield, G. Zhang, I.S. Metcalfe, The impact of sulfur contamination on the performance of La0.6Sr0.4Co0.2Fe0.8O3 (-) (delta) oxygen transport membranes, Solid State Ionics, 262 (2014) 262-265.

[45] H. Luo, T. Klande, Z. Cao, F. Liang, H. Wang, J. Caro, A CO2-stable reduction-tolerant Nd-containing dual phase membrane for oxyfuel CO2 capture, Journal of Materials Chemistry A, 2 (2014) 7780-7787.

[46] A.J.B. H.J.M Bouwmeester, Chapter 14: Dense ceramic membranes for oxygen separation, in: P.J.G.a.H.J.M. Bouwmeester (Ed.) CRC Handbook of Solid State Electrochemistry, CRC Press, Boca Raton, 1997.

[47] Z. Wang, H. Liu, X. Tan, Y. Jin, S. Liu, Improvement of the oxygen permeation through perovskite hollow fibre membranes by surface acid-modification, Journal of Membrane Science, 345 (2009) 65-73.

[48] Y. Wei, Q. Liao, Z. Li, H. Wang, Enhancement of oxygen permeation through U-shaped K2NiF4-type oxide hollow fiber membranes by surface modifications, Separation and Purification Technology, 110 (2013) 74-80.

[49] L. Navarrete, C. Solis, J.M. Serra, Boosting the oxygen reduction reaction mechanisms in IT-SOFC cathodes by catalytic functionalization, Journal of Materials Chemistry A, 3 (2015) 16440-16444.

[50] C. Gaudillere, J. Garcia-Fayos, J.M. Serra, Oxygen Permeation Improvement under CO2-Rich Environments through Catalytic Activation of Hierarchically Structured Perovskite Membranes, ChemPlusChem, (2014) n/a-n/a.

[51] H. Bouwmeester, A. Burggraaf, in *Handbook of Solid State Electrochemistry*, CRC Press, (1997).

[52] C. Gaudillere, J. Garcia-Fayos, J. Serra, Enhancing oxygen permeation through hierarchically-structured perovskite membranes elaborated by freeze-casting, Journal of Materials Chemistry A (doi: 10.1039/C3TA14069E), (2013).

[53] S. Baumann, W.A. Meulenberg, H.P. Buchkremer, Manufacturing strategies for asymmetric ceramic membranes for efficient separation of oxygen from air, Journal of the European Ceramic Society, 33 (2013) 1251-1261.

[54] J.M. Gozalvez-Zafrilla, A. Santafe-Moros, S. Escolastico, J.M. Serra, Fluid dynamic modeling of oxygen permeation through mixed ionic-electronic conducting membranes, Journal of Membrane Science, 378 (2011) 290-300.

[55] P.F. Haworth, S. Smart, J.M. Serra, J.C.D. da Costa, Combined investigation of bulk diffusion and surface exchange parameters of silver catalyst coated yttrium-doped BSCF membranes, Physical Chemistry Chemical Physics, 14 (2012) 9104-9111.

[56] H. Kusaba, Y. Shibata, K. Sasaki, Y. Teraoka, Surface effect on oxygen permeation through dense membrane of mixed-conductive LSCF perovskite-type oxide, Solid State Ionics, 177 (2006) 2249-2253.

[57] S. Fang, C. Chen, L. Winnubst, Effect of microstructure and catalyst coating on the oxygen permeability of a novel CO2-resistant composite membrane, Solid State Ionics, 190 (2011) 46-52.

[58] S.J. Xu, W.J. Thomson, Oxygen permeation rates through ion-conducting perovskite membranes, Chemical Engineering Science, 54 (1999) 3839-3850.

[59] X. Tan, N. Liu, B. Meng, J. Sunarso, K. Zhang, S. Liu, Oxygen permeation behavior of La0.6Sr0.4Co0.8Fe0.2O3 hollow fibre membranes with highly concentrated CO2 exposure, Journal of Membrane Science, 389 (2012) 216-222.

[60] J. Yi, M. Schroeder, T. Weirich, J. Mayer, Behavior of Ba(Co, Fe, Nb)O3-delta Perovskite in CO2-Containing Atmospheres: Degradation Mechanism and Materials Design, Chemistry of Materials, 22 (2010) 6246-6253.

[61] M. Balaguer, J. Garcia-Fayos, C. Solis, J.M. Serra, Fast oxygen separation through SO2- and CO2-stable dual-phase membranes based on NiFe2O4-Ce0.8Tb0.2O2-δ, Chemistry of Materials, (2013).

[62] T. Wall, Y. Liu, C. Spero, L. Elliott, S. Khare, R. Rathnam, F. Zeenathal, B. Moghtaderi, B. Buhre, C. Sheng, R. Gupta, T. Yamada, K. Makino, J. Yu, An overview on oxyfuel coal combustion-State of the art research and technology development, Chemical Engineering Research & Design, 87 (2009) 1003-1016.

[63] Y. Hu, J. Yan, H. Li, Effects of flue gas recycle on oxy-coal power generation systems, Applied Energy, 97 (2012) 255-263.

[64] A. Kaiser, S. Foghmoes, C. Chatzichristodoulou, M. Sogaard, J.A. Glasscock, H.L. Frandsen, P.V. Hendriksen, Evaluation of thin film ceria membranes for syngas membrane reactors-Preparation, characterization and testing, Journal of Membrane Science, 378 (2011) 51-60.

[65] M.P. Lobera, J.M. Serra, S.P. Foghmoes, M. Sogaard, A. Kaiser, On the use of supported ceria membranes for oxyfuel process/syngas production, Journal of Membrane Science, 385 (2011) 154-161.

[66] M. Balaguer, C. Solis, S. Roitsch, J.M. Serra, Engineering microstructure and redox properties in the mixed conductor Ce0.9Pr0.1O2-[small delta] + Co 2 mol%, Dalton Transactions, (2014).

[67] C. Gaudillere, J. Garcia-Fayos, M. Balaguer, J.M. Serra, Enhanced Oxygen Separation through Robust Freeze-Cast Bilayered Dual-Phase Membranes, Chemsuschem, 7 (2014) 2554-2561.

7. CONCLUSIONS AND REMARKS

7. Conclusions and remarks.

Different materials and architectures were considered and studied throughout the present thesis in order to characterize them for industrial applications involving an O_2 supply system. The results presented in this thesis led to the following conclusions:

BSCF membranes

- Membrane thickness reduction resulted in a $J(O_2)$ improvement but in a lower magnitude than the predicted by Wagner equation. It was found that surface reactions limitation becomes more important at lower thicknesses as well as the use of porous supports results in additional resistances, thus lowering the expected performance.
- For the case of 160 μm-thick monolithic membranes $J(O_2)$ improved when activating membranes, with an improvement at 1000 ºC from 7.97 to 10.99 $ml \cdot min^{-1} \cdot cm^{-2}$ if activated only sweep side, and reaching 12 $ml \cdot min^{-1} \cdot cm^{-2}$ if both membrane sides are activated
- The catalytic activation 60 μm-thick asymmetric membranes with BSCF+5% Pd catalytic layer resulted in a 3-fold improvement of O_2 fluxes at 600 ºC (3 $ml \cdot min^{-1} \cdot cm^{-2}$ O_2 under Air/Ar gradient) and an unprecedented O_2 peak flux of 98 $ml \cdot min^{-1} \cdot cm^{-2}$ at 950 ºC under O_2/Ar gradient.
- ODHE reaction conducted on activated BSCF membranes coated with porous BSCF layers resulted in the achievement of a 81% C_2H_4 yield.
- BSCF capillaries produced 30 $ml \cdot min^{-1}$ at 900 ºC with only a 3 cm-long tube, and 2 $ml \cdot min^{-1}$ at 550 ºC, under O_2/Ar gradient. With this geometry up to a 30% of O_2 contained in the feed was extracted at 900 ºC.
- OCM reaction conducted on a BSCF capillary activated with a packed bed consisting of Mn-Na_2WO_4/SiO_2 catalyst resulted in the production of C_2 with a yield of 13.5% at a CH_4 conversion of 60%. A broad parametric study allowed the identification of the optimal OCM conditions when supplying 2 $ml \cdot min^{-1} \cdot cm^{-2}$ O_2 at low space velocities (2,353 $ml \cdot h^{-1} \cdot g^{-1}$). Further improvements in the CMR design is needed for optimizing these results.

LSCF tape-casted membranes

- For the LSCF tape casted membrane the increase in sweep flow rate had a very positive impact in the $J(O_2)$, obtaining higher improvements in the temperature range from 1000 to 850ºC, and a less visible effect at lower temperatures.
- The increase in the pO_2 in the feed (porous substrate side) and the use of He instead of N_2 allow increasing significantly the flux, thus proving the effect of the porous support on the feed gas diffusion.
- $J(O_2)$ decreased under rich-CO_2 environments at 900ºC due to competitive adsorption between CO_2 and O_2. On the other hand, CO_2 allowed improving the $J(O_2)$ at 1000 ºC due to better sweeping capability compared

to Ar, reaching a permeation of 5.6 ml·min^{-1}·cm^{-2} with a 100% CO_2 sweeping.
- Surface exchange reactions were improved by membrane catalytic activation with LSCF porous layer, up to ca. 300% of *J(O_2)* improvement at low temperatures.
- A peak oxygen flux of 13.3 ml·min^{-1}·cm^{-2} was reached at 1000ºC for the tape casted activated membrane when using O_2 as feed.

LSCF freeze-casted membranes

- Permeation tests proved the beneficial effect of freeze casted porous supports over the O_2 fluxes with a maximum value of 6.8 ml·min^{-1}·cm^{-2} at 1000 ºC.
- Short-term test under oxyfuel conditions in the presence of 50% CO_2 suggested that the sample was apparently stable. *J(O_2)* decreased under CO_2 operation at 850 ºC but initial *J(O_2)* values were recovered once CO_2 was removed.
- Catalytic membrane activation with LSCF porous layer led to a maximum *J(O_2)* of 16.3 ml·min^{-1}·cm^{-2} at 1000 ºC when pure O_2 was fed.
- Negative effect of CO_2 on *J(O_2)* was alleviated, especially at 950 and 900ºC, when activating membrane with a porous LSCF layer, allowing an improvement from ca. 2.2 to 3 ml·min^{-1}·cm^{-2} at 900 ºC under full-CO_2 atmospheres.
- The activated membrane operation was evaluated at 850 ºC under 50% CO_2 sweep gas over a period of 92 hours, leading to a degradation rate of 4.27·10^{-2} ml·min^{-1}·cm^{-2} per day

CGO membrane

- An oxygen flux of ca. 0.35 ml·min^{-1}·cm^{-2} was obtained at 1000 ºC under Air/Ar gradient, whereas 0.47 and 1.55 ml·min^{-1}·cm^{-2} were obtained when sweeping with CO_2 and 10% CH_4 in Ar, respectively.
- Oxygen partial pressure variation in feed side resulted in the obtaining of 1.2 ml·min^{-1}·cm^{-2} at 1000 ºC when pure O_2 was used.
- CO_2 presented a beneficial effect in *J(O_2)* at 1000 ºC with a slight improvement from 0.4 up to 0.47 ml·min^{-1}·cm^{-2}, and a lack of negative influence at lower temperatures.
- A peak *J(O_2)* of 7.8 ml·min^{-1}·cm^{-2} when using a 75% CH_4 in Ar sweep gas was obtained at 1000 ºC, corresponding to a 22-fold improvement in the oxygen permeation with respect to Ar sweeping.

NFO-CTO dual-phase membranes

- Fluorite phase content (CTO) improved the ionic conductivity while preserving enough electronic conductivity, thus enhancing the *J(O_2)* from 0.12 up to 0.25 (ml·min^{-1}·cm^{-2})·mm at 1000 ºC when increasing CTO content from 40% to 60%.

- Oxygen fluxes of 0.13 and 0.09 ml·min^{-1}·cm^{-2} at 850 ºC were obtained for a 0.59 mm-thick 50NFO-50CTO membrane under CO_2 and 250 ppm SO_2 in CO_2 sweep conditions, respectively.
- XRD, BSD-SEM and EDS analysis on the spent 50NFO-50CTO membrane after prolonged CO_2 and SO_2 testing confirmed material stability when exposed to oxyfuel environments.
- EIS tests on 60NFO-40CTO dual-phase material determined a strong influence of SO_2 in the oxygen oxidation/reduction reactions, with significant increases in R_p. It was also confirmed the material stability after SO_2 expositions, not suffering any structural degradation and recovering the initial R_p values.
- The activation of 60NFO-40CTO porous backbones and their study by EIS allowed the identification of Ce and Pr catalysts as the most active for boosting oxygen surface reactions. All these findings were later confirmed by $J(O_2)$ tests on activated 60NFO-40CTO membranes.
- Activation of membranes with Pr catalyst yield an 6-fold improvement in $J(O_2)$ under Air/Ar gradient with respect to the reference case at 850 ºC. Ce-activation enhanced up to 2 times the $J(O_2)$ under atmospheres containing 250 ppm of SO_2 at 850 ºC.
- A 10 μm-thick 60NFO-40CTO membrane deposited on a LSCF freeze cast support reached O_2 peak values of 4.8 and 12 ml·min^{-1}·cm^{-2} at 1000 ºC in Ar when air and pureO_2 were fed, respectively.

The main objectives of the present thesis were to develop MIEC membranes and membrane architectures for the production of O_2, as well as their implementation in the oxygen supply units in industrial processes, such as power generation and chemicals production. Several materials and cases studied herein have achieved this purpose. A highly stable material such as 60NFO-40CTO composite has shown an outstanding performance under oxyfuel-like conditions, further improved when combined with a highly-performing freeze cast porous support. This can pave the way for the achievement of high and stable $J(O_2)$ if thin supported composite membranes are considered. Furthermore, a performance optimization has been possible by addressing catalytic activation strategies, as it has been demonstrated for all the activated membranes that have been studied in this thesis.

Several advances have also been achieved in the study of CO_2 and SO_2 effect on oxygen permeation, identifying competitive adsorption processes on active sites as possibly the main responsible of the loss in permeation under oxyfuel conditions. Further work on this topic and the application of strategies for alleviating or even eliminating this phenomena would result in a significant performance improvement under such environments.

LSCF was found to be a promising material yielding very interesting fluxes with a fair stability when exposed to CO_2. Nevertheless further tests would be required for confirming its performance and stability under longer periods thus defining its most suitable field of application.

BSCF, despite its limited stability presents a big potential for providing outstanding oxygen fluxes, as can be seen with the results presented in this thesis. The application of catalytic strategies and the improvement on the porous supports used for the asymmetric membranes can lead the way to the obtaining of $J(O_2)$ much higher than the herein reported. Furthermore, its consideration for the conduction of chemical reactions should be a topic of big interest taking into account the promising results that have been observed.

8. SCIENTIFIC CONTRIBUTION

8. Scientific contribution.

8.1. Publications.

M.P. Lobera, M. Balaguer, **J. Garcia-Fayos** and J.M. Serra. *Catalytic Oxide-Ion Conducting Materials for Surface Activation of* $Ba_{0.5}Sr_{0.5}Co_{0.8}Fe_{0.2}O_{3-\delta}$ *Membranes*. Chemistry Select. Volume 2, Issue 10, 2949–2955 (2017).

D. Marcano, G. Mauer, Y.J. Sohn, R. Vassen, **J. Garcia-Fayos** and J.M. Serra. *Controlling the stress state of* $La_{1-x}Sr_xCo_yFe_{1-y}O_{3-\delta}$ *oxygen transport membranes on porous metallic supports deposited by plasma spray–physical vapor process*. Journal of Membrane Science 503, 1 – 7 (2016).

D. Marcano, G. Mauer, Y.J. Sohn, R. Vassen, **J. Garcia-Fayos** and J.M. Serra. *The Role of Oxygen Partial Pressure in Controlling the Phase Composition of* $La_{1-x}Sr_xCo_yFe_{1-y}O_{3-\delta}$ *Oxygen Transport Membranes Manufactured by Means of Plasma Spray-Physical Vapor Deposition*. Journal of Thermal Spray Technology 25 (4), 631-638 (2016)

J. Garcia-Fayos, M. Balaguer and J.M. Serra. *Dual-Phase Oxygen Transport Membranes for Stable Operation in Environments Containing Carbon Dioxide and Sulfur Dioxide*. ChemSusChem 8 (24), 4242-4249 (2015)

J. Garcia-Fayos, V.B. Vert, M. Balaguer, C. Solis, C. Gaudillere and J.M. Serra. *Oxygen transport membranes in a biomass/coal combined strategy for reducing* CO_2 *emissions: Permeation study of selected membranes under different* CO_2*-rich atmospheres*. Catalysis Today 257, 221-228 (2015)

C. Gaudillere, **J. Garcia-Fayos**, M. Balaguer and J.M. Serra. *Enhanced oxygen separation through robust freeze-cast bilayered dual-phase membranes*. ChemSusChem 7 (9), 2554-2561 (2014)

C. Gaudillere, **J. Garcia-Fayos** and J.M. Serra. *Oxygen permeation improvement under* CO_2*-rich environments through catalytic activation of hierarchically-structured perovskite membranes*. ChemPlusChem 79 (12), 1720-1725 (2014)

C. Gaudillere, **J. Garcia-Fayos** and J.M. Serra. *Enhancing oxygen permeation through hierarchically-structured perovskite membrane elaborated by freeze-casting*. Journal of Materials Chemistry A 2 (11), 3828-3833 (2014)

M. Ramirez; **J. Garcia-Fayos**, C. Solis and J.M. Serra. *Fast oxygen separation through* SO_2*- and* CO_2*-stable dual-phase membranes based on* $NiFe_2O_4$*-*$Ce_{0.8}Tb_{0.2}O_{2-\delta}$. Chemistry of Materials 25 (24), 4986-4993 (2013)

J.M. Serra, **J. Garcia-Fayos**, S. Baumann, F. Schulze-Küppers and W. Meulenberg. *Oxygen permeation through tape-cast asymmetric all-*$La_{0.6}Sr_{0.4}Co_{0.2}Fe_{0.8}O_{3-\delta}$ *membranes*. Journal of Membrane Science 447, 297-305 (2013)

M.P. Lobera, M. Balaguer, **J. Garcia-Fayos** and J.M. Serra. *Rare Earth-doped Ceria Catalysts for ODHE Reaction in a Catalytic Modified MIEC Membrane Reactor*. ChemCatChem 4 (12), 2102-2111 (2012)

M.P. Lobera, S. Escolástico, **J. Garcia-Fayos** and J.M. Serra. *Ethylene Production by ODHE in Catalytic Modified* $Ba_{0.5}Sr_{0.5}Co_{0.8}Fe_{0.2}O_{3-\delta}$ *Membrane Reactors*. ChemSusChem 5 (8), 1587-1596 (2012)

8.2. Patents.

José Manuel Serra Alfaro; **Julio García Fayos**; Laura Navarrete Algaba; Vicente Bernardo Vert Belenguer. *Catalytic layer and use thereof in oxygen-permeable membranes.* Assignee: Consejo Superior de Investigaciones Científicas. WO2016001465 A1. 2016.

8.3. Congress participations.

Oral presentations

C. Gaudillere, J. Escribano, **J. García-Fayos** and J.M. Serra. *Fabrication of gas separation ceramic membranes with hierarchical porous planar and tubular support by Freeze-Casting*. 6th International Conference on Shaping of Advanced Ceramics. Montpellier, France (2016)

J. García-Fayos, R. Ruhl, M. Balaguer, H. Bouwmeester, J.M. Serra, D. Gryaznov, E. Kotomin, M. Schroeder, E. Persoon, J.M. Bermúdez and M. Millán. *Catalyst development for oxygen transport membranes in the framework of EU FP7 GREEN-CC Graded Membranes for Energy Efficient New Generation Carbon Capture Process*. 14th International Conference on Inorganic Membranes. Atlanta, USA (2016)

J. García-Fayos, R. Ruhl, M. Balaguer, H. Bouwmeester, L. Navarrete and J.M. Serra. *Oxygen permeation optimization of* CO_2 *and* SO_2 *stable dual-phase membranes by means of surface catalytic activation under oxyfuel-like conditions*. 14th International Conference on Inorganic Membranes. Atlanta, USA (2016)

J. Garcia-Fayos, M. Balaguer, C. Solis and J.M. Serra. *Dual phase materials for the oxygen supply under harsh* CO_2 *and* SO_2*-containing environments*. 14th Conference of the European Ceramic Society. Toledo, Spain (2015)

C. Gaudillere, **J. García-Fayos**, M. Balaguer and J. M. Serra. *Enhanced oxygen separation through robust freeze-cast bilayered dual-phase membrane: application* *to* $La_{0.6}Sr_{0.4}Co_{0.2}Fe_{0.8}O_{3-x}$ *perovskite and* $NiFe_2O_4/Ce_{0.8}Tb_{0.2}O_{2-x}$ *dual-phase membrane*. Electroceramics XIV. Bucarest, Rumania (2014)

J. García-Fayos, S. Escolástico, W. A. Meulenberg and J.M. Serra. *Production of pure Oxygen by means of ceramic membranes based on* $La_{0.58}Sr_{0.4}Co_{0.2}Fe_{0.8}O_{3-\delta}$. 9th Ibero-american Congress on Membrane Science and Technology. Santander, Spain (2014)

J. García-Fayos, W. A. Meulenberg and J. M. Serra. *Oxygen production by means of ceramic membranes based on* $La_{0.58}Sr_{0.4}Co_{0.2}Fe_{0.8}O_{3-\delta}$. 11th International Conference on Catalysis in Membrane Reactors. Porto, Portugal (2013)

J. García-Fayos, C. Gaudillere, S. Escolástico, J. M. Serra, S. Baumann and W. A. Meulenberg. *Oxygen permeation studies on catalytically activated asymmetric ceramic membranes based on* $Ba_{0.5}Sr_{0.5}Co_{0.8}Fe_{0.2}O_{3-\delta}$ *and* $La_{0.58}Sr_{0.4}Co_{0.2}Fe_{0.8}O_{3-\delta}$. 13th International Conference of the European Ceramic Society. France (2013)

Selected posters presentations

J. M. Bermudez, **J. Garcia-Fayos**, T. Ramizez-Reina, G. Reed, M. Millan and J. M. Serra. *Thermochemical stability of* $NiFe_2O_4$-$Ce_{0.8}Tb_{0.2}O_{2-\delta}$ *under real conditions for its application in 4-end module oxygen transport membranes for oxycombustion*. 14th International Conference on Inorganic Membranes. Atlanta, USA (2016)

C. Gaudillere, **J. Garcia-Fayos**, J. M. Serra and S. Escolastico. *Freeze-Casting Technique for the Manufacture of Hierarchical Porous Planar and Tubular Support for Gas Separation Ceramic Membranes.* 20th International Conference on Solid State Ionics. Keystone, Colorado, USA (2015)

J. Garcia-Fayos, M. Balaguer and J. M. Serra. *Dual Phase Composite Materials as Oxygen Suppliers under Harsh* CO_2 *and* SO_2*-Containing Environments.* 20th International Conference on Solid State Ionics. Keystone, Colorado, USA (2015)

C. Gaudillere, **J. García-Fayos** and J.M. Serra. *Freeze-casting as innovative route for the manufacture of highly-oriented membrane porous support*. Electroceramics XIV. Bucarest, Rumania (2014)

J. García-Fayos, C. Gaudillere, S. Escolástico, V. B. Vert and J. M. Serra. *Efficiency and sustainability improvement in Biomass-based processes by means of the use of Oxygen Production Membranes*. 4th International Workshop of UBIOCHEM. Valencia, Spain (2013)

J. M. Gozálvez-Zafrilla, M. A. Santafé, **J. García-Fayos**, S. Escolástico and J. M. Serra. *Inorganic membranes for green chemical production and clean power generation.* Inorganic Membranes Summer School: "Inorganic membranes for green chemical production and clean power generation". Valencia, Spain (2013)

J. M. Serra, **J. García-Fayos**, C. Solís, S. Escolástico, S. Baumann and W. A. Meulenberg. *Oxygen production by catalytically activated asymmetric membranes based on* $Ba_{0.5}Sr_{0.5}Co_{0.8}Fe_{0.2}O_{3-\delta}$ *and* $La_{0.58}Sr_{0.4}Co_{0.2}Fe_{0.8}O_{3-\delta}$. 19th International Conference on Solid State Ionics, SSI19. Kyoto, Japan (2013)

J. M. Serra, **J. García-Fayos**, M. Balaguer, C. Solís and S. Escolástico. *Oxygen-permeability through* CO_2*-tolerant* Fe_2NiO_4-$Ce_{0.8}Tb_{0.2}O_{2-\delta}$ *dual phase membrane* 19th International Conference on Solid State Ionics, SSI19. Kyoto, Japan (2013)

J. M. Serra, **J. García-Fayos**, S. Escolástico and M. P. Lobera. *Catalytic membrane reactors for ODHE based on oxygen transport membranes*. 12th International Conference on Inorganic Membranes. The Netherlands (2012)

9. Acronyms and symbols.

Acronym	**Definition**
ASU	Air Separation Unit
BSD	Back Scattered electron Detector
BSCF	$Ba_{0.5}Sr_{0.5}Co_{0.8}Fe_{0.2}O_{3-\delta}$
CCS	Carbon Capture and Storage
CGO	$Ce_{0.8}Gd_{0.2}O_{2-\delta}$
CMR	Catalytic Membrane Reactor
CTO	$Ce_{0.8}Tb_{0.2}O_{2-\delta}$
EC	Electrical Conductivity
ECR	Electrical Conductivity Relaxation
EDS	Energy dispersive x-ray spectroscopy
EIS	Electrochemical Impedance Spectroscopy
FE-SEM	Field Emissions Scanning Electron Microscopy
GC	Gas Chromatograph
GDC	Gadolinium doped Ceria
LSCF	$La_{0.6}Sr_{0.4}Co_{0.2}Fe_{0.8}O_{3-\delta}$
LSM	$La_{0.8}Sr_{0.2}MnO_{3-\delta}$
MIEC	Mixed Ionic-Electronic Conductivity
NFO	Fe_2NiO_4
OCM	Oxidative Coupling of Methane
ODHE	Oxidative De-Hydrogenation of Ethane
OTM	Oxygen Transport Membrane
PF	Pore Former
PIE	Pulse Isotopic Exchange
POM	Partial Oxidation of Methane
PSA	Pressure Swing Adsorption
R_{BULK}	Bulk diffusion resistance
R_{CP}	Concentration polarization resistance
R_{SUPP}	Gas diffusion resistance in porous support
R_S	Surface exchange resistance
SiC	Silicon Carbide
TEC	Thermal Expansion Coefficient
TG	Thermogravimetry
TPD	Temperature Programmed Desorption
XRD	X-Ray Diffraction
YSZ	Yttria Stabilized Zirconia

Symbol	Definition	Units
$A_{effective}$	Effective area of a membrane	cm^2
a	Conductivity probe width	cm
b	Conductivity probe thickness	cm
D_{chem}	Chemical diffusion coefficient	$cm^2 \cdot s^{-1}$
d_p	Particle size	mm
E_a	Apparent activation energy	$kJ \cdot mol^{-1}$
F	Faraday constant (value = 96485.33)	$C \cdot mol^{-1}$
F_i	Molar flow rate	$mol \cdot min^{-1}$
$GHSV$	Gas Hourly Space Velocity	$ml \cdot h^{-1} \cdot g_{cat}{}^{-1}$
l	Distance between electrodes in the conductivity probe	cm
$J(O_2)$	Oxygen permeation flux	$ml \cdot min^{-1} \cdot cm^{-2}$
k_{chem}	Surface exchange coefficient	$cm \cdot s^{-1}$
L	Membrane thickness	mm
L_C	Membrane characteristic thickness	mm
pO_2	Oxygen partial pressure	bar
Q	Gas flow	$ml \cdot min^{-1}$
R	Resistance	Ω
R_p	Polarization resistance	$\Omega \cdot cm^2$
S	Product selectivity	%
σ_k	Material conductivity	$S \cdot cm^{-1}$
σ_{ion}	Ionic conductivity	$S \cdot cm^{-1}$
σ_{el}	Electronic conductivity	$S \cdot cm^{-1}$
σ_{amb}	Ambipolar conductivity	$S \cdot cm^{-1}$
t	time	min / h
T	Temperature	ºC / K
n_k	Charge number	
∇n_k	Electrochemical potential gradient	
$\nabla \mu_k$	Chemical potential gradient	
$\nabla \phi_k$	Electrical potential gradient	
X	Conversion	%
Y	Product yield	%
Z	System impedance	Ω
Z’	Real impedance	$\Omega \cdot cm^2$
Z”	Imaginary impedance	$\Omega \cdot cm^2$

10. Figures and Tables list.

10.1. Figures.

Figure 1.1: Ideal fluorite structure. Cations are represented as blue atoms, occupying face-centred positions and the corners of the unit cell. Image from [10] 27

Figure 1.2: (a) Perovskite unit cell and (b) BO_6 octahedral coordination around B cation. Image extracted from [12] 28

Figure 1.3: Schematic picture of dual-phase membranes. Image extracted from [15]. 29

Figure 1.4: Steps involved in the permetion of oxygen through an oxygen transport membrane. 30

Figure 1.5: Description of the oxygen anions diffusion through the oxygen vacancies present in a perovskite's crystal lattice. Image adapted from [27]. 31

Figure 1.6: Details of Air Separation Unit (ASU) technologies oriented to CCS applications (extracted from [71]). 39

Figure 1.7: Praxair's high temperature processes with integrated OTMs. 41

Figure 1.8: Air Products and Chemicals Inc. ITM developments for oxygen production. Extracted from [88]. 42

Figure 1.9: Coupling of multiple reactions in an OTM. Image adapted from [96]. 44

Figure 2.10: Scheme of the fabrication of the Gd-doped ceria. 57

Figure 2.11: Scheme of the Pechini synthesis routine for dual-phase materials fabrication. 58

Figure 2.12: Main steps for the fabrication of membranes, electrolytes and rectangular probes. 59

Figure 2.13: Main steps for the deposition of catalytic layers on membranes (upper route) and deposition of electrodes on CGO electrolytes (lower route). 61

Figure 2.14: Bragg's Law. Diffraction of X-rays on a crystalline material. Image extracted from [5]. 63

Figure 2.15: Four-point configuration for DC conductivity measurements. 65

Figure 2.16: Impedance results as function of the imaginary and real impedance. Inset represents the equivalent electrical circuit fitting for the EIS measurement response. 67

Figure 2.17: Connections between the Solartron equipment 1470E and 1455A module, with the electrochemical cell. 68

Figure 2.18: PH2 Reactor control program Front Panel. 69

Figure 2.19: Experimental setup permeation scheme. The membrane is pressed by a spring sited in the lid. 70

Figure 2.20: Simplified diagram of the lab-scale reactor for the conduction of capillary membrane studies. 71

Figure 2.21: Schematic description of the experimental set-up considered for performing tests on BSCF capillaries. 72

Figure 3.22: SEM images corresponding to a 0.38 mm-thick BSCF membrane a) Surface microstructure and b) fracture cross-section. 79

Figure 3.23: Fracture cross-sections (SEM images) of 20 μm-thick supported BSCF membranes. 80

Figure 3.24: a) Oxygen permeation in dependence of temperature for various BSCF membranes. b) Oxygen permeation in dependence of membrane thickness. Q_{feed} = 300 ml·min^{-1}, Q_{sweep} = 300 ml·min^{-1}. 81

Figure 3.25: Sweep flow variation effect on oxygen permeation for different thick membranes at 950 ºC (left) and graphical description of the polarization concentration phenomena over permeate side surface (right). 83

Figure 3.26: Simplified model of the gas diffusion and oxygen permeation in monolithic (left) and supported (right) membranes. 84

Figure 3.27: Oxygen permeation dependence with temperature for the thin supported BSCF membranes. Tests performed using Air or pure O_2 feeding (300 ml·min^{-1}) and Argon sweeping (750 ml·min^{-1}). 85

Figure 3.28: Fracture cross-sections (SEM images) of BSCF membranes without (A) and with (B) a BSCF catalytic layer. 86

Figure 3.29: $J(O_2)$ variation in dependence of temperature for activated/non-activated monolithic BSCF membranes. Synthetic air (pO_2 = 0.21 atm) as feed, Argon as sweep. Q_{air}, Q_{sweep} = 300 ml·min^{-1}. 86

Figure 3.30: SEM cross section images of a BSCF_PF + 5% Pd activated membrane. 88

Figure 3.31: Oxygen permeation in dependence of temperature and different catalytic coatings applied on a 60 μm-thick supported BSCF membrane. Tests performed under Air/Ar gradient (300 ml·min^{-1} Air, 750 ml·min^{-1} Argon). 89

Figure 3.32: Oxygen permeation in dependence of temperature and different catalytic coatings applied on a 60 μm-thick supported BSCF membrane. Tests performed under Air/Ar gradient (300 ml·min^{-1} Air, 750 ml·min^{-1} Argon). 90

Figure 3.33: SEM images of the fracture cross section of the BSCF catalytic layer on BSFC membranes after a catalytic test. a) 12 μm thickness, b) the addition of a pore former to the screen-printing ink; 13 μm thickness, c) the addition of a pore former to the screen-printing ink; 26 μm thickness. 92

Figure 3.34: Ethylene selectivity versus ethane conversion for experiments performed with BSCF MRs. Different porosities of the catalytic layer were considered. T=850 ºC, ethane diluted with argon, $Q_{Reaction\ side}$=400 ml·min^{-1}, $Q_{Feed\ side}$=210 ml·min^{-1} (pO_2=0.04 atm). 93

Figure 3.35: Catalytic performance of the modified BSCF MRs in the ODHE reaction as a function of the thickness of the catalytic layer: 13 and 26 μm. a) Ethane conversion and ethylene selectivity; b) ethylene yields obtained in BSCF MRs. T=850 ºC, ethane diluted with argon, $Q_{Reaction\ side}$=400 ml·min^{-1}, $Q_{Feed\ side}$=210 ml·min^{-1} (pO_2=0.04 atm). 94

Figure 3.36: Catalytic performance of the modified BSCF MR in the ODHE reaction in terms of ethylene selectivity as a function of ethane conversion. Data for various catalytic dense MRs reported in literature: 1) Mirodatos et al. [37]; 2) Akin and Lin [31]; 3) Yang et al. [30]; 4) Caro et al. [42]; 5) Wang et al. [40] 95

Figure 3.37: Catalytic tests with high ethane concentrations in the feed stream. Ethylene productivity obtained with the catalytic coating and ethylene selectivity versus ethane conversion (inset) are shown. T=850 ºC, ethane diluted with argon, QReaction side=400 ml·min^{-1}. 96

Figure 3.38: BSCF capillaries used during permeation/reaction characterization. Dead end closing detailed in picture below. 98

Figure 3.39: SEM cross-section views of a BSCF capillary. 98

Figure 3.40: Oxygen permeation dependence with temperature when varying sweep flow rates (left) and pO_2 in feed stream (right). Q_{feed} = 200 ml·min^{-1} 100

Figure 3.41: Graphic representation of the SiC particles reducing the effective surface area for oxygen permeation. 102

Figure 3.42: Comparison of the oxygen permeation corresponding to a capillary and a planar disk-shaped membranes. Flow conditions for capillary: Q_{feed} = 200 ml·min^{-1}, Q_{sweep} = 300 ml·min^{-1}. Flow conditions for disk: Q_{feed} = 300 ml·min^{-1}, Q_{sweep} = 300 ml·min^{-1}. 102

Figure 3.43: Simplified reaction scheme of a kinetic model for OCM. Adapted from Stansch et al. [51] 103

Figure 3.44: Schematic representation of the experimental set used for the OCM tests. 104

Figure 3.45: Effect of the variation of space velocity on the methane conversion, products selectivity, C_2 yield and oxygen permeation. 106

Figure 3.46: Product yields in dependence of methane conversion. 107

Figure 3.47: Effect of the variation of CH_4 content in reactant gas stream on the methane conversion, products selectivity, C_2 yield and oxygen permeation. 108

Figure 3.48: Contour plot displaying $J(O_2)$ (in ml·min^{-1}·cm^{-2}) when varying pO_2 in feed and GHSV. 110

Figure 3.49: Contour plot displaying X_{CH4} (%) when varying GHSV and $J(O_2)$. 111

Figure 3.50: Contour plot displaying S_{C2} (%) when varying GHSV and $J(O_2)$. 112

Figure 3.51: Contour plot displaying Y_{C2} (%) when varying GHSV and $J(O_2)$.... 113

Figure 3.52: Contour maps displaying C_2H_4/C_2H_6 relation when varying GHSV and $J(O_2)$............ 114

Figure 3.53: SEM images of (a) surface of a fresh BSCF capillary, (b) surface of an OCM-tested BSCF capillary, and (c) reaction side cross-section view of a BSCF capillary after OCM test. 115

Figure 3.54: XRD patterns of fresh and OCM-tested BSCF capillaries compared to BSCF structure. 115

Figure 4.55: Fracture cross sections (SEM images) of the two membranes before oxygen permeation measurement: (a and b) bare, (c) with porous activation layer. 126

Figure 4.56: Variation of oxygen flux as a function of temperature and sweep gas flow rate. The feed consisted of synthetic air. (Inset: relative oxygen flux improvement in % with respect to Q_{Ar} = 300 ml·min^{-1}). 127

Figure 4.57: Variation of oxygen flux as a function of temperature and sweep gas flow rate. The feed consisted of pure oxygen. (Inset: relative oxygen flux improvement in % with respect to Q_{Ar} = 300 ml·min^{-1}). 129

Figure 4.58: Oxygen permeation flux as a function of temperature and feed stream composition. (Q_{sweep} = 300 ml·min^{-1} Argon). Inset: Relative improvement (with respect to pO_2 = 0.21 atm in He results) of the oxygen flux as a function of temperature and pO_2 in the feed (Q_{sweep} = 300 ml·min^{-1} Argon). 130

Figure 4.59: Thermal evolution of the oxygen flux in a wider temperature range (1000 - 600ºC) in air and pure oxygen. (Q_{sweep} = 300 ml·min^{-1} Argon). Inset: Relative improvement (with respect to pO_2 = 0.21 atm in N_2 results) of the oxygen flux as a function of temperature and pO_2 in the feed.(Q_{sweep} = 300 ml·min^{-1} Argon.)..... 132

Figure 4.60: Concentration profiles across the asymmetric membrane thickness and the corresponding model resistances........ 133

Figure 4.61: LSCF phase transition (rhombohedral ↔ cubic symmetry) as a function of temperature: Percentage of the cubic perovskite in the material as calculated from HT-XRD experiments in air. The line is a guide to the eye....... 134

Figure 4.62: Effect of the catalytic surface activation: Thermal evolution of the permeation flux for the bare and activated membrane using air as feed and argon as sweep gas. Q_{air}=300 ml·min^{-1}, Q_{sweep}=300 ml·min^{-1}. Logarithmic scale. 135

Figure 4.63: Comparison between the measured oxygen fluxes for the bare and activated membrane in dependence of temperature. Q_{O2}=300 ml·min^{-1}, Q_{sweep}=300 ml·min^{-1}. Logarithmic scale........ 135

Figure 4.64: Oxygen permeation fluxes as a function of CO_2 content (in Ar) in the sweep stream. 136

Figure 4.65: Thermogravimetric analysis of LSCF power in air and air with 5% CO_2. 137

Figure 4.66: a) SEM cross-section of the LSCF asymmetric membrane b) magnified view of dense layer in Zone I section, c) oriented pores detail of Zone III and d) optical image of a fracture free-casted support monolith 139

Figure 4.67: Oxygen permeation of three LSCF membranes: Square symbol: monolithic membrane, triangle symbol: asymmetric membrane developed by Jülich and circular symbol: freeze-cast asymmetric membrane. Air and sweep sides fed with 300 mL.min^{-1}.. 141

Figure 4.68: Oxygen permeation flux as a function of Q_{feed} and of the temperature for the freeze-cast asymmetric membrane .Q_{sweep} = 300 ml·min^{-1} and pO_2 in feed = 0.21 atm 142

Figure 4.69: Normalized pressure drop ΔP across two porous support (filled symbol: support elaborated by freeze-casting, empty symbol: support of the asymmetric membrane developed by tape-casting) as a function of the Ar flow rate and at 900ºC. 143

Figure 4.70: Oxygen permeation in dependence of CO_2 content in sweep stream at different temperatures... 144

Figure 4.71: $J(O_2)$ evolution at 850 ºC when increasing and decreasing CO_2 content in sweep stream.. 145

Figure 4.72: Oxygen permeation evolution when rising and dropping T after CO_2 exposure. Test carried out under Air/Argon gradient. 145

Figure 4.73: $J(O_2)$ evolution in dependence of time under 50% CO_2 at 900 ºC. 146

Figure 4.74: FE-SEM images of the surface of the LSCF dense layer (**a**), of the surface of the catalytic porous LSCF layer (**b**), focus on the dense / catalytic porous layers interface (**c**) and global cross-section of the whole asymmetric membrane consisting of the vertically oriented channels porous layer (**1d**), the non-organized porous layer (**2d**), the dense LSCF layer (**3d**) and the 30 µm-thick LSCF porous catalytic layer (**4d**). 147

Figure 4.75: XRD patterns of the starting LSCF powder sintered, of the activated LSCF freeze-cast membrane before and after permeation and stability tests under CO_2. 148

Figure 4.76: Oxygen permeation flux through the activated freeze-cast asymmetric membrane as a function of temperature and of pO_2 in the feed flow................. 149

Figure 4.77: Oxygen permeation flux as a function of inverse temperature for two membranes: LSCF freeze-cast asymmetric membrane: solid symbols; activated LSCF freeze-cast asymmetric membrane: empty symbols Feed gas: 300 mL min^{-1} of air. Sweep gas: 300 mL min^{-1} of argon.. 150

Figure 4.78: Oxygen permeation flux through the activated freeze-cast asymmetric membrane (solid symbols) and through the freeze-cast asymmetric membrane (empty symbols) as a function of temperature and of the CO_2 content in the sweep gas 152

Figure 4.79: Arrhenius plot for the oxygen flux through the activated membrane for different CO_2 contents. Inset: comparison of CO_2 effect as a function of temperature for the bare and activated membranes. 152

Figure 4.80: Oxygen permeation flux at 850 ºC as a function of time for the activated freeze-cast membrane under a 50% CO_2-containing flux in argon as sweep gas (total flux 300 ml·min^{-1}). The feed stream is composed by 300 ml·min^{-1} of air. 153

Figure 5.81: SEM images of an as fabricated asymmetric CGO membrane: a) Membrane fracture cross section. b) Surface of CGO dense top layer. c) and d) Fracture cross section details of the porous support. 165

Figure 5.82: XRD pattern of an as-fabricated asymmetric CGO membrane. 166

Figure 5.83: Oxygen permeation in dependence of temperature under different sweep environments: Ar, CO_2 and 10% CH_4 in Ar (300 ml·min^{-1}). Synthetic air feeding for all the cases (300 ml·min^{-1}) 167

Figure 5.84: Oxygen permeation dependence on pO_2 in feed stream at different temperatures. Fill symbols correspond to O_2/He mixtures whereas void symbols correspond to O_2/N_2 mixtures. 169

Figure 5.85: Oxygen fluxes in dependence of CO_2 content in sweep stream at different temperatures- Air feeding (300 ml·min^{-1}). 170

Figure 5.86: Oxygen permeation in dependence of methane content in the sweep stream (300 ml·min^{-1}) at 1000 ºC. Synthetic air as feed gas (300 ml·min^{-1}). 171

Figure 5.87: Experimental procedure for the CO_2 stability. Synthetic air feeding (300 ml·min^{-1}) in all the steps. 172

Figure 5.88: Oxygen permeation evolution with time under Air/15% CO_2 in Ar gradient at 750 ºC. 173

Figure 5.89: Effect of increasing temperature in J(O_2) after 48 hours exposition under 15% CO_2 in Argon. 173

Figure 5.90: XRD measurements before and after CO_2 annealing during 48 hours at 750 ºC. 174

Figure 5.91: Raman spectra of CGO-Pd powder before and after CO_2 annealing. 175

Figure 5.92: a) Surface SEM image of an as-fabricated CGO membrane, b) surface and c) cross section pictures of a Pr-activated CGO membrane after test. d) XRD measurement of CGO membrane after test. 176

Figure 5.93: EDS mapping analysis performed on Pd particles. 177

Figure 6.94: XRD patterns of NFO-CTO composite membranes at room temperature compared with CeO_2 fluorite and Fe_2NiO_4 spinel structure. 185

Figure 6.95: a) SEM image of the cross section corresponding to 50% NFO – 50% CTO composite. b) BSD-SEM detailed view of the interface catalytic layer-membrane on 50% NFO – 50% CTO composite. c) BSD-SEM images of composites membranes with different CTO content. 186

Figure 6.96: a) Arrhenius plot of the total electrical conductivity in air for the considered composite formulations. b) Total electrical conductivity in air of the NFO-CTO composites as a function of the CTO content, measured at 800 °C. c) Logarithm total electrical conductivity at 800 °C as a function of the pO_2. 187

Figure 6.97: a) Oxygen permeation as a function of temperature for different membrane compositions when using 100 $ml·min^{-1}$ synthetic air feeding and 300 $ml·min^{-1}$ Argon sweeping. (Inset: Oxygen permeation in dependence of temperature when sweeping with CO_2.) b) Ambipolar conductivity and c) oxygen permeation in dependence of CTO content (in %) at several temperatures. 188

Figure 6.98: a) Oxygen permeation of 50% NFO – 50% CTO membrane as a function of CO_2 content in sweep stream (300 $ml·min^{-1}$) when feeding with synthetic air (100 $ml·min^{-1}$) at several temperatures. b) Oxygen permeation of 50% NFO – 50% CTO membrane in dependence of temperature when sweeping with 100% CO_2 and 250 ppm SO_2 in CO_2 (150 $ml·min^{-1}$). Synthetic air feeding (100 $ml·\ min^{-1}$). 190

Figure 6.99: Oxygen permeation evolution with time, at different sweeping conditions and temperatures of 50% NFO -50% CTO membrane. From these results Figure 6.98b is built. 191

Figure 6.100: a) Oxygen permeation of 50% NFO – 50% CTO membrane at 850 ºC in function of time under Argon and CO_2 sweeping (150 $ml·min^{-1}$). b) Oxygen permeation of 50% NFO – 50% CTO membrane at 850 ºC in dependence of time under Argon and 250 ppm SO_2 in CO_2 sweeping (150 $ml·min^{-1}$). 193

Figure 6.101: a) BSD-SEM picture corresponding to 50% NFO -50% CTO membrane interface after testing. b) EDS mapping corresponding to area depicted in Figure 5a after testing. c) XRD patterns of 50% NFO -50% CTO membrane after testing. 194

Figure 6.102: a) Nyquist plot and b) BODE plot at different gas compositions at 850 ºC for a 60NFO-40CTO electrode. c) BODE plot corresponding to electrode performance under 5% O_2 in N_2 before and after SO_2 exposure at 850 ºC. d) SEM image of the cross-section corresponding to the symmetric cell measured by means of EIS. 196

Figure 6.103: Polarization resitance (left) and Nyquist plots (right) in dependence of gas composition and temperature. 197

Figure 6.104: XRD patterns of some 60NFO-40CTO activated cases and a comparison with respect the not activated case (Ref). Au peaks belong to gold contacts. 198

Figure 6.105: Polarization resistance values of dual-phase backbones infiltrated with different elements. Values extracted from EIS measurements performed at 850 ºC. 199

Figure 6.106: BODE plots of the different catalysts under the tested environments at 850 ºC. Molybdenum-infiltrated case is presented in Insets. 200

Figure 6.107: BODE plots of 5% O_2 in N_2 tests before and after SO_2 exposure. 201

Figure 6.108: BSD-SEM pictures of different 60NFO-40CTO backbones: (a) not activated, (b) Pr-infiltrated, (c) Ce-infiltrated and (d) Al-infiltrated, after EIS tests. 202

Figure 6.109: Oxygen permeation tests on bare and activated membranes. (a) Oxygen permeation in dependence of temperature under clean conditions (Air/Ar gradient). (b) Oxygen permeation as function of time under different environments at 850 ºC. For all the tests air was used as feed gas (100 ml·min^{-1}) and mixtures of Ar as sweep gas (150 ml·min^{-1}). 203

Figure 6.110: a) Inverse of polarization resistance under different environments and % value loss for every catalyst when exposing to SO_2. b) J(O_2) values under different environments and permeation loss when adding SO_2 to the sweep. ... 206

Figure 6.111: XRD patterns of the NFO/CTO dual-phase prepared by a one-pot Pechini synthesis and sintered at 1200 ºC, of the LSCF perovskite and of both mixtures of NFO/CTO and LSCF powders annealed 50 hours at 1000 ºC and 6 hours at 1400 ºC. 207

Figure 6.112: Cross sections of the coated freeze-cast support (**a**), cross section of the non-organized porosity layer and composite dense top layer (**b**) cross section focus on the interface between the LSCF freeze-cast support and the NFO/CTO dense top-layer (**c**) and surface of NFO/CTO dense top-layer (**d**). 208

Figure 6.113: XRD patterns of the NFO/CTO dual-phase elaborated by a one-pot Pechini method and sintered at 1200 ºC, of the LSCF perovskite and of dense top-layer after sintering 6 hours at 1400 ºC. 209

Figure 6.114: Oxygen permeation as a function of temperature for two membranes. Solid symbols: Freeze-cast membrane constituted by a LSCF support and a 8 µm 60NFO-40CTO dual phase dense top-layer. Empty symbols: Monolithic 0.68 mm thick 60NFO-40CTO dense membrane. Q_{feed} = 300 ml·min^{-1}. Q_{sweep} = 300 ml·min^{-1}. 210

Figure 6.115: a) Oxygen permeation in dependence of temperature and sweep gas flow. Air/Ar gradient. Q_{feed} = 300 ml·min^{-1}. b) Oxygen permeation in dependence of pO_2 in feed stream. Argon sweeping. Q_{feed} = 300 ml·min^{-1}. 211

Figure 6.116: Oxygen permeation flux through the asymmetric membrane as a function of temperature and of the CO_2 content in the sweep gas. 212

Figure 6.117: Influence of 10% of methane in the sweep gas over oxygen permeation flux through the asymmetric membrane. Feed gas: 300 ml·min^{-1} of air. Sweep gas: 300 ml· min^{-1}. 213

Figure 6.118: Oxygen permeation flux at 950 ºC as a function of time for the asymmetric freeze-cast membrane under a 50% CO_2-containing flux in argon as sweep gas (total flux 300 ml·min^{-1}). The feed stream is composed by 300 ml·min^{-1} of air. 214

10.2. Tables.

Table 1.1: World use of oxygen for the production of chemicals and steel in 2004 [55]. 46

Table 3.2: Apparent activation energy (E_a) (kJ·mol^{-1}) derived from Figure 3.24 J(O_2) measurements for the different activated. 81

Table 3.3: Catalytic activation conducted on BSCF asymmetric membranes...... 87

Table 3.4: Apparent activation energy (E_a) (kJ·mol^{-1}) derived from Figure 3.31 J(O_2) measurements for the different activated membranes. 89

Table 3.5: Pros and cons of OTMs depending on the geometry for laboratory scale applications. 97

Table 3.6: Percentage of oxygen separated from feed stream through the BSCF capillaries for different tested conditions. Q_{sweep} variation was performed when feeding with pO_2 = 0.21 bar. pO_2 in feed variation was carried out when sweeping with 400 ml·min^{-1} Ar. 101

Table 3.7: C_2 selectivities and yields for different OCM studies conducted on CMRs. 104

Table 3.8: Results of the parametric study conducted on BSCF capillaries at 900 ºC, 10% CH_4 in the reaction stream. 109

Table 4.9: Apparent activation energy (E_a) (kJ·mol^{-1}) derived from J(O_2) measurements for different sweep gas flow rates and pO_2 in feed stream (Q_{feed} = 300 ml·min^{-1}) 128

Table 4.10: Apparent activation energy (E_a) (kJ·mol^{-1}) derived from oxygen permeation measurements using different feed gas compositions ($Q_{feed, sweep}$ = 300 ml(STP)·min^{-1}) 131

Table 6.11: Apparent activation energy (E_a) (KJ·mol^{-1}) derived from oxygen permeation measurements for different dual-phase compositions (pO_2 in feed = 0.21 atm, Q_{feed} = 100 ml(STP)·min^{-1},Q_{sweep} = 300 ml(STP)·min^{-1}) 189

Table 6.12: Apparent activation energy (E_a) (KJ·mol^{-1}) derived from oxygen permeation measurements for different sweeping conditions (pO_2 in feed = 0.21 atm, Q_{feed} = 100 ml(STP)·min^{-1},Q_{sweep} = 150 ml(STP)·min^{-1}) 192

Table 6.13: EIS test conditions. 196

Table 6.14: Apparent activation energy (E_a) (kJ·mol^{-1}) derived from oxygen permeation measurements shown in Figure 6.109. 204

Table 6.15: Activation energy as a function of temperature for the freeze-cast membrane and for the monolithic 0.68 mm thick 60NFO-40CTO membranes.. 210

```
RANDOMIZE USR 0 L
```